UNIVERSITY OF CALIFORNIA SAN DIEGO

SAN DIEGO STATE UNIVERSITY

Understanding of the Structure-Function Relationship of Tumor-Relevant IDH1 Mutants: A Kinetic Investigation

A dissertation submitted in partial satisfaction of the requirements for the degree

Doctor in Philosophy

in

Chemistry

by

Diego Enri Avellaneda Matteo

Committee in Charge:

University of California San Diego

Professor Patricia Jennings
Professor Katja Lindenberg

San Diego State University

Professor Christal Sohl, Chair
Professor Sanford Bernstein
Professor Tom Huxford

2020

This dissertation of Diego Enri Avellaneda Matteo is approved, and it is acceptable in quality and form for publication on microfilm and electronically:

_____

_____

_____

_____

_____

Chair

University of California San Diego

San Diego State University

2020

DEDICATION

I would like to dedicate this dissertation to my wife, my daughter, my mother, my brother and aunts, and my dad, who rests in peace, for their unconditional love and support throughout my graduate school career.

TABLE OF CONTENTS

LIST OF ABREVIATIONS

AML	Acute Myeloid Leukemia
TCA Cycle	Tricarboxylic Acid Cycle
GBM	Glioblastoma Multiforme
k_{cat}	Turnover Rate Constant
K_M	Michaelis-Menten Constant
k_{cat}/K_M	Catalytic Efficiency
°C	Degree Celsius
mM	Millimolar
SDS-PAGE	Sodium Dodecyl Sulfate Polyacrylamide Gel Electrophoresis
CD	Circular Dichroism
T_m	Melting Temperature
nmols	Nanomoles
µM	Micromolar
FDA	Food Drug Administration
Ni-NTA	Nickle Nitrilotriacetic Acid
OD_{600}	Optical Density at 600 nm
SAXS	Small-Angle X-Ray Scattering

MD	Molecular Dynamics
TB	Terrific Broth
RMSF	Root Mean Square Fluctuation
ND	Not Determined
Å	Angstrom
ITC	Isothermal Titration Calorimetry
IC_{50}	Inhibitory Concentration at 50%
FPLC	Fast Protein Liquid Chromatography
UPLC	Ultra-Performance Liquid Chromatography
W	Watts
K	Kelvin
WT	Wild Type
MS	Mass Spectrometer
HDX-MS	Hydrogen/Deuterium Exchange – Mass Spectrometer
K_D	Dissociation Constant
Da	Dalton
PDB	Protein Data Bank
SEC	Size Exclusion Chromatography

Small Molecules:

ICT	Isocitrate
αKG	α-ketoglutarate
D2HG	D-2-Hydroxyglutarate
$NADP^+$	Nicotinamide Adenine Dinucleotide Phosphate Oxidized
NADPH	Nicotinamide Adenine Dinucleotide Phosphate Reduced
DTT	Dithiothreitol
IPTG	1-thiol-β-D-galactopyranoside
β-ME	β-Mercaptoethanol
DMSO	Dimethyl sulfoxide

Proteins:

IDH1	Isocitrate Dehydrogenase 1
IDH2	Isocitrate Dehydrogenase 2
IDH3	Isocitrate Dehydrogenase 3
BSA	Bovine Serum Albumin

LIST OF FIGURES

Chapter 1 Figures

Chapter 2 Figures

LIST OF TABLES

Chapter 2 Tables

Chapter 3 Tables

Chapter 4 Tables

ACKNOWLEDGEMENTS

Chapter 2 is reproduced and re-written in full with permission from Avellaneda Matteo, D.; Grunseth, A. J.; Gonzalez, E. R.; Anselmo, S. L.; Kenedy, M. A.; Moman, P.; Scott, D. A; Hoang, A.; and Sohl, C. D. Molecular mechanisms of isocitrate dehydrogenase 1 (IDH1) mutations identified in tumors: The role of size and hydrophobicity at residue 132 on catalytic efficiency. *J Biol Chem* **2017**, 292 (19), 7971-7983. Copyright 2017 Journal of Biological Chemistry. The dissertation author was the first author.

Chapter 3 is reproduced and re-written in full with permission from Avellaneda Matteo, D.; Wells, G. A.; Luna, L. A.; Grunseth, A. J.; Zagnitko, O.; Scott, D. A.; Hoang, A.; Luthra, A.; Swairjo, M. A.; Schiffer, J. M.; Sohl, C. D., Inhibitor potency varies widely among tumor-relevant human isocitrate dehydrogenase 1 mutants. *Biochem J* **2018,** *475* (20), 3221-3238. Copyright 2018 Biochemical Journal. The dissertation author was the first author.

I would like to thank Dr. Christal Sohl for guiding, teaching, supporting, and mentoring me throughout these few years. When I joined Dr. Christal Sohl's laboratory, we lacked all instrumentations since she was a new PI in the department. I would also like to thank Dr. Sohl for have given me the opportunity to help her laboratory become so successful from the ground up. During my time at the Sohl Laboratory, I met wonderful people who I am thankful to have had the opportunity to call colleagues and friends. I would also like to thank Dr. David Scott and Dr. Olga Zagnitko for the D2HG quantification from Chapter 1 and 2. I would like to thank Dr. Jamie Schiffer for performing such extensive MD simulations and for allowing me to observe and learn a very complexed methodology. I would like to thank Dr. Manal Swairjo and Dr. Amit Luthra for performing SAXS experiments and teaching me the data analysis. I would like to thank Dr. Steve Silletti for performing hydrogen deuterium exchange experiments for chapter 4 and taking the time

to teach me the data analysis. I would like to thank Dr. Andrey Bobkov for performing ITC experiments for chapter 4. I would like to thank all other authors who helped me in the lab to get these experiments completed. I would like to thank my beautiful wife and family for all their support even when things got tough. To Matthew Mealka, thanks for staying out shooting crystals overnight so many times. I am beyond grateful to be a recipient of the Arne N. Wick Pre-Doctoral Research Fellowship from the California Metabolic Research Foundation for the Academic Year 2019-2020.

VITA

Education

2015	B.S. Biochemistry San Jose State University
2020	Ph.D. Chemistry University of California San Diego and San Diego State University

Employment History

2013-2015	Undergraduate Research Assistant San Jose State University, San Jose, CA
2014-2015	General Chemistry Workshop Facilitator San Jose State University, San Jose, CA
2015-2019	Teaching Assistant San Diego State University, San Diego, CA

Publications

Chambers, J. M.; Miller, W.; Quichocho, G.; Upadhye, V.; **Avellaneda Matteo, D.**; Bobkov, A. A.; Sohl, C. D.; Schiffer, J. M., Water Networks and Correlated Motions in Mutant Isocitrate Dehydrogenase 1 (IDH1) Are Critical for Allosteric Inhibitor Binding and Activity. *Biochemistry* **2020**, *59* (4), 479-490

Avellaneda Matteo, D.; Wells, G. A.; Luna, L. A.; Grunseth, A. J.; Zagnitko, O.; Scott, D. A.; Hoang, A.; Luthra, A.; Swairjo, M. A.; Schiffer, J. M.; Sohl, C. D., Inhibitor potency varies widely among tumor-relevant human isocitrate dehydrogenase 1 mutants. *Biochem J* **2018,** *475* (20), 3221-3238.

Avellaneda Matteo, D.; Grunseth, A. J.; Gonzalez, E. R.; Anselmo, S. L.; Kennedy, M. A.; Moman, P.; Scott, D. A.; Hoang, A.; Sohl, C. D., Molecular mechanisms of isocitrate dehydrogenase 1 (IDH1) mutations identified in tumors: The role of size and hydrophobicity at residue 132 on catalytic efficiency. *J Biol Chem* **2017,** *292* (19), 7971-7983.

Awards and Fellowships

2017	The Chemistry and Biochemistry Department Graduate Research Award
2018-2020	The Chancellor Doctoral Incentive Program
2019-2020	Tom Ragan Memorial Endowed Fellowship
2019-2020	Arne N. Wick Predoctoral Fellowship

ABSTRACT OF THE DISSERTATION

Understanding of the Structure-Function Relationship of Tumor-Relevant IDH1 Mutants: A Kinetic Investigation

by

Diego Enrique Domingo Avellaneda Matteo

Doctor of Philosophy in Chemistry

University of California San Diego, 2020

San Diego State University, 2020

Professor Christal D. Sohl, Chair

Changes in cancer cell metabolism were first described by Otto Warburg in the early 1900s, but it was not until relatively recently that specific metabolic enzymes were shown to drive tumorigenesis and tumor growth. An example of a metabolic enzyme driving tumor formation is isocitrate dehydrogenase 1. Mutations in isocitrate dehydrogenase 1 (IDH1), more specificly at residue 132, were first linked to brain cancer in 2008. IDH1 is responsible for converting isocitrate and $NADP^+$ to α-ketoglutarate (αKG) and NADPH. The latter two metabolites are crucial for many

metabolic cell processes. However, when IDH1 is mutated, this enzyme cannot perform its normal catalysis, but instead gains a neomorphic activity of converting αKG to D-2-hydroxyglutarte (D2HG), depleting NADPH. D2HG promotes oncogenesis by inhibiting αKG -dependent enzymes, including those involved in gene regulation. The goal of this dissertation is to understand the structure-function relationship of tumor-relevant IDH1 mutants using, kinetic and other biophysical methods.

Steady-state kinetics was used to characterize the catalytic profile of several tumor-relevant and experimental IDH1 mutants. These mutants had a wide range in catalytic efficiency, providing a foundation for predicting disease severity depending on the mutant seen in patients. Inhibition studies revealed that small molecule inhibitor affinity varied widely among mutant IDH1 forms, providing a solid foundation for predicting how patients may respond to therapeutics as well as possible resistance mutation that may arise from targeted therapy. Lastly, a comprehensive catalytic cycle for D2HG production by tumor-relevant IDH1 mutants was established using pre-steady-state kinetics as well as biochemical and biophysical methodologies. This work determined a wide variation in intrinsic rate constants associated to substrate binding, thus revealing key kinetic features driving the neomorphic reaction. This highlighted kinetic features that may help explain the mechanistic differences observed among IDH1 mutants.

1. Introduction

1.1. What is cancer?

Cancer is a disease associated to the second leading cause of death worldwide[1]. In 2014, the number of patients with cancer in the United States was over a million people, with over five hundred thousand deaths[2]. Cancer is the uncontrolled growth of cells due to accumulation of genetic alterations throughout the genome, leading to the formation of tumors. A cancerous tumor is complex in terms of its cellular composition and heterogeneous nature. Tumor heterogeneity arises from a variety of genetic alterations including random mutations[3], and as well as from differences in the tumor microenvironment[4]. The tumor microenvironment is made up with interactions between malignant and non-malignant cells[5], with constant communication driven by cytokines, growth factors, and components of the immune system (Figure 1), and can include changes in intracellular and extracellular pH, oxygen levels, and other physical features that can drive tumor growth and metastasis[5-7]. Moreover, tumor heterogeneity leads to therapeutic challenges since a tumor is made up of difference types of cells that may respond differently to drugs. Although tumor heterogeneity is an important issue, cancer researchers, throughout time, have established key tumorigenic characteristics that all cancers do in order to survive, the hallmarks of cancer.

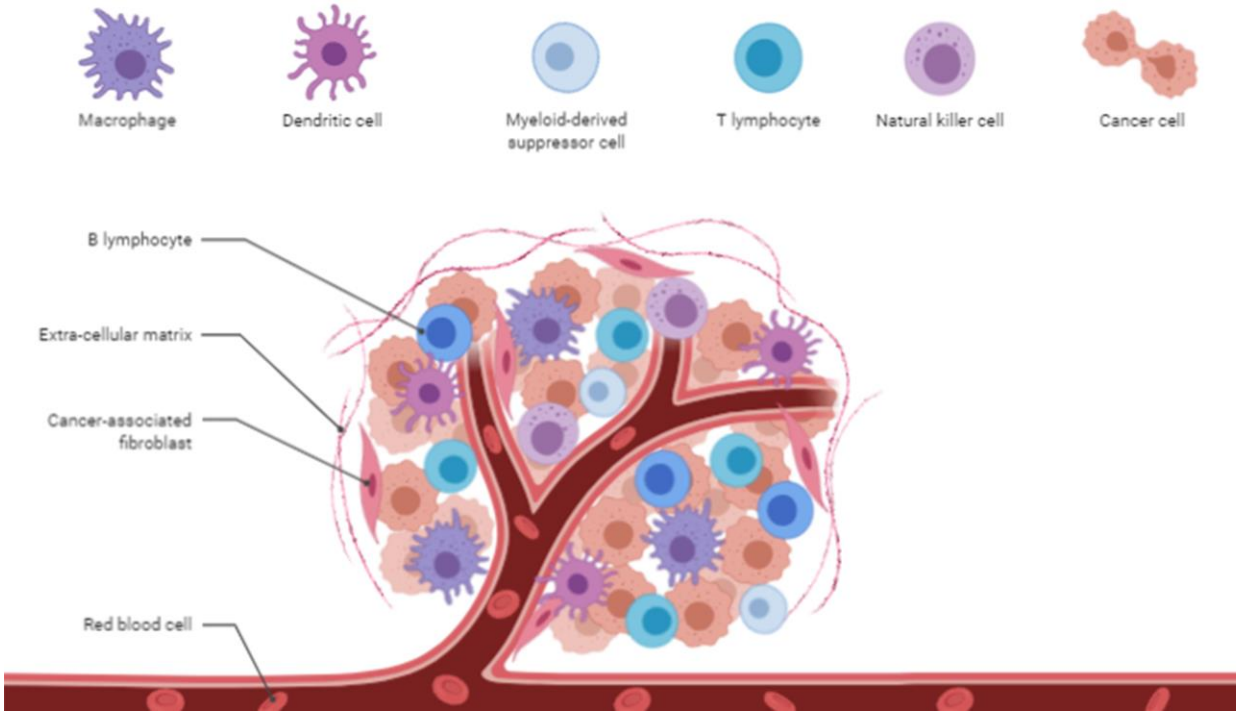

Figure 1. A cartoon representation of a tumor microenvironment. A cancerous tumor is complex consisting of cancerous and non-cancerous cells. Immune cells produce cytokines which are involved in inflammation. The tumor creates blood vessels to fulfill their metabolic needs and to be able to metastasize. This Figure was created in biorender.com

1.2.The Hallmarks of Cancer

There are ten hallmarks of cancer, including cancer metabolism, that have been described[8, 9]. These hallmarks are important for cancer cells to grow uncontrolled as well as to metastasize to other organs, and have allowed cancer researchers to have a better understanding of cancer biology[8]. The original hallmarks of cancer are the ability to evade cell death, sustain proliferative signaling, evade growth suppressors, activate invasion and metastasis, enable replicative immortality, and induce angiogenesis[8]. There have been great advances in each of these hallmarks of cancer, allowing researchers to explain many phenomena associated with this complex disease.

The emerging hallmarks of cancer are the ability to deregulate cellular energetics (cancer metabolism) as well as avoid immune destruction[8]. Alterations in cellular metabolism allow malignant cells to find ways to satisfy energetic needs during fast and uncontrolled growth. Many metabolic pathways may be upregulated while others are downregulated or even completely shut down. Therefore, a deeper understanding of the metabolic shifts that cancer cells employ allows researcher to widen their knowledge of cancer biology, ultimately identifying new pathways to target therapeutically.

1.3. Cancer Metabolism

Cells gain their energy by metabolizing various nutrients through many pathways. For example, when glucose enters the cell, it goes through glycolysis, a ten-step metabolic pathway. During this process, glucose gets catabolized to two pyruvate molecules and a net gain of two ATP molecules and one NADH molecule that is required for the electron transport chain and oxidative phosphorylation. In aerobic conditions, pyruvate is taken into the TCA cycle to produce electron-carrying molecules such as NADH and $FADH_2$. These molecules carry electrons through different enzymatic complexes to produce ATP, while oxygen is converted to water. Glycolysis is a cytosolic process while the TCA cycle and electron transport chain reaction happen in the mitochondria (Figure 2). The largest source of energy produced within these metabolic processes are via the TCA cycle and the electron transport chain during oxidative phosphorylation.

When cells become cancerous, they undergo shifts in metabolic processes. Otto Warburg was the first to describe changes in cancer cell metabolism a century ago[10]. He found that cancer cells shift their main energy from the electron transport chain and oxidative phosphorylation to glycolysis even under aerobic conditions[10, 11]. This is known as aerobic glycolysis, or the Warburg

effect. While Warburg initially postulated that such metabolic rewiring was due to mitochondrial defects, we now know this is usually not the case.

A reliance on glycolysis allows down-regulation of the TCA cycle since the demands of those electron carrier molecules is less. Glycolysis is in turn upregulated to meet energy demand. Since the amount of NAD^+ is reduced but is still required for glycolysis, lactate dehydrogenase can convert pyruvate and NADH to lactate and NAD^+ (Figure 2) to fulfill this need. The production of NAD^+ by lactate dehydrogenase is crucial to keep glycolysis running. Interestingly, the Warburg effect is not the only example of metabolic alterations found in cancer; other metabolic enzymes have been linked to alterations in enzymatic activity. Isocitrate dehydrogenase 1 (IDH1) is an example where a point mutation facilitates a change in metabolism. IDH1 will be described in detail throughout this dissertation.

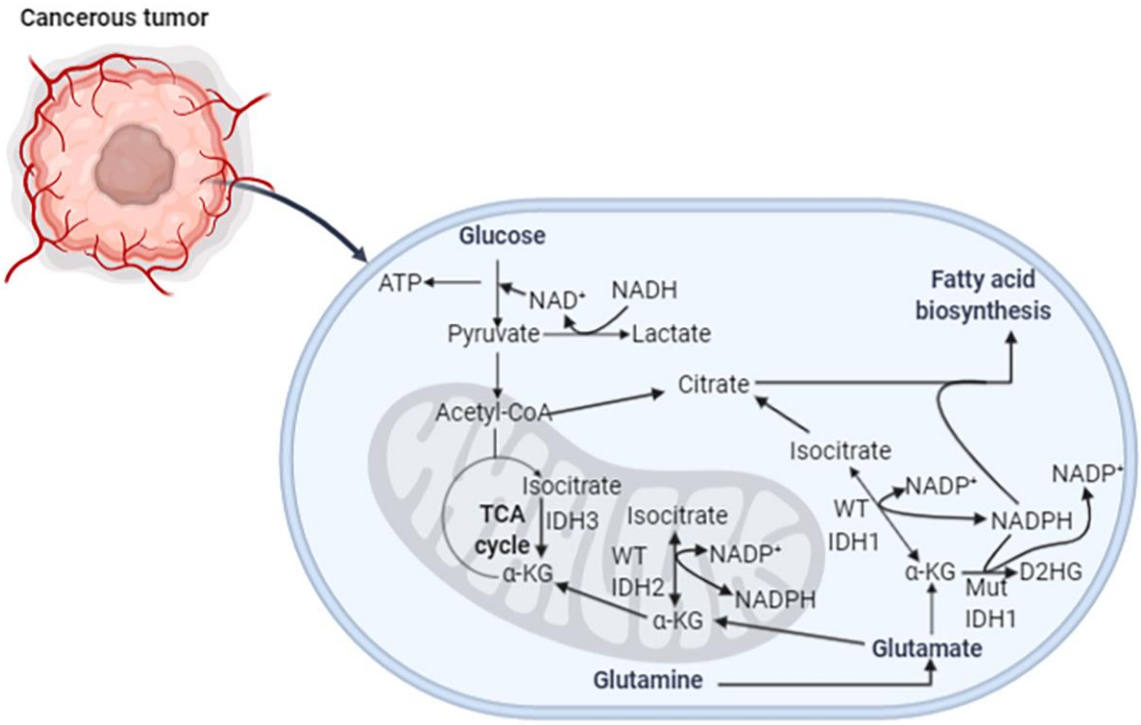

Figure 2. A cartoon representation of different metabolic pathways in the cell. During the Warburg effect, the TCA cycle is downregulated while glycolysis is upregulated. Lactate dehydrogenase converts pyruvate to lactate by taking intracellular NADH to produce NAD^+ required for glycolysis. This Figure was created in biorander.com

1.4.The Discovery of IDH1 Mutations in Gliomas

Gliomas are the most common as well as the deadliest type of brain cancer[12], with glioblastoma multiforme (GBM) serving as the most aggressive and lethal form of glioma[13]. Moreover, the average survival rate of patients harboring GBMs is 15 months[14]. Parsons and colleagues performed an extensive sequencing of over 20,000 protein-encoding genes in patients with gliomas[12]. They found that IDH1 mutations were very common in patients with GBMs[12], with those patients having longer survival rates than those with WT IDH1[12]. This observation and the importance of targeting IDH1 mutations with therapeutics is still under study; however, molecular mechanisms be described in detail later in this dissertation. Later that same year, Balss and colleagues further characteried the specific mutation in the IDH1 gene[15].

1.5. Incidence of IDH1 Mutations in Cancer

Soon after Parsons and colleagues discovered that the IDH1 gene was mutated in high frequencies in patients harboring GBMs[12], deeper details about these mutations were discovered[15]. Balss and colleagues found that mutations in the IDH1 protein sequence affected a particular amino acid R132[15]. This residue is important since it coordinates the carboxylate at carbon three of the substrate isocitrate (ICT)[15, 16]. The frequency in which mutations at R132 were found in gliomas were as high as 80%, and over 88% in more advanced secondary glioblastomas (grade IV secondary glioma)[15, 17]. In gliomas, the most common IDH1 mutation is R132H, followed by R132C, R132S, R132G, R132L, and R132V[15]. Although IDH1 mutations are primarily seen in gliomas, other cancers such as chondrosarcomas and acute myeloid leukemias (AML) have also been found to have IDH1 mutations[18]. However, in AML, the most common IDH1 mutant is R132C IDH1[18]. In another study including a small sample size of chondrosarcoma tumors, half of the patients had showed IDH1 mutations, including R132C and R132Q[19], the latter of which will

be described in detail in this dissertation. The high frequency of mutations as well as the diversity of the R132 mutants intrigued the scientific community and has become a hot area of study in cancer research.

1.6. IDH1 Activity and Function

The family of isocitrate dehydrogenases have three isoforms (IDH1, IDH2, and IDH3) (Figure 2). IDH1 and IDH2 are homodimeric metabolic enzymes responsible for the reversible-$NADP^+$-and Mg^{2+}-dependent oxidative decarboxylation of ICT to α-ketoglutarate (αKG) in the cytosol and peroxisomes of the cell[16, 20] (Figures 2, 3A, 4A). IDH2 catalyzes the same reaction as IDH1 with the same co-factors, but it is located in the mitochondria and is also linked to cancer (Figure 2)[21]. Although IDH3 performs the same chemistry, it is a tetrameric NAD^+-dependent enzyme that catalyzes this reaction non-reversibly (Figure 2). Likely, due to its critical role in the TCA cycle, mutations in this enzyme have not been linked to cancer. IDH2 and IDH3 will not be described in detail in this dissertation.

The reaction that IDH1 catalyzes yields important metabolic intermediates involved in other metabolic pathways and gene regulation. NADPH is essential for many metabolic processes such as lipid biosynthesis as well as mitigating reactive oxygen species by the regeneration of oxidized glutathione (Figure 2)[22]. αKG is used in the TCA cycle by αKG dehydrogenase to yield electron carriers that are crucial for production of ATP in the electron transport chain (Figure 2). Moreover, many αKG-dependent enzymes are involved in DNA repair and DNA and histone demethylation, such as methylcytosine dioxygenases and JmjC lysine demthylases[23-25]. Due to the loss of normal activity observed upon acquisition of point mutations at residue R132, IDH1 could

be considered a tumor suppressor gene. However, in 2009, Dang and colleagues discovered a novel effect of mutations in IDH1[26] and that changed the way we describe its role in cancer.

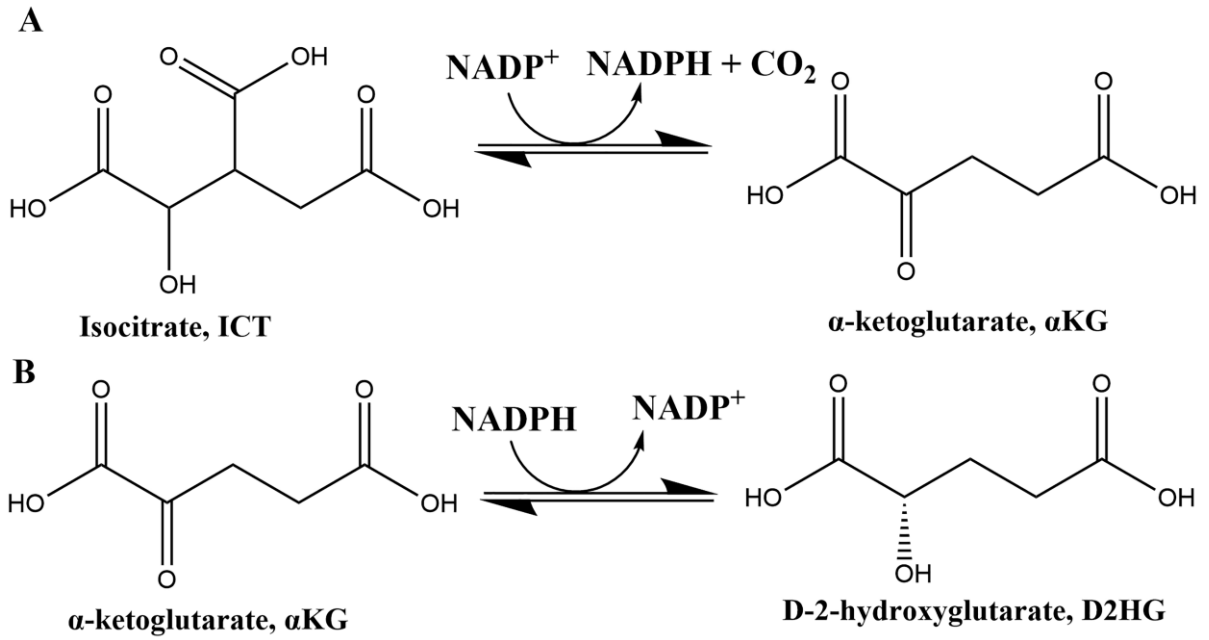

Figure 3. A. Oxidative decarboxylation of ICT to αKG producing NADPH and CO_2. This is the reaction performed by WT IDH1. **B.** Reduction of αKG to D2HG depleting NADPH. This is the reaction performed by mutant IDH1

IDH1 mutations are found heterozygously in patients[27], and it is postulated that mutant IDH1 forms heterodimers of a WT and mutant monomer[17, 27]. When R132 is mutated, IDH1 loses its ability to convert ICT to αKG, and hence it was initially labeled as a tumor suppressor gene[28]. Surprisingly, R132 IDH1 mutants also gain a neomorphic reaction: the NADPH-and Mg^{2+}-dependent reduction of αKG to form D-2-hydroxyglutarate (D2HG) (Figure 3B)[26]. D2HG is an oncometabolite since its production generates pro-tumor environment. Specifically, it acts as a competitive inhibitor against αKG-dependent enzymes, many of which are involved in gene regulation and DNA repair[29], including the inhibition of DNA and histone dimethylases[25]. Therefore, patients harboring IDH1 mutations have hypermethylated genomes, leading to cell de-

differentiation[30]. Due to these downstream effects resulting from D2HG, IDH1 point mutations are better described as oncogenes.

D2HG is a dead-end metabolite in that it does not get metabolized further, and can build up to mM levels in patients[31]. In 2014, Pusch and colleagues measured intracellular concentrations of this oncometabolite derived from cancer patients[31]. D2HG levels in tumor and cells varied depending on the IDH1 mutation present, with a trend of R132G>R132C>R132H IDH1 (listed in order from highest to lowest D2HG levels)[31]. These observations led our interest in understanding how the enzymatic activity of these mutants drove tumor levels of D2HG as well as establishing how physical characteristics, such as size and degree of hydrophobicity of the mutation at R132, affecting neomorphic activity[20]. This work will be described in Chapter II.

1.7. The Structure of IDH1

The first human IDH1 crystal structure was published by Xu and colleagues in 2004[16]. The enzyme is a dimer with 414 residues per monomer (Figure 4A)[16]. IDH1 is mostly α-helical with a few β-sheets[16]. The residues in the active site that interact with ICT are T77, S94, R100, R109, R132, Y139, and D275 of one monomer and K212', T214', and D252' of the other monomer (Figure 4B)[16]. These residues are all well-conserved except for T214, which it is replaced with an asparagine in bacterial IDH[16]. Xu and colleagues described that the enzyme has a regulatory domain made up the by α-10 helix[16]. This regulatory segment starts at N271 and ends at G286[16]. When the substrate is not bound to the enzyme D279 interacts with S94 to support the open, inactive conformation[16]. This interaction mimics the phosphorylation of a serine in bacterial IDH, which uses a different regulatory strategy than the human form[16]. When ICT binds to the active site, D279 loses this interaction with S94, and instead S94 interacts with the substrate ICT[16]. This drives the folding of the regulatory segment through D275 interacting with the metal cation and

ICT[16] to help support the oxidative decarboxylation of ICT to form αKG. The mechanism of folding of the regulatory segment is particularly important in terms of inhibitor binding, and it will be described later in this introduction.

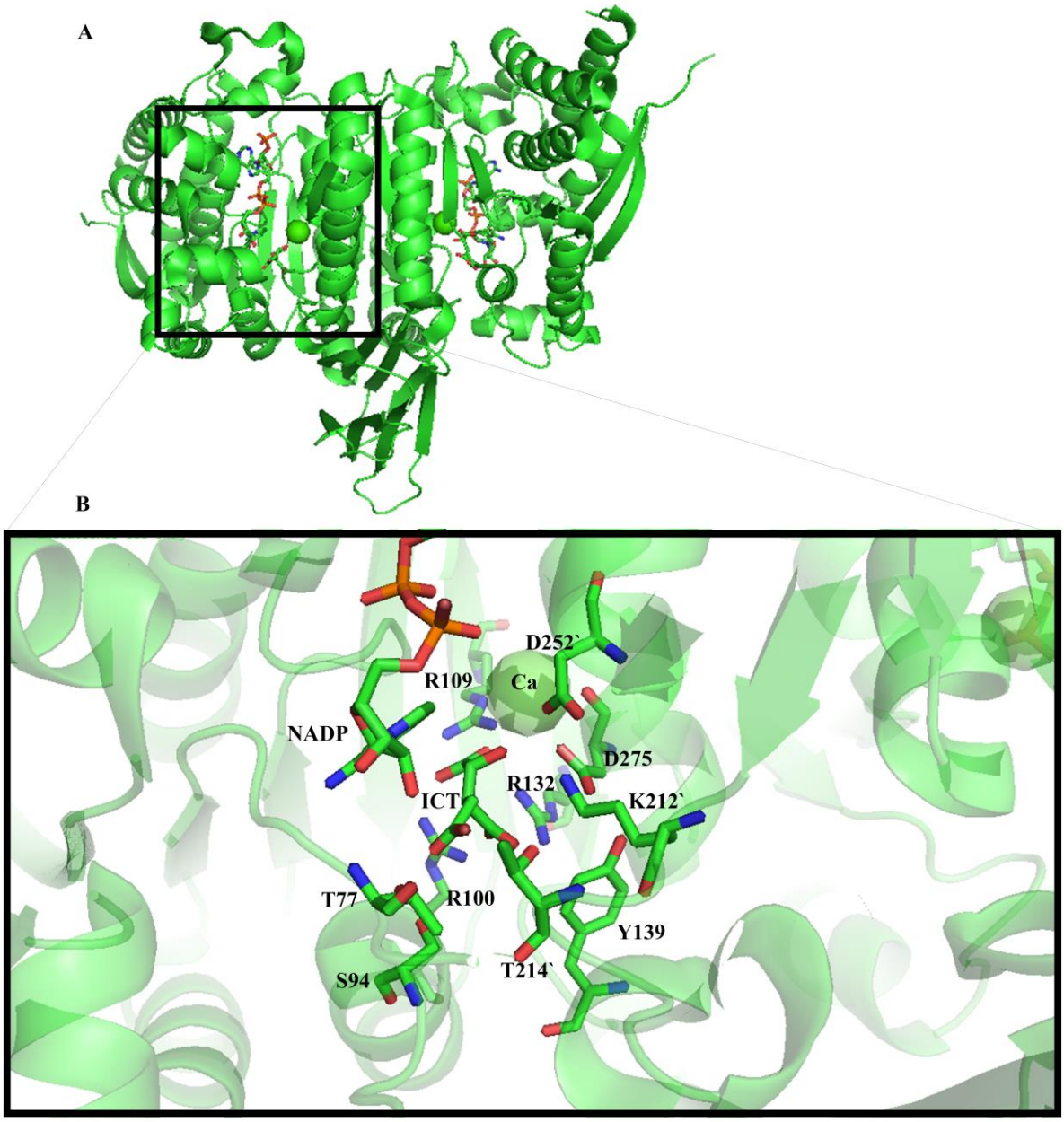

Figure 4. A. Crystal structure of WT IDH1 (PDB code 1T0L[16]) as a homodimer. The structure of IDH1 consists mostly of α-helices. **B.** A closed-up view of the active site of WT IDH1 bound to $NADP^+$, ICT, and Ca^{2+}. Highlighted are the residues in the active site as described by Xu and colleagues in 2004[16].

In 2010, Yang and colleagues used structural biology and biochemical kinetic assays to describe the altered activity of R132H IDH1[32]. There, the authors showed that in the case of WT IDH1, there is an initial binding site for isocitrate, and then IDH1 closes into a pre-transition state that is required for catalytic activity[16, 32]. However, R132H IDH1 does not have this initial ICT binding state due to the lost interaction of R132H with D275[32]. In the WT form of the protein, R132 interacts with ICT to facilitate the final conformational change consists of the initial binding state to the closed pre-transition state[32]. In contrast, R132H IDH1 binds to ICT but does not undergo this final conformational change required for catalysis[32]. Although the final folding of the regulatory domain does not occur with R132H IDH1 bound to ICT, closure to the catalytically active conformation happens when αKG binds to mutant IDH1, allowing conversion of αKG to D2HG[27, 33]. Crystallographic studies on mutant IDH1 enzymes with inhibitors show that these small molecule inhibitors bind at the dimer interface of the protein while the regulatory segment is not folded, or only partially folded due to the lost interaction of R132H with the helix, providing a possible mechanism of inhibitor selectivity.

1.8. The Selective Inhibition of IDH1 Mutants and FDA Approved Drugs

In order to minimize toxicity, anti-cancer therapeutics used in precision medicines must be highly selective for their target. Inhibitors of IDH1 are indeed specific for the mutant form of IDH1, with poor binding to WT IDH1 and IDH2[34, 35]. Agios Pharmaceuticals has devloped IDH1 and IDH2 inhibitors that have been approved by the FDA (Figure 5A and B). The IDH2 inhibitor enasidenib lowers the production of D2HG by the mutant enzyme and it has been approved to treat patients with AML[36]. When D2HG level are lowered, cells resume differentiation pathways[36]. This result is particularly important since this drug is more specific than current chemotherapies and is less toxic. Soon after the approval of enasidenib, the first IDH1 inhibitor, AG-120 (ivosidenib)

was approved by the FDA to treat IDH1 mutations in AML[37]. This drug is an optimization of AGI-5198 (Figure 5D), an allosteric inhibitor in IDH1[37]. This drug has a similar mechanism as enasidenib; by reducing the amounts of D2HG, cells are capable of resuming differentiation pathways[37]. As previously discussed, D2HG acts as a competitive inhibitor to many αKG-dependent histone demethylases. As a result of genome hypermethylation, genes involved in gene differentiation become regulated differentely[29]. Therefore, when intracellular concentrations of D2HG are decreased by inhibition of IDH1, αKG-dependent histone demethylases can resume catalyzing demethylation chemistries[37]. There are many compounds that are commercially available that have the same binding mechanism as the approved FDA drugs. Examples of IDH1 inhibitors include ML309[34] and AGI-5198[38] (Figure 5C and D).

ML309 and AGI-5198 are very selective for mutant IDH1 enzymes with low nM IC_{50} values versus high μM IC_{50} values for WT[34, 39, 40]. Inhibitor binding at the interface of the dimer precludes αKG binding since the regulatory domain remains unwound pushing the enzyme to an open-inactive conformation[16, 41, 42]. In 2017, Xie and colleagues performed a study to explain the selectivity of IDH1 inhibitors[42]. They showed that mutations at R132 ablates an important interaction with N271 in IDH1, preventing folding of the helix[42]. In contrast, this domain is folded as a helix in the holo form of WT[42]. Whether this mechanism fully explains the selectivity for mutant IDH1 remains to be understood. Notably, apo forms of both mutant and WT IDH1 have this domain fully unwound, though it is a stable loop in the case of WT, and unresolved in the mutant form. Further, crystal structures also show a fully helical regulatory helix when R132H IDH1 is bound αKG[27]. Currently, our group is further investigating the mechanisms of selectivity of IDH1 inhibitors[43]. Steady and pre-steady-state kinetics allow enzymologists to better understand

of how an enzyme behaves at catalyzing a specific reaction, aiding in the design of more specific and potent drugs for these targets.

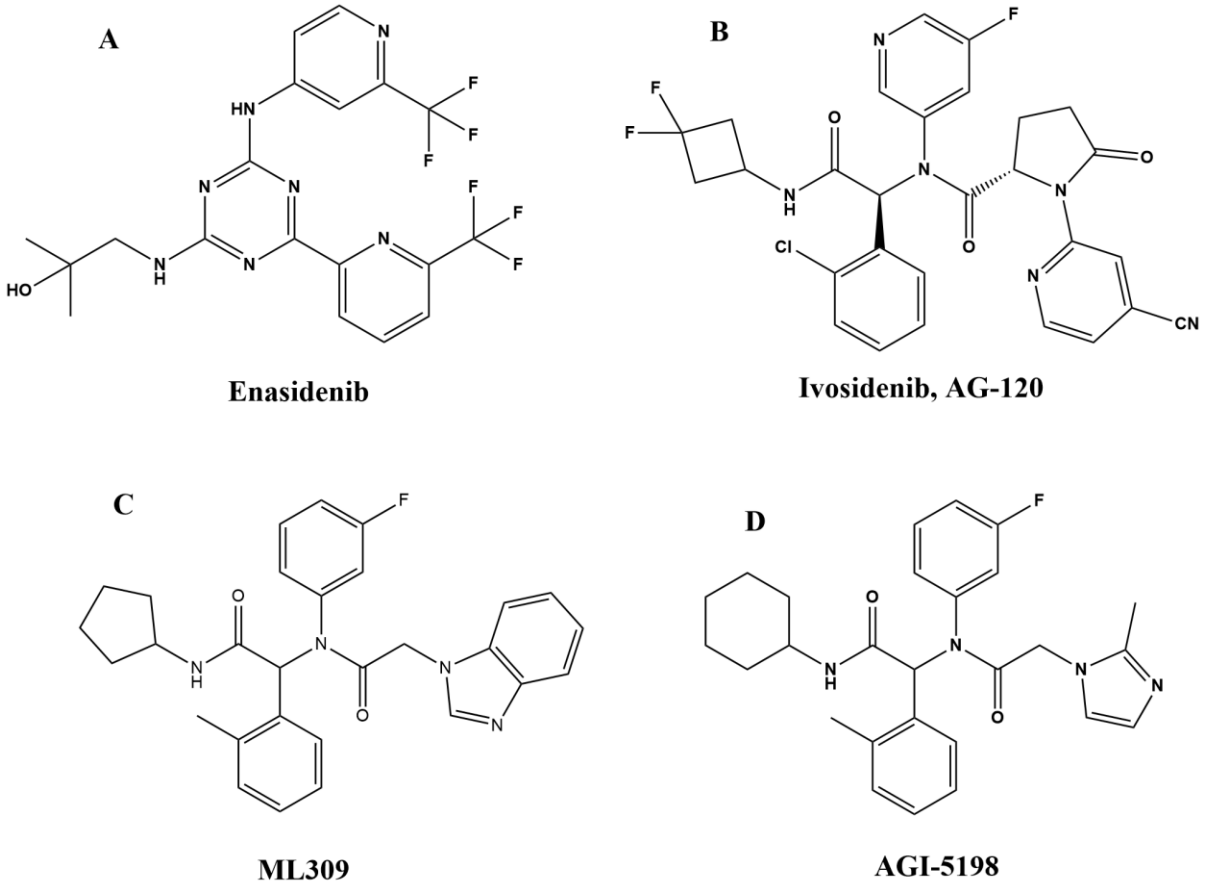

Figure 5. A. Structure of Enasidenib, the IDH2 FDA approved inhibitor for AML. **B.** Structure of Ivosidenib, the IDH1 FDA approved inhibitor for AML and an optimization of AGI-5198. **C.** Structure of ML309. This inhibitor has the same scaffold as AGI-5198. Only two groups are different at each end of the structure of the inhibitor. **D.** Structure of AGI-5198, the precursor of the FDA approved Ivosidenib.

1.9. Steady-State and Pre-Steady State Enzyme Kinetics

Enzymologists can use steady-state and pre-steady-state kinetic experiments, two very powerful methods, to determine the catalytic mechanisms of enzymes. Steady-state kinetic strategies were first described by Michaelis and Menten in the early 1900s[44]. In this study, they described how certain molecules, now known as enzymes, bind to a substrate and then perform catalysis[44]. The model they described is a simplification of the steps undertaken by enzymes in a catalytic cycle. They described a rapid binding equilibrium of enzyme and substrate, followed by irreversible product formation and release (Figure 6A)[44]. In steady-state kinetic experiments, there is an excess of substrate relative to enzyme, pushing the equilibrium of enzyme-substrate binding forward such that the concentration of enzyme bound to substrate is relatively unchanged and multiple turnovers are allowed. Therefore, the rate that is observed, k_{cat}, describes the slowest step of catalysis. With some derivation, they obtained a hyperbolic function ($kobs = kcat \times [S] / Km + [S]$) that describes the rate of product formation of enzymes at steady-state conditions (Figure 6A).

This function provides three very important enzymatic parameters. The first is the catalytic rate (k_{cat}). This is the first-order rate constant that describesthe maximal rate of catalysis corresponding to the slowest step of the catalytic cycle. The second is the Michaelis-Menten constant (K_M), which is the substrate concentration at half of k_{cat} (Figure 6A). Finally, the most informative parameter is the catalytic efficiency (k_{cat}/K_M), which describes the probability of substrate turnover when substrate is bound to the enzyme. Each parameter alone can be compared between different mutational variants of an enzyme and among different proteins as well. However, a very fast enzyme may not be highly efficient since its K_M may be high. This means

that the substrate concentration needs to be high in order to achieve its maximum catalytic rate. Therefore, when using catalytic efficiencies, we combined the other two kinetic parameters in order to assess which enzyme is more catalytically efficient. Steady-state kinetic methods can help us to derive hypotheses to predict how these enzymes function in their native environment and when challenged by mutation, changes in substrate concentration, or other variations. However, this method has limitations since it can only determine precisely the k_{cat} and K_M. A catalytic cycle contains at minimum, substrate binding, conformational change, chemistry, and product release (Figure 6B). Unlike steady-state kinetics is in within the second timeframes, pre-steady-state kinetics help us determine rates happening within the millisecond. Thus, only pre-steady state kinetic methods allow us to ascertain reaction mechanisms – the individual steps of catalysis. Additionally, in cells, the amount of substrate compared to enzyme is not always in vast excess as required in steady-state kinetic experiments. An example that will be discussed later in this dissertation is measuring the rate of chemistry in the catalytic cycle of IDH1.

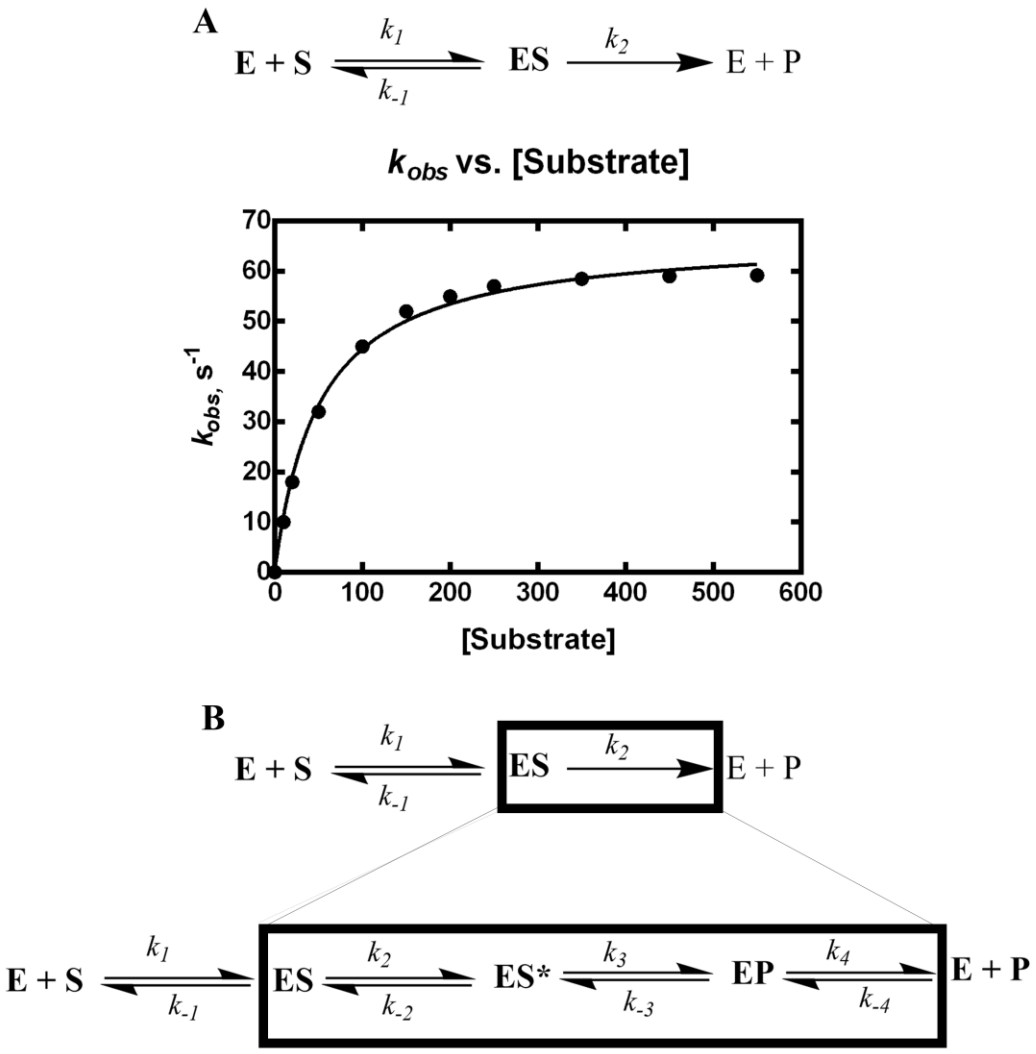

Figure 6. A. Simplified model of enzyme catalysis. Excess substrate binds to enzyme unchanged before catalysis. The graph is the hyperbolic function derived by Michaelis-Menten. K_{cat} is the maximum turnover rate. K_M is the concentration of substrate at half of k_{cat}. The catalytic efficiency (k_{cat}/K_M) is a second ordered rate constant that represents a tangent line to the linear portion of the hyperbolic function. **6B.** A more complex catalytic cycle shows rates that are not observable in a steady-state kinetic assay. Pre-steady-state kinetic methods allow one to experimentally determine many rate constants that are part of a more complex catalytic cycle.

There are many differences in experimental setups to properly measure individual rate constants in a catalytic cycle (Figure 6B). The beauty of pre-steady state kinetics is that when designing the proper experiment, it may be possible to detect specific steps in the catalytic cycle as well as a combination of steps. Usually, steady-state kinetic experiments are measured in the second to minute time frame, while pre-steady-state experiments occur in the millisecond to second timeframe. Since this time frame is significantly shorter, specialized equipment like a stopped-flow spectrophotometer or a rapid chemical quench must be used (Figure 7). These instruments allow us to rapidly mix two solutions and make measurements within a thousand points per second. Without these types of instruments, measuring pre-steady state rates is impossible. Although steady state and pre-steady state kinetic methods are powerful tools for measuring rates and finding experimental evidence of steps in the catalytic cycle, enzymatic studies become even stronger when combining it with biophysical methods such as X-ray crystallography.

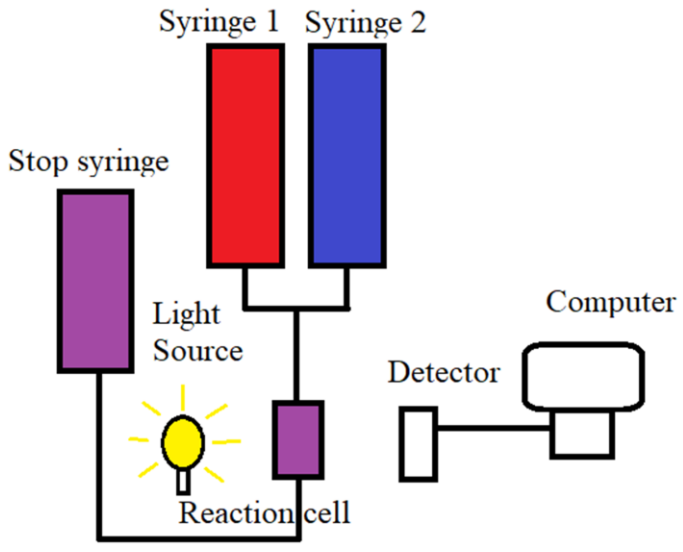

Figure 7. Schematic diagram of a stopped-flow spectrophotometer. Syringe 1 and 2 are pushed simultaneously with compressed gas to allow for rapid mixing. The solutions mix before reaching the reaction cell where the light source excites the photo active molecule. The solution ends at the stop syringe. The light sensed by the detector and the computer processes the data. This instrument allows enzymologists to measure rates happening in the millisecond time frame.

1.10. Combining Kinetics with Crystallography

X-ray crystallography works well in tandem with kinetics to help explain mechanistic features of an enzyme. One strength of X-ray crystallography is that it is possible to see specific interactions between enzyme and substrate, though this is a single snapshot of the enzyme at a particular conformation that may or may not be physiologically relevant. Dynamic information is also not readily available. Crystallographers may aim to crystalize the enzyme in different conditions, such as inclusion of exclusion of ligands, in order to compare different conformations. Crystallography also allows scientists to formulate hypotheses based on the interactions seen.

When Yang and colleagues described the mechanism of ICT binding and catalysis, they used X-ray crystallography and steady-state kinetics with IDH1 mutants to measure their catalytic efficiencies[32]. The mutations they designed affected residues involved in substrate binding, converting residues such as T77, S94, R100, R109, R132, Y139, K212, D252, and D275 to alanine mutants and then measured the catalytic effects[32]. They observed an overall decrease in k_{cat} in all mutants, and a wide range of effects in K_M[32]. The higher K_M values measured were associated with residues that interact with the carboxylate groups of ICT, such as R100 and R132[32]. Although K_M should not be confused with K_D, it gives an idea of the affinity that an enzyme has towards a specific substrate. Therefore, the authors were able to clarify the residues that interact with the substrate via X-ray crystallography and use kinetics to assess the catalytic effect of interrupting interactions with ICT. Enzyme structures solved by X-ray crystallography can also provide insight of allosteric and inhibitor binding sites, providing important information about how to increase affinity of the small molecule inhibitors for their targets.

1.11. Experimental Rationale to Fulfill Gap in Knowledge

Pusch's finding regarding the difference of D2HG concentrations measured in tumor depending on the R132 IDH1 mutant present raised the question of how the kinetic parameters related to D2HG production varied among each mutant[20, 31]. Although several groups have performed kinetic studies on many IDH1 mutants, there is little agreement of kinetic results within groups and many patients have not been characterized at all[26, 32, 45]. Therefore, we performed an extensive kinetic study to understand how physical characteristics, such as size and hydrophobicity, of several IDH1 R132 mutants drive D2HG production[20]. This work elucidates how each R132 mutant behaves kinetically as well as provides tools for predicting how D2HG concentrations and disease severity might present in patients presenting with less common IDH1 R132 mutations. An important discovery from this work led us to study how IDH1 inhibitors work a wide range of IDH1 R132 mutants.

IDH1 inhibitors have been tested, for the most part, with R132H and R132C[34, 35]. A full study of inhibition with several R132 IDH1 mutants has been lacking. Moreover, our discovery of R132Q IDH1 as the only mutant studied to date that preserves WT activity, raised the question of whether this mutant also binds mutant IDH1 inhibitors with similar affinity[20, 40]. Moreover, we worked with collaborators to perform molecular dynamic studies to understand key conformational changes that would correlate enzymatic activity with inhibition sensitivity[40]. This work elucidates the effects of IDH1 inhibitors for a wide range of R132 mutants, predicting the likelihood of each IDH1 mutant to respond to therapeutics, as well as finding possible mutants that may be resistant.

Finally, Rendina and colleagues described the mechanism of binding for the neomorphic reaction as being ordered sequential[27]. However, they did not describe the catalytic cycle of R132 mutants when producing D2HG. Further, a structure of R132Q IDH1 has not been solved and

determining binding conformations for this mutant is lacking. Therefore, a complete structure-function characterization of important IDH1 has not been performed. Our work seeks to establish the catalytic cycle of IDH1 mutants when performing the neomorphic reaction, as well as to identify key kinetic features of metabolic dehydrogenases at performing NADPH-reduction of α-keto acids. Additionally, the structure of R132Q IDH1 will elucidate key conformations that make this mutant unique and will aid in the development of inhibitors selective for this mutant.

1.12. References

1. Hassanpour, S. H.; Dehghani, M., Review of cancer from perspective of molecular. *J Cancer Res Pract* **2017,** *4* (4), 127-129.

2. Siegel, R.; Naishadham, D.; Jemal, A., Cancer statistics, 2013. *CA Cancer J Clin* **2013,** *63* (1), 11-30.

3. Nowell, P. C., The clonal evolution of tumor cell populations. *Science* **1976,** *194* (4260), 23-8.

4. Charles, N.; Ozawa, T.; Squatrito, M.; Bleau, A. M.; Brennan, C. W.; Hambardzumyan, D.; Holland, E. C., Perivascular nitric oxide activates notch signaling and promotes stem-like character in PDGF-induced glioma cells. *Cell Stem Cell* **2010,** *6* (2), 141-52.

5. Balkwill, F. R.; Capasso, M.; Hagemann, T., The tumor microenvironment at a glance. *J Cell Sci* **2012,** *125* (Pt 23), 5591-6.

6. Hao, G.; Xu, Z. P.; Li, L., Manipulating extracellular tumour pH: an effective target for cancer therapy. *RSC Advances* **2018,** *8* (39), 22182-22192.

7. Izumi, H.; Torigoe, T.; Ishiguchi, H.; Uramoto, H.; Yoshida, Y.; Tanabe, M.; Ise, T.; Murakami, T.; Yoshida, T.; Nomoto, M.; Kohno, K., Cellular pH regulators: potentially promising molecular targets for cancer chemotherapy. *Cancer Treat Rev* **2003,** *29* (6), 541-9.

8. Hanahan, D.; Weinberg, R. A., Hallmarks of cancer: the next generation. *Cell* **2011,** *144* (5), 646-74.

9. Hanahan, D.; Weinberg, R. A., The hallmarks of cancer. *Cell* **2000,** *100* (1), 57-70.

10. Warburg, O., Über den Stoffwechsel der Carcinomzelle. *Klin Wochenschr* **1925,** *4*, 534-536.

11. Warburg, O., Origin of cancer cells. *Oncologia* **1956,** *9* (2), 75-83.

12. Parsons, D. W.; Jones, S.; Zhang, X.; Lin, J. C.; Leary, R. J.; Angenendt, P.; Mankoo, P.; Carter, H.; Siu, I. M.; Gallia, G. L.; Olivi, A.; McLendon, R.; Rasheed, B. A.; Keir, S.; Nikolskaya, T.; Nikolsky, Y.; Busam, D. A.; Tekleab, H.; Diaz, L. A., Jr.; Hartigan, J.; Smith, D. R.; Strausberg, R. L.; Marie, S. K.; Shinjo, S. M.; Yan, H.; Riggins, G. J.; Bigner, D. D.; Karchin, R.; Papadopoulos, N.; Parmigiani, G.; Vogelstein, B.; Velculescu, V. E.; Kinzler, K. W., An integrated genomic analysis of human glioblastoma multiforme. *Science* **2008,** *321* (5897), 1807-12.

13. Louis, D. N.; Ohgaki, H.; Wiestler, O. D.; Cavenee, W. K.; Burger, P. C.; Jouvet, A.; Scheithauer, B. W.; Kleihues, P., The 2007 WHO classification of tumours of the central nervous system. *Acta Neuropathol* **2007,** *114* (2), 97-109.

14. Stupp, R.; Mason, W. P.; van den Bent, M. J.; Weller, M.; Fisher, B.; Taphoorn, M. J.; Belanger, K.; Brandes, A. A.; Marosi, C.; Bogdahn, U.; Curschmann, J.; Janzer, R. C.; Ludwin, S. K.; Gorlia, T.; Allgeier, A.; Lacombe, D.; Cairncross, J. G.; Eisenhauer, E.; Mirimanoff, R. O., Radiotherapy plus concomitant and adjuvant temozolomide for glioblastoma. *N Engl J Med* **2005,** *352* (10), 987-96.

15. Balss, J.; Meyer, J.; Mueller, W.; Korshunov, A.; Hartmann, C.; von Deimling, A., Analysis of the IDH1 codon 132 mutation in brain tumors. *Acta Neuropathol* **2008,** *116* (6), 597-602.

16. Xu, X.; Zhao, J.; Xu, Z.; Peng, B.; Huang, Q.; Arnold, E.; Ding, J., Structures of human cytosolic NADP-dependent isocitrate dehydrogenase reveal a novel self-regulatory mechanism of activity. *J Biol Chem* **2004,** *279* (32), 33946-57.

17. Bleeker, F. E.; Lamba, S.; Leenstra, S.; Troost, D.; Hulsebos, T.; Vandertop, W. P.; Frattini, M.; Molinari, F.; Knowles, M.; Cerrato, A.; Rodolfo, M.; Scarpa, A.; Felicioni, L.; Buttitta, F.; Malatesta, S.; Marchetti, A.; Bardelli, A., IDH1 mutations at residue p.R132 (IDH1(R132)) occur frequently in high-grade gliomas but not in other solid tumors. *Hum Mutat* **2009,** *30* (1), 7-11.

18. Cerami, E.; Gao, J.; Dogrusoz, U.; Gross, B. E.; Sumer, S. O.; Aksoy, B. A.; Jacobsen, A.; Byrne, C. J.; Heuer, M. L.; Larsson, E.; Antipin, Y.; Reva, B.; Goldberg, A. P.; Sander, C.; Schultz, N., The cBio cancer genomics portal: an open platform for exploring multidimensional cancer genomics data. *Cancer Discov* **2012,** *2* (5), 401-4.

19. Hirata, M.; Sasaki, M.; Cairns, R. A.; Inoue, S.; Puviindran, V.; Li, W. Y.; Snow, B. E.; Jones, L. D.; Wei, Q.; Sato, S.; Tang, Y. J.; Nadesan, P.; Rockel, J.; Whetstone, H.; Poon, R.; Weng, A.; Gross, S.; Straley, K.; Gliser, C.; Xu, Y.; Wunder, J.; Mak, T. W.; Alman, B. A., Mutant IDH is sufficient to initiate enchondromatosis in mice. *Proc Natl Acad Sci U.S.A* **2015,** *112* (9), 2829-34.

20. Avellaneda Matteo, D.; Grunseth, A. J.; Gonzalez, E. R.; Anselmo, S. L.; Kennedy, M. A.; Moman, P.; Scott, D. A.; Hoang, A.; Sohl, C. D., Molecular mechanisms of isocitrate

dehydrogenase 1 (IDH1) mutations identified in tumors: The role of size and hydrophobicity at residue 132 on catalytic efficiency. *J Biol Chem* **2017,** *292* (19), 7971-7983.

21. Mardis, E. R.; Ding, L.; Dooling, D. J.; Larson, D. E.; McLellan, M. D.; Chen, K.; Koboldt, D. C.; Fulton, R. S.; Delehaunty, K. D.; McGrath, S. D.; Fulton, L. A.; Locke, D. P.; Magrini, V. J.; Abbott, R. M.; Vickery, T. L.; Reed, J. S.; Robinson, J. S.; Wylie, T.; Smith, S. M.; Carmichael, L.; Eldred, J. M.; Harris, C. C.; Walker, J.; Peck, J. B.; Du, F.; Dukes, A. F.; Sanderson, G. E.; Brummett, A. M.; Clark, E.; McMichael, J. F.; Meyer, R. J.; Schindler, J. K.; Pohl, C. S.; Wallis, J. W.; Shi, X.; Lin, L.; Schmidt, H.; Tang, Y.; Haipek, C.; Wiechert, M. E.; Ivy, J. V.; Kalicki, J.; Elliott, G.; Ries, R. E.; Payton, J. E.; Westervelt, P.; Tomasson, M. H.; Watson, M. A.; Baty, J.; Heath, S.; Shannon, W. D.; Nagarajan, R.; Link, D. C.; Walter, M. J.; Graubert, T. A.; DiPersio, J. F.; Wilson, R. K.; Ley, T. J., Recurring mutations found by sequencing an acute myeloid leukemia genome. *N Engl J Med* **2009,** *361* (11), 1058-66.

22. Jo, S. H.; Son, M. K.; Koh, H. J.; Lee, S. M.; Song, I. H.; Kim, Y. O.; Lee, Y. S.; Jeong, K. S.; Kim, W. B.; Park, J. W.; Song, B. J.; Huh, T. L., Control of mitochondrial redox balance and cellular defense against oxidative damage by mitochondrial NADP+-dependent isocitrate dehydrogenase. *J Biol Chem* **2001,** *276* (19), 16168-76.

23. Yi, C. Q.; Jia, G. F.; Hou, G. H.; Dai, Q.; Zhang, W.; Zheng, G. Q.; Jian, X.; Yang, C. G.; Cui, Q. A.; He, C. A., Iron-catalysed oxidation intermediates captured in a DNA repair dioxygenase. *Nature* **2010,** *468* (7321), 330-333.

24. Figueroa, M. E.; Abdel-Wahab, O.; Lu, C.; Ward, P. S.; Patel, J.; Shih, A.; Li, Y.; Bhagwat, N.; Vasanthakumar, A.; Fernandez, H. F.; Tallman, M. S.; Sun, Z.; Wolniak, K.; Peeters, J. K.; Liu, W.; Choe, S. E.; Fantin, V. R.; Paietta, E.; Lowenberg, B.; Licht, J. D.; Godley, L. A.; Delwel, R.; Valk, P. J.; Thompson, C. B.; Levine, R. L.; Melnick, A., Leukemic IDH1 and IDH2 mutations result in a hypermethylation phenotype, disrupt TET2 function, and impair hematopoietic differentiation. *Cancer Cell* **2010,** *18* (6), 553-67.

25. Chowdhury, R.; Yeoh, K. K.; Tian, Y. M.; Hillringhaus, L.; Bagg, E. A.; Rose, N. R.; Leung, I. K.; Li, X. S.; Woon, E. C.; Yang, M.; McDonough, M. A.; King, O. N.; Clifton, I. J.; Klose, R. J.; Claridge, T. D.; Ratcliffe, P. J.; Schofield, C. J.; Kawamura, A., The oncometabolite 2-hydroxyglutarate inhibits histone lysine demethylases. *EMBO Rep* **2011,** *12* (5), 463-9.

26. Dang, L.; White, D. W.; Gross, S.; Bennett, B. D.; Bittinger, M. A.; Driggers, E. M.; Fantin, V. R.; Jang, H. G.; Jin, S.; Keenan, M. C.; Marks, K. M.; Prins, R. M.; Ward, P. S.; Yen, K. E.; Liau, L. M.; Rabinowitz, J. D.; Cantley, L. C.; Thompson, C. B.; Vander Heiden, M. G.; Su, S. M., Cancer-associated IDH1 mutations produce 2-hydroxyglutarate. *Nature* **2009,** *462* (7274), 739-44.

27. Rendina, A. R.; Pietrak, B.; Smallwood, A.; Zhao, H.; Qi, H.; Quinn, C.; Adams, N. D.; Concha, N.; Duraiswami, C.; Thrall, S. H.; Sweitzer, S.; Schwartz, B., Mutant IDH1 enhances the production of 2-hydroxyglutarate due to its kinetic mechanism. *Biochemistry* **2013,** *52* (26), 4563-77.

28. Zhao, S.; Lin, Y.; Xu, W.; Jiang, W.; Zha, Z.; Wang, P.; Yu, W.; Li, Z.; Gong, L.; Peng, Y.; Ding, J.; Lei, Q.; Guan, K. L.; Xiong, Y., Glioma-derived mutations in IDH1 dominantly inhibit IDH1 catalytic activity and induce HIF-1alpha. *Science* **2009,** *324* (5924), 261-5.

29. Xu, W.; Yang, H.; Liu, Y.; Yang, Y.; Wang, P.; Kim, S. H.; Ito, S.; Yang, C.; Wang, P.; Xiao, M. T.; Liu, L. X.; Jiang, W. Q.; Liu, J.; Zhang, J. Y.; Wang, B.; Frye, S.; Zhang, Y.; Xu, Y. H.; Lei, Q. Y.; Guan, K. L.; Zhao, S. M.; Xiong, Y., Oncometabolite 2-hydroxyglutarate is a competitive inhibitor of alpha-ketoglutarate-dependent dioxygenases. *Cancer Cell* **2011,** *19* (1), 17-30.

30. Lu, C.; Ward, P. S.; Kapoor, G. S.; Rohle, D.; Turcan, S.; Abdel-Wahab, O.; Edwards, C. R.; Khanin, R.; Figueroa, M. E.; Melnick, A.; Wellen, K. E.; O'Rourke, D. M.; Berger, S. L.; Chan, T. A.; Levine, R. L.; Mellinghoff, I. K.; Thompson, C. B., IDH mutation impairs histone demethylation and results in a block to cell differentiation. *Nature* **2012,** *483* (7390), 474-8.

31. Pusch, S.; Schweizer, L.; Beck, A. C.; Lehmler, J. M.; Weissert, S.; Balss, J.; Miller, A. K.; von Deimling, A., D-2-Hydroxyglutarate producing neo-enzymatic activity inversely correlates with frequency of the type of isocitrate dehydrogenase 1 mutations found in glioma. *Acta Neuropathol Commun* **2014,** *2*, 19.

32. Yang, B.; Zhong, C.; Peng, Y.; Lai, Z.; Ding, J., Molecular mechanisms of "off-on switch" of activities of human IDH1 by tumor-associated mutation R132H. *Cell Res* **2010,** *20* (11), 1188-200.

33. Pietrak, B.; Zhao, H.; Qi, H.; Quinn, C.; Gao, E.; Boyer, J. G.; Concha, N.; Brown, K.; Duraiswami, C.; Wooster, R.; Sweitzer, S.; Schwartz, B., A tale of two subunits: how the neomorphic R132H IDH1 mutation enhances production of alphaHG. *Biochemistry* **2011,** *50* (21), 4804-12.

34. Davis, M. I.; Gross, S.; Shen, M.; Straley, K. S.; Pragani, R.; Lea, W. A.; Popovici-Muller, J.; Delabarre, B.; Artin, E.; Thorne, N.; Auld, D. S.; Li, Z.; Dang, L.; Boxer, M. B.; Simeonov, A., Biochemical, cellular and biophysical characterization of a potent inhibitor of mutant isocitrate dehydrogenase IDH1. *J Biol Chem* **2014,** *289*, 13717-13725.

35. Popovici-Muller, J.; Saunders, J. O.; Salituro, F. G.; Travins, J. M.; Yan, S.; Zhao, F.; Gross, S.; Dang, L.; Yen, K. E.; Yang, H.; Straley, K. S.; Jin, S.; Kunii, K.; Fantin, V. R.; Zhang, S.; Pan, Q.; Shi, D.; Biller, S. A.; Su, S. M., Discovery of the first potent inhibitors of mutant IDH1 that lower tumor 2-HG in vivo. *ACS Med Chem Lett* **2012,** *3* (10), 850-5.

36. Stein, E. M.; DiNardo, C. D.; Pollyea, D. A.; Fathi, A. T.; Roboz, G. J.; Altman, J. K.; Stone, R. M.; DeAngelo, D. J.; Levine, R. L.; Flinn, I. W.; Kantarjian, H. M.; Collins, R.; Patel, M. R.; Frankel, A. E.; Stein, A.; Sekeres, M. A.; Swords, R. T.; Medeiros, B. C.; Willekens, C.; Vyas, P.; Tosolini, A.; Xu, Q.; Knight, R. D.; Yen, K. E.; Agresta, S.; de Botton, S.;

Tallman, M. S., Enasidenib in mutant IDH2 relapsed or refractory acute myeloid leukemia. *Blood* **2017,** *130* (6), 722-731.

37. Popovici-Muller, J.; Lemieux, R. M.; Artin, E.; Saunders, J. O.; Salituro, F. G.; Travins, J.; Cianchetta, G.; Cai, Z.; Zhou, D.; Cui, D.; Chen, P.; Straley, K.; Tobin, E.; Wang, F.; David, M. D.; Penard-Lacronique, V.; Quivoron, C.; Saada, V.; de Botton, S.; Gross, S.; Dang, L.; Yang, H.; Utley, L.; Chen, Y.; Kim, H.; Jin, S.; Gu, Z.; Yao, G.; Luo, Z.; Lv, X.; Fang, C.; Yan, L.; Olaharski, A.; Silverman, L.; Biller, S.; Su, S. M.; Yen, K., Discovery of AG-120 (Ivosidenib): a first-in-class mutant IDH1 inhibitor for the treatment of IDH1 mutant cancers. *ACS Med Chem Lett* **2018,** *9* (4), 300-305.

38. Rohle, D.; Popovici-Muller, J.; Palaskas, N.; Turcan, S.; Grommes, C.; Campos, C.; Tsoi, J.; Clark, O.; Oldrini, B.; Komisopoulou, E.; Kunii, K.; Pedraza, A.; Schalm, S.; Silverman, L.; Miller, A.; Wang, F.; Yang, H.; Chen, Y.; Kernytsky, A.; Rosenblum, M. K.; Liu, W.; Biller, S. A.; Su, S. M.; Brennan, C. W.; Chan, T. A.; Graeber, T. G.; Yen, K. E.; Mellinghoff, I. K., An inhibitor of mutant IDH1 delays growth and promotes differentiation of glioma cells. *Science* **2013,** *340* (6132), 626-30.

39. Deng, G.; Shen, J.; Yin, M.; McManus, J.; Mathieu, M.; Gee, P.; He, T.; Shi, C.; Bedel, O.; McLean, L. R.; Le-Strat, F.; Zhang, Y.; Marquette, J. P.; Gao, Q.; Zhang, B.; Rak, A.; Hoffmann, D.; Rooney, E.; Vassort, A.; Englaro, W.; Li, Y.; Patel, V.; Adrian, F.; Gross, S.; Wiederschain, D.; Cheng, H.; Licht, S., Selective inhibition of mutant isocitrate dehydrogenase 1 (IDH1) via disruption of a metal binding network by an allosteric small molecule. *J Biol Chem* **2015,** *290* (2), 762-74.

40. Avellaneda Matteo, D.; Wells, G. A.; Luna, L. A.; Grunseth, A. J.; Zagnitko, O.; Scott, D. A.; Hoang, A.; Luthra, A.; Swairjo, M. A.; Schiffer, J. M.; Sohl, C. D., Inhibitor potency varies widely among tumor-relevant human isocitrate dehydrogenase 1 mutants. *Biochem J* **2018,** *475* (20), 3221-3238.

41. Merk, A.; Bartesaghi, A.; Banerjee, S.; Falconieri, V.; Rao, P.; Davis, M. I.; Pragani, R.; Boxer, M. B.; Earl, L. A.; Milne, J. L.; Subramaniam, S., Breaking Cryo-EM resolution barriers to facilitate drug discovery. *Cell* **2016,** *165* (7), 1698-707.

42. Xie, X.; Baird, D.; Bowen, K.; Capka, V.; Chen, J.; Chenail, G.; Cho, Y.; Dooley, J.; Farsidjani, A.; Fortin, P.; Kohls, D.; Kulathila, R.; Lin, F.; McKay, D.; Rodrigues, L.; Sage, D.; Toure, B. B.; van der Plas, S.; Wright, K.; Xu, M.; Yin, H.; Levell, J.; Pagliarini, R. A., Allosteric mutant IDH1 inhibitors reveal mechanisms for IDH1 mutant and isoform selectivity. *Structure* **2017,** *25* (3), 506-513.

43. Chambers, J. M.; Miller, W.; Quichocho, G.; Upadhye, V.; Avellaneda Matteo, D.; Bobkov, A. A.; Sohl, C. D.; Schiffer, J. M., Water networks and correlated motions in mutant isocitrate dehydrogenase 1 (IDH1) are critical for allosteric inhibitor binding and activity. *Biochemistry* **2020,** *59* (4), 479-490.

44. Michaelis, L.; Menten, M. L.; Johnson, K. A.; Goody, R. S., The original Michaelis constant: translation of the 1913 Michaelis-Menten paper. *Biochemistry* **2011,** *50* (39), 8264-9.

45. Leonardi, R.; Subramanian, C.; Jackowski, S.; Rock, C. O., Cancer-associated isocitrate dehydrogenase mutations inactivate NADPH-dependent reductive carboxylation. *J Biol Chem* **2012,** *287* (18), 14615-20.

2. Molecular Mechanisms of Isocitrate Dehydrogenase 1 (IDH1) Mutations Identified in Tumors: The Role of Size and Hydrophobicity at Residue 132 on Catalytic Efficiency

2.1. Abstract

Isocitrate dehydrogenase 1 (IDH1) is responsible for the $NADP^+$-dependent oxidative decarboxylation of ICT to αKG in the cytosol and peroxisomes of the cell. Mutations in the IDH1 gene has been linked to over 80% of lower grade gliomas and secondary glioblastomas patients, primarily affecting residue 132, which aids to coordinate substrate binding. Other mutations in the active site of IDH1 have been also linked to tumors. IDH1 mutations usually result in the loss of normal catalytic activity, but many gain a new reaction, which is the NADPH-dependent reduction of αKG to D2HG. D2HG is a proposed oncometabolite since it competitively inhibits many αKG dependent enzymes involved in gene regulation and DNA repair. Some IDH1 kinetic parameters have been previously published for several mutants IDH1, and there is evidence that these mutants vary widely in the production of D2HG. In this chapter, we report that most IDH1 mutations identified in cancer are severely affected in catalyzing the normal oxidation reaction, and the catalytic efficiencies to produce D2HG vary within them up to ~640-fold. Common IDH1 mutations have moderate efficiencies to produce D2HG, whereas more rare mutations show very low or high efficiencies. Therefore, we designed several experimental R132 mutants IDH1 to assess the features required for D2HG production. We showed that smaller and more hydrophobic residues support the neomorphic reaction. Interestingly, we also report one mutant that has a high catalytic efficiency for the neomorphic reaction and conserves some activity of the normal oxidation reaction. These kinetic studies show catalytic features of mutations found in majority of patients with lower grade gliomas.

2.2. Introduction

Otto Warburg first described changes in metabolism in tumor cells about a hundred years ago[1-3], but whether enzymes behaved as tumor suppressors or oncogenes has been described relatively recently. A striking example of metabolic enzymes playing an important role in tumorigenesis is the dimeric isocitrate dehydrogenase 1 and 2 (IDH1 and IDH2). The normal function of these enzymes is the $NADP^+$-and Mg^{2+}-dependent reversible oxidative decarboxylation of ICT to αKG (Figure 1A). IDH1 catalyzes this reaction in the cytosol and peroxisomes of the cell, while IDH2 in the mitochondria. IDH3 also performs the same reaction in the mitochondria (during the TCA cycle), although it has not been linked to cancer and it is non-reversible and NAD^+-dependent.

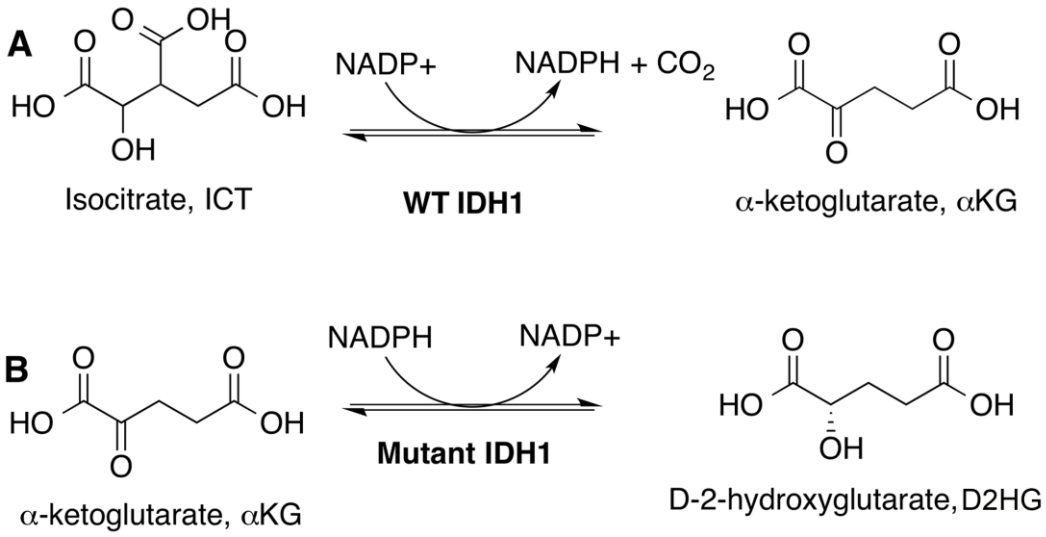

Figure 1. WT and mutant IDH1 catalytic activities. Shown are the **A.** normal oxidative decarboxylation, and **B.** the neomorphic reduction.

Mutations in IDH1 and IDH2 were first described in glioblastoma multiforme in a large sequencing study of patients harboring this disease[4], and it was found that over 80% of patients with grade II/III gliomas and secondary glioblastomas were found to have mutations in the IDH1

gene, most commonly R132H and R132C[5-9]. IDH1 mutants lose the ability to convert ICT to αKG[10], suggesting that they would behave as tumor suppressors, in part through altering the levels of hypoxia-inducible transcription factor-1α[11]. Nevertheless, mutations in the IDH1 gene are heterozygous dominant, meaning that expressions of this gene in tumors likely yield heterodimers of mutant IDH1 with WT IDH1. Previous studies showed that mutant IDH1/2 are capable of catalyzing the NADPH-dependent reduction of αKG to D2HG[12-14] (Figure 1B). D2HG is a proposed oncometabolite since it competitively inhibits many αKG dependent enzymes such as histone demethylases, resulting in alterations of gene regulation and cell de-differentiation[15, 16]. As a matter of fact, cancer patients harboring IDH1 mutations show hypermethylation phenotypes[17-19] that resulted from D2HG inhibiting histones and DNA demethylases. The oncometabolite D2HG can recapitulate tumorigenic phenotypes in cancer models[20, 21], but studies that have measured the global metabolomic changes between mutant IDH1 and D2HG treatment have shown differences[22, 23]. This indicates that loss of the normal reaction and/or changes in NADPH levels may also play a crucial role. The development of selective therapeutic targets is well underway with FDA approved drugs for IDH1 treating acute myeloid leukemia[8, 24-26].

The fact that a point mutation allows IDH1 to perform a new catalytic activity suggests important mechanistic changes, and many previous studies have used kinetics and structural methods to explore the new activity of mutant IDH1[12, 27-32]. IDH1 mutants produce varying concentrations of D2HG[32], with interesting alterations in conformational change as previously described in crystal structure studies of R132H IDH1[28, 29, 31]. The kinetic parameters published up to date vary widely, thus making it very difficult to perform comparisons. Interestingly, some IDH1 mutations do not perform the NADPH-dependent reduction of αKG[33, 34], suggesting that just

the loss of the normal reaction has important consequences, or maybe they are just passenger mutations.

Here, we report a thorough catalytic study of a wide spectrum of IDH1 mutations, including many seen in tumors as well as several mutants designed to clarify catalytic features. We showed that IDH1 mutants vary widely in catalytic efficiencies; with the more polar and larger residues at position 132 supporting the normal reaction, while smaller and more hydrophobic residues driving the neomorphic reaction. This study provides important insight of which mutations at position 132 produce D2HG efficiently. This study would also provide important information revealing the features of driver mutations present in most patients with lower grade gliomas and secondary glioblastomas.

2.3. Materials and Methods

2.3.1. Materials

Dithiothreitol (DTT), isopropyl 1-thio-β-D-galactopyranoside (IPTG), Titron X-100, α-ketoglutaric acid sodium salt (αKG), DL-isocitric acid trisodium salt hydrate, and magnesium chloride ($MgCl_2$) were obtained from Fisher Scientific (Hampton, NH). β-Mercaptoethanol (β-ME) was obtained from MP Biomedicals located in Santa Ana, CA. Both β-Nicotinamide adenine dinuclotide phosphate reduced trisodium salt (NADPH) and β-Nicotinamide adenine dinucleotide phosphate disodium salt ($NADP^+$) were obtained from EMD Millipore (Darmstadt, Germany). Nickel-nitrilotriacetic acid (Ni-NTA) resin was obtain from Qiagen (Valencia, CA). Stain free gels (4-12%) were obtained from Bio-Rad Laboratories (Hercules, CA). Protease inhibitor Tablets were obtained from Roche Applied Science (Penzberg, Germany).

2.3.2. Plasmid Mutagenesis

pET-28b, containing an *N*-terminal histag, was used for all IDH1 constructs. To generate the different mutations, site-directed mutagenesis (Kapa Bioscience, Wilmington, MA) was used to create R132C (forward primer, 5'-GGTTAAACCGATCATTATTGGTTGCCATGCCTATGGTGATCAGTATC-3', reverse primer 5'-GATACTGATCACCATAGGCATGGCAACCAATATGATCGGTTTAACC-3'), R100Q (forward primer 5'-GCCGAATGGCACCATTCAGAATATTCTGGG-3', reverse primer 5'CCCAGAATATTCTGAATGGTGCCATTCGGGC-3'), A134D (forward primer, 5'-GGTCGTCATGATTATGGTGATCAGTATCG-3', reverse primer 5'-CGATACTGATCACCATAATCATGACGACC-3'), H133Q (forward primer 5'-AACCGATCATTATTGGTCGTCAGGCCTATGGTGATC-3', reverse primer 5'-GATCACCATAGGCCTGACGACCAATAATGATCGGTT-3'), R132G (forward primer, 5'-AACCGATCATTATTGGTGGTCATGCCTATGGTGATC-3', reverse primer 5'-GATCACCATAGGCATGACCACCAATAATGATCGGTT-3'), R132A (forward primer 5'-GGTTAAACCGATCATTATTGGTGCGCATGCCTATGGTGATCAGTATC-3', reverse primer 5'- GATACTGATCACCATAGGCATGCGCACCAATAATGATCGGTTTAACC-3'), R132Q (forward primer 5'-GTTAAACCGATCATTATTGGTCAGCATGCCTATGGTGATCAGTATC-3', reverse primer 5'-GATACTGATCACCATAGGCATGCTGACCAATAATGATCGGTTTAAC-3'), R132K (forward primer 5'-GGGTTAAACCGATCATTATTGGTAAACATGCCTATGGTGATCAGTATCG-3', reverse primer 5'-CGATACTGATCACCATAGGCATGTTTACCAATAATGATCGGTTTAACCC-3'), R132W (forward primer 5'-

GGTTAAACCGATCATTATTGGTTGGCATGCCTATGGTGATCAGTATC, reverse primer 5'-GATACTGATCACCATAGGCATGCCAACCAATAATGATCGGTTTAACC-3'), and R132N (forward primer 5'-CGATACTGATCACCATAGGCATGGTTACCAATAATGATCGGTTTAACCC-3', reverse primer 5'-GGGTTAAACCGATCATTATTGGTAACCATGCCTATGGTGATCAGTATCG-3'). All primers were purchased from IDT (Coralville, IW). R132H and wildtype (WT) were obtained from Charles Rock from St. Jude's Hospital. All mutants were generated by Dr. Christal Sohl.

2.3.3. Protein Expression and Purification

IDH1 (WT and mutants) were transformed into BL21 gold (DE3) cells. The transformed cells were incubated at 37 ºC in 0.5-2 L of terrific broth media (TB) containing 30 μg/mL at 200 RPM until reaching an optical density at 600 nm of 1.0-1.2. Then, the temperature was dropped to about 18-20 ºC and the RPMs were reduced to 130. The cultures were induced using 1 mM (final) of IPTG. The cells were pelleted at 8000 RPM for 15 minutes. The pellets were resuspended using lysis buffer (20 mM Tris, pH 7.5, at 4 ºC, 500 mM NaCl, 0.1% Triton X-100, and a crushed and dissolved protease inhibitor Tablet). The cells were lysed via sonication and the supernatant was collected by centrifugation of the homogenates at 12000 RPM for 1 h. The lysates were collected and loaded into a Ni-NTA affinity column. After the lysate was loaded, the resin was washed with Ni-buffer 1 (50 mM Tris, pH 7.5, at 4 ºC, 500 mM NaCl, and 5 mM β-ME) and eluted with Ni-buffer 2 (50 mM tris, pH 7.5, at 4 ºC, 500 mM NaCl, 500 mM imidazole at pH 7.5, and 5 mM β-ME). The elution was concentrated and dialyzed in storage buffer overnight (50 mM Tris, pH 7.5, at 4 ºC, 100 mM NaCl, 20% glycerol, and 1 mM DTT). Purity of each mutant was confirmed to be over 95% via SDS-PAGE (stain-free 4-12% gels). The concentrations of purified IDH WT and mutants were calculated via obtaining the absorbance at 280 nm using an extinction coefficient of

64143 $M^{-1}cm^{-1}$. The proteins were flash frozen in liquid nitrogen and stored at -80 ºC. Due to loss of activity overtime after flash freezing, the enzymes were discarded no later than 2 months after purification. I purified most mutants except for WT and H133Q IDH1.

2.3.4. Steady State Kinetic Assays

Kinetic assays were performed at 21 ºC and 37 ºC, with two protein preparations per enzyme used to confirm reproducibility. The lower temperature assays were performed to compare our data with published results, and the higher temperature assays were used to get rates at physiologically relevant conditions. An 8452 diode array spectrophotometer (Olis, Atlanta, GA) was used for most kinetic assays. For the conversion of ICT to αKG, assays were performed in a quartz cuvette containing reaction buffer (50 mM Tris, pH 7.5, either at ambient temperature or 37 ºC, 150 mM NaCl, 10 mM $MgCl_2$, and 1 mM DTT) and IDH1 (100 nM for H133Q, R100Q, R132C, R132G, R132A, and R132Q, and 500 nM for A134D, R132H, R132W, R132K, and R132N). The contents of the cuvette were pre-incubated at the assay temperature for 3 min. After pre-incubation, the reactions were initiated by adding saturating concentrations of $NADP^+$ while titrating ICT (to determine $K_{M,ICT}$), or adding saturating concentrations of ICT while titrating $NADP^+$ (to determine $K_{M,NADP^+}$). NADPH formation was monitored at 340 nm. For conversion of αKG to D2HG, the same reaction buffer was used (500 nM enzyme concentrations were used for all mutants, except R132H and R132A IDH1, where 200 nM was used). These assays were also pre-incubated at the desired temperature. The reactions were initiated by adding saturating concentration of NADPH while titrating αKG (to determine $K_{M,\ \alpha KG}$), and vice versa. The pH of αKG was adjusted to 7.0 before use. The depletion of NADPH was monitored at 340 nm. The slope of the linear range of the assay was converted from abs/s to nM/s using the extinction coefficient for NADPH (6.22 $cm^{-1}mM^{-1}$). In order to convert V_0 to k_{obs} (s^{-1}), each slope was divided

by the respective enzyme concentration used in the assay. The result of this conversion for each concentration of substrate was plotted using GraphPad Prism (GraphPad Software, La Jolla, CA) and fit using a hyperbolic function in order to determine both k_{cat} and K_M.

Since the conversion of ICT to αKG by WT was too fast to confidently obtain slopes from the diode array, an RSM-1000 stopped-flow spectrophotometer (OLIS) was used in absorbance mode to increase the point density within the linear range of the assay. The concentration of WT IDH1 was reduced to 30 nM (final) and reactions were performed in replicates of 3-5. The parameters were obtained in the same way as previously mentioned. Due to low $K_{M,\ NADPH}$ values observed for the IDH1 mutants, a DM 45 spectrofluorometer (OLIS) was used for the titrations of NADPH for R100Q, R132H, and R132C IDH1 (50 nM), and $NADP^+$ titrations for WT IDH1 (3 nM) after generating a standard curve of concentrations of NADPH. The standard curve of NADPH concentrations was generated each time the instrument was used to accurately calculate the rates. I generated steady-state kinetic data for R132H, R132C, R132Q, R132G, R132N, R132A, R100Q and H133Q IDH1).

2.3.5. GC/MS Analysis of D2HG Formation

To confirm D2HG, rather than ICT, was formed by certain mutants, 19 μM IDH1 (R100Q, R132G, R132A, R132K, R132N, R132Q, and R132W) was incubated in reaction buffer, and the reaction was initiated with 240 μM of NADPH and 240 μM of αKG and monitored at 340 nm for 100 s. An aliquot of the reaction was removed and 0.13 M EDTA was used to chelate the Mg^{2+} and quench the reaction. Then, the aliquot was lyophilized to dryness. The dried aliquots were redissolved in 50% methanol containing *L*-norvaline as an internal standard, and re-dried using a lyophilizer (MiVac, SP Scientific, Warminster, PA). *L*-norvaline, αKG, D2HG, and ICT (1 mM) were prepared to use as standards. The standards and incubations were derivatized with O-

isobutylhydroxylamine hydrochloride and *N*-tert-butyldimethylsilytrifluoroacetamide and analyzed using GC/MS. All measurements were performed in duplicates. I performed the reactions while the D2HG quantification was performed by Dr. David Scott (Sanford Burnham Prebys)

2.3.6. Thermal Stability Assays Using Circular Dichroism

In order to assess the stability of all enzymes, Circular dichroism (CD) spectrophotometry was used. IDH1 was diluted to about 5 μM in a buffer containing 10 mM potassium phosphate at pH 7.5 and 100 mM NaCl. The experiment was initiated at 5 ºC and the temperature was increased to 70 ºC in 1º increments. As the secondary structure of IDH1 is governed mostly by α-helices, signal at 222 nm was monitored, which corresponds to α-helicity. The data was analyzed using Igor software package (WaveMetrics) and fit to a Santoro-Bolen equation[35]. I performed these assays along with Eric Gonzalez.

2.3.7. Structure Modeling of IDH1 Mutations

PDB code 4KZO[29] an IDH1 structure containing αKG and $NADP^+$, and 1T0L[36] a structure containing ICT and $NADP^+$, were used to model IDH1 mutations. Ligand-restraint generation and optimization of cif files were created using eLBOW in Phenix software[37], and mutations were created using COOT[38]. Geometry minimization in the Phenix software[37] was used to regularize geometries of each mutant IDH1 model bound to ligands, with 500 maximum iterations and 5 macrocycles. These models were generated by Dr. Christal Sohl.

2.4. Results

2.4.1. Structural Modeling and Thermal Stability of IDH1 Mutations

The structures of WT and R132H IDH1 bound to both substrates, either ICT with $NADP^+$, or αKG and $NADP^+$, have been published[12, 29, 31, 36]. A cryo-EM structure of R132C IDH1 showed the enzyme in complex with NADPH[39]. In order to understand structure differences in R132C, R132G, R100Q, A134D, and H133Q IDH1, we created models of these mutants with previously published IDH1 structure of R132H IDH1 in complex with αKG, $NADP^+$, and Ca^{2+} (PDB: 4KZO)[29], and WT IDH1 in complexed with ICT, $NADP^+$, and Ca^{2+} (PDB: 1T0L)[36], using geometry minimization in Phenix[37]. The resulted structures were aligned to the R132H IDH1 initial structure using PyMOL[40] (Figure 2). These models showed minimal changes in the overall structure, which was consistent with previous structural studies of R132H IDH1. The catalytic residue Y139 has a more pronounced movement when ICT binds as compared to bound αKG, likely as a result of the absence of the carboxylate in αKG.

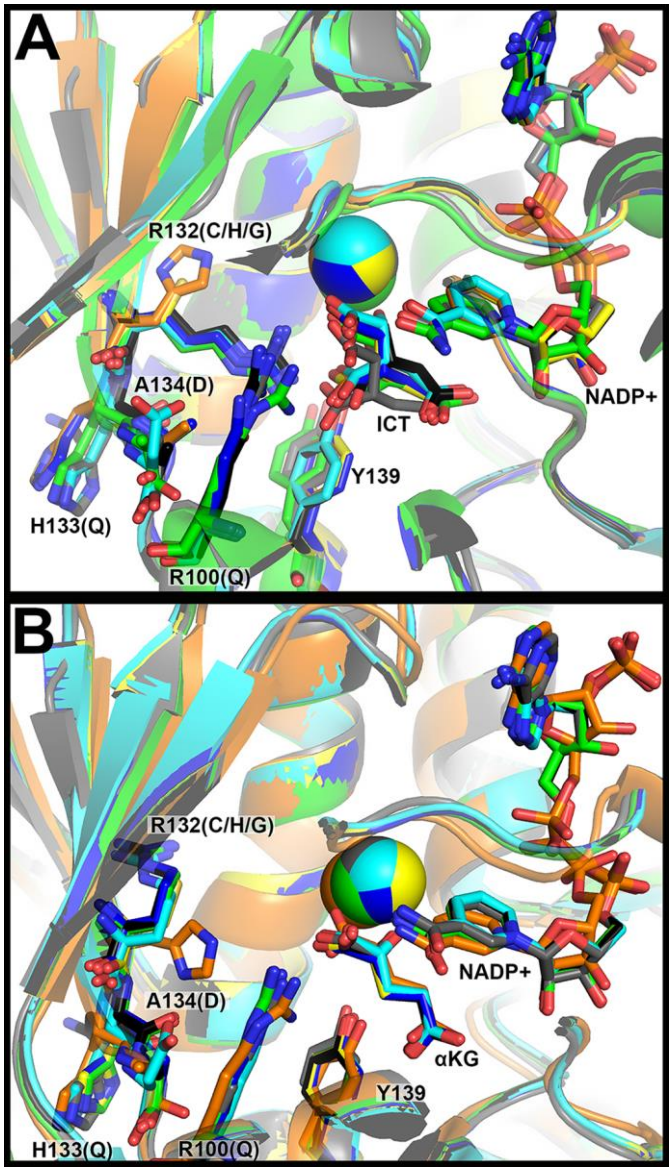

Figure 2. Structural modeling of IDH1 mutations identified in tumors. **A.** The structure of WT IDH1 complexed with ICT, $NADP^+$, and Ca^{2+} (PDB 1T0L[36]) and **B.** R132H IDH1 complexed with αKG, $NADP^+$, and Ca^{2+} (PDB 4KZO[30]) were used to model additional mutations. In both panels, WT IDH1 is shown in green, A134D in cyan, H133Q in black, R100Q in dark blue, R132H in orange, R132C in yellow, and R132G in grey. Substrates and residues that are mutated are highlighted in stick format, as well as catalytic residue Y139. Ca^{2+} is shown as a sphere. Ligand restraint generation and optimization of provided cif files were generated using eLBOW in the Phenix software suite[37], and mutations were made using Coot[38]. Geometry Minimization (Phenix software suite)[37] was used to regularize geometries of the models, with 500 iterations and 5 macro cycles

To study the mechanistic features of mutant IDH1 enzymes, we created mutant cDNA constructs and heterologously expressed and purified in *E. coli* as homodimers, achieved a purity of over 95% after Ni-NTA affinity chromatography (Supplemental Figure S1A). We performed thermal stability assays using circular dichroism to assess the changes in melting temperature (T_m). The changes in T_m were small, ranging from 46.8 ^oC for R132C to 51.9 ^oC for R100Q IDH1, compared to WT IDH1 (49.1 ^oC) (Supplemental Figure S2A). The changes in T_m were about 5% from R132C to WT IDH1 as well as from WT to R100Q IDH1.

2.4.2. Efficiency of Reactions Catalyzed by IDH1 Mutants Found in Tumors

R132H and R132C IDH1 mutants are the most common mutations in gliomas[41]. R132G IDH1 has been linked with higher frequency in chondrosarcomas[42, 43] than in gliomas, and this mutant has been known to produce D2HG[32]. R100Q IDH1, analogous to R140Q IDH2, a D2HG producer in mutant IDH2-driven cancers, is relatively rare[44]. Finally, the very rare A134D and H133Q IDH1 mutants are found in thyroid cancer and they are thought to have low activity in the normal reaction[33, 44]. We performed steady-state kinetic assays to understand the catalytic efficiencies (k_{cat}/K_M) of these mutants when performing the conversion of ICT to αKG (normal reaction) and αKG to D2HG (neomorphic reaction), by observing the production and depletion of NADPH respectively. All the mutants had decreased in activity for the normal reaction, ranging from 3.5-fold for H133Q IDH1 to 1,340-fold for the other IDH1 mutants (Figure 3, Supplemental Figure S3, Table 1). The decreased in catalytic efficiencies were due to reduce k_{cat} and K_M.

Table 1. Kinetic parameters for the normal reaction, conversion of ICT to αKG, catalyzed by IDH1. Values result from fits of kinetic data using two different enzyme preparations. The standard error was determined from the deviance from these hyperbolic fits (Fig. 3, Supplemental Fig. S3).

IDH1	Hydrophilicity scale at residue 132	van der Waals volume of side chain at residue 132, Å^3)	k_{cat}, s^{-1} (37° C)	$K_{M,,ICT}$, mM (37°C)	$K_{M,NADP+}$, mM (37°C)	Efficiency, mM^{-1} s^{-1} ($k_{cat}/K_{M,ICT}$, 37°C)	k_{cat}, s^{-1} (21° C)	$K_{M,ICT}$, mM (21°C)	$K_{M,NADP+}$, mM (21°C)	Efficiency, mM^{-1} s^{-1} ($k_{cat}/K_{M,ICT}$, 21°C)
WT	-14 (R)	148 (R)	85 ± 4	0.22 ± 0.02	0.08 ± 0.03	3.9 ± 0.4 × 10^2	11.0 ± 0.4	0.015 ± 0.003	0.03 ± 0.01	7.3 ± 1.3 × 10^2
H133Q	-14 (R)	148 (R)	45 ± 2	0.40 ± 0.08	0.16 ± 0.02	1.1 ± 0.2 × 10^2	9.4 ± 0.6	0.28 ± 0.07	0.101 ± 0.008	35 ± 9
A134D	-14 (R)	148 (R)	2.3 ± 0.2	8 ± 2	1.2 ± 0.3	0.29 ± 0.08	0.200 ± 0.008	2.7 ± 0.3	0.7 ± 0.1	0.074 ± 0.003
R100Q	-14 (R)	148 (R)	5.6 ± 0.4	8 ± 2	0.18 ± 0.02	0.7 ± 0.2	1.40 ± 0.06	9 ± 1	0.070 ± 0.006	0.16 ± 0.02
R132H	8 (H)	118 (H)	2.4 ± 0.1	4.2 ± 0.6	1.6 ± 0.5	0.57 ± 0.08	0.120 ± 0.006	6 ± 1	1.0 ± 0.9	0.020 ± 0.003
R132C	49 (C)	86 (C)	4.4 ± 0.1	8.2 ± 0.8	0.75 ± 0.07	0.54 ± 0.05	1.61 ± 0.08	5.3 ± 0.8	0.58 ± 0.08	0.30 ± 0.05
R132G	0 (G)	48 (G)	9.3 ± 0.6	7 ± 1	0.067 ± 0.007	1.3 ± 0.2	1.0 ± 0.06	3.6 ± 0.6	0.14 ± 0.02	0.28 ± 0.05

For the neomorphic reaction, the catalytic efficiencies varied widely (Figure 4m Supplemental Figure S4, Table 2). The catalytic efficiency of A134D and H133Q IDH1 could not be determined because only saturating concentrations of αKG showed rates that were higher than the signal-to-noise threshold. Therefore, only the upper limit of the k_{cat} was determined as observed rates (Figure 4, B and D) since K_M values could not be determined. R132G IDH1 had the highest catalytic efficiency for D2HG production (~125-fold higher than WT IDH1), due to decreased K_M values and increased k_{cat} values. The catalytic efficiencies of R132C and R132H IDH1 were lower than R132G IDH1, with lower K_M for R132C compared to R132H IDH1 (Table 2). These results

may indicate that the production of D2HG in tumors by both R132G and R132C IDH1 could be more significant than R132H IDH1 when considering the available cytosolic concentrations of αKG. These results were also in agreement with the D2HG concentrations measured in glioma tissues by Pusch and colleagues[32]. R100Q IDH1 was not very efficient at the neomorphic reaction due to its high K_M (Table 2).

Table 2. Kinetic parameters for the neomorphic reaction, conversion of αKG to D2HG, catalyzed by IDH1. Values result from fits of kinetic data using two different enzyme preparations. The standard error was determined from the deviance from these hyperbolic fits (Fig. 4, Supplemental Fig. S4).

IDH 1	**Hydrophilicity scale at residue 132**	**van der Waals volume of side chain at residue 132, Å^3 [b]**	**k_{cat}, s^{-1} (37° C)**	**$K_{M,\alpha KG}$ mM (37°C)**	**$K_{M,NADPH}$ mM (37°C)**	**Efficiency, mM^{-1} s^{-1} ($k_{cat}/K_{M,\alpha KG}$, 37°C)**	**k_{cat}, s^{-1} (21° C)**	**$K_{M,\alpha KG}$ mM (21°C)**	**$K_{M,NADPH}$, mM (21°C)**	**Efficiency, mM^{-1} s^{-1} ($k_{cat}/K_{M,\alpha KG}$, 21°C)**
WT	-14 (R)	148 (R)	0.019 ± 0.001	0.5 ± 0.3	≤ 0.010	0.04 ± 0.02	≤ 0.017	ND	ND	ND
H133Q	-14 (R)	148 (R)	≤ 0.016	ND	ND	ND	≤ 0.034	ND	ND	ND
A134D	-14 (R)	148 (R)	≤ 0.019	ND	ND	ND	≤ 0.020	ND	ND	ND
R100Q	-14 (R)	148 (R)	0.34 ± 0.02	12 ± 2	0.005 ± 0.003	0.028 ± 0.005	0.128 ± 0.006	10 ± 1	≤ 0.0025	0.013 ± 0.001
R132H	8 (H)	118 (H)	4.2 ± 0.3	1.1 ± 0.3	≤ 0.025	3.8 ± 0.9	0.43 ± 0.04	1.8 ± 0.6	≤ 0.005	0.24 ± 0.08
R132C	49 (C)	86 (C)	1.60 ± 0.07	0.36 ± 0.05	0.010 ± 0.009	4.4 ± 0.6	0.84 ± 0.03	0.36 ± 0.06	≤ 0.025	2.3 ± 0.4
R132G	0 (G)	48 (G)	1.59 ± 0.09	0.34 ± 0.08	< 0.025	5 ± 1	0.45 ± 0.02	0.30 ± 0.05	≤ 0.025	1.5 ± 0.2

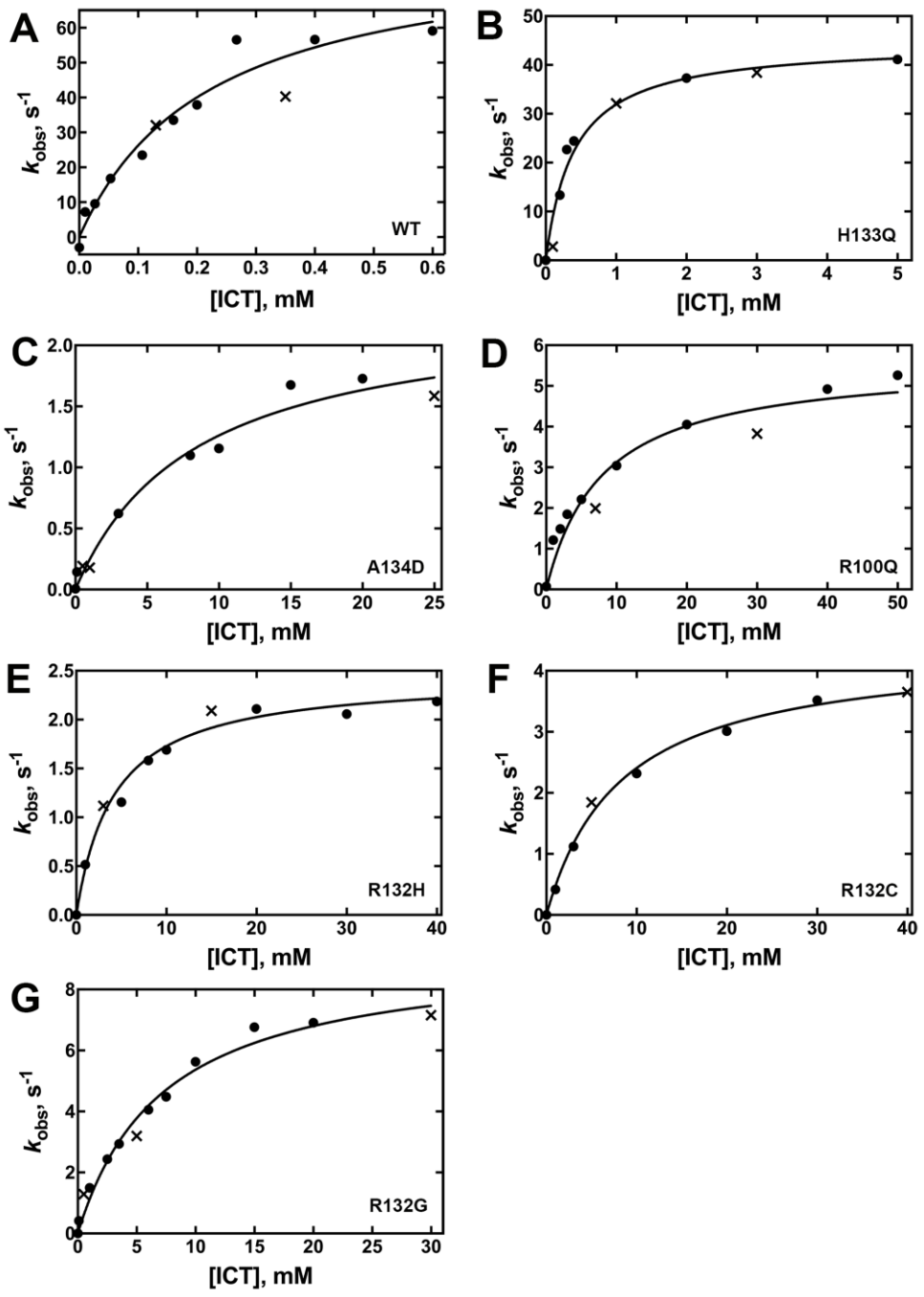

Figure 3. Concentration dependence of ICT concentration on the observed rate of NADPH production in the normal reaction (37 ºC). The determined k_{obs} values were obtained from two different enzyme preparations to ensure reproducibility. The k_{obs} values resulting from each of the two enzyme preparations are distinguished by using either a circle or an × in the plots. The observed rate constants (k_{obs}) were calculated from the linear range of the slopes of plots of concentration versus time using GraphPad Prism software (GraphPad, San Diego, CA). These k_{obs} values were then fit to a hyperbolic equation to generate k_{cat} and K_m values, and the standard error listed in Table 1 results from the deviance from these hyperbolic fits is indicated. The determined k_{obs} values were obtained from two different enzyme preparations to ensure reproducibility. Results from assays at 21 ºC are shown in Supplemental Fig. S3. **A.** WT IDH1. **B.** H133Q IDH1. **C.** A134D IDH1. **D.** R100Q IDH1. **E.** R132H IDH1. **F.** R132C IDH1. **G.** R132G IDH1.

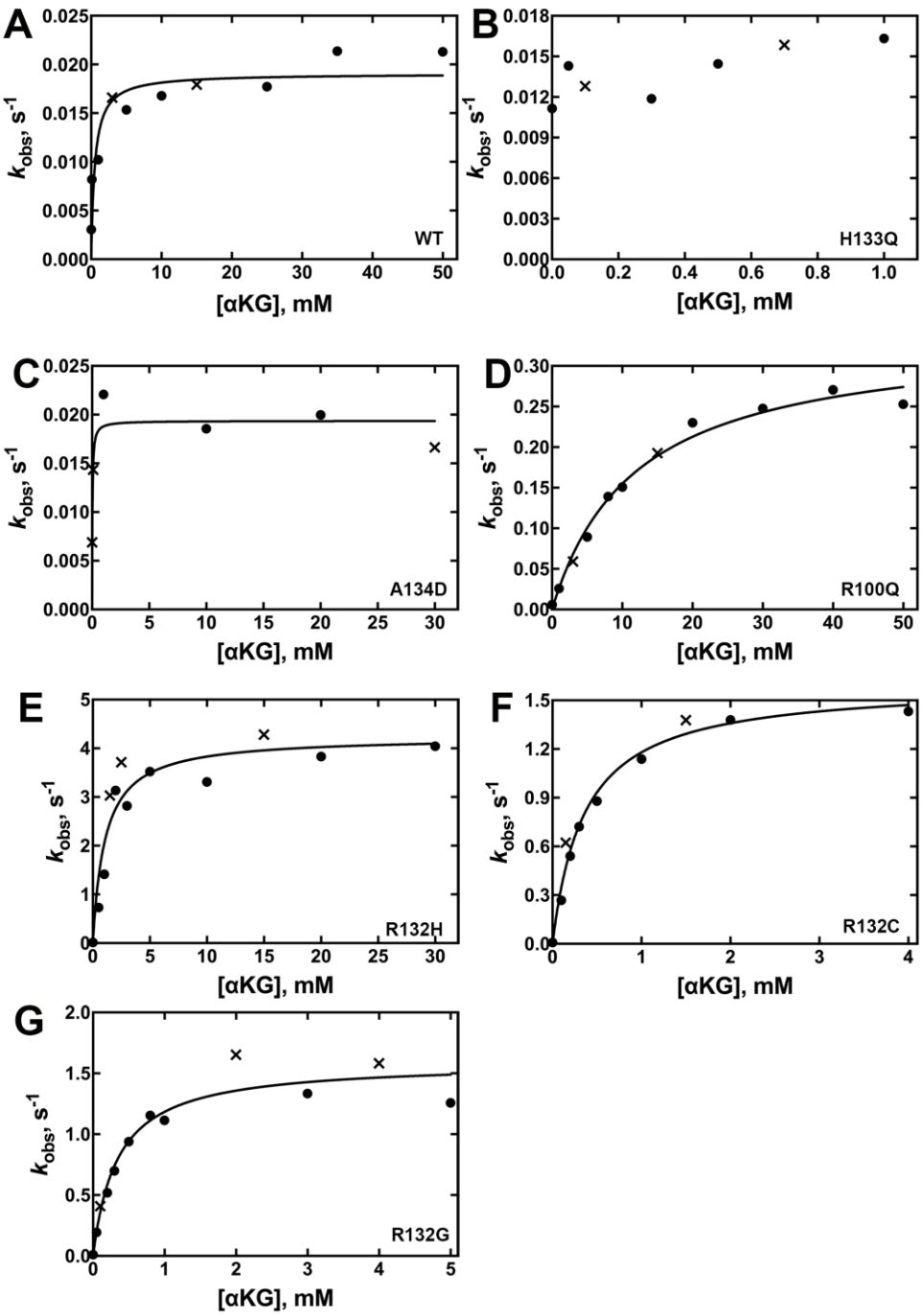

Figure 4. Concentration dependence of αKG concentration on the observed rate of NADPH depletion in the neomorphic reaction (37 ºC). The determined k_{obs} values were obtained from two different enzyme preparations to ensure reproducibility. The k_{obs} values resulting from each of the two enzyme preparations are distinguished by using either a circle or an × in the plots. The observed rate constants (k_{obs}) were calculated from the linear range of the slopes of plots of concentration versus time using GraphPad Prism software (GraphPad, San Diego, CA). These k_{obs} values were then fit to a hyperbolic equation to generate k_{cat} and K_m values, and the standard error results from the deviance from these hyperbolic fits is indicated. K_m values and efficiency are in terms of [αKG]. Due to limits of detection, K_m values could not be obtained for low efficiency IDH1 enzymes since only saturating k_{obs} rates could be detected. In this case, k_{obs} rates are reported, which approximate k_{cat} rates. Results from assays at 21 ºC are shown in Supplemental Fig. S4. **A.** WT IDH1. **B.** H133Q IDH1. **D.** R100Q IDH1. **E.** R132H IDH1. **F.** R132C IDH1. **G.** R132G IDH1.

2.4.3. GC/MS Analysis Confirms D2HG Production by IDH1 Tumor Mutants

Leonardi and colleagues studied the conversion of αKG to ICT (Figure 1A) and found that lower pH and a source of CO_2, as sodium bicarbonate, drive the reverse reaction, and concluded that IDH1 mutants are kinetically deficient for αKG and ICT interconversion[27]. Nevertheless, we sought to confirm whether R100Q and R132G IDH1 produce D2HG instead of ICT upon incubation with αKG and NADPH. R132H and R132C IDH1 have been well established as D2HG producers[12]; therefore, these mutants were not used for this study. We used Gas chromatography/mass spectrometry (GC/MS) to quantify the nmol of D2HG, αKG and ICT produced (data not shown) (Figure 5). R132G IDH1 generated high levels of D2HG compared to R100Q IDH1. These results were consistent with our kinetic studies (Figure 4 and 5). Less than 0.1nmols of ICT were measured, confirming that depletion of NADPH in these assays was associated with D2HG production.

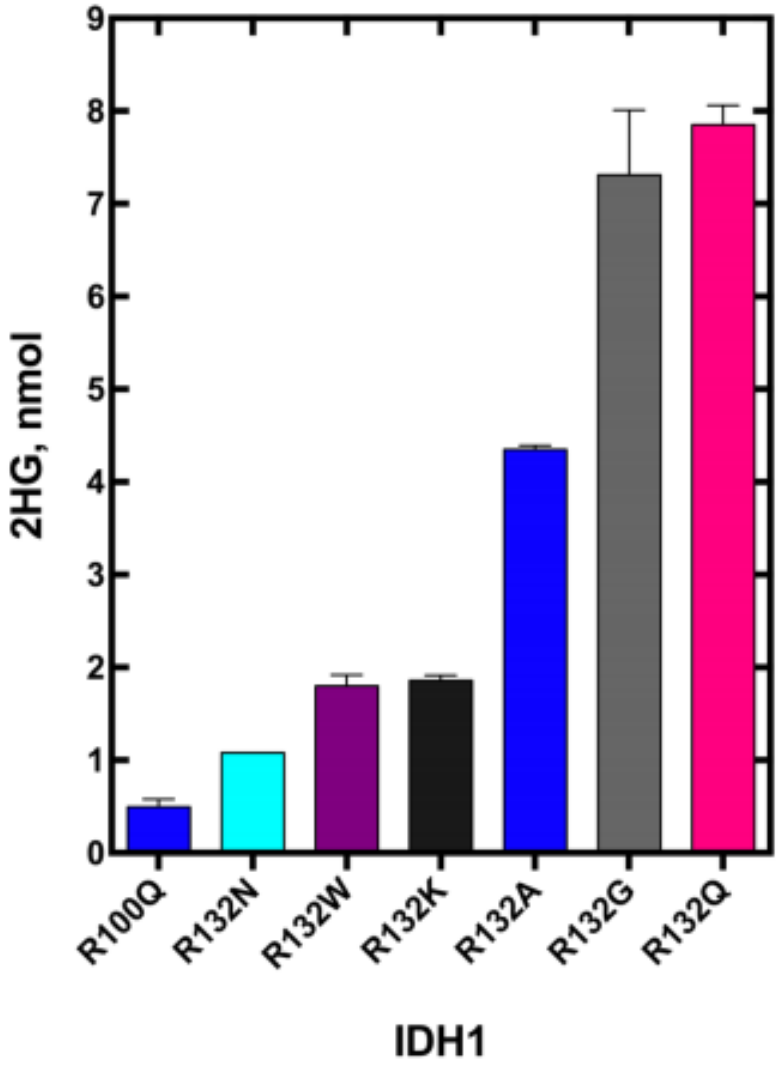

Figure 5. Absolute quantitation of 2HG present in an incubation of IDH1 mutants with αKG and NADPH. Measurements are reported as a calculated mean with standard error of the mean (SEM). Only trace amounts of ICT (< 0.1 nmol, based on limits of detection) were generated under these experimental conditions, indicating that NADPH oxidation was coupled to 2HG production, rather than ICT production.

2.4.4. Generation of IDH1 Mutants Engineered to Explore Mechanistic Features of D2HG Production

Besides R132H, R132C, and R132G IDH1, other R132 mutants have been linked to gliomas, such as R132S, R132L, and R132V IDH1[5, 6, 45, 46]. Previous kinetic assays have shown that R132S and R132L IDH1 had similar catalytic rates compared to R132H and R132C when producing D2HG[12, 27]. HEK293T cells expressing R132S and R132L showed similar levels of D2HG compared to cell lines expressing R132C and R132H[32]. All these mutants vary in the degree of hydrophobicity at residue 132, and they all have lower van der Waals volumes compared to WT. However, the role of the size and hydrophobicity of each mutant at position 132 when producing D2HG has not been studied.

We created IDH1 R132 mutants to help us elucidate the limits of hydrophobicity[47] and van der Waals volume[48] that would allow for D2HG production. R132A IDH1 has not been reported in tumors[49, 50] and is an example of a small hydrophobic residue, similar to R132G. Unsurprisingly, R132A IDH1 has been shown to be deficient in the normal reaction[31], but it is not known if R132A IDH1 can catalyze the neomorphic reaction. A second mutant, R132N IDH1, has also not been identified in tumors, but was selected since asparagine has smaller van der Waals volume and similar polarity to arginine, which is found in WT IDH1. R132Q IDH1 has been reported in chondrosarcomas, and a mouse model harboring this mutant reported D2HG levels up to 20-fold higher compared to R132H IDH1 *in vitro*[43, 51]. This mutant has similar hydrophobicity to arginine but a smaller van der Waals volume. R132K IDH1 is homologous to the most common IDH2 mutation seen in leukemia, R172K IDH2[10, 45]. R132K IDH1 has not been identified in tumors, and its kinetic features have not yet been determined. This mutant is similar to WT since both hydrophobicity and van der Waals volume are comparable (K versus R). Lastly, R132W has not

identified in tumors, and it represents the most extreme scenario for high hydrophobicity and van der Waals volume.

2.4.5. Structural Modeling and Thermal Stability of Engineered IDH1 Mutations

Since no crystal structure has been reported for any of these experimental mutants, we created models for each mutant using previously published R132H IDH1 in complex with αKG, $NADP^+$, and Ca^{2+} (4KZO)[29]. We used geometry minimization with Phenix[37] and aligned the resulted models using PyMOL[40] (Figure 6). Changes in the active site as well as the overall structure of the enzyme were small. When looking at the active site, the size of the mutation at R132 needed modest adjustment to avoid steric hindrance.

All the experimental mutants were heterologously expressed and purified to >95% after Ni-NTA affinity chromatography (Supplemental Figure S1B). We performed thermal stability assays using circular dichroism and we observed that the T_m shifts were minimal (Supplemental Figure S2B). R132K IDH1 showed the highest T_m at 49.8 ^oC.

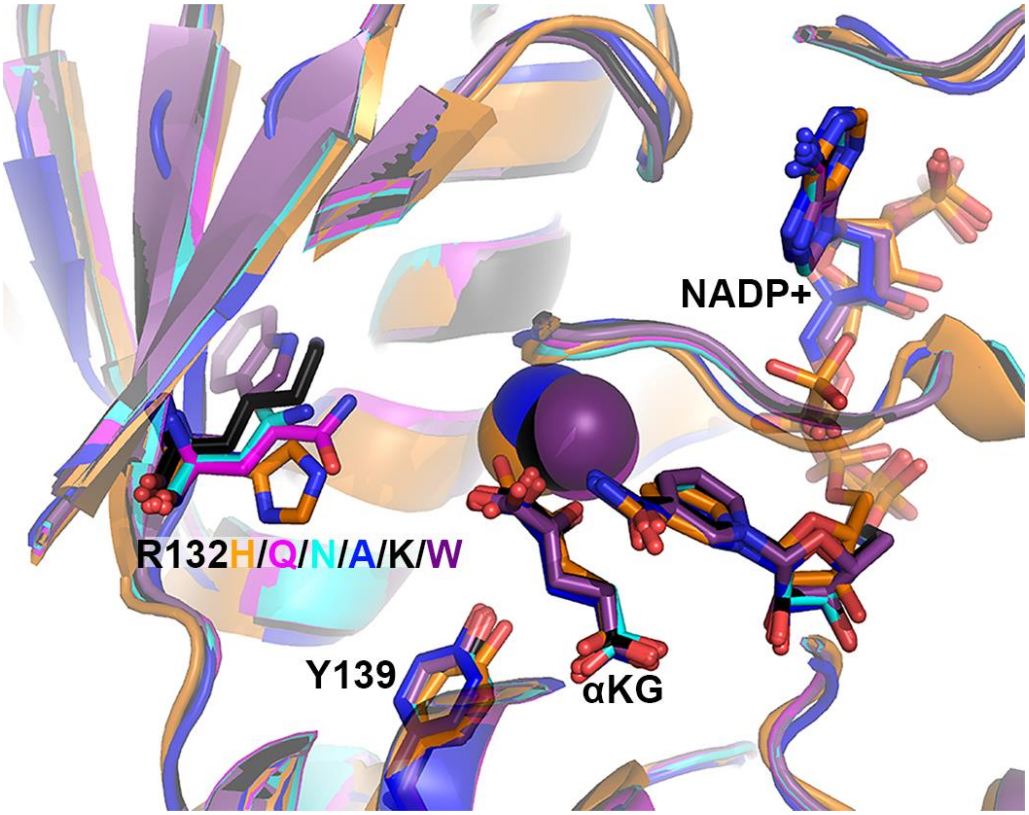

Figure 6. Structural models of experimental IDH1 mutants. The structure of R132H IDH1 complexed with αKG, $NADP^+$, and Ca^{2+} (PDB 4KZO) was used to model mutations of the tool IDH1 mutations. R132H IDH1 is shown in orange, R132Q in magenta, R132N in cyan, R132A in dark blue, R132K in black, and R132W in purple. Substrates and residues that are mutated are highlighted in stick format, as well as catalytic residue Y139. Ca^{2+} is shown as a sphere. Ligand restraint generation and optimization of provided cif files were generated using eLBOW in the Phenix software suite, and mutations were made using Coot. Geometry Minimization (Phenix software suite) was used to regularize geometries of the models, with 500 iterations and 5 macro cycles.

2.4.6. Kinetic Analysis of Engineered IDH1 Mutants

The catalytic efficiencies of each mutant at the normal reaction was assessed and plotted against ranking hydrophobicity[47] as well as against van der Waals volume[48] (Figure 7A and 7B). All mutants had low catalytic efficiencies for the normal reaction driven by a decreased in k_{cat} and an increase in K_M (Table 3, Supplemental Figure S5). Only R132Q and R132K IDH1 were able to conserve some degree of normal activity, with showing a 33 and 56-fold decrease in catalytic

efficiency, respectively. The remaining mutants had decreased catalytic efficiencies for the normal reaction of over 220-fold.

Table 3. Kinetic parameters for the normal reaction, conversion of ICT to αKG, catalyzed by IDH1. Values result from fits of kinetic data using two different enzyme preparations. The standard error is determined from the deviance from these hyperbolic fits (Supplemental Fig. S5).

IDH1	Hydrophilicity scale at residue 132[a]	van der Waals volume of side chain at residue 132, Å^3 [b]	k_{cat}, s^{-1} (37°C)	$K_{m,ICT}$, mM (37°C)	Efficiency, mM^{-1} s^{-1} ($k_{cat}/K_{m,ICT}$, 37°C)
R132W	97 (W)	163 (W)	1.21 ± 0.08	3.6 ± 0.6	0.34 ± 0.06
R132A	41 (A)	67 (A)	10.4 ± 0.2	5.7 ± 0.4	1.8 ± 0.1
R132Q	-10 (Q)	114 (Q)	9.2 ± 0.3	0.8 ± 0.2	12 ± 3
R132K	-23 (K)	135 (K)	7.2 ± 0.4	1.1 ± 0.2	7 ± 1
R132N	-28 (N)	96 (N)	0.047 ± 0.001	1.5 ± 0.1	0.031 ± 0.008

These experimental IDH1 mutants were also assessed for the neomorphic reaction (Figure 7, Supplemental Figure S6). R132Q IDH1 was the most efficient of all R132 tumor-relevant and experimental mutants, with 4-fold higher catalytic efficiency compared to the second most efficient mutant, R132G IDH1. A decrease in catalytic efficiency was observed for all other R132 mutants, with R132A having comparable efficiency to R132G, R132C, and R132H IDH1. R132N, R132K, R132W and WT IDH1 had dramatically decreased catalytic efficiencies when performing the neomorphic reaction. The low catalytic efficiency observed for R132N IDH1 was primarly driven by a very high K_M (Table 4). This result suggested that the production of D2HG by this enzyme was not physiologically relevant, since these high concentrations of αKG are not typically observed in the cell.

Table 4. Kinetic parameters for the neomorphic reaction, conversion of αKG to 2HG, catalyzed by IDH1. Values result from fits of kinetic data using two different enzyme preparations. The standard error is determined from the deviance from these hyperbolic fits (Supplemental Fig. S6).

IDH1	Hydrophilicity scale at residue 132[a]	van der Waals volume of side chain at residue 132, Å^3 [b]	k_{cat}, s^{-1} (37ºC)	$K_{m,\alpha KG}$, mM (37ºC)	Efficiency, mM^{-1} s^{-1} ($k_{cat}/K_{m,\alpha KG}$, 37ºC)
R132W	97 (W)	163 (W)	0.54 ± 0.01	0.82 ± 0.08	0.659 ± 0.007
R132A	41 (A)	67 (A)	0.37 ± 0.01	0.11 ± 0.02	3.4 ± 0.6
R132Q	-10 (Q)	114 (Q)	4.7 ± 0.2	0.26 ± 0.04	18 ± 3
R132K	-23 (K)	135 (K)	0.57 ± 0.02	0.61 ± 0.07	0.9 ± 0.1
R132N	-28 (N)	96 (N)	0.79 ± 0.06	10 ± 2	0.08 ± 0.02

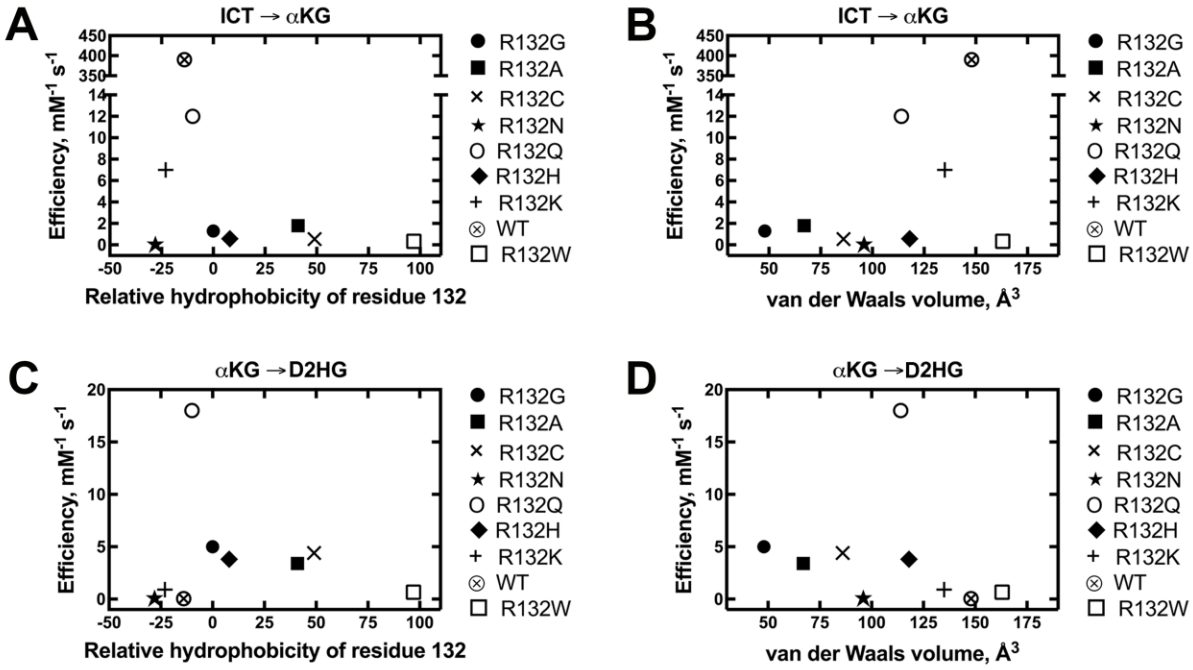

Figure 7. Comparisons of catalytic efficiency by IDH1 with mutations at residue 132. The observed rate constants (k_{obs}) were calculated from the linear range of the slopes of plots of concentration versus time, and then fit to a hyperbolic equation to generate k_{cat} and K_M values. All experiments were performed at 37 ºC. These catalytic parameters result from fits of kinetic data resulting from two different enzyme preparations to ensure reproducibility. **A.** Relative catalytic efficiencies (k_{cat}/K_M) of the conversion of ICT to αKG using K_M values for ICT are plotted against relative hydrophobicity. **B.** Relative catalytic efficiencies (k_{cat}/K_M) of the conversion of ICT to αKG using K_M values for ICT are plotted against van der Waals volume. **C.** Relative catalytic efficiencies (k_{cat}/K_M) of the conversion of αKG to 2HG using K_M values for αKG are plotted against relative hydrophobicity. **D.** Relative catalytic efficiencies (k_{cat}/K_M) of the conversion of αKG to 2HG using K_M values for αKG are plotted against van der Waals volume.

2.4.7. GC/MS Analysis Confirms D2HG Production by Engineered IDH1 Mutants

We sought to confirm whether the depletion of NADPH in our kinetic assays corresponded D2HG or ICT production. We used GC/MS to quantify the levels of D2HG, ICT, and αKG for each experimental mutant. R132Q and R132G IDH1 catalysis led to the highest concentrations of D2HG, supporting our kinetic analysis, followed by R132A (Figure 5). The levels of ICT were difficult to detect at lower than 0.1nmol produced. These results suggested that the depletion of NADPH resulted from αKG to D2HG production, rather than ICT, under these experimental conditions.

2.5. Discussion

In this study, we performed an extensive steady-state kinetic characterization of mutant IDH1 seen in tumors (R132H, R132C, R132G, R132Q, R100Q, A134D, and H133Q IDH1) and additional experimental mutants (R132A, R132K, R132N, and R132W), as well as WT IDH1 in to investigate the effects of hydrophobicity and van der Waals volume at residue 132 in driving the neomorphic reaction. Our reported k_{cat} for WT IDH1 is in closed agreement with previous reported rates ranging from ~9 to 12s^{-1} [28, 29, 31], at room temperature; while, other studies have shown catalytic rates to be much higher[12, 14]. K_M values previously reported, for both normal reaction ligands, range from 5 to 65 μM at room temperature[12, 14, 27-29, 31], which are comparable to our values (Table 1). Moreover, plasma concentration of αKG have been quantified to be around 23 μM[52], which are also comparable to our measured K_M values.

H133Q IDH1 was the second most efficient enzyme, after WT IDH1, at catalyzing the normal reaction, and was unable to catalyze the neormophic reaction, indicating that this mutant could be a passenger mutation when found in tumors (Table 1 and 2). R100Q IDH1 had very high

K_M values for ICT and αKG, which meant a reduction in catalytic efficiency for both reactions (Table 1 and 2). Interestingly, R140Q IDH2, analogous to R100Q, is the most common mutation found in AML[53], but kinetic characterization for IDH2 mutants were limited[30, 54]. On the other hand, R100 coordinates the C3 carboxylate group of ICT and the carbonyl group αKG[29, 36], which may explain the high K_M for these substrates. Therefore, structural characterization of R100Q IDH1, aligned with R140Q IDH2, may provide important insight in structural differences that may elucidate any differences between these two analogous mutations. Our data suggests that R100Q IDH1 is a poor D2HG producer.

The second most common IDH2 associated to AML is R172K[55], which it is homologous to R132K IDH1. The very low catalytic efficiency of R132K IDH1 for the neomorphic reaction was also surprising (Table 4). Therefore, a structural characterization of R132K IDH1 aligned with R172K IDH2 is important to assess any structural differences that may allow for differences in function between these two mutations. Low levels of D2HG produced *in vitro* for both R132K and R100Q IDH1 may provide insights of why each mutation is not seen in gliomas or is extremely rare.

Some IDH1 mutants show K_M values for αKG in the neomorphic reaction that are higher than the physiological concentrations of this metabolite. However, IDH1 mutations likely form WT/mutant heterodimers, and a weakness in our work is that we studied mutant/mutant IDH1 homodimers. The local concentration of αKG in WT/mutant IDH1 heterodimer may be higher due to production of this metabolite by the WT monomer, since substrate channeling between both monomers may still be possible, though recent reports suggest this is unlikely[56]. In cells, D2HG production is increased as long as the WT IDH1 activity is conserved[30]. However, in cases where the K_M is very large, (e.g. R100Q IDH1), the presence of the WT monomer may not be sufficient

to produce adequate αKG to drive the reaction forward. A future direction is to express WT and each mutant separately, combine the lysates and then purify heterodimers with a sequence of affinity chromatography columns as described previously[27, 28]. One challenge is that it would be possible for the WT/mutant heterodimers to interconvert to WT/WT and mutant/mutant homodimers.

In 2014, Pusch and colleagues quantified D2HG levels in cells and in tumor tissue by R132G, R132C, R132H IDH1[32]. In both scenarios, R132G IDH1 produced the most D2HG, followed by R132C and then R132H IDH1[32]. They also reported that R100Q had the lowest levels of D2HG produced in cells[32]. These findings agree with our steady-state kinetic analysis of these mutants (Table 2). Moreover, *in vitro* kinetic analysis by Pusch and colleagues showed that the $K_{M,\ \alpha KG}$ value was highest for R100Q, followed by R132H, R132G, and R132C IDH1[32]. These results also agree with our reported K_M values. Other groups have also performed kinetic analysis for R132C, R132H, and/or R132G IDH1, but k_{cat} and K_M values have only been reported for R132H and R132C IDH1 (Table 2).

An interesting observation by Pusch and colleagues was that the amount of D2HG produced is not directly proportional to the frequency of mutations in gliomas[32]. These results agree with our steady-state kinetic data where the rare R132G and R132Q IDH1 mutants were the most catalytic efficient at D2HG production, while R132H and R132C IDH1 were less efficient but more common in gliomas, though, R132H IDH1 is less common than R132C and R132G in chondrosarcomas[43].

We observed a trend in hydrophobicity of the R132 mutations when performing the normal reaction (Figure 7A). Lysine, arginine, and glutamine rank very closely when comparing relative hydrophobicity[47]. These mutants showed the highest catalytic efficiency when converting ICT to

αKG (Table 1 and 3). The catalytic efficiencies can also be driven by the size and shapes of the mutations. However, R132N IDH1 was surprisingly inactive since the van der Waals volume was similar to those that perform the normal reaction (i.e. more hydrophilic)[47]. The catalytic inefficiency of R132N IDH1 was mostly driven by very low k_{cat} values, while having similar K_M values as compared to other experimental R132 IDH1 mutants. This may be a result of a shift in orientation of Y139, or asparagine failing to orient ICT properly. A crystal structure of this mutant would provide insights as to why this mutant catalyzes the normal reaction so poorly. Residues more hydrophobic than R132Q IDH1 had dramatically decreased catalytic efficiency when converting ICT to αKG (Figure 7A). With the exception of R132H and R132W IDH1, all other mutants had lower van der Waals volumes as compared to R132K, WT, and R132Q IDH1. This suggested that the size of the mutant was also important for efficient catalysis of the normal reaction. It is important to also take into consideration the shape of the residue; histidine and lysine have similar van der Waals volume, but one is ring-shaped and the other one rod shaped. When considering all aspects, more polar, bigger, and longer residues appeared to support the normal reaction.

For the neomorphic reaction, trends were not as clear but conversion of αKG to D2HG may be driven more by hydrophobicity than by size (Figure 7, C and D). The more hydrophobic residues, excluding R132W IDH1, were the most efficient at catalyzing the neomorphic reaction, though, a very notable exception to this was the highly catalytically efficient R132Q IDH1. Smaller residues also tended to high more efficient D2HG production, though there were again notable exceptions of this trend.

An important discovery of this work is the dual activity of R132Q IDH1. This mutant was the only variant capable of supporting both reactions (Tables 3 and 4). The catalytic efficiency of

R132Q IDH1 in both reactions was mostly driven by high k_{cat} values. Other catalytic features, such as the conversion of αKG to ICT, will be interesting to compare to WT IDH1 catalysis.

This work represents the first large-scale kinetic characterization of several tumor relevant IDH1 mutants as well as engineered mutants that provide mechanistic insight. We observed that IDH1 mutants were deficient in catalyzing the normal reaction, showing large variation in the neormorphic reaction. This work also provides important insights on identifying mutants that may have a more oncogenic, tumor suppressive, or passenger role in tumors.

2.6. References

1. Warburg, O., Über den Stoffwechsel der Carcinomzelle. *Klin Wochenschr* **1925,** *4*, 534-536.

2. Warburg, O., Origin of cancer cells. *Oncologia* **1956,** *9* (2), 75-83.

3. Racker, E., Bioenergetics and the problem of tumor growth. *Am Sci* **1972,** *60* (1), 56-63.

4. Parsons, D. W.; Jones, S.; Zhang, X.; Lin, J. C.; Leary, R. J.; Angenendt, P.; Mankoo, P.; Carter, H.; Siu, I. M.; Gallia, G. L.; Olivi, A.; McLendon, R.; Rasheed, B. A.; Keir, S.; Nikolskaya, T.; Nikolsky, Y.; Busam, D. A.; Tekleab, H.; Diaz, L. A., Jr.; Hartigan, J.; Smith, D. R.; Strausberg, R. L.; Marie, S. K.; Shinjo, S. M.; Yan, H.; Riggins, G. J.; Bigner, D. D.; Karchin, R.; Papadopoulos, N.; Parmigiani, G.; Vogelstein, B.; Velculescu, V. E.; Kinzler, K. W., An integrated genomic analysis of human glioblastoma multiforme. *Science* **2008,** *321* (5897), 1807-12.

5. Balss, J.; Meyer, J.; Mueller, W.; Korshunov, A.; Hartmann, C.; von Deimling, A., Analysis of the IDH1 codon 132 mutation in brain tumors. *Acta Neuropathol* **2008,** *116* (6), 597-602.

6. Bleeker, F. E.; Lamba, S.; Leenstra, S.; Troost, D.; Hulsebos, T.; Vandertop, W. P.; Frattini, M.; Molinari, F.; Knowles, M.; Cerrato, A.; Rodolfo, M.; Scarpa, A.; Felicioni, L.; Buttitta, F.; Malatesta, S.; Marchetti, A.; Bardelli, A., IDH1 mutations at residue p.R132 (IDH1(R132)) occur frequently in high-grade gliomas but not in other solid tumors. *Hum Mutat* **2009,** *30* (1), 7-11.

7. Losman, J. A.; Kaelin, W. G., Jr., What a difference a hydroxyl makes: mutant IDH, (R)-2-hydroxyglutarate, and cancer. *Genes Dev* **2013,** *27* (8), 836-52.

8. Dang, L.; Yen, K.; Attar, E. C., IDH mutations in cancer and progress toward development of targeted therapeutics. *Ann Oncol* **2016,** *27* (4), 599-608.

9. Dang, L.; Jin, S.; Su, S. M., IDH mutations in glioma and acute myeloid leukemia. *Trends Mol Med* **2010,** *16* (9), 387-97.

10. Yan, H.; Parsons, D. W.; Jin, G.; McLendon, R.; Rasheed, B. A.; Yuan, W.; Kos, I.; Batinic-Haberle, I.; Jones, S.; Riggins, G. J.; Friedman, H.; Friedman, A.; Reardon, D.; Herndon, J.; Kinzler, K. W.; Velculescu, V. E.; Vogelstein, B.; Bigner, D. D., IDH1 and IDH2 mutations in gliomas. *N Engl J Med* **2009,** *360* (8), 765-73.

11. Zhao, S.; Lin, Y.; Xu, W.; Jiang, W.; Zha, Z.; Wang, P.; Yu, W.; Li, Z.; Gong, L.; Peng, Y.; Ding, J.; Lei, Q.; Guan, K. L.; Xiong, Y., Glioma-derived mutations in IDH1 dominantly inhibit IDH1 catalytic activity and induce HIF-1alpha. *Science* **2009,** *324* (5924), 261-5.

12. Dang, L.; White, D. W.; Gross, S.; Bennett, B. D.; Bittinger, M. A.; Driggers, E. M.; Fantin, V. R.; Jang, H. G.; Jin, S.; Keenan, M. C.; Marks, K. M.; Prins, R. M.; Ward, P. S.; Yen, K. E.; Liau, L. M.; Rabinowitz, J. D.; Cantley, L. C.; Thompson, C. B.; Vander Heiden, M. G.; Su, S. M., Cancer-associated IDH1 mutations produce 2-hydroxyglutarate. *Nature* **2009,** *462* (7274), 739-44.

13. Ward, P. S.; Patel, J.; Wise, D. R.; Abdel-Wahab, O.; Bennett, B. D.; Coller, H. A.; Cross, J. R.; Fantin, V. R.; Hedvat, C. V.; Perl, A. E.; Rabinowitz, J. D.; Carroll, M.; Su, S. M.; Sharp, K. A.; Levine, R. L.; Thompson, C. B., The common feature of leukemia-associated IDH1 and IDH2 mutations is a neomorphic enzyme activity converting alpha-ketoglutarate to 2-hydroxyglutarate. *Cancer Cell* **2010,** *17* (3), 225-34.

14. Gross, S.; Cairns, R. A.; Minden, M. D.; Driggers, E. M.; Bittinger, M. A.; Jang, H. G.; Sasaki, M.; Jin, S.; Schenkein, D. P.; Su, S. M.; Dang, L.; Fantin, V. R.; Mak, T. W., Cancer-associated metabolite 2-hydroxyglutarate accumulates in acute myelogenous leukemia with isocitrate dehydrogenase 1 and 2 mutations. *J Exp Med* **2010,** *207* (2), 339-44.

15. Xu, W.; Yang, H.; Liu, Y.; Yang, Y.; Wang, P.; Kim, S. H.; Ito, S.; Yang, C.; Wang, P.; Xiao, M. T.; Liu, L. X.; Jiang, W. Q.; Liu, J.; Zhang, J. Y.; Wang, B.; Frye, S.; Zhang, Y.; Xu, Y. H.; Lei, Q. Y.; Guan, K. L.; Zhao, S. M.; Xiong, Y., Oncometabolite 2-hydroxyglutarate is a competitive inhibitor of alpha-ketoglutarate-dependent dioxygenases. *Cancer Cell* **2011,** *19* (1), 17-30.

16. Chowdhury, R.; Yeoh, K. K.; Tian, Y. M.; Hillringhaus, L.; Bagg, E. A.; Rose, N. R.; Leung, I. K.; Li, X. S.; Woon, E. C.; Yang, M.; McDonough, M. A.; King, O. N.; Clifton, I. J.; Klose, R. J.; Claridge, T. D.; Ratcliffe, P. J.; Schofield, C. J.; Kawamura, A., The oncometabolite 2-hydroxyglutarate inhibits histone lysine demethylases. *EMBO Rep* **2011,** *12* (5), 463-9.

17. Lu, C.; Ward, P. S.; Kapoor, G. S.; Rohle, D.; Turcan, S.; Abdel-Wahab, O.; Edwards, C. R.; Khanin, R.; Figueroa, M. E.; Melnick, A.; Wellen, K. E.; O'Rourke, D. M.; Berger, S. L.; Chan, T. A.; Levine, R. L.; Mellinghoff, I. K.; Thompson, C. B., IDH mutation impairs histone demethylation and results in a block to cell differentiation. *Nature* **2012,** *483* (7390), 474-8.

18. Turcan, S.; Rohle, D.; Goenka, A.; Walsh, L. A.; Fang, F.; Yilmaz, E.; Campos, C.; Fabius, A. W.; Lu, C.; Ward, P. S.; Thompson, C. B.; Kaufman, A.; Guryanova, O.; Levine, R.; Heguy, A.; Viale, A.; Morris, L. G.; Huse, J. T.; Mellinghoff, I. K.; Chan, T. A., IDH1 mutation is sufficient to establish the glioma hypermethylator phenotype. *Nature* **2012,** *483* (7390), 479-83.

19. Figueroa, M. E.; Abdel-Wahab, O.; Lu, C.; Ward, P. S.; Patel, J.; Shih, A.; Li, Y.; Bhagwat, N.; Vasanthakumar, A.; Fernandez, H. F.; Tallman, M. S.; Sun, Z.; Wolniak, K.; Peeters, J. K.; Liu, W.; Choe, S. E.; Fantin, V. R.; Paietta, E.; Lowenberg, B.; Licht, J. D.; Godley, L. A.; Delwel, R.; Valk, P. J.; Thompson, C. B.; Levine, R. L.; Melnick, A., Leukemic IDH1 and IDH2 mutations result in a hypermethylation phenotype, disrupt TET2 function, and impair hematopoietic differentiation. *Cancer Cell* **2010,** *18* (6), 553-67.

20. Losman, J. A.; Looper, R. E.; Koivunen, P.; Lee, S.; Schneider, R. K.; McMahon, C.; Cowley, G. S.; Root, D. E.; Ebert, B. L.; Kaelin, W. G., Jr., (R)-2-hydroxyglutarate is sufficient to promote leukemogenesis and its effects are reversible. *Science* **2013,** *339* (6127), 1621-5.

21. Ma, S.; Jiang, B.; Deng, W.; Gu, Z. K.; Wu, F. Z.; Li, T.; Xia, Y.; Yang, H.; Ye, D.; Xiong, Y.; Guan, K. L., D-2-hydroxyglutarate is essential for maintaining oncogenic property of mutant IDH-containing cancer cells but dispensable for cell growth. *Oncotarget* **2015,** *6* (11), 8606-20.

22. Reitman, Z. J.; Jin, G.; Karoly, E. D.; Spasojevic, I.; Yang, J.; Kinzler, K. W.; He, Y.; Bigner, D. D.; Vogelstein, B.; Yan, H., Profiling the effects of isocitrate dehydrogenase 1 and 2 mutations on the cellular metabolome. *Proc Natl Acad Sci U.S.A* **2011,** *108* (8), 3270-5.

23. Oizel, K.; Gratas, C.; Nadaradjane, A.; Oliver, L.; Vallette, F. M.; Pecqueur, C., D-2-Hydroxyglutarate does not mimic all the IDH mutation effects, in particular the reduced etoposide-triggered apoptosis mediated by an alteration in mitochondrial NADH. *Cell Death Dis* **2015,** *6*, e1704.

24. Popovici-Muller, J.; Lemieux, R. M.; Artin, E.; Saunders, J. O.; Salituro, F. G.; Travins, J.; Cianchetta, G.; Cai, Z.; Zhou, D.; Cui, D.; Chen, P.; Straley, K.; Tobin, E.; Wang, F.; David, M. D.; Penard-Lacronique, V.; Quivoron, C.; Saada, V.; de Botton, S.; Gross, S.; Dang, L.; Yang, H.; Utley, L.; Chen, Y.; Kim, H.; Jin, S.; Gu, Z.; Yao, G.; Luo, Z.; Lv, X.; Fang, C.; Yan, L.; Olaharski, A.; Silverman, L.; Biller, S.; Su, S. M.; Yen, K., Discovery of AG-120 (Ivosidenib): a first-in-class mutant IDH1 inhibitor for the treatment of IDH1 mutant cancers. *ACS Med Chem Lett* **2018,** *9* (4), 300-305.

25. Wang, F.; Travins, J.; DeLaBarre, B.; Penard-Lacronique, V.; Schalm, S.; Hansen, E.; Straley, K.; Kernytsky, A.; Liu, W.; Gliser, C.; Yang, H.; Gross, S.; Artin, E.; Saada, V.; Mylonas, E.; Quivoron, C.; Popovici-Muller, J.; Saunders, J. O.; Salituro, F. G.; Yan, S.; Murray, S.; Wei, W.; Gao, Y.; Dang, L.; Dorsch, M.; Agresta, S.; Schenkein, D. P.; Biller, S. A.; Su, S. M.; de Botton, S.; Yen, K. E., Targeted inhibition of mutant IDH2 in leukemia cells induces cellular differentiation. *Science* **2013,** *340* (6132), 622-6.

26. Yen, K.; Travins, J.; Wang, F.; David, M. D.; Artin, E.; Straley, K.; Padyana, A.; Gross, S.; DeLaBarre, B.; Tobin, E.; Chen, Y.; Nagaraja, R.; Choe, S.; Jin, L.; Konteatis, Z.; Cianchetta, G.; Saunders, J. O.; Salituro, F. G.; Quivoron, C.; Opolon, P.; Bawa, O.; Saada, V.; Paci, A.; Broutin, S.; Bernard, O. A.; de Botton, S.; Marteyn, B. S.; Pilichowska, M.; Xu, Y.; Fang, C.; Jiang, F.; Wei, W.; Jin, S.; Silverman, L.; Liu, W.; Yang, H.; Dang, L.; Dorsch, M.; Penard-Lacronique, V.; Biller, S. A.; Su, S. M., AG-221, a first-in-class therapy targeting acute myeloid leukemia harboring oncogenic IDH2 mutations. *Cancer Discov* **2017,** *7* (5), 478-493.

27. Leonardi, R.; Subramanian, C.; Jackowski, S.; Rock, C. O., Cancer-associated isocitrate dehydrogenase mutations inactivate NADPH-dependent reductive carboxylation. *J Biol Chem* **2012,** *287* (18), 14615-20.

28. Pietrak, B.; Zhao, H.; Qi, H.; Quinn, C.; Gao, E.; Boyer, J. G.; Concha, N.; Brown, K.; Duraiswami, C.; Wooster, R.; Sweitzer, S.; Schwartz, B., A tale of two subunits: how the neomorphic R132H IDH1 mutation enhances production of alphaHG. *Biochemistry* **2011,** *50* (21), 4804-12.

29. Rendina, A. R.; Pietrak, B.; Smallwood, A.; Zhao, H.; Qi, H.; Quinn, C.; Adams, N. D.; Concha, N.; Duraiswami, C.; Thrall, S. H.; Sweitzer, S.; Schwartz, B., Mutant IDH1 enhances the production of 2-hydroxyglutarate due to its kinetic mechanism. *Biochemistry* **2013,** *52* (26), 4563-77.

30. Ward, P. S.; Lu, C.; Cross, J. R.; Abdel-Wahab, O.; Levine, R. L.; Schwartz, G. K.; Thompson, C. B., The potential for isocitrate dehydrogenase mutations to produce 2-hydroxyglutarate depends on allele specificity and subcellular compartmentalization. *J Biol Chem* **2013,** *288* (6), 3804-15.

31. Yang, B.; Zhong, C.; Peng, Y.; Lai, Z.; Ding, J., Molecular mechanisms of "off-on switch" of activities of human IDH1 by tumor-associated mutation R132H. *Cell Res* **2010,** *20* (11), 1188-200.

32. Pusch, S.; Schweizer, L.; Beck, A. C.; Lehmler, J. M.; Weissert, S.; Balss, J.; Miller, A. K.; von Deimling, A., D-2-Hydroxyglutarate producing neo-enzymatic activity inversely correlates with frequency of the type of isocitrate dehydrogenase 1 mutations found in glioma. *Acta Neuropathol Commun* **2014,** *2*, 19.

33. Hemerly, J. P.; Bastos, A. U.; Cerutti, J. M., Identification of several novel non-p.R132 IDH1 variants in thyroid carcinomas. *Eur J Endocrinol* **2010,** *163* (5), 747-55.

34. Zhang, C.; Moore, L. M.; Li, X.; Yung, W. K.; Zhang, W., IDH1/2 mutations target a key hallmark of cancer by deregulating cellular metabolism in glioma. *Neuro Oncol* **2013,** *15* (9), 1114-26.

35. Santoro, M. M.; Bolen, D. W., Unfolding free energy changes determined by the linear extrapolation method. 1. Unfolding of phenylmethanesulfonyl alpha-chymotrypsin using different denaturants. *Biochemistry* **1988,** *27* (21), 8063-8.

36. Xu, X.; Zhao, J.; Xu, Z.; Peng, B.; Huang, Q.; Arnold, E.; Ding, J., Structures of human cytosolic NADP-dependent isocitrate dehydrogenase reveal a novel self-regulatory mechanism of activity. *J Biol Chem* **2004,** *279* (32), 33946-57.

37. Adams, P. D.; Afonine, P. V.; Bunkoczi, G.; Chen, V. B.; Davis, I. W.; Echols, N.; Headd, J. J.; Hung, L. W.; Kapral, G. J.; Grosse-Kunstleve, R. W.; McCoy, A. J.; Moriarty, N. W.; Oeffner, R.; Read, R. J.; Richardson, D. C.; Richardson, J. S.; Terwilliger, T. C.; Zwart, P. H., PHENIX: a comprehensive Python-based system for macromolecular structure solution. *Acta Crystallogr Sect D-Biol Crystallogr* **2010,** *66* (Pt 2), 213-21.

38. Emsley, P.; Cowtan, K., Coot: model-building tools for molecular graphics. *Acta Crystallogr Sect D-Biol Crystallogr* **2004,** *60* (Pt 12 Pt 1), 2126-32.

39. Merk, A.; Bartesaghi, A.; Banerjee, S.; Falconieri, V.; Rao, P.; Davis, M. I.; Pragani, R.; Boxer, M. B.; Earl, L. A.; Milne, J. L.; Subramaniam, S., Breaking Cryo-EM resolution barriers to facilitate drug discovery. *Cell* **2016,** *165* (7), 1698-707.

40. Schrodinger, LLC. The PyMOL Molecular Graphics System, Version 1.8.0.4.

41. Ichimura, K.; Pearson, D. M.; Kocialkowski, S.; Backlund, L. M.; Chan, R.; Jones, D. T.; Collins, V. P., IDH1 mutations are present in the majority of common adult gliomas but rare in primary glioblastomas. *Neuro Oncol* **2009,** *11* (4), 341-7.

42. Grassian, A. R.; Pagliarini, R.; Chiang, D. Y., Mutations of isocitrate dehydrogenase 1 and 2 in intrahepatic cholangiocarcinoma. *Curr Opin Gastroenterol* **2014,** *30* (3), 295-302.

43. Hirata, M.; Sasaki, M.; Cairns, R. A.; Inoue, S.; Puviindran, V.; Li, W. Y.; Snow, B. E.; Jones, L. D.; Wei, Q.; Sato, S.; Tang, Y. J.; Nadesan, P.; Rockel, J.; Whetstone, H.; Poon, R.; Weng, A.; Gross, S.; Straley, K.; Gliser, C.; Xu, Y.; Wunder, J.; Mak, T. W.; Alman, B. A., Mutant IDH is sufficient to initiate enchondromatosis in mice. *Proc Natl Acad Sci U.S.A* **2015,** *112* (9), 2829-34.

44. Ward, P. S.; Cross, J. R.; Lu, C.; Weigert, O.; Abel-Wahab, O.; Levine, R. L.; Weinstock, D. M.; Sharp, K. A.; Thompson, C. B., Identification of additional IDH mutations associated with oncometabolite R(-)-2-hydroxyglutarate production. *Oncogene* **2012,** *31* (19), 2491-8.

45. Hartmann, C.; Meyer, J.; Balss, J.; Capper, D.; Mueller, W.; Christians, A.; Felsberg, J.; Wolter, M.; Mawrin, C.; Wick, W.; Weller, M.; Herold-Mende, C.; Unterberg, A.; Jeuken, J. W.; Wesseling, P.; Reifenberger, G.; von Deimling, A., Type and frequency of IDH1 and IDH2 mutations are related to astrocytic and oligodendroglial differentiation and age: a study of 1,010 diffuse gliomas. *Acta Neuropathol* **2009,** *118* (4), 469-74.

46. Agarwal, S.; Sharma, M. C.; Jha, P.; Pathak, P.; Suri, V.; Sarkar, C.; Chosdol, K.; Suri, A.; Kale, S. S.; Mahapatra, A. K.; Jha, P., Comparative study of IDH1 mutations in gliomas by immunohistochemistry and DNA sequencing. *Neuro Oncol* **2013,** *15* (6), 718-26.

47. Monera, O. D.; Sereda, T. J.; Zhou, N. E.; Kay, C. M.; Hodges, R. S., Relationship of sidechain hydrophobicity and alpha-helical propensity on the stability of the single-stranded amphipathic alpha-helix. *J Pept Sci* **1995,** *1* (5), 319-29.

48. Richards, F. M., The interpretation of protein structures: total volume, group volume distributions and packing density. *J Mol Biol* **1974,** *82* (1), 1-14.

49. Gao, J.; Aksoy, B. A.; Dogrusoz, U.; Dresdner, G.; Gross, B.; Sumer, S. O.; Sun, Y.; Jacobsen, A.; Sinha, R.; Larsson, E.; Cerami, E.; Sander, C.; Schultz, N., Integrative analysis of complex cancer genomics and clinical profiles using the cBioPortal. *Sci Signal* **2013,** *6* (269), pl1.

50. Cerami, E.; Gao, J.; Dogrusoz, U.; Gross, B. E.; Sumer, S. O.; Aksoy, B. A.; Jacobsen, A.; Byrne, C. J.; Heuer, M. L.; Larsson, E.; Antipin, Y.; Reva, B.; Goldberg, A. P.; Sander, C.; Schultz, N., The cBio cancer genomics portal: an open platform for exploring multidimensional cancer genomics data. *Cancer Discov* **2012,** *2* (5), 401-4.

51. Liu, A.; Hou, C.; Chen, H.; Zong, X.; Zong, P., Genetics and epigenetics of glioblastoma: applications and overall incidence of IDH1 mutation. *Front Oncol* **2016,** *6*, 16.

52. Halamkova, L.; Mailloux, S.; Halamek, J.; Cooper, A. J.; Katz, E., Enzymatic analysis of alpha-ketoglutaramate--a biomarker for hyperammonemia. *Talanta* **2012,** *100*, 7-11.

53. Marcucci, G.; Maharry, K.; Wu, Y. Z.; Radmacher, M. D.; Mrozek, K.; Margeson, D.; Holland, K. B.; Whitman, S. P.; Becker, H.; Schwind, S.; Metzeler, K. H.; Powell, B. L.; Carter, T. H.; Kolitz, J. E.; Wetzler, M.; Carroll, A. J.; Baer, M. R.; Caligiuri, M. A.; Larson, R. A.; Bloomfield, C. D., IDH1 and IDH2 gene mutations identify novel molecular subsets within de novo cytogenetically normal acute myeloid leukemia: a Cancer and Leukemia Group B study. *J Clin Oncol* **2010,** *28* (14), 2348-55.

54. Dinardo, C. D.; Propert, K. J.; Loren, A. W.; Paietta, E.; Sun, Z.; Levine, R. L.; Straley, K. S.; Yen, K.; Patel, J. P.; Agresta, S.; Abdel-Wahab, O.; Perl, A. E.; Litzow, M. R.; Rowe, J. M.; Lazarus, H. M.; Fernandez, H. F.; Margolis, D. J.; Tallman, M. S.; Luger, S. M.; Carroll, M., Serum 2-hydroxyglutarate levels predict isocitrate dehydrogenase mutations and clinical outcome in acute myeloid leukemia. *Blood* **2013**.

55. Koszarska, M.; Bors, A.; Feczko, A.; Meggyesi, N.; Batai, A.; Csomor, J.; Adam, E.; Kozma, A.; Orban, T. I.; Lovas, N.; Sipos, A.; Karaszi, E.; Dolgos, J.; Fekete, S.; Reichardt, J.; Lehoczky, E.; Masszi, T.; Tordai, A.; Andrikovics, H., Type and location of isocitrate dehydrogenase mutations influence clinical characteristics and disease outcome of acute myeloid leukemia. *Leuk Lymphoma* **2013,** *54* (5), 1028-35.

56. Dexter, J. P.; Ward, P. S.; Dasgupta, T.; Hosios, A. M.; Gunawardena, J.; Vander Heiden, M. G., Lack of evidence for substrate channeling or flux between wildtype and mutant isocitrate dehydrogenase to produce the oncometabolite 2-hydroxyglutarate. *J Biol Chem* **2018,** *293* (52), 20051-20061.

2.7. Supplemental information

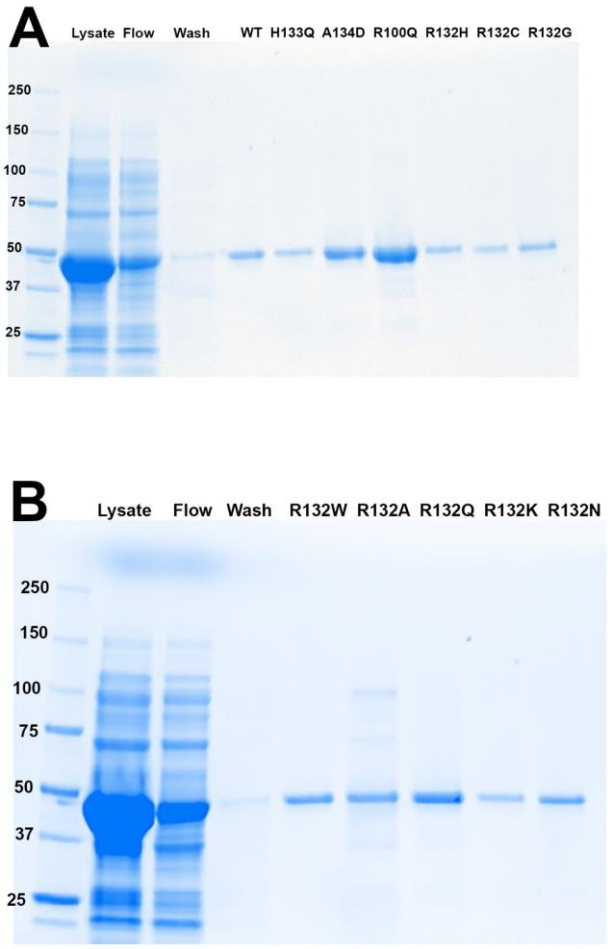

Supplemental Figure S1. Purification of WT and mutant. **A.** SDS-PAGE analysis of the IDH1 tumor mutants. **B.** SDS-PAGE analysis of the IDH1 experimental mutants. Lysate indicates the whole cell lysate. Flow indicates the flow-through after loading the lysate onto a nickel-NTA column, and Wash indicates the flow-through after a buffer wash prior to elution. 4-12% BioRad Stain-free gels were used.

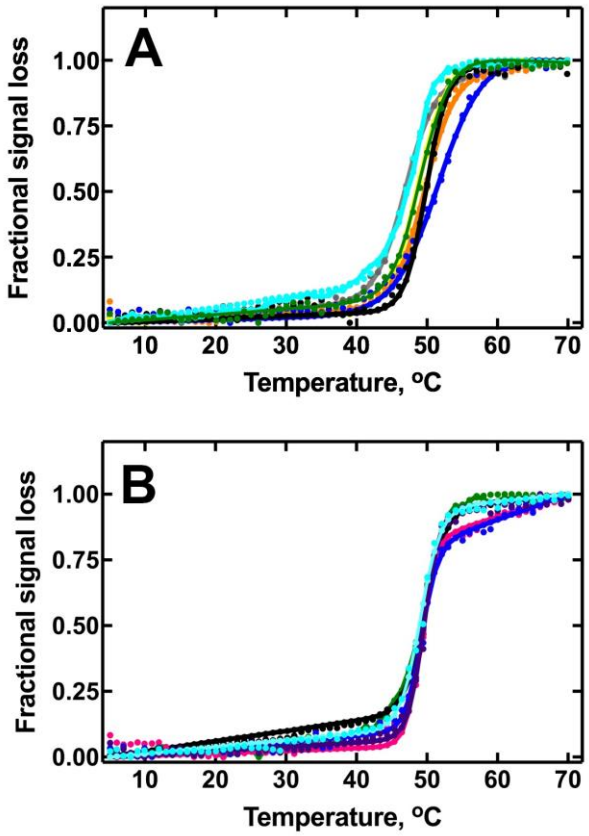

Supplemental Figure S2. Thermal melt curves employing circular dichroism were used to determine the melting temperature (T_m) of IDH1 mutants. (A) WT IDH1 is shown in green (T_m = 49.1 ± 0.1 ºC); A134D in cyan (T_m = 48.7 ± 0.1 ºC); H133Q in black (T_m = 49.9 ± 0.1 ºC); R100Q in dark blue (T_m = 51.9 ± 0.1 ºC); R132H in orange (T_m = 49.7 ± 0.1 ºC); R132C in yellow (T_m = 46.8 ± 0.1 ºC); and R132G in grey (T_m = 46.9 ± 0.1 ºC). (B) WT IDH1 is shown in green (T_m = 49.1 ± 0.1 ºC); R132W is in purple (T_m = 49.5 ± 0.1 ºC); R132A in dark blue (T_m = 49.2 ± 0.1 ºC); R132N in cyan (T_m = 49.1 ± 0.1 ºC); R132Q in magenta (T_m = 49.0 ± 0.1 ºC); and R132K in black (T_m = 49.8 ± 0.1 ºC).

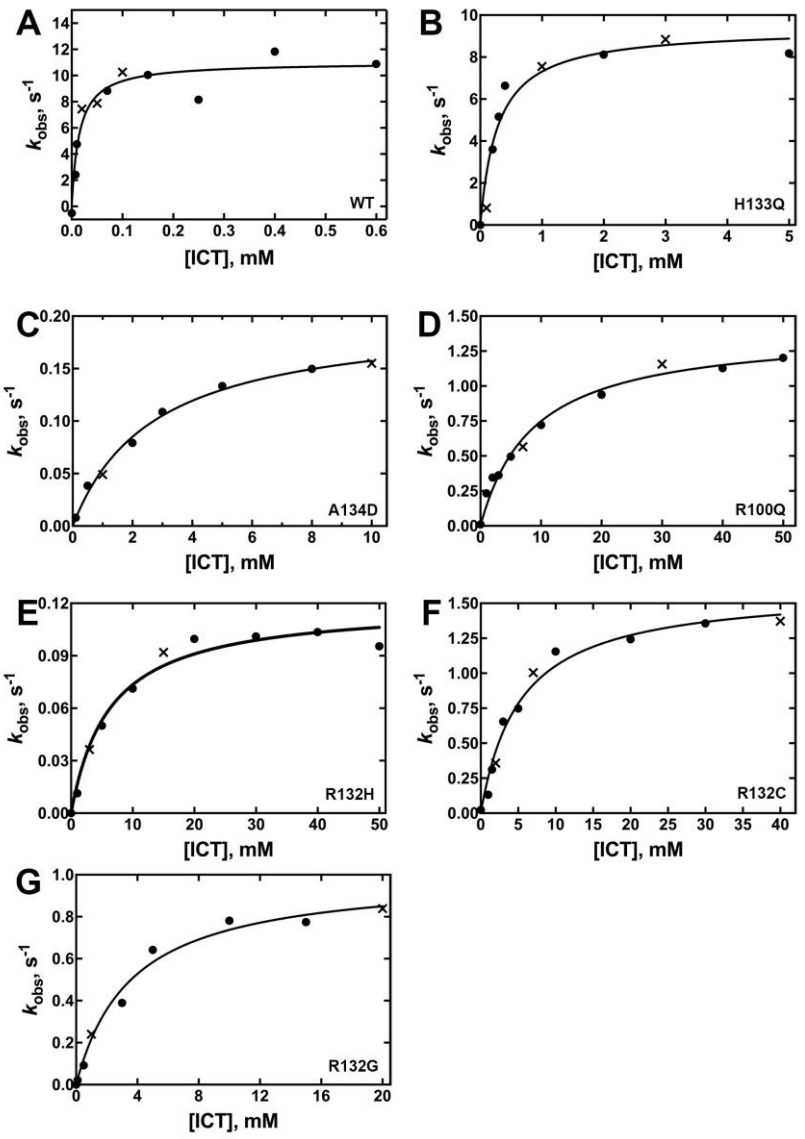

Supplemental Figure S3. Concentration dependence of ICT concentration on the observed rate of NADPH production in the normal reaction, conversion of ICT to αKG (21 ºC). The determined k_{obs} values were obtained from two different enzyme preparations to ensure reproducibility. The k_{obs} values resulting from each of the two enzyme preparations are distinguished by using either a circle or an × in the plots. The observed rate constants (k_{obs}) were calculated from the linear range of the slopes of plots of concentration versus time using GraphPad Prism software (GraphPad, San Diego, CA.) These k_{obs} values were then fit to a hyperbolic equation to generate k_{cat} and K_m values, and the standard error results from the deviance from these hyperbolic fits is indicated. K_m values and efficiency are in terms of [ICT]. **A.** WT IDH1. **B.** H133Q IDH1. **C.** A134D IDH1. **D.** R100Q IDH1. **E.** R132H IDH1. **F.** R132C IDH1. **G.** R132G IDH1.

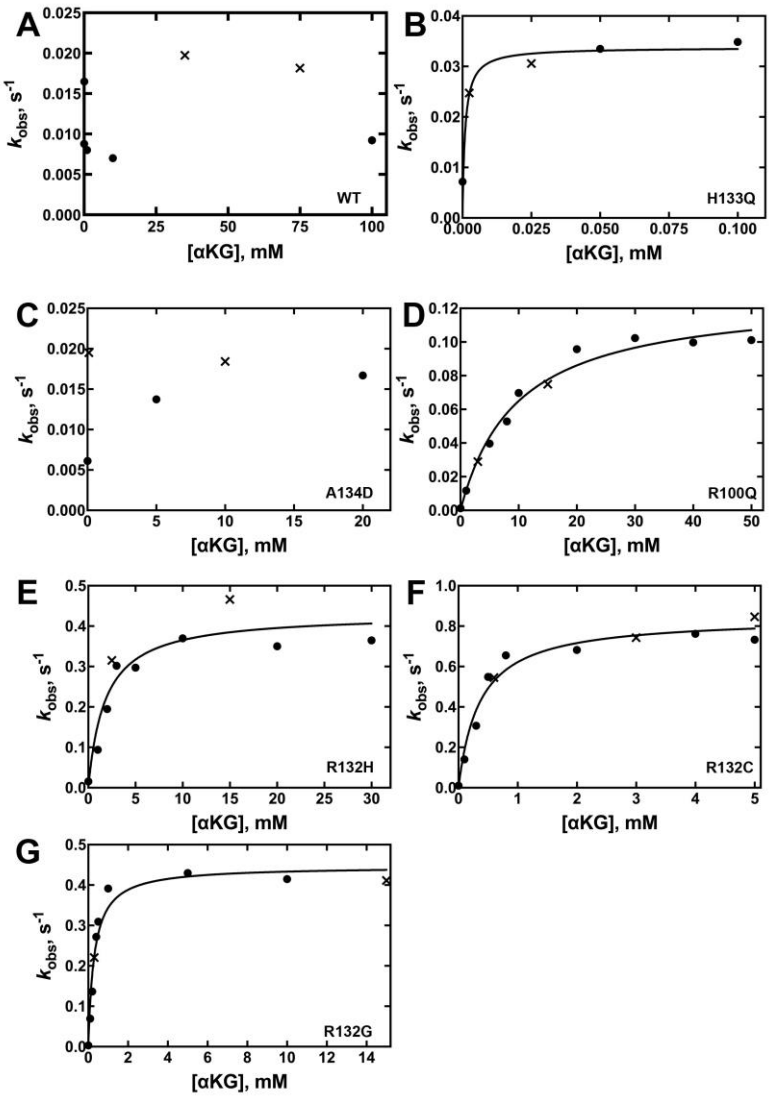

Supplemental Figure S4. Concentration dependence of αKG concentration on the observed rate of NADPH depletion in the neomorphic reaction (21 ºC). The determined k_{obs} values were obtained from two different enzyme preparations to ensure reproducibility. The k_{obs} values resulting from each of the two enzyme preparations are distinguished by using either a circle or an × in the plots. The observed rate constants (k_{obs}) were calculated from the linear range of the slopes of plots of concentration versus time using GraphPad Prism software (GraphPad, San Diego, CA). These k_{obs} values were then fit to a hyperbolic equation to generate k_{cat} and K_m values, and the standard error results from the deviance from these hyperbolic fits is indicated. K_m values and efficiency are in terms of [αKG]. **A.** WT IDH1. **B.** H133Q IDH1. **C.** A134D IDH1. **D.** R100Q IDH1. **E.** R132H IDH1. **F.** R132C IDH1. **G.** R132G IDH1.

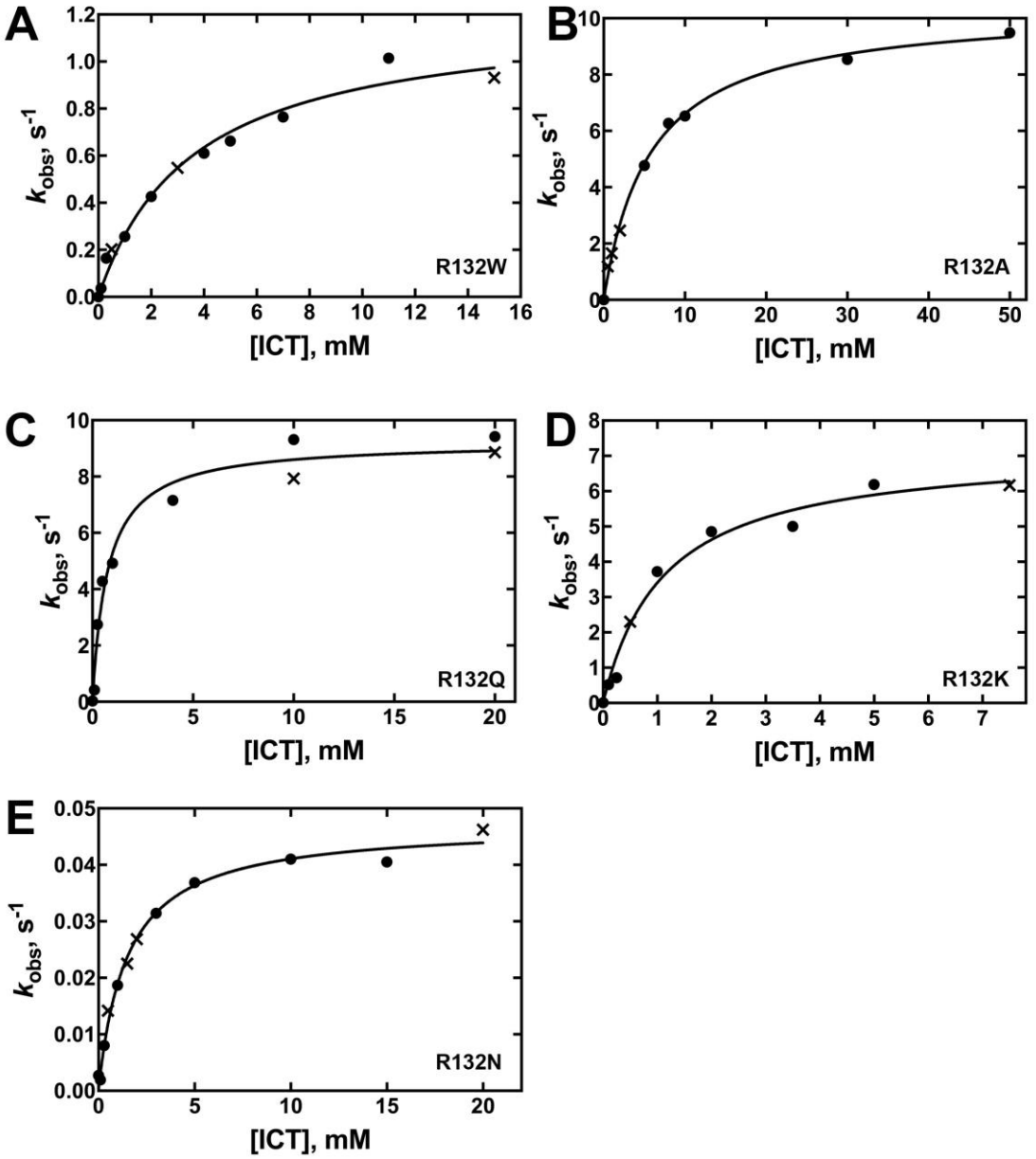

Supplemental Figure S5. Concentration dependence of ICT concentration on the observed rate of NADPH production in the normal reaction (37 ºC). The determined k_{obs} values were obtained from two different enzyme preparations to ensure reproducibility. The k_{obs} values resulting from each of the two enzyme preparations are distinguished by using either a circle or an × in the plots. The observed rate constants (k_{obs}) were calculated from the linear range of the slopes of plots of concentration versus time using GraphPad Prism software (GraphPad, San Diego, CA). These k_{obs} values were then fit to a hyperbolic equation to generate k_{cat} and K_m values, and the standard error results from the deviance from these hyperbolic fits is indicated. K_m values and efficiency are in terms of [ICT]. **A.** R132W IDH1. **B.** R132A IDH1. **C.** R132Q IDH1. **D.** R132K IDH1. **E.** R132N IDH1.

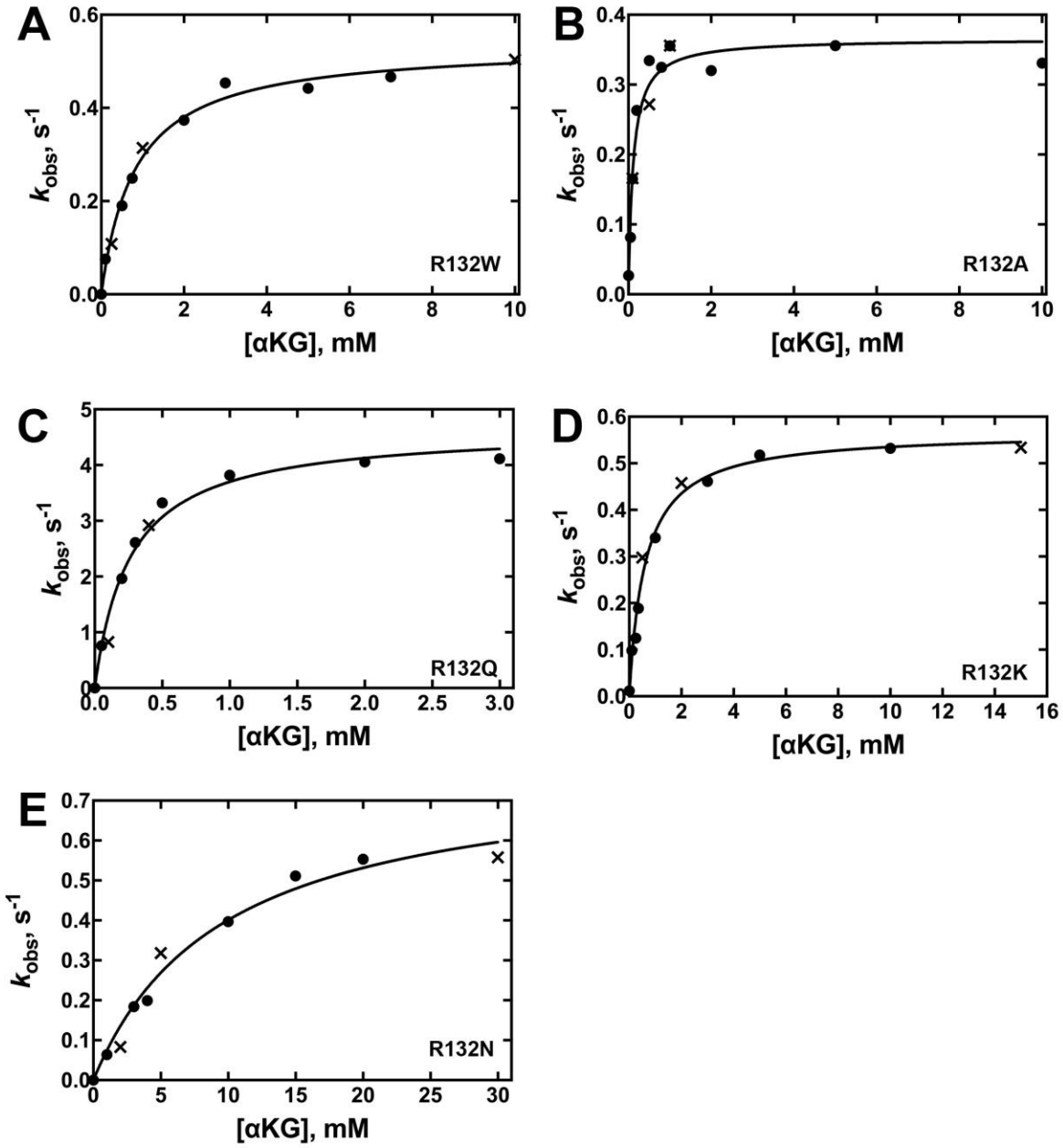

Supplemental Figure S6. Concentration dependence of αKG concentration on the observed rate of NADPH depletion in the neomorphic reaction (37 ºC). The determined k_{obs} values were obtained from two different enzyme preparations to ensure reproducibility. The k_{obs} values resulting from each of the two enzyme preparations are distinguished by using either a circle or an × in the plots. The observed rate constants (k_{obs}) were calculated from the linear range of the slopes of plots of concentration versus time using GraphPad Prism software (GraphPad, San Diego, CA). These k_{obs} values were then fit to a hyperbolic equation to generate k_{cat} and K_m values, and the standard error results from the deviance from these hyperbolic fits is indicated. K_m values and efficiency are in terms of [αKG]. **A.** R132W IDH1. **B.** R132A IDH1. **C.** R132Q IDH1. **D.** R132K IDH1. **E.** R132N IDH1.

2.8. Acknowledgment

Chapter 2 is reproduced and re-written in full with permission from Diego Avellaneda Matteo, Adam J. Grunseth, Eric R. Gonzalez, Stacy L. Anselmo, Madison A. Kennedy, Precious Moman, David A. Scott, An Hoang, and Christal D. Sohl. Molecular mechanisms of isocitrate dehydrogenase 1 (IDH1) mutations identified in tumors: The role of size and hydrophobicity at residue 132 on catalytic efficiency. *J Biol Chem* **2017**, 292 (19), 7971-7983

3. Inhibitor Potency Varies Widely Among Tumor-Relevant Human Isocitrate Dehydrogenase 1 Mutants

3.1. Abstract

Mutations in isocitrate dehydrogenase 1 (IDH1) are linked in high frequencies to low-grade gliomas as well as in chondrosarcomas and acute myeloid leukemias. Most tumor relevant IDH1 mutations have a significant decrease in activity when performing the oxidation of ICT to αKG, while gaining the neomorphic activity of converting αKG to D2HG, which drives tumor formation. Previously, we described two different reactivities of IDH1 mutants: a deficiency in the normal reaction with moderate production of D2HG, or moderate αKG production and high D2HG formation (R132Q IDH1). In this work, we identified a third type of reactivity where there is a low αKG formation and high D2HG production (R132L IDH1). Additionally, we identified unique structural features of R132Q IDH1, and showed that inhibitors had low affinity for this mutant. Biochemical and cell-based inhibition assays showed that most IDH1 mutants were very susceptible to inhibition, while R132Q IDH1 showed up to 16,300-fold increase in IC_{50} versus R132H IDH1. Only inhibitors capable of inhibiting WT IDH1 were also effective against R132Q IDH1. These results suggested that patients harboring R132Q IDH1 mutations may not respond well to mutant IDH1 therapeutics. Molecular dynamic simulations showed that a pair of helices near the $NADP^+$/NADPH binding site in R132Q IDH1 switched between conformations that were more WT-like or more mutant-like, highlighting mechanisms for WT activity conservation. Dihedral angle changes at the dimer interface as well as buried surface area charges suggested a possible mechanism for loss of inhibition affinity seen by R132Q IDH1. This work provides a solid foundation for predicting how patients harboring different IDH1 mutations may respond to

therapeutics as well as identifies possible resistance mutations that may arise during treatment with these mutant IDH1 inhibitors.

3.2. Introduction

Changes in tumor metabolism were first described by Otto Warburg about a century ago[1, 2]. Within the last few decades, it has been shown that dysfunctional metabolic enzymes can drive tumor formation and growth[3]. Examples of dysfunctional enzymes are isocitrate dehydrogenase 1 (IDH1) and isocitrate dehydrogenase 2 (IDH2) mutational variants, which are linked to cancers like gliomas, chondrosarcomas, and acute myeloid leukemia (AML)[4-8]. IDH1 and IDH2 catalyze the $NADP^+$ and Mg^{2+}-dependent oxidative carboxylation of ICT to αKG (normal reaction)[5, 9]. Mutations in these enzymes reduce significantly the ability to catalyze the normal reaction, while also conferring a neomorphic reaction consisting of the NADPH and Mg^{2+}-dependent reduction of αKG to D2HG (Figure 1)[10]. D2HG is an oncometabolite since it competitively inhibits many αKG-dependent enzymes involved in gene regulation, including methylcytosine dioxygenases and JmjC lysine demethylases, allowing for genome hypermethylation[11, 12].

Most IDH1 tumor-relevant mutations happen at residue 132, which it is important for substrate coordination[13]. The most common IDH1 mutant in gliomas is R132H (90% of cases), but other mutations have been observed, such as R132C, R132G, R132Q, R132L, R132S, and R132V IDH1[14]. R132V is the only IDH1 mutation that does not occur with a single base mutation. In chondrosarcomas, the frequencies of mutations in the IDH1 gene are lower. In a small study, out of 43 chondrosarcoma tumor samples, 20 had IDH1 mutations, where the most commons were R132C (60%), R132G (25%) and the remaining were R132L, R132Q, and R132H[15]. Additionally, a mouse model containing the R132Q IDH1 mutation was created and it showed that this mutation can lead to tumor formation[15, 16]. In chapter 2, we performed an extensive steady state kinetic

characterization of several tumor-relevant IDH1 mutants, showing wide variation of catalytic efficiencies for both the normal and the neomorphic reaction[17]. Although a discreate trend was observed in terms of van der Waals volume and hydrophobicity[17], the mechanistic details of these wide variation in catalytic efficiencies are still under investigation.

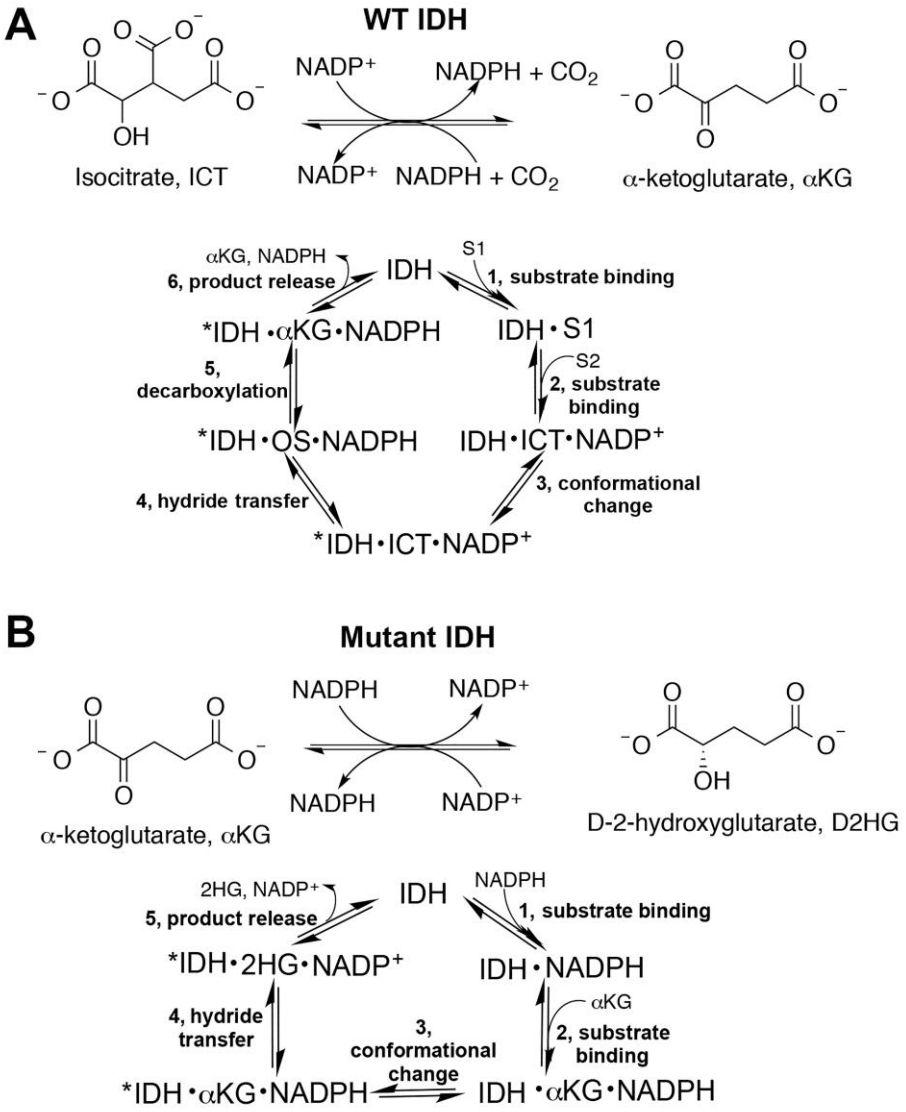

Figure 1. Reactions catalyzed by WT and mutant IDH1. **A.** WT IDH1 catalyzes the reversible, $NADP^+$-dependent oxidation of ICT to αKG (OS, oxalosuccinate). **B.** Mutant IDH1 is typically deficient in the normal reaction shown in (A), and instead acquires a neomorphic reaction, the NADPH-dependent reduction of αKG to generate the oncometabolite, D2HG. For both reactions, the predicted catalytic cycle is also shown. This figure was originally published in https://portlandpress.com/biochemj/article-lookup/doi/10.1042/BCJ20180424 Avellaneda Matteo, D.; Wells, G. A.; Luna, L. A.; Grunseth, A. J.; Zagnitko, O.; Scott, D. A.; Hoang, A.; Luthra, A.; Swairjo, M. A.; Schiffer, J. M.; Sohl, C. D., Inhibitor potency varies widely among tumor-relevant human isocitrate dehydrogenase 1 mutants. *Biochem J* **2018,** *475* (20), 3221-3238.

IDH1 and IDH2 are therapeutic targets for IDH-driven cancers[18], with many groups creating small molecule inhibitors with extremely high selectivity for R132H and R132C IDH1 over WT IDH1. The FDA has approved small molecule inhibitors synthetized by Agios Pharmaceuticals for IDH1[19, 20] and IDH2[21, 22]. Crystal and cryo-EM structures show R132H and R132C IDH1 bound to small molecular inhibitors at an allosteric site between α9 and α10 helices in both monomers, and at the dimer interface (Supplemental Figure S1)[23, 24]. Recently, it has been proposed that a local conformational changes of the α10 helix drives inhibitor selectivity, at least in part, against R132H IDH1 while leaving WT IDH1 unaffected[23, 25, 26] (Supplemental Figure S1). Structural characterization is limited to R132H, R132C, and WT IDH1. Although inhibitors designed to be selective for patients with R132H and R132C IDH1 mutants would benefit most patients harboring IDH1 mutations, a large variation in catalytic efficiencies among tumor-relevant mutants suggests that some mutants may not respond properly to these inhibitors. Moreover, studying less common IDH1 mutants, capable of producing D2HG may highlight possible resistant mutations that may arise during targeted treatment. This issue has already been linked to the IDH2 FDA-approved drug enasidenib[27]. Therefore, a detailed mechanistic study of several IDH1 mutants is important to understand fundamental catalytic features, predict patient response to therapeutics, and identify certain mutants that may be resistant to these therapeutics.

In this work, we have performed extensive kinetic, structural, and inhibitory characterizations of tumor-relevant IDH1 mutants affecting residue 132. We showed that R132Q IDH1 has unique properties including low affinity for mutant IDH1 inhibitors. We used molecular dynamics (MD) simulation to probe movement around the $NADP^+$ and the inhibitor binding site that may drive catalytic activity and inhibitor selectivity for these mutants. This work is important

to provide fundamental information regarding how each mutant is affected by inhibitors, informing future drug design, and identifying possible paths of resistance that may develop in treatment.

3.3. Materials and Methods

3.3.1. Materials

Tris-hydrochloride, sodium chloride, magnesium chloride hexahydrate, αKG sodium salt, and resazurin were obtained from Fisher (Hampton, NH). DL-isocitric acid trisodium salt hydrate was obtained from MP Biomedicals (Santa Ana, CA). Both NADPH tetrasodium salt and $NADP^+$ disodium salt were obtained from Calbiochem (San Diego, CA). Diaphorase from *Clostridium kluyveri* and dimethyl sulfoxide (DMSO) were obtained from Sigma-Aldrich (St. Louis, MO). Bovine serum albumin (BSA) was obtained from SeraCare Lifescience (Milford, MA). ML309 was obtained from Sigma-Aldrich (St. Louis, MO). AGI-5198 was obtained from Selleckchem (Houston, TX). Lastly, GSK864 was obtained from Cayman Chemical Company (Ann Arbor, MI). Nickel-nitrilotriacetic acid (Ni-NTA) resin was obtain from Qiagen (Valencia, CA).

3.3.2. Protein Expression and Purification

The expression and purification of WT and mutant IDH1 enzymes were performed as described in the previous chapter[17]. In short, plasmids were transformed in BL21 gold (DE3) cells and incubated in TB media at 37ºC until reaching an OD_{600} of 1.0-1.2. Once the OD was reached, cultures were induced with 1mM IPTG as previously described[17] at 18ºC for 18-22hrs. WT and mutant IDH1 enzymes were purified using Ni-NTA affinity column chromatography reaching ~95% purity. The eluted enzymes were concentrated, and flash frozen in liquid nitrogen, and finally stored at -80ºC for no more than two months. WT, R132H, and R132Q IDH1 were assessed

using small-angle X-ray scattering (SAXS) analysis described in supplementary Figure S2 and Table s1.

3.3.3. Steady-State Kinetic Assays

The activity of WT and mutant IDH1 enzymes were measured at 37ºC and in steady-state conditions as described previously in this dissertation[17]. To calculate rates of product formation, the molar extinction coefficient of NADPH (6.22 $cm^{-1}mM^{-1}$) was used. For fluorescence measurements, a standard curve of concentrations of NADPH was created to quantify product formation. The observe rates (k_{obs}) were calculated by dividing the rates of formation of NADPH (nM/s) by concentration of enzyme (nM) to yield rates in s^{-1}. The observed rates were plotted to a hyperbolic Michaelis-Menten function using Graphpad Prism (GraphPad Software, La Jolla, CA) to get k_{cat} and K_M values. As previously described in Chapter 2, each IDH1 construct was purified at least twice to assess prep-to-prep variability and reproducibility. I obtained rates for R132L, R132V, and R132S IDH1 (neomorphic reaction), while Lucas Luna and Adam Grunseth obtained rates for R132L, R132S, and R132V IDH1 for the normal reaction.

3.3.4. Molecular Dynamics Simulations

Schrodinger PrepWizard[28-31] was used to prepare apo IDH1 structures (PDB: 1T09[25]) for molecular dynamics (MD) simulations. IDH1 $NADP^+$-bound and $NADP^+/Ca^{2+}$-bound structures (4KZO[32]) were prepared using CHARMMGUI (Supplemental Tables S2 and S3). Within Bioluminate[33], the crystallographic waters from the PDB structures were kept when preparing them for simulations. The systems were protonated at pH 7.4 and the pK_a values for titraTable residues were determined using the Maestro integrated program (PROPKA)[34]. The protein dynamics was verified by analysis of root-mean-squared deviations (RMSD) (Supplemental

Figure S3). The systems were solvated in a TIP3P model[34] . The charge of IDH1 was balanced with the addition of five sodium ions. The concentration of sodium chloride was set to 150 mM in to mimic the salt concentration in cells. The parameterization for the MD systems was performed using AMBER 16 package ($NADP^+$-bound system), while the systems coordinates from the previous preparation were parameterized with CHARMMGUI using charmm36m force field parameters[35]. The IDH1 proteins bound to calcium were parameterized as previously described[36]. $NADP^+$ was parameterized using in-house parameters in CHARMM.

MD simulations were performed using NVIDIA GK110 (GeForce GTX Titan) GPUs with the CUDA version of PMEMD in AMBER16[37] for the systems with $NADP^+$ is bound. The simulations systems previously described were energy minimized using the CPU version of AMBER 16 and equilibrated with the GPU version of AMBER16[37, 38]. The energy minimization was performed in one step with 2,500 steps of steepest-descent algorithm and the other 2500 steps with conjugated-gradient algorithm. Then, five steps of equilibration were performed, including hearing. The first step was a 25 ps of hydrogen only minimization using a restrain weight of 250 kcal/mol on the protein and solvent. The second step was a 4 ps of hydrogen minimization with a restrain of 20 kcal/mol on the protein and salt atoms. The third step was a 20 ps heating of water with a restrain of 20 kcal/mol on the proteins and salt atoms. The fourth step was a 40 ps of full equilibration. Finally, the systems were equilibrated using harmonic equilibration at 298.15 K over four sequential 500 ps replicates, while the restrain potential on the backbone on each step was decreased, starting at 4 kcal/mol and ending at 1 kcal/mol.

AMBER16 runs were performed as an NPT ensemble at 218.15 K and a pressure of 1 bar over a time period of 2 fs time step and particle mesh Ewald[39] electrostatic approximation and a non-bonding cutoff of 12 Å. Five replicates of simulation for each system were performed over

110 ns time period. For each simulation, MD trajectories were calculated using ipython jupyter notebook environment[40] with PYTRAJ[41], MDTRAJ[42], and numpy, along with cpptraj and visual molecular dynamics (VMD) in order to visualize the trajectories. The frames were aligned according to the backbone atoms. In order to perform the dihedral angles, distance, buried surface area, root-mean-squared of fluctuation (RMSF), and hydrogen bond-based measurements, Pytraj was used. VMD[43] and Maestro[44] were used for image taking (Supplemental Figure S3).

VolMap Tool is a VMD plugin[43] that was used to create images of the average buried cavities for each mutant and WT IDH1 simulations. SiteMap[45] was used to understand the volume and size of the binding pockets between the two protein dimers. Site 1 and 2 were identified in PDB codes 4KZO and 3INM and these volumes were outlined (Supplemental Figure S5). Simulations described here were all performed by Dr. Jamie Schiffer.

3.3.5. Biochemical IDH1 Inhibition Assays

The biochemical inhibition assays were performed as previously published[19]. In short, the concentrations of AGI-5198 and ML309 ranged from 5 nM to 50 μM for all mutants besides R132Q and WT IDH1, where these concentrations ranged from 5 nM to 500 μM. For GSK864, the concentrations used of this inhibitor for WT, R132Q, and R132H IDH1 ranged from 5 nM to 50 μM. For all mutant IDH1 inhibition assays, the proteins were incubated with inhibitors for 30 min in ice prior to allowing them to react. Then, 20 mM Tris-HCl pH 7.5 ambient temperature, 10 mM of magnesium chloride, 150 mM sodium chloride, 0.05% BSA, 4 μM NADPH and 4 nM IDH1-inhibitor preincubated complexed were mixed in a flat-bottom black 96-well plate from Corning Incorporated (Kennebunck, ME). Reactions were initiated by adding αKG with concentrations matching previously reported K_M. The final volume for each well was 100 μL, and each concentration of inhibitor was done in triplicates. The concentration of DMSO remained

constant at 1% final (%v/v). After incubating the reaction mixture for one hour, 50 μL of diaphorase-resazurin solution (diaphorase had a final concentration of 12 μg/mL and resazurin 33 μM) was added to each well and incubated for 10 min at ambient temperature. The role of the diaphorase-resazurin solution was to react with any remaining NADPH to allow us to quantify very low levels of NADPH. Resofurin was measured at 544 nm (excitation wavelength) and 590 nm (emission wavelength) using an Infinite$_{M200}$ Tecan plate reader (Mannedorf, Switzerland). WT IDH1 inhibition assays were performed using concentrations of ICT and $NADP^+$ matching their respective published K_M values[17]. Since high amounts of NADPH would be produced and thus no sensitivity limitations were predicted, the resazurin diaphorase solution was not used. Instead, NADPH levels were directly assessed using an Infinite$_{M200}$ Tecan plate reader by exciting at 340 nm and emitting at 450 nm. Two protein purifications were performed for each mutant and WT IDH1 to assess reproducibility, except for R132Q IDH1, which was performed with three different protein purifications with AGI-5198 and GSK864. The data was plotted as % activity as a function of log of the inhibitor concentrations. The % activities were plotted using GraphPad software. The 95% confidence intervals were obtained by deviation of the data from the fitted function. I was responsible for all of these experiments

3.3.6. Transient Cell Line Generation

To generate mammalian cell lines that transiently expressed WT, R132H, or R132Q IDH1, pcDNA3-Flag-IDH1-R132H[9] was obtained from Addgene (Cambridge, MA, plasmid 62907). R132Q IDH1 construct was created via side-directed mutagenesis using Kapakit from Kapa Biosystems (Wilmington, MA). The primers were as follows: forward primer 5'-AAAACCTATCATCATAGGTCAGCATGCTTATGGGGATCAATAC-3'; reverse primer 5'-GTATTGATCCCCATAAGCATGCTGACCTATGATGATAGGTTTT -3'. WT IDH1 was

created by the same method using the following primers: forward primer 5'-GTAAAACCTATCATCATAGGTCGTCAT- GCTTATGGGGATCAATAC -3'; reverse primer 5'- GTATTGATCCCCATAAGCATGACGACCTATGATGATAGGTTTTAC -3'. All sequences were confirmed by Retrogen (San Diego, CA). All primers were obtained from IDT (Coralville, IW).

HEK293T cells and HeLa cells were cultured in Dulbecco's Modified Eagle Medium (DMEM) (Thermo Fisher, Waltham, MA) with 10% fetal bovine serum (FBS) at 5% carbon dioxide at 37 ºC. Cells were obtained from ATCC, and they were tested for mycoplasma by ATCC before use. The cells were passaged between 1-2 times between thawing and usage. The cells were transfected once they reached 60% confluency with polyethylenimine (PEI). The three constructs previously described in this section were used for HEK293T cells while R132Q IDH1 was used for HeLa cells. In short, $3x10^6$ cells were seeded in a 10 cm plate, and 24 h later, 20 μg of plasmid DNA was incubated at ambient temperature for 10 min with 30 μg of PEI in DMEM. The resulting solution was added carefully dropwise to the plate containing the seeded cells. After 24 h, the old media containing the transfecting solution was removed and replaced with new media. The expression of each IDH1 protein was confirmed via Western blot analysis using an anti-Flag (ThermoFisher Scientific) or anti-actin primary antibodies (Santa Cruz Biotechnology) and ECL Plex goat-anti-rabbit IgG-Cy5 secondary antibody (GE Healthcare). All experiments described here were performed by Grace A. Wells

3.3.7. Cellular Inhibition Assays

HEK293T cells transiently expressing R132Q, R132H, and WT IDH1 as well as HeLa cells transiently expressing R132Q IDH1 were used to perform cellular inhibition assays. $3x10^5$ cells/well were seeded in six-well plates. The optimal IDH1 expression was determined via

Western blot analysis and the inhibition assay was started 72 h post-transfection. The concentrations of AGI-5198 were 0, 20, 40, 90, 180, 500, and 3000 nM (0.2% DMSO final). Lower concentrations of AGI-5198 were used for HeLa cells, and untransfected HEK293T and HeLa cells were used as controls. The cells were placed in the incubator for 48 h before the metabolites were extracted with a solution of 50% methanol containing *L*-norvaline, which was used as standard. These experiments were all performed by Grace A. Wells. The quantification of D2HG was performed via gas chromatography-mass spectrometry (GC-MS) was previously described by Dr. David Scott[17, 46].

3.4. Results

3.4.1. IDH1 Mutations Identified in Tumors Show Different Catalytic Properties that Can Be Broadly Grouped into Three Types.

As described in Chapter 2, we performed extensive steady-state kinetic studies on a series of IDH1 mutants known to drive tumor formation[17]. We expanded this work by adding additional mutants in order to establish kinetic, inhibitory, and structural features of IDH1 mutants. Here, we added the tumor-relevant R132L, R132S, and R132V IDH1 mutants, and reported their catalytic efficiencies for the normal and neomorphic reaction (Table 1)[17]. R132L, R132S, and R132V IDH1 had low catalytic efficiencies for the normal reaction, consistent with most of the R132 mutants that we have reported[17]. Notably, R132L IDH1 was nearly as efficient at D2HG production as R132Q IDH1. The high catalytic efficiency of R132L IDH1 was mostly driven by a low K_M since its k_{cat} was the lowest among the mutants (Table 1). All mutants were more efficient at converting αKG to D2HG than the most common IDH1 mutant seen in patients, R132H IDH1. Overall, this kinetic study showed unique properties of R132Q IDH1 and allowed us to group these mutants into three distinct categories. The first type describes mutants that are deficient in catalyzing the

normal reaction but are moderately efficient at the neomorphic reaction (R132G, R132V, R132S, R132H, and R132C IDH1). The second group had very low catalytic efficiency for the normal reaction while maintaining high efficiency the neomorphic reaction (R132L IDH1). Lastly, R132Q IDH1 is the only IDH1 mutant reported to date that had high catalytic efficiencies for both reactions.

Table 1. Steady-state kinetic parameters for the normal reaction catalyzed by IDH1, conversion of ICT to αKG, and for the neomorphic reaction catalyzed by IDH1, conversion of αKG to D2HG. At least two enzyme preparations were used to obtain k_{obs} rates (at 37 ºC), which were plotted against substrate concentration and fit to a hyperbolic function. The S. E. shown is determined from the deviation resulting from hyperbolic fits of plots of k_{obs} versus substrate concentration in order to calculate catalytic efficiency (k_{cat}/K_M, mM^{-1} s^{-1}). In some cases, maximal rates were still achieved at concentrations of NADPH that approached the limit of detection, and thus K_m values are listed as ≤ or < than the lowest concentration tested. This table was originally published in https://portlandpress.com/biochemj/article-lookup/doi/10.1042/BCJ20180424 Avellaneda Matteo, D.; Wells, G. A.; Luna, L. A.; Grunseth, A. J.; Zagnitko, O.; Scott, D. A.; Hoang, A.; Luthra, A.; Swairjo, M. A.; Schiffer, J. M.; Sohl, C. D., Inhibitor potency varies widely among tumor-relevant human isocitrate dehydrogenase 1 mutants. *Biochem J* **2018,** *475* (20), 3221-3238.

IDH1	**k_{cat}, s^{-1}, ICT → αKG**	**$K_{M,\ ICT}$, mM, ICT → αKG**	**$K_{M,\ NADP+}$, mM, ICT → αKG**	**k_{cat}/K_M, mM^{-1} s^{-1}, ICT → αKG**	**k_{cat}, s^{-1}, αKG → D2HG**	**$K_{M,\ αKG}$, mM, αKG → D2HG**	**$K_{M,\ NADPH}$, mM, αKG → D2HG**	**k_{cat}/K_M, mM^{-1} s^{-1}, αKG → D2HG**
WT[17]	85 ± 4	0.22 ± 0.02	0.08 ± 0.03	$3.9 \times 10^2 \pm 0.4 \times 10^2$	0.019 ± 0.001	0.5 ± 0.3	≤ 0.010	0.04 ± 0.02
R132H	2.4 ± 0.1	4.2 ± 0.6	1.6 ± 0.5	0.57 ± 0.08	1.44 ± 0.05[a]	1.5 ± 0.2[a]	≤ 0.025	1.0 ± 0.1[a]
R132C[17]	4.4 ± 0.1	8.2 ± 0.8	0.75 ± 0.07	0.54 ± 0.05	1.60 ± 0.07	0.36 ± 0.05	0.010 ± 0.009	4.4 ± 0.6
R132G[17]	9.3 ± 0.6	7 ± 1	0.067 ± 0.007	1.3 ± 0.2	1.59 ± 0.09	0.34 ± 0.08	< 0.025	5 ± 1
R132Q[17]	9.2 ± 0.3	0.8 ± 0.2	0.22 ± 0.05[b]	12 ± 3	4.7 ± 0.2	0.26 ± 0.04	< 0.005[b]	18 ± 3
R132L	4.0 ± 0.1	2.2 ± 0.2	0.055 ± 0.009	1.8 ± 0.2	0.79 ± 0.05	0.05 ± 0.01	< 0.005	16 ± 3
R132S	5.6 ± 0.2	3.9 ± 0.7	0.059 ± 0.009	1.4 ± 0.3	1.32 ± 0.07	0.20 ± 0.04	< 0.005	7 ± 1
R132V	1.38 ± 0.09	1.6 ± 0.4	0.073 ± 0.008	0.9 ± 0.2	1.10 ± 0.01	0.134 ± 0.006	< 0.005	8.2 ± 0.4

3.4.2. Molecular Dynamics Simulations Show Residue 132 Helps Dictate Features of the $NADP^+$-Binding Pocket

Since R132Q IDH1 can catalyze the normal reaction and is highly efficient for D2HG production, we decided to perform MD simulations to understand key changes that allows this mutant to have dual activity at short timescale and atomic levels. We also decided to perform MD simulations using a mutant from each category described above, plus WT IDH1, as comparison. We performed four replicates of MD simulations for R132H, R132Q, R132L, and WT IDH1 homodimers in complexed with $NADP^+$ and Ca^{2+} as well as $NADP^+$ alone. With these simulations we sought to understand key changes in protein structure that would make a mutant more WT-like or mutant-like in terms of reactivity. Since there are no reported crystal structures for R132Q and R132L IDH1, we searched for one structure that would be most similar to the transition states for both reactions.

Several crystal structures of IDH1 were available and thus, we assessed which crystal structure would be ideal for our computer simulations (Supplemental Tables S2 and S3). To assess the best possible structures, we considered substrates bound, surface area of buried ligands (including $NADP^+$, αKG, and ICT), the distances between the center of mass of α4 and α11 helices, and the center of mass of the α10 helix, the distance between R132 and D275, the presence or absence of the α10 helix density, volume of buried cavity from SiteMap[47, 48], resolution and the number of missing side chains. We excluded all the structures that had missing loops. We chose the structure of IDH1 complexed with $NADP^+$, Ca^{2+}, and αKG since having the ligands and metal cation would more likely reveal a transition state-like conformation or catalytically active complex (PDB 4KZO[32]). This structure was in the most closed state and had a well-resolved α10 helix (Figure 2).

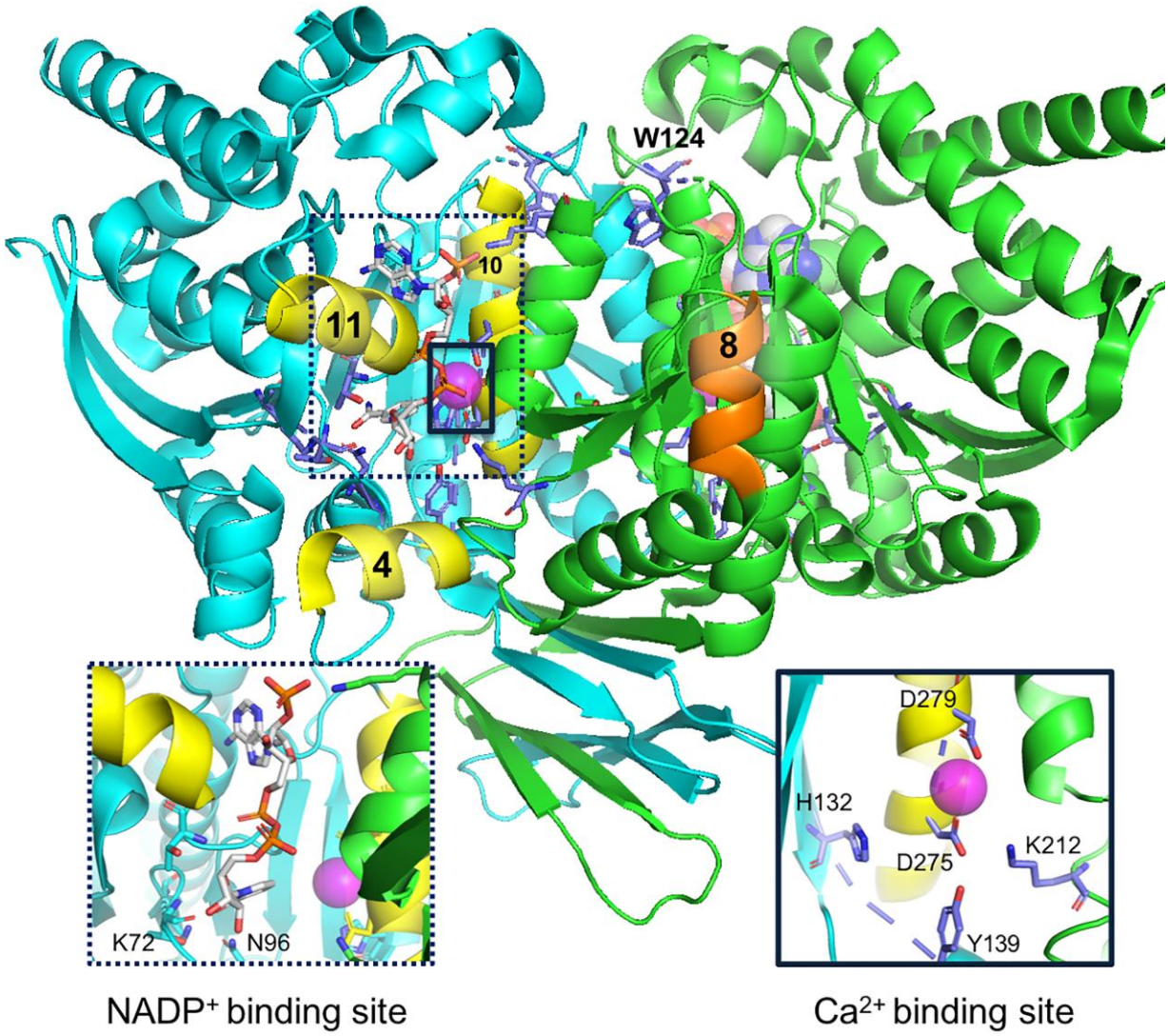

Figure 2. IDH1 Dimeric structure (PDB 4KZO[31]). α-Helices 4, 8, 10, and 11 are labeled for reference and colored in yellow (monomer A, helices 4, 10, 11) and orange (monomer B, helix 8). The $NADP^+$ and Ca^{2+} binding sites are expanded in the labeled sub-panels. Calcium is shown as a pink sphere. $NADP^+$ is colored based on atoms, with nitrogen (blue), oxygen (red), phosphorus (orange), and carbon (gray) shown. Image was generated with PyMol. This figure was originally published in https://portlandpress.com/biochemj/article-lookup/doi/10.1042/BCJ20180424 Avellaneda Matteo, D.; Wells, G. A.; Luna, L. A.; Grunseth, A. J.; Zagnitko, O.; Scott, D. A.; Hoang, A.; Luthra, A.; Swairjo, M. A.; Schiffer, J. M.; Sohl, C. D., Inhibitor potency varies widely among tumor-relevant human isocitrate dehydrogenase 1 mutants. *Biochem J* **2018,** *475* (20), 3221-3238.

Simulations were performed in the absence of αKG and both with and without of Ca^{2+}. The rationale was to understand the impact of Ca^{2+} binding on the stability of mutant IDH1, and to study motions around the $NADP^+$ binding pocket (Figure 2). The RMSF of the $NADP^+$ atoms in the binding pocket in both monomers were measured after aligning the simulations to the backbone of the enzyme dimer. We assumed that an enzyme that conserved WT activity would have $NADP^+$ more stably bound (lower RMSF) while enzymes with lower WT activity (R132L and R132H IDH1) would have less stable binding of $NADP^+$ (higher RMSF). Although K_M does not represent thermodynamic affinity of the enzyme to a substrate, we show that lower concentrations of ICT were required to saturate the enzyme for WT and R132Q IDH1, while higher concentrations were required for R132L and R132H IDH1 (Table 1).

Our MD simulations show that in the B monomers, the atomic-level RMSF of $NADP^+$ bound to R132L and R132H IDH1 was larger than that observed in R132Q and WT IDH1 (Figure 3 and Supplemental Table S5). Moreover, the atomic-level RMSF for $NADP^+$ complexed with R132Q IDH1 was higher than WT for monomer B, but lower in monomer A. When averaging the atoms in the nicotinamide moiety, the averaged RMSF for R132L IDH1 per monomer (4.2 ± 0.4 Å and 4.7 ± 0.4 Å) and R132H IDH1 per monomer (5.0 ± 0.4 Å and 5.4 ± 0.3 Å) trended higher than WT IDH1 per monomer (4.3 ± 0.6 Å and 4.2 ± 0.7 Å) and R132Q (3.6 ± 0.2 Å and 4.3 ± 0.4 Å). The differences in RMSF seen within monomers for WT, R132L, and R132H were within a single standard deviation. Simulations of R132Q IDH1 complexed with $NADP^+$ and Ca^{2+} showed large atomic-RMSF for $NADP^+$ in monomer B compared with $NADP^+$ in monomer A. This suggested a deviation in the dynamics communicated across the dimer interface for mutants relative to WT and other IDH1 mutants. Measurements of IDH1 homodimers crystal structures

showed a monomer-to-monomer structural variability in $NADP^+$ and $NADP^+/Ca^{2+}/\alpha KG$ bound states (PDB: 1T09[25] and 4KZO[32]) (Supplemental Table S2).

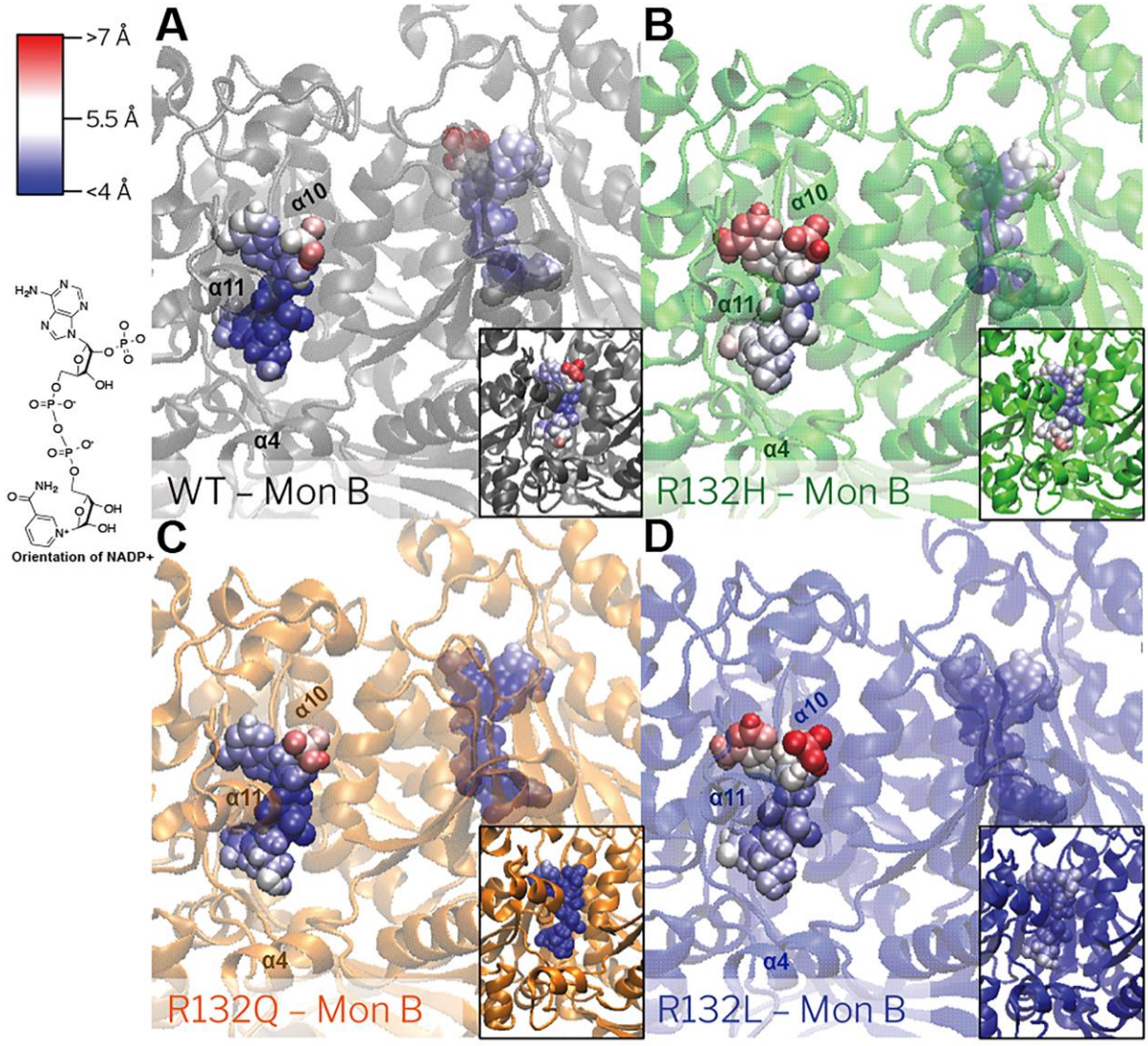

Figure 3. $NADP^+$ RMSF in WT, R132Q, R132H, and R132L IDH1 simulations with Ca^{2+} bound. The RMSF per atom is colored onto each atom for **A.** WT IDH1 (gray), **B.** R132H IDH1 (green), **C.** R132Q IDH1 (orange), and **D.** R132L IDH1 (blue). The $NADP^+$ atoms that fluctuate more than 7 Å are in red, while the atoms which fluctuation less than 4 Å are in blue. Gradations between the two is modulated with white. The orientation of $NADP^+$ in the crystal structures is shown. This figure was originally published in https://portlandpress.com/biochemj/article-lookup/doi/10.1042/BCJ20180424 Avellaneda Matteo, D.; Wells, G. A.; Luna, L. A.; Grunseth, A. J.; Zagnitko, O.; Scott, D. A.; Hoang, A.; Luthra, A.; Swairjo, M. A.; Schiffer, J. M.; Sohl, C. D., Inhibitor potency varies widely among tumor-relevant human isocitrate dehydrogenase 1 mutants. *Biochem J* **2018,** *475* (20), 3221-3238.

Differences in hydrogen bonding pattern were also found for $NADP^+$ and each mutant, especially within the nicotinamide moiety (Supplemental Figures S7 and S8). There were two

regions of $NADP^+$ where hydrogen bonding was monitored. The first region was the ester oxygen in the nicotinamide ribose and T311 (Supplemental Figure S7). The second region was the amide oxygen of the nicotinamide and residues T75, N96, and K72 (Supplemental Figure S8). When comparing crystal structures of R132H IDH1 bound to $NADP^+$ versus NADPH, the only difference in the binding pose was within the hydrogen bonding of the amide oxygen of the nicotinamide (atom name O7N; Supplemental Table S5). Thus, we predicted this region could be the better differentiator between features associated with $NADP^+$ binding, which was required for the normal reaction, versus NADPH binding, which was required for the neomorphic reaction. In the crystal structure of $NADP^+$-bound R132H IDH1[32], there were three hydrogen bonds between the amide oxygen of the nicotinamide and IDH1, while in its NADPH-bound form there are none[23]. From all-atom MD, WT IDH1 made the largest number of hydrogen bond interactions with the nicotinamide ribose in the $NADP^+/Ca^{2+}$-bound simulations, while all mutants showed fewer interactions at this site (Supplemental Figure S7). However, WT and R132Q IDH1 were more likely to form stable hydrogen bonds with the amide oxygen of the nicotinamide of $NADP^+$ than R132H and R132L IDH1 (Supplemental Figure S8). This may be an indication that R132Q IDH1 was simulated to bind $NADP^+$ with a more WT-like affinity, suggesting some qualitative agreement between these simulations and our experimental findings.

Results from all-atom MD also revealed that the R132 residue is critical for positioning the orientation of the β-sheets in both monomers of IDH1. The distance between the center of mass of the β carbons of residue 132 and the center of mass of the carbonyl carbon of D275 for the WT, R132H, R132Q, and R132L IDH1 simulations were measured in the Ca^{2+}-bound and the Ca^{2+}-unbound simulations (Figure 4). R132 from one monomer coordinates to D275 in the α10 helix of the other monomer. The trend in the distance between these two residues in the mutant and WT

IDH1 simulations for Ca^{2+}-bound simulations was as follows: R132L > R132H > R132Q >> WT IDH1. In Ca^{2+}-unbound simulations, the trend in distances between these two residues in the mutant and WT IDH1 simulations was: WT > R132L > R132Q > R132H IDH1. This modeled difference in interaction distance between R132 and D275 in turn appeared to cause a change in the positioning of the β-sheet relative to the dimer interface (Figure 4C). This tilt in the β-sheet was also seen in the crystal structure of R132H IDH1 bound to inhibitors[23] (Supplemental Figure S1C,E). In turn, this tilt of the β-sheet shifted the positions of the α4 and α11 helices. Helices α4 and α11 neighbor the $NADP^+$-binding site and were connected in sequence through loops to the β3 and β14 sheets, respectively (Figure 4). This rearrangement of β-sheets and α-helices opened the active site of IDH1. This opening suggested a possible explanation for the RMSF and hydrogen bond distances seen, which could be measured by the change in the angle between the center of mass β3, β11, and α10 helix (Figure 4C). This measurement also revealed that one of the WT IDH1 monomers opened greater over simulation than the other (Figure 4F). This same difference in openness over the simulation occurred with the following trend: WT>R132Q>R132>R132L IDH1, the same trend that was expected given the trend in the distance between R132 and D275 and the anchoring role of this residue interaction in the closed state. This result was expected knowing the anchoring interaction between R132 and D275 in the closed state. Interestingly, in the Ca^{2+}-unbound simulations, the residue 132 to D275 distances were longer for WT IDH1 compared with the Ca^{2+}-bound simulations, suggesting a role for divalent cations in the structures of the WT active site compared with the mutants. In all mutants, the α4/11 to α10 distances remained more stable over the MD trajectory in the Ca^{2+}-unbound simulations than in the Ca^{2+}-bound simulations.

During the Ca^{2+}-bound simulations of R132Q IDH1, the openness of the monomers as well as the R132Q-D275 distances showed WT-like characteristics within two out of the four replicates, while R132H/R132L IDH1-like characteristics for the remaining two replicates (Figure 4). These results may provide an explanation for the R132Q IDH1 dual activity since this mutant seemed able to adopt either a more mutant-like conformation or a more WT-like conformation. On the other hand, in the simulations where Ca^{2+} was not bound, the trend was not observed, meaning that the structural changes of the β-sheets and α4/11 were also dependent on the coordination of D275 with Ca^{2+}.

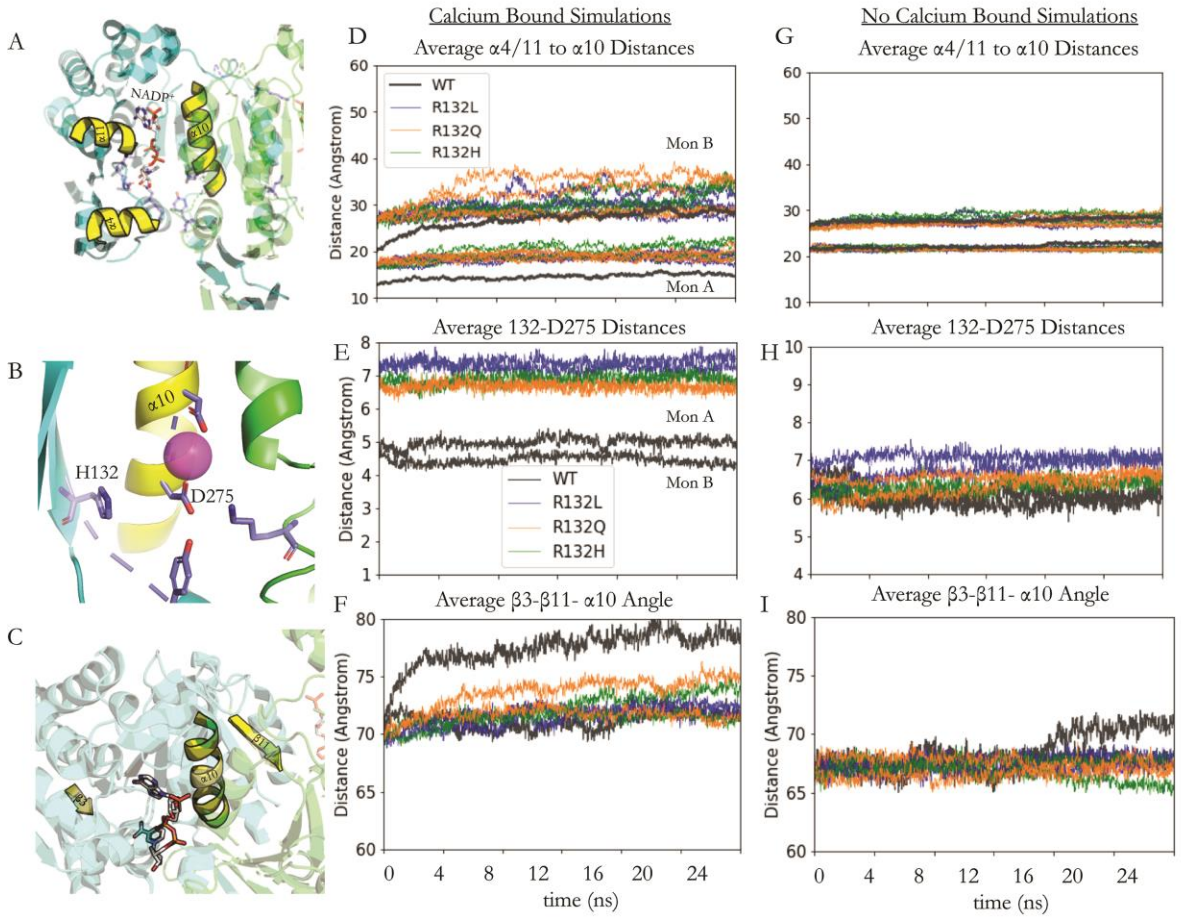

Figure 4. NADP$^+$ binding site conformational changes in R132Q, R132H, and R132L IDH1 simulations. **A.** The relative positions of the α-helices 4 and 11 (α4/11), and α10 near the NADP$^+$ binding site (Figure 2). **B.** Zoomed-in view of H132, D275 on α10, and Ca^{2+} (pink sphere). **C.** The positions of β3, β11, and α10 are highlighted to give context for the center of mass angles measured in F/I. **D/G.** The average distances between the α4/11 residues and the α10 residues on the other side of the NADP$^+$ binding site are shown for Ca^{2+}-bound simulations **D.** and Ca^{2+}-unbound simulations **G**. The distances for each of the four replicate simulations for the R132L (blue), R132Q (orange), and R132H (green) IDH1 simulations are displayed while the average of the WT simulations is shown in gray for clarity. The standard deviation in the WT IDH1 simulations for monomer B (Mon B) is 2.23 Å, whereas the standard deviation for the WT IDH1 simulations for monomer A (Mon A) is 1.91 Å. **E/H**. The average distances between the residue 132 center of mass and D275 center of mass over all four replicates of each mutant/WT trajectory for Ca^{2+}-bound simulations **E.** and Ca^{2+}-unbound simulations **H.**. **F/I.** The angles between the center of mass for β3, β11, and α10 are averaged over all four replicates of each mutant/WT trajectory for Ca^{2+}-bound simulations **F.** and Ca^{2+}-unbound simulations **H.** This figure was originally published in https://portlandpress.com/biochemj/article-lookup/doi/10.1042/BCJ20180424 Avellaneda Matteo, D.; Wells, G. A.; Luna, L. A.; Grunseth, A. J.; Zagnitko, O.; Scott, D. A.; Hoang, A.; Luthra, A.; Swairjo, M. A.; Schiffer, J. M.; Sohl, C. D., Inhibitor potency varies widely among tumor-relevant human isocitrate dehydrogenase 1 mutants. *Biochem J* **2018,** *475* (20), 3221-3238.

3.4.3. R132Q IDH1 is Refractory to Inhibition in Biochemical Assays

Since the catalytic efficiencies among IDH1 mutants varied largely, we decided to study how these mutants interacted with three commercially available mutant IDH1 inhibitors, ML309[49], AGI-5198[19], and GSK864[50] (Figure 5A). Previously, these compounds were tested for their ability to inhibit R132H and R132C IDH1 activity, with biochemical and cellular IC_{50} values in the nM range[19, 49-52]. These inhibitors have not been tested against a wider spectrum of IDH1 mutants. Figure 5 and Table 2 show the results for the biochemical IC_{50} assays for ML309 and AGI-5198 against mutant IDH1 inhibitors using an established protocol of resazurin/diaphorase-NADPH coupled reaction as the readout for NADPH levels[19]. We show that all mutant IDH1 enzymes had low to mid nM IC_{50} values, except R132Q IDH1. For ML309, the IC_{50} value was125-fold higher for R132Q IDH1 than R132H IDH1, and 16-fold lower compared to WT IDH1. For AGI-5198, the IC_{50} value was >16000 higher for R132Q IDH1 compared to R132H IDH1, and 1.5-fold lower than WT IDH1. Additionally, since R132L IDH1 was inhibited effectively, these results suggest that conserving WT activity drives loss of inhibitor affinity, rather than highly efficient D2HG production.

Table 2. Biochemical IC_{50} measurements for selective inhibitors of IDH1 mutants**.** Percent activity of an incubation of IDH1, NADPH, and αKG with increasing concentrations of inhibitor were determined, and plotted against log[inhibitor] and fit to a sigmoidal function. The 95% confidence intervals are shown as determined from the deviation from these fits. This table was originally published in https://portlandpress.com/biochemj/article-lookup/doi/10.1042/BCJ20180424 Avellaneda Matteo, D.; Wells, G. A.; Luna, L. A.; Grunseth, A. J.; Zagnitko, O.; Scott, D. A.; Hoang, A.; Luthra, A.; Swairjo, M. A.; Schiffer, J. M.; Sohl, C. D., Inhibitor potency varies widely among tumor-relevant human isocitrate dehydrogenase 1 mutants. *Biochem J* **2018,** *475* (20), 3221-3238.

IDH1	**ML309 IC_{50}, μM, [confidence interval]**	**AGI-5198 IC_{50}, μM, [confidence interval]**
WT	80, [60 – 100]	1000, [480 – 2,100]
R132H	0.04, [0.03 – 0.05]	0.04, [0.03 – 0.06]
R132Q	5, [4 – 7]	650, [330-1,300]
R132C	0.04, [0.02 – 0.07]	0.2, [0.07 – 0.4]
R132G	0.09, [0.07 – 0.1]	0.23, [0.20 – 0.27]
R132L	0.01, [0.009 – 0.14]	0.009, [0.008 – 0.011]
R132S	0.1, [0.096 – 0.15]	0.3, [0.2 – 0.5]
R132V	0.0035, [0.0027 – 0.0044]	0.02, [0.02 – 0.03]

Inhibition of R132H, R132Q, and WT IDH1 by GSK864, a pan-inhibitor[53], was also tested. The biochemical IC_{50} values for WT IDH1 and GSK864 have been reported as high nM (~470 nM) and very low nM IC_{50} values for R132H, R132C, and R132H IDH1 (9-17 nM)[50]. Therefore, we decided to test R132Q IDH1 with GSK864 to see whether this mutant has similar inhibition profile as WT IDH1. The biochemical IC_{50} value for R132Q IDH1 with GSK864 was only 1.5-fold lower than WT IDH1, but 34-fold higher than R132H IDH1 (Figure 5 and Table 3). Therefore, these results indicate that R132Q IDH1 also behaves like WT IDH1 in terms of inhibition profile. In short, conservation of normal activity (ICT to αKG) was associated to loss of inhibition by mutant IDH1 inhibitors, unless the inhibitor was nonselective.

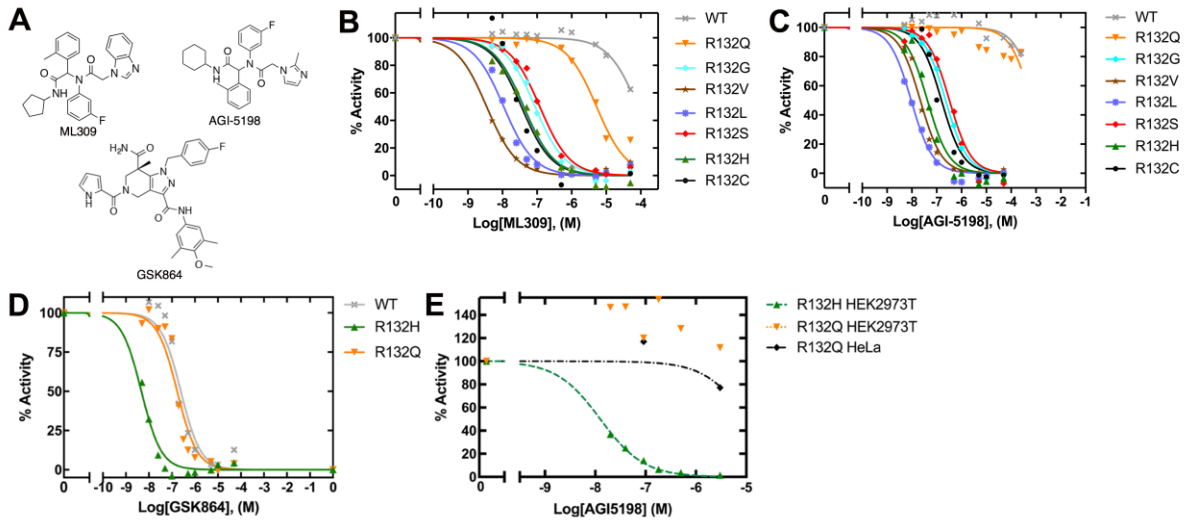

Figure 5. Biochemical and cellular inhibition by ML309, AGI-5198, and GSK864 **A.** Selective mutant IDH1 inhibitors (ML309 and AGI-5198) designed to target R132H and R132C IDH1, and the pan-inhibitor GSK864 are commercially available. The loss of catalytic conversion of αKG to D2HG in the case of mutant IDH1, or conversion of ICT to αKG in WT IDH1, was measured upon inhibition by **B.** ML309, **C.** AGI-5198, and **D.** GSK864 to obtain biochemical (protein-based) IC_{50} values. **E.** The ability of AGI-5198 to inhibit mutant IDH1 in HEK293T cells transiently expressing R132H IDH1 or R132Q IDH1 and HeLa cells transiently expressing R132Q IDH1 was determined by quantifying cellular D2HG levels using GC-MS. An IC_{50} value of 0.013 μM with a confidence interval of [0.011 to 0.014] for AGI-5198 was calculated for R132H IDH1 in HEK293T cells based upon a fit of the plot shown. An IC_{50} value could not be determined for R132Q IDH1 as concentrations of AGI-5198 required are beyond solubility limits of the compound. Expression of R132Q IDH1 in both HEK2973 and HeLa cells support this finding. Additional information is shown in Supplementary Figure S9. This figure was originally published in https://portlandpress.com/biochemj/article-lookup/doi/10.1042/BCJ20180424 Avellaneda Matteo, D.; Wells, G. A.; Luna, L. A.; Grunseth, A. J.; Zagnitko, O.; Scott, D. A.; Hoang, A.; Luthra, A.; Swairjo, M. A.; Schiffer, J. M.; Sohl, C. D., Inhibitor potency varies widely among tumor-relevant human isocitrate dehydrogenase 1 mutants. *Biochem J* **2018,** *475* (20), 3221-3238.

3.4.4. The Selective Inhibitor AGI-5198 Does Not Effectively Inhibit D2HG Production in Cells Expressing R132Q IDH1

To test the R132Q IDH1 inhibition profile in cells, we performed cellular inhibition assays using HEK293T cells transiently expressing WT, R132H, and R132Q IDH1, and HeLa cells transiently expressing R132Q IDH1 (Supplemental Figure S6). After 48 h of treatment with varying concentrations of AGI-5198, D2HG levels were assayed using GC-MS. R132H IDH1 transiently expressed in HEK293T cells showed significantly lower D2HG levels at inhibitor concentrations as low as 20 nM, but no inhibition was observed for R132Q IDH1 in HEK293T cells at high concentrations of AGI-5198 (Figure 4 and Supplemental Figure S9). In HeLa cells

transiently expressing R132Q IDH1, a moderate inhibition was observed using AGI-5198 (Figure 5 and Supplemental Figure S9). These results support our biochemical findings that mutant IDH1 inhibitors are not selective for R132Q IDH1. Moreover, the basal D2HG concentration in cells transiently expressing R132Q IDH1 were higher than cells transiently expressing R132H IDH1, which has also been previously reported[16]. These results also support the increase in catalytic efficiency for the neomorphic reaction of R132Q IDH1 compared to R132H IDH1 (Table 1) in that D2HG levels were much higher in cell lines expressing R132Q IDH1 compared to R132H IDH1.

Table 3. Biochemical IC_{50} measurements for the pan-inhibitor GSK864. Percent activity of an incubation of IDH1, NADPH, and αKG with increasing concentrations of inhibitor were determined, and plotted against log[inhibitor] and fit to a sigmoidal function. The 95% confidence intervals are shown as determined from the deviation from these fits. This table was originally published in https://portlandpress.com/biochemj/article-lookup/doi/10.1042/BCJ20180424 Avellaneda Matteo, D.; Wells, G. A.; Luna, L. A.; Grunseth, A. J.; Zagnitko, O.; Scott, D. A.; Hoang, A.; Luthra, A.; Swairjo, M. A.; Schiffer, J. M.; Sohl, C. D., Inhibitor potency varies widely among tumor-relevant human isocitrate dehydrogenase 1 mutants. *Biochem J* **2018,** *475* (20), 3221-3238.

IDH1	**GSK864 IC_{50}, μM, [confidence interval]**
WT	0.24, [0.15 – 0.40]
R132H	0.005, [0.004 – 0.008]
R132Q	0.17, [0.11 – 0.25]

3.4.5. Using MD Simulations to Probe Buried Cavity Dynamics at the Dimer Interface

A crystal structure of WT IDH1 bound to ICT, $NADP^+$, and Ca^{2+} show two pockets between the α9/α10 helices at the inhibitor binding site that are not solvent accessible (Supplemental Figure S4; site 1 and site 2). The positioning of the α9 and α10 helices determines the size of the binding site, with the α10 helix being partially unwound when R132H-IDH1 is bound to the inhibitor, yielding a larger binding site (Supplemental Figure S1D and Tables S2 and

S3). The $NADP^+$ bound R132H IDH1 crystal structures are very dynamic with many regions with unresolved electron density (Supplemental Figure S1F). Ca^{2+} acts competitively with mutant IDH1 inhibitors since there are residues in the α10 helix that coordinate the metal, and Ca^{2+} is absent in crystal structures when the enzyme is bound to $NADP^+$ or inhibitor only[23, 26, 54, 55]. Moreover, crystal structure of WT IDH1 in the absence of Ca^{2+} also has the α10 helix unwound[25].

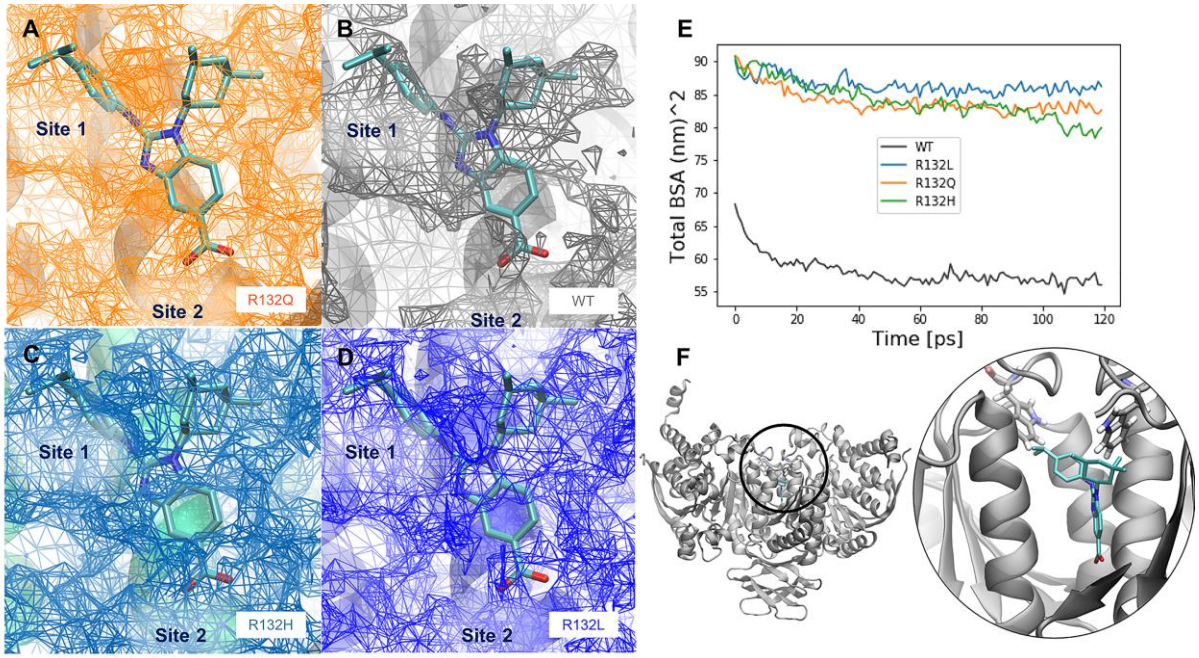

Figure 6. Inhibitor binding site differences in R132Q, R132H, and R132L IDH1 simulations**.** A BAY 1436032 analogue, for which a crystal structure in complex with R132H IDH1 has been solved previously (PDB 5LGE[53]), was overlaid with our IDH1 models, which are the average structures from each set of MD simulations. The surface of the buried inhibitor binding pockets averaged across all four simulations are shown in the interface between the monomers where known inhibitors (including the BAY 1436032 analogue) bind for the **A.** R132Q IDH1, **B.** WT IDH1, **C.** R132H IDH1, and **D.** R132L IDH1 simulations. The relative locations of the buried cavity site 1 and site 2, as determined from crystal structures (Supplementary Figure S4) are labeled in A-D. **E.** The sizes of the average cavity can be compared to the differences in the total buried surface area averaged over all four replicates of simulations. **F.** The position of this buried cavity is shown both in zoomed-out and zoomed-in views, along with the positions of residue W124, a possible lid residue for exposing the inhibitor bindings sites. The color scheme for the inhibitor atoms is the same used in Supplementary Figure S1. Note that in A-D, the mesh represents empty space available for inhibitor binding. This figure was originally published in https://portlandpress.com/biochemj/article-lookup/doi/10.1042/BCJ20180424 Avellaneda Matteo, D.; Wells, G. A.; Luna, L. A.; Grunseth, A. J.; Zagnitko, O.; Scott, D. A.; Hoang, A.; Luthra, A.; Swairjo, M. A.; Schiffer, J. M.; Sohl, C. D., Inhibitor potency varies widely among tumor-relevant human isocitrate dehydrogenase 1 mutants. *Biochem J* **2018,** *475* (20), 3221-3238.

The effect of R132 mutants on the average inhibitor-binding cavity volumes and the buried surface area of the dimer interface was calculated in the IDH1 homodimer MD simulations (Figure 6). For all three mutants, the size of the buried cavity was much larger than that calculated in WT

IDH1 simulation in the presence of $NADP^+$ and Ca^{2+}. In simulations of IDH1 bound to only $NADP^+$, the inhibitor-binding site was maintained at a small volume in all mutants, similar to WT IDH1. This suggests that the inhibitor-binding site opening occurs once IDH1 is already in the dynamic open state, since IDH1 simulations in the presence of Ca^{2+} demonstrate little structural variability between the open/closed states compared with simulations in the absence of Ca^{2+} (Figure 4B, C).

In Ca^{2+}-bound simulations, the buried surface area of all three mutants was greater than the buried surface area of the WT IDH1 cavity. The increase in buried surface area with increased in cavity volume seemed counter-intuitive. However, this can be explained by the fact that as the cavity expands, there is a corresponding increase in the interfacial surfaces along the perimeter of the buried cavity. Interestingly, all three mutants showed similar sizes in the cavity, although in these models, the α10 helix was intact. In the absence of αKG and Ca^{2+}, R132H IDH1 crystal structures were disordered in this region, resulting in a potentially enlarged inhibitor-binding pocket[23]. Overall, these findings suggest that structural changes primarily in the dimer interface in the absence of Ca^{2+} and in the $NADP^+$/NADPH-binding sites may help drive some of the kinetic and inhibition-binding properties observed in R132Q IDH1 versus R132H and R132L IDH1.

3.5. Discussion

In this work, we report that the kinetic, structural, and inhibitory profile of R132Q IDH1 is significantly different than that observed for tumor-relevant IDH1 mutants studied here. Most mutant IDH1 enzymes show a relatively low catalytic efficiency for the neomorphic and normal reaction, while R132L IDH1 had very high and low catalytic efficiencies for D2HG and αKG production, respectively. R132Q IDH1 was the only mutant with moderate αKG production activity and high catalytic efficiency for the neomorphic reaction. Previous work using cellular

models of IDH1-driven tumor have shown that the D2HG levels of HEK293T cells expressing R132Q IDH1 were higher than those cells expressing R132H IDH1[16], but it is not understood whether these mutants drive differences in phenotype and patient prognosis. Pusch and colleagues have previously indicated that lower D2HG level may be more favorable for tumorigenesis, based on the high frequency of R132H IDH1 in cancer[56]. Our kinetic work supports this observation since most IDH1 mutants had moderate neomorphic activity, with the lowest catalytic efficiency seen for the most common mutation, R132H IDH1. R132Q and R132L IDH1 were highly efficient for D2HG production, thus rapidly depleting NADPH and αKG, and may have a different degree of impact on tumorigenesis. Nevertheless, it is difficult to predict how each mutant would affect patient prognosis since all IDH1 mutations are heterozygous, with thus WT activity partially maintained.

In the previous chapter, we showed that, generally, smaller and more hydrophobic residues drove the neomorphic reaction[17], although R132Q IDH1 did not follow that trend. The high catalytic efficiency for R132L IDH1 in the neomorphic reaction supports our previous findings[17]. However, Pusch and colleagues described that HEK293T cell expressing R132G IDH1 had the highest intracellular D2HG concentrations followed by R132L, R132C, R132S, and R132H IDH1[56]. These results are in agreement with what we previously described in our kinetic work except for R132G IDH1, which we indicated as a moderate D2HG producer[17]. However, we focus on assessing activity using kinetic catalytic efficiency (k_{cat}/K_M), and thus it is not fair to compare these rates directly with Pusch and colleagues, who assess activity in terms of pmol/μg of protein[56]. Our kinetic work agrees with Pusch and colleagues results since we both report that the $K_{M,\ \alpha KG}$ values are higher for R132G IDH1 than most IDH1 mutants except for R132H and R132C IDH1[56], indicating a lower efficiency for R132G IDH1 (Table 1). However, it is possible that R132L IDH1

does not follow this trend in tumors since its high catalytic efficiency is driven by a very low K_M. Since metabolism is quite complexed in cellular and *in vivo* settings, it is difficult to make a direct comparison with our biochemical work. Neverhteless, our kinetic work can provide some rationale to the trends that are observed, such as the high D2HG concentrations in cellular and in animal models seen in R132Q driven-tumors.

We used MD simulations to understand structural features among the three different types of mutants (R132Q, R132H, and R132L IDH1) relative to WT IDH1 that drive catalytic efficiency and inhibitor binding. We found that the atomic RMSF values of $NADP^+$ in WT and R132Q IDH1 were lower than in R132L and R132H IDH1 in both monomers. Moreover, we also found that there is variability between monomers of each mutant. This variability suggests that there could be an allosteric pathway between the IDH1 active site of each monomer, and mutation of the R132 residue not only affects the $NADP^+$-binding site, but also may negatively impact important allosteric communications between the active sites of each monomer required for WT activity. Pietrak and colleagues describe how the conversion of ICT to D2HG is coupled between the two monomers in the WT-mutant IDH1 heterodimer[57]. Residue R132 in the WT IDH1 monomer coordinates with the C-3 carboxylate group of ICT, likely favoring the binding of ICT over αKG[57]. Once the conversion of ICT to αKG is completed by the WT IDH1 monomer, αKG may be tunneled to the mutant monomer where D2HG is produced[57], although recent work has called that into question[58]. Moreover, R132 is anchored by D275 while the latter residue coordinates with the divalent cation. Therefore, when the inter-residue network is disrupted by mutation at R132, there is a difference in the degree of closure of each monomer in the closed state at the nanosecond timescale. Due to the differences in $NADP^+$ binding in WT IDH1 versus mutant forms of the enzyme, it is possible that residue R132 also plays a role in gating $NADP^+$ versus NADPH to help

favor the normal reaction. Moreover, this difference in binding may also be influenced by inter-subunit allostery. Future work includes expressing and purifying WT-mutant IDH1 heterodimer to study the kinetic and inhibitory profiles of the more physiological relevant mutant form.

Examining hydrogen bonding at the ester oxygen of the nicotinamide riboside did not highlight any preference of $NADP^+$-binding for WT IDH1 and R132Q IDH1 compared to R132L and R132H IDH1. However, when monitoring hydrogen bond formation in the amide oxygen of the nicotinamide, which had the greatest differences in hydrogen bonding patterns when comparing crystal structures of $NADP^+$-bound and NADPH-bound IDH1, we show that R132Q IDH1 can form the largest number of stable hydrogen bonds among IDH1 mutants. Therefore, since R132H and R132L IDH1 are less able to form hydrogen bond at this location compared to R132Q and WT IDH1, this might explain the preference of R132H and R132L IDH1 for NADPH-dependent reactions instead of $NADP^+$-dependent reactions. Moreover, it is worth studying how R132H and R132L IDH1 catalyze the normal reverse reaction (αKG to ICT). Overall, R132Q IDH1 displayed conformations that were either more WT-like or mutant-like. This is seen as large fluctuations in distances between helices near the active site (Figure 4B) and the variability in hydrogen bond formation with the ester oxygen of the nicotinamide riboside (Supplemental Figure S7).

To have a better understanding of how the inhibitors bind at the dimer interface, we overlaid our MD simulation results with a structure of R132H IDH1 bound to an analog of the pan-inhibitor BAY1436032[54]. Both the analog and BAY1436032 are similar in structure to the inhibitors we studied in this chapter. A crystal structure of R132H IDH1 complexed with BAY1436032 was used in our model since crystal structures of IDH1 complexed with the inhibitors we studied in this chapter have not been reported. The reported cryo-EM structure of

R132C IDH1 bound to ML309 do not report electron density presumably corresponding to ML309 in the inhibitor binding pocket[24]. The average dimer interface cavity of each mutant holoenzyme and WT IDH1 is overlaid with the BAY1436032 analog in Supplemental Figure S10[54]. In MD simulations performed on WT IDH1 (Figure 6) in complex with only $NADP^+$, the cavity at the dimer interface did not overlap with cavity where the BAY1436032 analog bound. Instead, residues in the α10 helix overlapped with the inhibitor. In MD simulations on the mutant form bound to $NADP^+$ and Ca^{2+}, the average cavity surface surrounded the inhibitor except for a phenyl ring of the carboxy-indole. Nevertheless, this binding site was able to accommodate the inhibitor better for both R132L and R132H IDH1 upon unwinding of the α10 helix[23]. This phenyl group is next to the *N*-terminus of the α-10 helix (Figure 6A-D), where this helix is usually unresolved in the crystal structures of R132H IDH1[23]. The α10 helix also contains D275, which interacts with R132 in WT IDH1. An interesting observation is that the isopropyl group of the phenyl ring is not accommodated as well in WT and R132Q IDH1, while this region is better accommodated in R132H and R132L IDH1 (Figure 6A-D). Therefore, partial unwinding of the α10 helix may be possible for R132Q IDH1. These observations may explain inhibitor affinity among mutant and WT IDH1 enzymes observed experimentally. Future work will be to perform similar MD simulations with a recent crystal structure of the pan-inhibitor AG-881, which was published before this work[59].

The indole group in the inhibitors BAY143602 and the analog is a moiety common well among IDH1 mutant inhibitors, with ML309 having an indole group while AGI-5198 has an imidazole group. The biochemical IC_{50} values for ML309 are usually lower than those measured for AGI-5198, suggesting that the indole group may support better inhibitor binding regardless of the *N*-terminal helix unwinding. The IC_{50} value for ML309 with R132Q IDH1 is 130-fold lower

than with AGI-5198, suggesting that R132Q IDH1 is better inhibited by the indole moiety-containing inhibitor. Therefore, we suggest that the inhibitor binding with the bulkier indole groups may be subject to unwinding of the *N*-terminus of the α10 helix. This could allow for binding of bulkier inhibitors such as GSK864 in the dimeric interface as seen in many crystal structures (Figure 5 Supplemental Table S3).

An interesting question is how the buried cavity can become solvent accessible for inhibitor binding. From simulations of the R132L and R132V IDH1 bound to $NADP^+$ and Ca^{2+}, the torsion angle changes in residue W124 enable opening of the buried inhibitor-binding cavity to solvent (Supplemental Figure S11). These torsion angles are not observed in holo simulations of R132Q, R132H, and WT IDH1. When the phi and psi angles change in W124, it results in a conformational change that leads to the buried cavity. Adjustment in the α9 and α10 helices provide enough space for W124 to move. Previously, tryptophan has been posited to serve as a gate to buried cavities, allowing these cavities to become solvent accessible in the microsecond timescale[60-63]. The movement of W124 may be part of a mechanism of opening the cavity allowing for inhibitor binding. The opening of the buried cavity is required for binding of inhibitors, and since R132H IDH1 shows high affinity for these compounds, the timescale of our simulations likely were not appropriate to observe movement of W124 in this mutational variant.

Although all-atom explicit solvent MD simulations showed interesting differences between the holo mutants and WT IDH1, and apo R132Q and WT IDH1, the short timescale (100 ns) of the simulations did not allow us to observe all the conformational changes that likely take place within each enzyme studied. Regardless of the short timescale, we observed significant differences for the average distances, $NADP^+$, atomic-level RMSF, torsion changes, and buried cavity

volumes of each of the IDH1 systems studied. Future work in the microsecond simulations may reveal conformational changes that we were not able to observe.

In this chapter, we used kinetic experiments as well as MD simulations to understand the catalytic, structural, and inhibitory features of many IDH1 mutants seen in cancer. We also expanded on our work from chapter 2 [17] and we showed that conservation of WT activity correlates with a significant loss of affinity for mutant IDH1 inhibitors. Changes in some α-helices may drive substrate and inhibitor-binding pockets, and the open/closed transition of the IDH1 monomer could explain some catalytic characteristics. Moreover, MD simulations show that R132Q IDH1 can have both WT-like and mutant-like conformation, providing a possible explanation of its dual activity. Moreover, R132Q IDH1 had higher affinity for inhibitors with bulkier indole rings instead of imidazole smaller groups as seen on AGI-5198, suggesting that in order to have inhibition of this mutant, an indole group may be required. This chapter highlights features of inhibitor binding and kinetics, allowing for future strategies for drug design for patients harboring mutations such as R132Q IDH1.

3.6. References

1. Warburg, O., Über den Stoffwechsel der Carcinomzelle. *Klin Wochenschr* **1925,** *4*, 534-536.

2. Warburg, O., Origin of cancer cells. *Oncologia* **1956,** *9* (2), 75-83.

3. DeBerardinis, R. J.; Chandel, N. S., Fundamentals of cancer metabolism. *Sci Adv* **2016,** *2* (5), e1600200.

4. Parsons, D. W.; Jones, S.; Zhang, X.; Lin, J. C.; Leary, R. J.; Angenendt, P.; Mankoo, P.; Carter, H.; Siu, I. M.; Gallia, G. L.; Olivi, A.; McLendon, R.; Rasheed, B. A.; Keir, S.; Nikolskaya, T.; Nikolsky, Y.; Busam, D. A.; Tekleab, H.; Diaz, L. A., Jr.; Hartigan, J.; Smith, D. R.; Strausberg, R. L.; Marie, S. K.; Shinjo, S. M.; Yan, H.; Riggins, G. J.; Bigner, D. D.; Karchin, R.; Papadopoulos, N.; Parmigiani, G.; Vogelstein, B.; Velculescu, V. E.; Kinzler, K. W., An integrated genomic analysis of human glioblastoma multiforme. *Science* **2008,** *321* (5897), 1807-12.

5. Yan, H.; Parsons, D. W.; Jin, G.; McLendon, R.; Rasheed, B. A.; Yuan, W.; Kos, I.; Batinic-Haberle, I.; Jones, S.; Riggins, G. J.; Friedman, H.; Friedman, A.; Reardon, D.; Herndon, J.; Kinzler, K. W.; Velculescu, V. E.; Vogelstein, B.; Bigner, D. D., IDH1 and IDH2 mutations in gliomas. *N Engl J Med* **2009,** *360* (8), 765-73.

6. Mardis, E. R.; Ding, L.; Dooling, D. J.; Larson, D. E.; McLellan, M. D.; Chen, K.; Koboldt, D. C.; Fulton, R. S.; Delehaunty, K. D.; McGrath, S. D.; Fulton, L. A.; Locke, D. P.; Magrini, V. J.; Abbott, R. M.; Vickery, T. L.; Reed, J. S.; Robinson, J. S.; Wylie, T.; Smith, S. M.; Carmichael, L.; Eldred, J. M.; Harris, C. C.; Walker, J.; Peck, J. B.; Du, F.; Dukes, A. F.; Sanderson, G. E.; Brummett, A. M.; Clark, E.; McMichael, J. F.; Meyer, R. J.; Schindler, J. K.; Pohl, C. S.; Wallis, J. W.; Shi, X.; Lin, L.; Schmidt, H.; Tang, Y.; Haipek, C.; Wiechert, M. E.; Ivy, J. V.; Kalicki, J.; Elliott, G.; Ries, R. E.; Payton, J. E.; Westervelt, P.; Tomasson, M. H.; Watson, M. A.; Baty, J.; Heath, S.; Shannon, W. D.; Nagarajan, R.; Link, D. C.; Walter, M. J.; Graubert, T. A.; DiPersio, J. F.; Wilson, R. K.; Ley, T. J., Recurring mutations found by sequencing an acute myeloid leukemia genome. *N Engl J Med* **2009,** *361* (11), 1058-66.

7. Kipp, B. R.; Voss, J. S.; Kerr, S. E.; Barr Fritcher, E. G.; Graham, R. P.; Zhang, L.; Highsmith, W. E.; Zhang, J.; Roberts, L. R.; Gores, G. J.; Halling, K. C., Isocitrate dehydrogenase 1 and 2 mutations in cholangiocarcinoma. *Hum Pathol* **2012,** *43* (10), 1552-8.

8. Borger, D. R.; Tanabe, K. K.; Fan, K. C.; Lopez, H. U.; Fantin, V. R.; Straley, K. S.; Schenkein, D. P.; Hezel, A. F.; Ancukiewicz, M.; Liebman, H. M.; Kwak, E. L.; Clark, J. W.; Ryan, D. P.; Deshpande, V.; Dias-Santagata, D.; Ellisen, L. W.; Zhu, A. X.; Iafrate, A. J., Frequent mutation of isocitrate dehydrogenase (IDH)1 and IDH2 in cholangiocarcinoma identified through broad-based tumor genotyping. *Oncologist* **2012,** *17* (1), 72-9.

9. Zhao, S.; Lin, Y.; Xu, W.; Jiang, W.; Zha, Z.; Wang, P.; Yu, W.; Li, Z.; Gong, L.; Peng, Y.; Ding, J.; Lei, Q.; Guan, K. L.; Xiong, Y., Glioma-derived mutations in IDH1 dominantly inhibit IDH1 catalytic activity and induce HIF-1alpha. *Science* **2009,** *324* (5924), 261-5.

10. Gross, S.; Cairns, R. A.; Minden, M. D.; Driggers, E. M.; Bittinger, M. A.; Jang, H. G.; Sasaki, M.; Jin, S.; Schenkein, D. P.; Su, S. M.; Dang, L.; Fantin, V. R.; Mak, T. W., Cancer-associated metabolite 2-hydroxyglutarate accumulates in acute myelogenous leukemia with isocitrate dehydrogenase 1 and 2 mutations. *J Exp Med* **2010,** *207* (2), 339-44.

11. Figueroa, M. E.; Abdel-Wahab, O.; Lu, C.; Ward, P. S.; Patel, J.; Shih, A.; Li, Y.; Bhagwat, N.; Vasanthakumar, A.; Fernandez, H. F.; Tallman, M. S.; Sun, Z.; Wolniak, K.; Peeters, J. K.; Liu, W.; Choe, S. E.; Fantin, V. R.; Paietta, E.; Lowenberg, B.; Licht, J. D.; Godley, L. A.; Delwel, R.; Valk, P. J.; Thompson, C. B.; Levine, R. L.; Melnick, A., Leukemic IDH1 and IDH2 mutations result in a hypermethylation phenotype, disrupt TET2 function, and impair hematopoietic differentiation. *Cancer Cell* **2010,** *18* (6), 553-67.

12. Chowdhury, R.; Yeoh, K. K.; Tian, Y. M.; Hillringhaus, L.; Bagg, E. A.; Rose, N. R.; Leung, I. K.; Li, X. S.; Woon, E. C.; Yang, M.; McDonough, M. A.; King, O. N.; Clifton, I. J.; Klose, R. J.; Claridge, T. D.; Ratcliffe, P. J.; Schofield, C. J.; Kawamura, A., The

oncometabolite 2-hydroxyglutarate inhibits histone lysine demethylases. *EMBO Rep* **2011,** *12* (5), 463-9.

13. Cerami, E.; Gao, J.; Dogrusoz, U.; Gross, B. E.; Sumer, S. O.; Aksoy, B. A.; Jacobsen, A.; Byrne, C. J.; Heuer, M. L.; Larsson, E.; Antipin, Y.; Reva, B.; Goldberg, A. P.; Sander, C.; Schultz, N., The cBio cancer genomics portal: an open platform for exploring multidimensional cancer genomics data. *Cancer Discov* **2012,** *2* (5), 401-4.

14. Dimitrov, L.; Hong, C. S.; Yang, C.; Zhuang, Z.; Heiss, J. D., New developments in the pathogenesis and therapeutic targeting of the IDH1 mutation in glioma. *Int J Med Sci* **2015,** *12* (3), 201-13.

15. Hirata, M.; Sasaki, M.; Cairns, R. A.; Inoue, S.; Puviindran, V.; Li, W. Y.; Snow, B. E.; Jones, L. D.; Wei, Q.; Sato, S.; Tang, Y. J.; Nadesan, P.; Rockel, J.; Whetstone, H.; Poon, R.; Weng, A.; Gross, S.; Straley, K.; Gliser, C.; Xu, Y.; Wunder, J.; Mak, T. W.; Alman, B. A., Mutant IDH is sufficient to initiate enchondromatosis in mice. *Proc Natl Acad Sci U.S.A* **2015,** *112* (9), 2829-34.

16. Jiang, B.; Zhang, J.; Xia, J.; Zhao, W.; Wu, Y.; Shi, M.; Luo, L.; Zhou, H.; Chen, A.; Ma, H.; Zhao, Q.; Suleman, M.; Lin, F.; Zhou, L.; Wang, J.; Zhang, Y.; He, Y.; Li, X.; Hung, L. M.; Mak, T. W.; Li, Q., IDH1 mutation promotes tumorigenesis by inhibiting JNK activation and apoptosis induced by serum starvation. *Cell Rep* **2017,** *19* (2), 389-400.

17. Avellaneda Matteo, D.; Grunseth, A. J.; Gonzalez, E. R.; Anselmo, S. L.; Kennedy, M. A.; Moman, P.; Scott, D. A.; Hoang, A.; Sohl, C. D., Molecular mechanisms of isocitrate dehydrogenase 1 (IDH1) mutations identified in tumors: The role of size and hydrophobicity at residue 132 on catalytic efficiency. *J Biol Chem* **2017,** *292* (19), 7971-7983.

18. Dang, L.; Yen, K.; Attar, E. C., IDH mutations in cancer and progress toward development of targeted therapeutics. *Ann Oncol* **2016,** *27* (4), 599-608.

19. Popovici-Muller, J.; Saunders, J. O.; Salituro, F. G.; Travins, J. M.; Yan, S.; Zhao, F.; Gross, S.; Dang, L.; Yen, K. E.; Yang, H.; Straley, K. S.; Jin, S.; Kunii, K.; Fantin, V. R.; Zhang, S.; Pan, Q.; Shi, D.; Biller, S. A.; Su, S. M., Discovery of the first potent inhibitors of mutant IDH1 that lower tumor 2-HG in vivo. *ACS Med Chem Lett* **2012,** *3* (10), 850-5.

20. DiNardo, C. D.; Stein, E. M.; de Botton, S.; Roboz, G. J.; Altman, J. K.; Mims, A. S.; Swords, R.; Collins, R. H.; Mannis, G. N.; Pollyea, D. A.; Donnellan, W.; Fathi, A. T.; Pigneux, A.; Erba, H. P.; Prince, G. T.; Stein, A. S.; Uy, G. L.; Foran, J. M.; Traer, E.; Stuart, R. K.; Arellano, M. L.; Slack, J. L.; Sekeres, M. A.; Willekens, C.; Choe, S.; Wang, H.; Zhang, V.; Yen, K. E.; Kapsalis, S. M.; Yang, H.; Dai, D.; Fan, B.; Goldwasser, M.; Liu, H.; Agresta, S.; Wu, B.; Attar, E. C.; Tallman, M. S.; Stone, R. M.; Kantarjian, H. M., Durable remissions with Ivosidenib in IDH1-mutated relapsed or refractory AML. *N Engl J Med* **2018,** *378* (25), 2386-2398.

21. Wang, F.; Travins, J.; DeLaBarre, B.; Penard-Lacronique, V.; Schalm, S.; Hansen, E.; Straley, K.; Kernytsky, A.; Liu, W.; Gliser, C.; Yang, H.; Gross, S.; Artin, E.; Saada, V.; Mylonas, E.; Quivoron, C.; Popovici-Muller, J.; Saunders, J. O.; Salituro, F. G.; Yan, S.; Murray, S.; Wei, W.; Gao, Y.; Dang, L.; Dorsch, M.; Agresta, S.; Schenkein, D. P.; Biller, S. A.; Su, S. M.; de Botton, S.; Yen, K. E., Targeted inhibition of mutant IDH2 in leukemia cells induces cellular differentiation. *Science* **2013,** *340* (6132), 622-6.

22. Yen, K.; Travins, J.; Wang, F.; David, M. D.; Artin, E.; Straley, K.; Padyana, A.; Gross, S.; DeLaBarre, B.; Tobin, E.; Chen, Y.; Nagaraja, R.; Choe, S.; Jin, L.; Konteatis, Z.; Cianchetta, G.; Saunders, J. O.; Salituro, F. G.; Quivoron, C.; Opolon, P.; Bawa, O.; Saada, V.; Paci, A.; Broutin, S.; Bernard, O. A.; de Botton, S.; Marteyn, B. S.; Pilichowska, M.; Xu, Y.; Fang, C.; Jiang, F.; Wei, W.; Jin, S.; Silverman, L.; Liu, W.; Yang, H.; Dang, L.; Dorsch, M.; Penard-Lacronique, V.; Biller, S. A.; Su, S. M., AG-221, a first-in-class therapy targeting acute myeloid leukemia harboring oncogenic IDH2 mutations. *Cancer Discov* **2017,** *7* (5), 478-493.

23. Xie, X.; Baird, D.; Bowen, K.; Capka, V.; Chen, J.; Chenail, G.; Cho, Y.; Dooley, J.; Farsidjani, A.; Fortin, P.; Kohls, D.; Kulathila, R.; Lin, F.; McKay, D.; Rodrigues, L.; Sage, D.; Toure, B. B.; van der Plas, S.; Wright, K.; Xu, M.; Yin, H.; Levell, J.; Pagliarini, R. A., Allosteric mutant IDH1 inhibitors reveal mechanisms for IDH1 mutant and isoform selectivity. *Structure* **2017,** *25* (3), 506-513.

24. Merk, A.; Bartesaghi, A.; Banerjee, S.; Falconieri, V.; Rao, P.; Davis, M. I.; Pragani, R.; Boxer, M. B.; Earl, L. A.; Milne, J. L.; Subramaniam, S., Breaking Cryo-EM resolution barriers to facilitate drug discovery. *Cell* **2016,** *165* (7), 1698-707.

25. Xu, X.; Zhao, J.; Xu, Z.; Peng, B.; Huang, Q.; Arnold, E.; Ding, J., Structures of human cytosolic NADP-dependent isocitrate dehydrogenase reveal a novel self-regulatory mechanism of activity. *J Biol Chem* **2004,** *279* (32), 33946-57.

26. Yang, B.; Zhong, C.; Peng, Y.; Lai, Z.; Ding, J., Molecular mechanisms of "off-on switch" of activities of human IDH1 by tumor-associated mutation R132H. *Cell Res* **2010,** *20* (11), 1188-200.

27. Intlekofer, A. M.; Shih, A. H.; Wang, B.; Nazir, A.; Rustenburg, A. S.; Albanese, S. K.; Patel, M.; Famulare, C.; Correa, F. M.; Takemoto, N.; Durani, V.; Liu, H.; Taylor, J.; Farnoud, N.; Papaemmanuil, E.; Cross, J. R.; Tallman, M. S.; Arcila, M. E.; Roshal, M.; Petsko, G. A.; Wu, B.; Choe, S.; Konteatis, Z. D.; Biller, S. A.; Chodera, J. D.; Thompson, C. B.; Levine, R. L.; Stein, E. M., Acquired resistance to IDH inhibition through trans or cis dimer-interface mutations. *Nature* **2018,** *559* (7712), 125-129.

28. Schrödinger Release 2018-3, Schrödinger Suite 2018-3 Protein Preparation Wizard.

29. Epik, Schrödinger, LLC, New York, NY, 2016.

30. Impact, Schrödinger, LLC, New York, NY, 2016.

31. Prime, Schrödinger, LLC, New York, NY, 2018.

32. Rendina, A. R.; Pietrak, B.; Smallwood, A.; Zhao, H.; Qi, H.; Quinn, C.; Adams, N. D.; Concha, N.; Duraiswami, C.; Thrall, S. H.; Sweitzer, S.; Schwartz, B., Mutant IDH1 enhances the production of 2-hydroxyglutarate due to its kinetic mechanism. *Biochemistry* **2013,** *52* (26), 4563-77.

33. Schrödinger Release 2018-3: BioLuminate, Schrödinger, LLC, New York, NY, 2018.

34. Jorgensen, W. L.; Chandrasekhar, J.; Madura, J. D.; Impey, R. W.; Klein, M. L., Comparison of simple potential functions for simulating liquid water. *J Chem Phys* **1983,** *79* (2), 926-935.

35. Huang, J.; MacKerell, A. D., Jr., CHARMM36 all-atom additive protein force field: validation based on comparison to NMR data. *J Comput Chem* **2013,** *34* (25), 2135-45.

36. Beglov, D.; Roux, B., Finite representation of an infinite bulk system: Solvent boundary potential for computer simulations. *J Chem Phys* **1994,** *100* (12), 9050-9063.

37. D. A. Case, D. S. C., T. E. Cheatham, III, T. A. Darden, R. E. Duke, T. J. Giese, H. Gohlke, A. W. Goetz, D. Greene, N. Homeyer, S. Izadi, A. Kovalenko, T. S. Lee, S. LeGrand, P. Li, C. Lin, J. Liu, T. Luchko, R. Luo, D. Mermelstein, K.M. Merz, G. Monard, H. Nguyen, I. Omelyan, A. Onufriev, F. Pan, R. Qi, D. R. Roe, A. Roitberg, C. Sagui, C .L. Simmerling, W. M. Botello-Smith, J. Swails, R. C. Walker, J. Wang, R. M. Wolf, X. Wu, L. Xiao, D. M. York and P. A. Kollman, AMBER 2017, University of California, San Francisco. **2017**.

38. Salomon-Ferrer, R.; Case, D. A.; Walker, R. C., An overview of the Amber biomolecular simulation package. *Wiley Interdiscip Rev Comput Mol Sci* **2013,** *3* (2), 198-210.

39. Darden, T.; York, D.; Pedersen, L., Particle mesh Ewald: An N·log(N) method for Ewald sums in large systems. *J Chem Phys* **1993,** *98* (12), 10089-10092.

40. Perez, F.; Granger, B. E., IPython: A System for Interactive Scientific Computing. *Computing in Science and Engg.* **2007,** *9* (3), 21-29.

41. Roe, D. R.; Cheatham, T. E., PTRAJ and CPPTRAJ: software for processing and analysis of molecular dynamics trajectory data. **2013,** *9* (7), 3084-3095.

42. McGibbon, Robert T.; Beauchamp, Kyle A.; Harrigan, Matthew P.; Klein, C.; Swails, Jason M.; Hernández, Carlos X.; Schwantes, Christian R.; Wang, L.-P.; Lane, Thomas J.; Pande, Vijay S., MDTraj: A modern open library for the analysis of molecular dynamics trajectories. *Biophys J* **2015,** *109* (8), 1528-1532.

43. Humphrey, W.; Dalke, A.; Schulten, K., VMD: visual molecular dynamics. *J Mol Graph* **1996,** *14* (1), 33-8, 27-8.

44. Schrödinger Release 2018-3: Maestro, Schrödinger, LLC, New York, NY, 2018.

45. Schrödinger, LLC: New York, NY 2018.

46. Ratnikov, B.; Aza-Blanc, P.; Ronai, Z. A.; Smith, J. W.; Osterman, A. L.; Scott, D. A., Glutamate and asparagine cataplerosis underlie glutamine addiction in melanoma. *Oncotarget* **2015,** *6* (10), 7379-89.

47. SiteMap, Schrödinger, LLC, New York, NY, 2018.

48. Halgren, T. A., Identifying and characterizing binding sites and assessing druggability. *J Chem Inf Model* **2009,** *49* (2), 377-89.

49. Davis, M. I.; Gross, S.; Shen, M.; Straley, K. S.; Pragani, R.; Lea, W. A.; Popovici-Muller, J.; Delabarre, B.; Artin, E.; Thorne, N.; Auld, D. S.; Li, Z.; Dang, L.; Boxer, M. B.; Simeonov, A., Biochemical, cellular and biophysical characterization of a potent inhibitor of mutant isocitrate dehydrogenase IDH1. *J Biol Chem* **2014,** *289*, 13717-13725.

50. Okoye-Okafor, U. C.; Bartholdy, B.; Cartier, J.; Gao, E. N.; Pietrak, B.; Rendina, A. R.; Rominger, C.; Quinn, C.; Smallwood, A.; Wiggall, K. J.; Reif, A. J.; Schmidt, S. J.; Qi, H.; Zhao, H.; Joberty, G.; Faelth-Savitski, M.; Bantscheff, M.; Drewes, G.; Duraiswami, C.; Brady, P.; Groy, A.; Narayanagari, S. R.; Antony-Debre, I.; Mitchell, K.; Wang, H. R.; Kao, Y. R.; Christopeit, M.; Carvajal, L.; Barreyro, L.; Paietta, E.; Makishima, H.; Will, B.; Concha, N.; Adams, N. D.; Schwartz, B.; McCabe, M. T.; Maciejewski, J.; Verma, A.; Steidl, U., New IDH1 mutant inhibitors for treatment of acute myeloid leukemia. *Nat Chem Biol* **2015,** *11* (11), 878-86.

51. Popovici-Muller, J.; Lemieux, R. M.; Artin, E.; Saunders, J. O.; Salituro, F. G.; Travins, J.; Cianchetta, G.; Cai, Z.; Zhou, D.; Cui, D.; Chen, P.; Straley, K.; Tobin, E.; Wang, F.; David, M. D.; Penard-Lacronique, V.; Quivoron, C.; Saada, V.; de Botton, S.; Gross, S.; Dang, L.; Yang, H.; Utley, L.; Chen, Y.; Kim, H.; Jin, S.; Gu, Z.; Yao, G.; Luo, Z.; Lv, X.; Fang, C.; Yan, L.; Olaharski, A.; Silverman, L.; Biller, S.; Su, S. M.; Yen, K., Discovery of AG-120 (Ivosidenib): a first-in-class mutant IDH1 inhibitor for the treatment of IDH1 mutant cancers. *ACS Med Chem Lett* **2018,** *9* (4), 300-305.

52. Rohle, D.; Popovici-Muller, J.; Palaskas, N.; Turcan, S.; Grommes, C.; Campos, C.; Tsoi, J.; Clark, O.; Oldrini, B.; Komisopoulou, E.; Kunii, K.; Pedraza, A.; Schalm, S.; Silverman, L.; Miller, A.; Wang, F.; Yang, H.; Chen, Y.; Kernytsky, A.; Rosenblum, M. K.; Liu, W.; Biller, S. A.; Su, S. M.; Brennan, C. W.; Chan, T. A.; Graeber, T. G.; Yen, K. E.; Mellinghoff, I. K., An inhibitor of mutant IDH1 delays growth and promotes differentiation of glioma cells. *Science* **2013,** *340* (6132), 626-30.

53. Chaturvedi, A.; Herbst, L.; Pusch, S.; Klett, L.; Goparaju, R.; Stichel, D.; Kaulfuss, S.; Panknin, O.; Zimmermann, K.; Toschi, L.; Neuhaus, R.; Haegebarth, A.; Rehwinkel, H.; Hess-Stumpp, H.; Bauser, M.; Bochtler, T.; Struys, E. A.; Sharma, A.; Bakkali, A.; Geffers, R.; Araujo-Cruz, M. M.; Thol, F.; Gabdoulline, R.; Ganser, A.; Ho, A. D.; von Deimling, A.;

Rippe, K.; Heuser, M.; Kramer, A., Pan-mutant-IDH1 inhibitor BAY1436032 is highly effective against human IDH1 mutant acute myeloid leukemia in vivo. *Leukemia* **2017,** *31* (10), 2020-2028.

54. Pusch, S.; Krausert, S.; Fischer, V.; Balss, J.; Ott, M.; Schrimpf, D.; Capper, D.; Sahm, F.; Eisel, J.; Beck, A. C.; Jugold, M.; Eichwald, V.; Kaulfuss, S.; Panknin, O.; Rehwinkel, H.; Zimmermann, K.; Hillig, R. C.; Guenther, J.; Toschi, L.; Neuhaus, R.; Haegebart, A.; Hess-Stumpp, H.; Bauser, M.; Wick, W.; Unterberg, A.; Herold-Mende, C.; Platten, M.; von Deimling, A., Pan-mutant IDH1 inhibitor BAY 1436032 for effective treatment of IDH1 mutant astrocytoma in vivo. *Acta Neuropathol* **2017,** *133* (4), 629-644.

55. Jones, S.; Ahmet, J.; Ayton, K.; Ball, M.; Cockerill, M.; Fairweather, E.; Hamilton, N.; Harper, P.; Hitchin, J.; Jordan, A.; Levy, C.; Lopez, R.; McKenzie, E.; Packer, M.; Plant, D.; Simpson, I.; Simpson, P.; Sinclair, I.; Somervaille, T. C.; Small, H.; Spencer, G. J.; Thomson, G.; Tonge, M.; Waddell, I.; Walsh, J.; Waszkowycz, B.; Wigglesworth, M.; Wiseman, D. H.; Ogilvie, D., Discovery and optimization of allosteric inhibitors of mutant isocitrate dehydrogenase 1 (R132H IDH1) displaying activity in human acute myeloid leukemia cells. *J Med Chem* **2016,** *59* (24), 11120-11137.

56. Pusch, S.; Schweizer, L.; Beck, A. C.; Lehmler, J. M.; Weissert, S.; Balss, J.; Miller, A. K.; von Deimling, A., D-2-Hydroxyglutarate producing neo-enzymatic activity inversely correlates with frequency of the type of isocitrate dehydrogenase 1 mutations found in glioma. *Acta Neuropathol Commun* **2014,** *2,* 19.

57. Pietrak, B.; Zhao, H.; Qi, H.; Quinn, C.; Gao, E.; Boyer, J. G.; Concha, N.; Brown, K.; Duraiswami, C.; Wooster, R.; Sweitzer, S.; Schwartz, B., A tale of two subunits: how the neomorphic R132H IDH1 mutation enhances production of alphaHG. *Biochemistry* **2011,** *50* (21), 4804-12.

58. Dexter, J. P.; Ward, P. S.; Dasgupta, T.; Hosios, A. M.; Gunawardena, J.; Vander Heiden, M. G., Lack of evidence for substrate channeling or flux between wildtype and mutant isocitrate dehydrogenase to produce the oncometabolite 2-hydroxyglutarate. *J Biol Chem* **2018,** *293* (52), 20051-20061.

59. Ma, R.; Yun, C. H., Crystal structures of pan-IDH inhibitor AG-881 in complex with mutant human IDH1 and IDH2. *Biochem Biophys Res Commun* **2018,** *503* (4), 2912-2917.
60. Mulder, F. A.; Mittermaier, A.; Hon, B.; Dahlquist, F. W.; Kay, L. E., Studying excited states of proteins by NMR spectroscopy. *Nat Struct Biol* **2001,** *8* (11), 932-5.

61. Fitzgerald, M. M.; Musah, R. A.; McRee, D. E.; Goodin, D. B., A ligand-gated, hinged loop rearrangement opens a channel to a buried artificial protein cavity. *Nat Struct Biol* **1996,** *3* (7), 626-31.

62. Nucci, N. V.; Fuglestad, B.; Athanasoula, E. A.; Wand, A. J., Role of cavities and hydration in the pressure unfolding of T4 lysozyme. *Proc Natl Acad Sci U.S.A* **2014,** *111* (38), 13846-13851.

63. Schiffer, J. M.; Feher, V. A.; Malmstrom, R. D.; Sida, R.; Amaro, R. E., Capturing invisible motions in the transition from ground to rare excited states of T4 lysozyme L99A. *Biophys J* **2016,** *111* (8), 1631-1640.

64. Bauer, W. J.; Luthra, A.; Zhu, G.; Radolf, J. D.; Malkowski, M. G.; Caimano, M. J., Structural characterization and modeling of the Borrelia burgdorferi hybrid histidine kinase Hk1 periplasmic sensor: A system for sensing small molecules associated with tick feeding. *J Struct Biol* **2015,** *192* (1), 48-58.

65. Konarev Petr, V.; Volkov Vladimir, V.; Sokolova Anna, V.; Koch Michel, H. J.; Svergun Dmitri, I., PRIMUS: a Windows PC-based system for small-angle scattering data analysis. *J Appl Cryst 36*, 1277-1282.

66. Svergun, D. I., Determination of the regularization parameter in indirect-transform methods using perceptual criteria. *J Appl Crystallogr* **1992,** *25*, 495-503.

67. Schneidman-Duhovny, D.; Hammel, M.; Tainer, J. A.; Sali, A., Accurate SAXS profile computation and its assessment by contrast variation experiments. *Biophys J* **2013,** *105* (4), 962-74.

68. Schneidman-Duhovny, D.; Hammel, M.; Tainer, J. A.; Sali, A., FoXS, FoXSDock and MultiFoXS: Single-state and multi-state structural modeling of proteins and their complexes based on SAXS profiles. *Nucleic Acids Res* **2016,** *44* (W1), W424-9.

69. Rambo, R. P.; Tainer, J. A., Characterizing flexible and intrinsically unstructured biological macromolecules by SAS using the Porod-Debye law. *Biopolymers* **2011,** *95* (8), 559-71.

70. Deng, G.; Shen, J.; Yin, M.; McManus, J.; Mathieu, M.; Gee, P.; He, T.; Shi, C.; Bedel, O.; McLean, L. R.; Le-Strat, F.; Zhang, Y.; Marquette, J. P.; Gao, Q.; Zhang, B.; Rak, A.; Hoffmann, D.; Rooney, E.; Vassort, A.; Englaro, W.; Li, Y.; Patel, V.; Adrian, F.; Gross, S.; Wiederschain, D.; Cheng, H.; Licht, S., Selective inhibition of mutant isocitrate dehydrogenase 1 (IDH1) via disruption of a metal binding network by an allosteric small molecule. *J Biol Chem* **2015,** *290* (2), 762-74.

71. Dang, L.; White, D. W.; Gross, S.; Bennett, B. D.; Bittinger, M. A.; Driggers, E. M.; Fantin, V. R.; Jang, H. G.; Jin, S.; Keenan, M. C.; Marks, K. M.; Prins, R. M.; Ward, P. S.; Yen, K. E.; Liau, L. M.; Rabinowitz, J. D.; Cantley, L. C.; Thompson, C. B.; Vander Heiden, M. G.; Su, S. M., Cancer-associated IDH1 mutations produce 2-hydroxyglutarate. *Nature* **2009,** *462* (7274), 739-44.

72. Levell, J. R.; Caferro, T.; Chenail, G.; Dix, I.; Dooley, J.; Firestone, B.; Fortin, P. D.; Giraldes, J.; Gould, T.; Growney, J. D.; Jones, M. D.; Kulathila, R.; Lin, F.; Liu, G.; Mueller, A.; van der Plas, S.; Slocum, K.; Smith, T.; Terranova, R.; Toure, B. B.; Tyagi, V.; Wagner, T.; Xie, X.; Xu, M.; Yang, F. S.; Zhou, L. X.; Pagliarini, R.; Cho, Y. S., Optimization of 3-

pyrimidin-4-yl-oxazolidin-2-ones as allosteric and mutant specific inhibitors of IDH1. *ACS Med Chem Lett* **2017,** *8* (2), 151-156.

73. Cho, Y. S.; Levell, J. R.; Liu, G.; Caferro, T.; Sutton, J.; Shafer, C. M.; Costales, A.; Manning, J. R.; Zhao, Q.; Sendzik, M.; Shultz, M.; Chenail, G.; Dooley, J.; Villalba, B.; Farsidjani, A.; Chen, J.; Kulathila, R.; Xie, X.; Dodd, S.; Gould, T.; Liang, G.; Heimbach, T.; Slocum, K.; Firestone, B.; Pu, M.; Pagliarini, R.; Growney, J. D., Discovery and evaluation of clinical candidate IDH305, a brain penetrant mutant IDH1 inhibitor. *ACS Med Chem Lett* **2017,** *8* (10), 1116-1121.

3.7. Supplemental information

SAXS was used to assess the quality and features of each of the IDH1 protein constructs. SAXS data were collected on the Bio-SAXS beamline BL4–2 at the Stanford Synchrotron Research Laboratory using a Rayonix MX225-HE CCD detector (Rayonix, Evanston, IL, USA) with a sample-to-detector distance of 1.7 m and a beam energy of 11 keV (λ = 1.127 Å). The momentum transfer (scattering vector) q was defined as $q = 4\pi \sin(\theta)/\lambda$, where 2θ is the scattering angle. The q scale was calibrated by silver behenate powder diffraction. All data were collected to a maximum q of 0.4 $Å^{-1}$. Scattering data were collected from the buffer alone and subtracted from the total protein solution scattering. For all samples, a 100 μL sample containing 42 μM of protein was prepared in buffer containing 20 mM Tris–HCl (pH 7.5 at ambient temperature), 100 mM NaCl, 1 mM DTT and specific ligands. For WT IDH1 and R132Q IDH1, 500 μM ICT, 100 μM $NADP^+$, and 10mM $CaCl_2$ were added. For R132Q and R132H IDH1, 500 μM αKG, 100 μM NADPH, and 10mM $CaCl_2$ were added. $CaCl_2$ was used to prevent catalytic turnover, but allow the required conformational change to occur [26]. SAXS experiments were also performed on apo enzymes under the same buffer conditions (20 mM Tris–HCl (pH 7.5) and 100 mM NaCl). Radii of gyration (R_g), extrapolated from the Guinier region of the Guinier plot, were computed using PRIMUS [64, 65]. P(r) functions were calculated using the program GNOM [66]. Theoretical scattering curves were computed from different structural models and compared to experimental scattering curves using the program FoXS [67, 68]. The structural parameters derived from the SAXS data are summarized in Supplementary Table S1, with experimental scattering data and Kratky plots shown in Supplementary Figure S2, show excellent consistency among WT and mutant forms of the protein in terms of protein size and folding. The apo form of the structure is larger, as the protein appears to clamp down over its substrates upon binding. The Porod-Debye exponent provides a new and reliable means for identifying flexibility in SAXS experiments [69]. Therefore, to check any

dynamic transition during catalysis, we determined the Porod-Debye exponent (P), deduced from the SAXS data. The consist values of Porod-Debye exponent, P, in all states further corroborate the absence of flexibility.

Supplemental Table S1. Parameters for SAXS analysis This table was originally published in https://portlandpress.com/biochemj/article-lookup/doi/10.1042/BCJ20180424 Avellaneda Matteo, D.; Wells, G. A.; Luna, L. A.; Grunseth, A. J.; Zagnitko, O.; Scott, D. A.; Hoang, A.; Luthra, A.; Swairjo, M. A.; Schiffer, J. M.; Sohl, C. D., Inhibitor potency varies widely among tumor-relevant human isocitrate dehydrogenase 1 mutants. *Biochem J* **2018,** *475* (20), 3221-3238.

	[Protein] (μM)[a]	R_g (Å) from Guinier plot[b,c]	I(0)[c]	Porod-Debye exponent (P)[d]	MM (Da)[e]
WT IDH1 ^{apo}	42	32.9 ± 0.1	124.22	2.2	102.72
WT IDH1$^{ICT+NADPH}$	42	32.1 ± 0.1	135.44	2.1	95.27
R132Q IDH1 ^{apo}	42	33.3 ± 0.2	129.79	2.2	105.60
R132Q IDH1$^{ICT+NADPH}$	42	32.3 ± 0.2	132.92	2.2	94.90
R132Q IDH1$^{\alpha KG+NADPH}$	42	32.02 ± 0.08	136.57	2.2	96.84
R132H IDH1 ^{apo}	42	34 ± 1	126.82	2.2	105.38
R132H IDH1$^{\alpha KG+NADPH}$	42	32 ± 2	121.66	2.1	96.13

[a]Molarity is based on the dimeric conformation.

[b]The radius of gyration (R_g) is the root mean squared distance (RMSD) from the center of mass to each electron.

[c]Determined by Guinier approximation in PRIMUS [64].

[d]The Porod-Debye exponents were calculated using the program Scatter (https://bl1231.als.lbl.gov/scatter/).

[e]Molecular masses (MM) are calculated by SAXSMoW (http://saxs.ifsc.usp.br/). Molecular mass from the protein sequence was determined to be 96,000 Da.

Supplemental Table S2. Characterization of IDH1 crystal structures without inhibitors bound This table was originally published in https://portlandpress.com/biochemj/article-lookup/doi/10.1042/BCJ20180424 Avellaneda Matteo, D.; Wells, G. A.; Luna, L. A.; Grunseth, A. J.; Zagnitko, O.; Scott, D. A.; Hoang, A.; Luthra, A.; Swairjo, M. A.; Schiffer, J. M.; Sohl, C. D., Inhibitor potency varies widely among tumor-relevant human isocitrate dehydrogenase 1 mutants. *Biochem J* **2018,** *475* (20), 3221-3238.

PDB	Mutant/ Isoform	Substrates Bound	Surface area buried by all ligands	Open versus Closed (Angles – Figure 4C)	α4/11-α10 (Å)	R132-D275 Distances (mon1/mon2)	SiteMap buried volume (Site 1, Site 2) Å^3	α10 density	Resolution (Å)	Missing Side Chains
1T0L [25]	WT	$NADP^+$, isocitrate, Ca^{2+}	873.94	66.3º/66.0º	20.12, 19.79	4.57, 4.14	75.89, 83.05	no	2.41	none
1T09 [25]	WT	$NADP^+$	908.27	70.1º, 65.3º	23.56, 20.8	5.53, 13.19		unraveled	2.7	none
5YFM[a]	WT	$NADP^+$, Mg^{2+}	874.02	76.4º, 76.2º	25.29, 25.28	5.92, 5.88	58.82, 73.23	no	2.4	K81, K233
4L03 [32]	WT	$NADP^+$, αKG, Ca^{2+}, ethylene glycol bound in to inhibitor pocket	618.35	65.2º, 65.2º	20.02, 23.1	6.05, 6.09	65.90, 87.04	no	2.1	K3, K81, E174, K350, K3, E36, K65, K81, K151, E174, K350, Q411, K413
4L04 [32]	WT	$NADP^+$, αKG, Ca^{2+}	972.05	65.7º, 66.9º	19.36, 19.00	6.07, 6.8	76.10, 95.65	no	2.87	E36, E80, K81, E174, K187, K233, E262, K350, K406, K413, S415
3MAR [26]	R132H	$NADP^+$	860			not resolved		yes	3.41	none
3MAP [26]	R132H	$NADP^+$, isocitrate	955.64			not resolved		yes	2.8	R140, V281, Q283, Y285, Y272
3MAS [26]	R132H	$NADP^+$, isocitrate	956.25			not resolved		yes	3.2	none
4KZO [32]	R132H	$NADP^+$, αKG, Ca^{2+}	735.63	65.0º, 65.1º	17.68, 17.95	7.10, 7.15	57.07, 80.4	no	2.2	K3, K81, E174, E36, K151, K350, Q411, K413
4UMY [70]	R132H	$NADP^+$	787.911	-		not resolved		yes	2.07	none
3INM [71]	R132H	NADPH, αKG, Ca^{2+}	762.31	67.9º,68.4º	18.38, 18.29	7.05, 6.95	55.27, 69.03	no	2.1	none

[a]To be published

Supplemental Table S3. Characterization of IDH1 crystal structures with inhibitors bound This table was originally published in https://portlandpress.com/biochemj/article-lookup/doi/10.1042/BCJ20180424 Avellaneda Matteo, D.; Wells, G. A.; Luna, L. A.; Grunseth, A. J.; Zagnitko, O.; Scott, D. A.; Hoang, A.; Luthra, A.; Swairjo, M. A.; Schiffer, J. M.; Sohl, C. D., Inhibitor potency varies widely among tumor-relevant human isocitrate dehydrogenase 1 mutants. *Biochem J* **2018,** *475* (20), 3221-3238.

PDB	Substrates Bound	Surface area buried by all ligands	Angle	α4/11-α10 (Å)	R132-D275 Distances (mon1/2) (Å)	SiteMap buried volume (Site 1 + Site 2) Å^3	α10 density	Resolution (Å)	Missing Side Chains	Inhibitor type	Inhibitor to monomer ratio
5SUN [23]	Inhibitor NADPH	1466.04		-	not resolved		Absent	2.477	none	neither	1 to 1
5TQH [72]	Inhibitor NADPH	1506.41		-	not resolved		Absent	2.2	none	neither	1 to 1
6B0Z [73]	Inhibitor NADPH	1768.67	106.2º	27.3	9.64	N/A[a]	N-terminal missing (chain A)	2.34	none	neither	3 to 2
5LGE [54]	Inhibitor NADPH	1160.88	108º, 54.3º	21.5, 21.83	7.95, 8.93	412.84	Present	2.7	none (but there are overlapping atoms)	indole	1 to 2
5L58 [55]	Inhibitor NADPH	1708.17		-	not resolved		Missing	3.04	Q138, T142, D160, N171, E173, E174, I215, L216, K217, K218	adamantane	1 to 1
5L57 [55]	Inhibitor NADPH	1694.84	79.0º, 87.2º	34.5, 30.61	8.19, 7.16	N/A[a]	Present	2.695	R100, Y135, Y167, K212, Y219, Y272, V281, K413,	adamantane	1 to 1
4UMX [70]	Inhibitor NADP$^+$	1123.92	59.7º, 66.0º	19.81, 20.78	7.98, 13.95	N/A[a]	Chain B missing	1.88	none	imidazole	1 to 2
5DE1 [50]	Inhibitor NADP$^+$	1558.4			not resolved		Missing	2.25	K3, K81, R140, K212, K243, D279, K350, K413, E62, E80, K93, Y135, R140, K164, E174, K217, K233, K270,	imidazole and indole	1 to 1
5SVF [23]	Inhibitor NADPH and citrate anion	1350.91			not resolved		Missing	2.34	none	neither	1 to 1
5I96 (IDH2) [22]	Inhibitor NADPH, Ca^{2+}	967.9	79.8º, 80.7º	26.4, 24.8	9.25, 10.36	241.13	Missing	1.55	none	indole	1 to 2

[a] Sites 1 and 2 (Supplementary Figure S4) merge together, join with the NADP$^+$ binding site of one chain, and become solvent accessible.

Supplemental Table S4. Distance between α11 and α8 – opening of IDH1 monomers This table was originally published in https://portlandpress.com/biochemj/article-lookup/doi/10.1042/BCJ20180424 Avellaneda Matteo, D.; Wells, G. A.; Luna, L. A.; Grunseth, A. J.; Zagnitko, O.; Scott, D. A.; Hoang, A.; Luthra, A.; Swairjo, M. A.; Schiffer, J. M.; Sohl, C. D., Inhibitor potency varies widely among tumor-relevant human isocitrate dehydrogenase 1 mutants. *Biochem J* **2018,** *475* (20), 3221-3238.

	R132 (WT), Å		**R132H, Å**		**R132Q, Å**		**R132L, Å**	
	No Ca^{2+}	**Ca^{2+}**	**No Ca^{2+}**	**Ca^{2+}**	**No Ca^{2+}**	**Ca^{2+}**	**No Ca^{2+}**	**Ca^{2+}**
MonomerA	31 ± 3	30 ± 3	27.9 ± 0.9	30 ± 2	28 ± 1	31 ± 4	28 ± 1	28.8 ± 0.9
MonomerB	34 ± 4	35 ± 4	27.8 ± 0.9	30 ± 2	28 ± 1	29.2 ± 0.9	27.4 ± 0.8	30 ± 3

Supplemental Table S5. $NADP^+$ RMSF from all-atom simulations Color scheme: ribose of adenine (green), adenine (gray), phosphates (yellow), ribose of nicotinamide (orange), nicotinamide (blue). This table was originally published in https://portlandpress.com/biochemj/article-lookup/doi/10.1042/BCJ20180424 Avellaneda Matteo, D.; Wells, G. A.; Luna, L. A.; Grunseth, A. J.; Zagnitko, O.; Scott, D. A.; Hoang, A.; Luthra, A.; Swairjo, M. A.; Schiffer, J. M.; Sohl, C. D., Inhibitor potency varies widely among tumor-relevant human isocitrate dehydrogenase 1 mutants. *Biochem J* **2018,** *475* (20), 3221-3238.

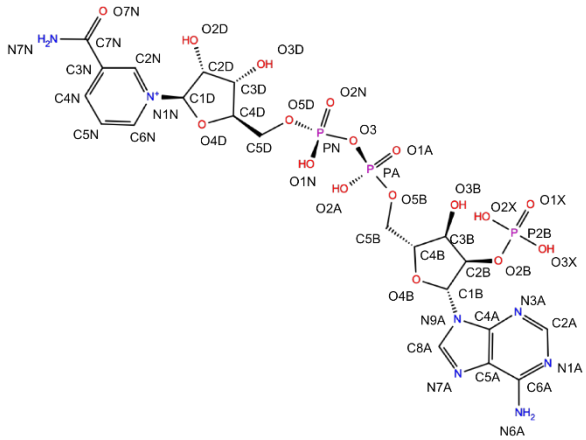

	R132H, Å		R132Q, Å		R132L, Å		R132, Å	
	Mon1	**Mon2**	**Mon1**	**Mon2**	**Mon1**	**Mon2**	**Mon1**	**Mon2**
C4B	4.232	4.949	3.601	4.334	3.611	4.924	4.496	4.187
H4B	4.201	4.779	3.657	4.388	3.732	4.972	4.693	4.322
O4B	4.101	5.036	3.526	4.462	3.52	5.045	4.445	4.241
C1B	4.258	5.415	3.633	4.695	3.795	5.405	4.815	4.537
H1B	4.361	5.586	3.796	4.897	3.875	5.534	5.137	4.755
C5A	4.804	5.977	3.913	4.705	4.184	5.766	4.668	4.788
N7A	4.753	5.866	3.673	4.625	3.975	5.442	4.778	4.8
C8A	4.477	5.638	3.517	4.598	3.758	5.276	4.732	4.694
H8A	4.489	5.543	3.393	4.589	3.597	5.078	4.883	4.879
N9A	4.37	5.604	3.657	4.652	3.853	5.464	4.685	4.555
N1A	5.371	6.388	4.563	4.989	4.748	6.507	4.876	5.351
C2A	5.246	6.289	4.588	5.008	4.694	6.515	5.04	5.262
H2A	5.602	6.49	4.938	5.191	4.966	6.885	5.401	5.65
N3A	4.884	6.022	4.305	4.896	4.417	6.18	4.971	4.911
C4A	4.628	5.853	3.947	4.736	4.141	5.804	4.707	4.68
C6A	5.177	6.243	4.232	4.831	4.519	6.125	4.728	5.089
N6A	5.508	6.416	4.306	4.863	4.692	6.171	4.844	5.318
H61A	5.558	6.416	4.34	4.799	4.753	6.016	4.939	5.516
H62A	5.885	6.319	4.49	5.037	4.875	6.4	5.091	5.463

Supplemental Table S5. $NADP^+$ RMSF from all-atom simulations Color scheme: ribose of adenine (green), adenine (gray), phosphates (yellow), ribose of nicotinamide (orange), nicotinamide (blue). This table was originally published in https://portlandpress.com/biochemj/article-lookup/doi/10.1042/BCJ20180424 Avellaneda Matteo, D.; Wells, G. A.; Luna, L. A.; Grunseth, A. J.; Zagnitko, O.; Scott, D. A.; Hoang, A.; Luthra, A.; Swairjo, M. A.; Schiffer, J. M.; Sohl, C. D., Inhibitor potency varies widely among tumor-relevant human isocitrate dehydrogenase 1 mutants. *Biochem J* **2018,** *475* (20), 3221-3238.

	R132H, Å		R132Q, Å		R132L, Å		R132, Å	
	Mon1	Mon2	Mon1	Mon2	Mon1	Mon2	Mon1	Mon2
C2B	4.434	6.651	3.641	4.827	4.048	5.64	5.16	4.747
H2B	4.497	5.519	3.655	4.835	4.225	5.812	5.132	4.709
O2B	4.59	5.686	3.785	5.473	4.23	6.225	5.888	5.314
P2B	4.991	5.699	3.865	5.884	4.568	6.73	6.54	5.682
O1X	5.331	6.213	4.288	5.98	4.964	7.18	7.137	6.006
O2X	5.183	6.503	4.094	6.332	4.714	6.979	6.825	5.705
O3X	5.388	6.476	4.082	6.321	4.845	6.908	6.735	6.355
HO2A	5.703	6.61	4.332	6.581	4.894	6.973	7.025	6.755
C3B	4.642	6.829	3.793	4.475	4.006	5.199	4.95	4.581
H3B	4.948	5.447	3.998	4.404	4.061	5.077	4.978	4.567
O3B	5.036	5.825	4.058	4.638	4.422	5.42	5.446	4.95
HO3A	5.294	5.612	4.353	4.849	4.587	5.714	5.866	5.312
C5B	4.244	5.806	3.533	4.126	3.34	4.647	4.189	3.788
H51A	4.391	4.797	3.58	4.098	3.462	4.525	4.404	3.896
H52A	4.148	4.721	3.534	4.138	3.2	4.648	4.137	3.768
PA	4.522	4.681	3.65	4.029	3.14	4.692	4.134	3.457
O1A	4.956	5.342	4.25	4.637	3.009	5.25	4.621	3.505
O2A	4.668	5.795	3.872	4.016	3.233	4.784	4.119	3.485
O5B	4.426	5.699	3.625	4.104	3.377	4.718	4.19	3.645
O3	4.435	5.115	3.543	4.054	3.534	4.582	4.246	3.718
PN	4.487	5.041	3.598	4.003	3.536	4.501	4.393	3.741
O1N	4.38	5.155	3.459	3.695	3.355	4.354	4.336	3.721
O2N	4.616	5.37	3.968	4.329	3.765	4.836	4.76	4.228
O5D	4.792	5.194	3.774	4.187	3.931	4.479	4.52	3.586
C5D	5.266	5.161	4.003	4.595	4.314	4.772	4.939	3.825
H51N	5.369	5.196	4.126	4.687	4.395	4.932	4.99	3.882

Supplemental Table S5. $NADP^+$ RMSF from all-atom simulations Color scheme: ribose of adenine (green), adenine (gray), phosphates (yellow), ribose of nicotinamide (orange), nicotinamide (blue). This table was originally published in https://portlandpress.com/biochemj/article-lookup/doi/10.1042/BCJ20180424 Avellaneda Matteo, D.; Wells, G. A.; Luna, L. A.; Grunseth, A. J.; Zagnitko, O.; Scott, D. A.; Hoang, A.; Luthra, A.; Swairjo, M. A.; Schiffer, J. M.; Sohl, C. D., Inhibitor potency varies widely among tumor-relevant human isocitrate dehydrogenase 1 mutants. *Biochem J* **2018,** *475* (20), 3221-3238.

	R132H, Å		R132Q, Å		R132L, Å		R132, Å	
	Mon1	Mon2	Mon1	Mon2	Mon 1	Mon 2	Mon1	Mon2
H52N	5.427	5.29	4.202	4.739	4.468	4.989	5.298	4.215
C2D	5.4	5.208	3.748	4.632	4.408	4.639	5.007	3.771
H2D	5.015	5.04	3.623	4.342	4.101	4.471	4.674	3.823
O2D	5.718	4.912	3.863	4.814	4.623	4.837	5.417	3.972
HO2N	5.627	5.074	3.945	4.869	4.71	5.179	5.447	4.155
C3D	5.736	5.129	3.99	4.902	4.662	4.811	5.427	4.076
H3D	5.642	5.13	4.048	4.812	4.572	4.831	5.497	4.308
O3D	6.344	5.031	4.227	5.34	5.101	5.043	6.074	4.554
HO3N	6.383	5.314	4.115	5.254	5.114	4.899	6.372	4.943
C1D	5.406	5.191	3.736	4.669	4.474	4.642	4.837	3.514
H1D	5.785	5.174	3.898	4.96	4.799	4.875	5.273	3.629
C4D	5.615	5.28	4.016	4.853	4.598	4.823	5.178	3.867
C4D	5.615	5.215	4.258	5.18	4.902	5.123	5.577	4.237
H4D	6.018	5.321	3.871	4.735	4.534	4.698	4.907	4.237
O4D	5.477	5.261	3.871	4.735	4.534	4.698	4.907	3.587
N1N	5.04	5.147	3.545	4.362	4.193	4.457	4.328	3.466
C6N	4.692	5.02	3.46	4.026	3.85	4.177	3.846	3.431
HN6	4.68	4.952	3.564	3.981	3.768	4.109	3.864	3.409
C5N	4.513	5.04	3.35	3.814	3.686	4.082	3.597	3.641
H5N	4.416	4.984	3.367	3.602	3.466	3.914	3.47	3.702
C4N	4.628	5.2	3.327	3.952	3.885	4.313	3.793	3.993
H41N	4.569	5.26	3.303	3.843	3.842	4.316	3.761	4.395
C3N	4.983	5.342	3.457	4.304	4.212	4.649	4.287	3.993
C2N	5.202	5.312	3.553	4.495	4.356	4.692	4.554	3.672
H2N	5.624	5.473	3.73	4.816	4.673	5.002	5.1	3.755
C7N	5.281	5.596	3.634	4.538	4.49	5.045	4.744	4.56
O7N	5.752	5.863	3.988	4.998	4.849	5.504	5.393	4.793
N7N	5.186	5.61	3.642	4.351	4.438	5.06	4.663	5.077
H71N	4.966	5.748	3.629	4.22	4.276	5.19	4.643	5.124
H72N	5.479	5.754	3.834	4.545	4.659	5.319	5.03	5.478
Average	5.02481	5.53124	3.8577	4.6703	4.2014	5.2196	4.9407	4.444
STD	0.55	0.52	0.34	0.58	0.53	0.77	0.75	0.76

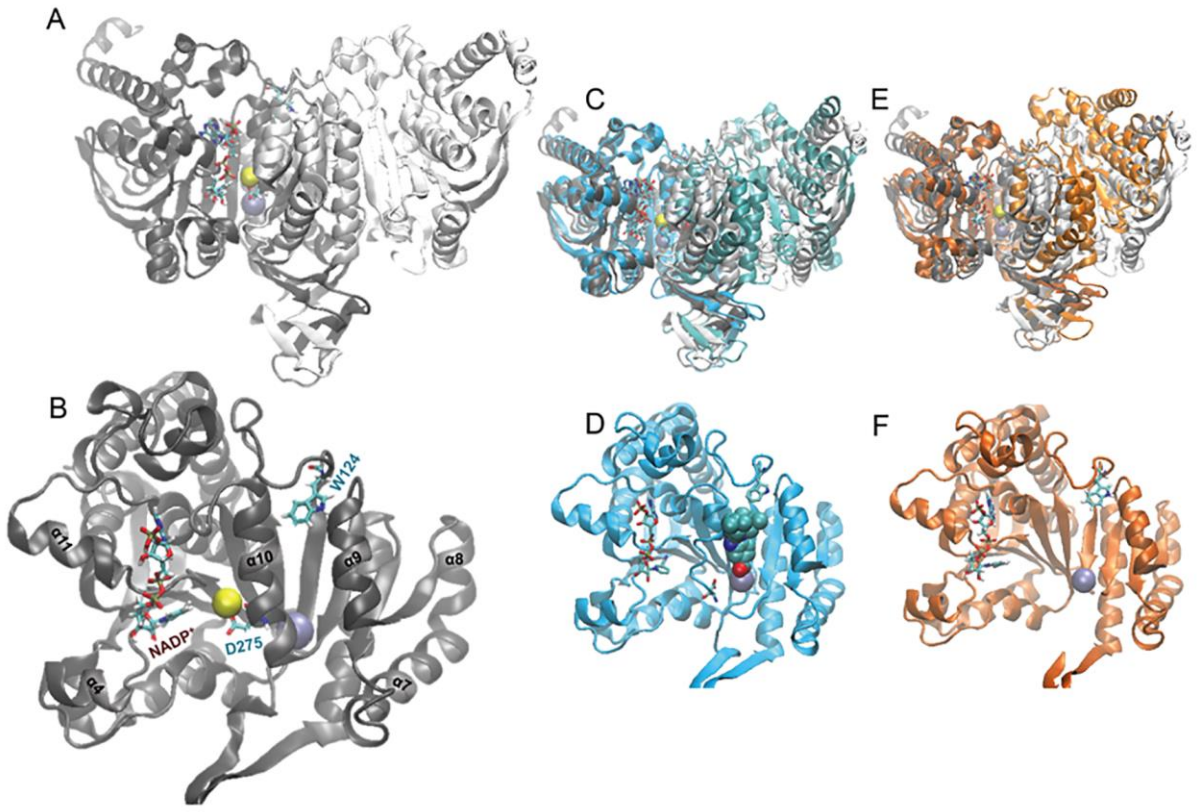

Supplemental Figure S1. A comparison of previously solved structures of WT and mutant IDH1 bound to $NADP^+$ used in MD simulations. The structure of IDH1 bound to $NADP^+$ used here for MD simulations (PDB 4KZO[31]) is shown for both dimers **A.** and as monomeric secondary structure units **B.**. Structures were aligned to monomer A (left monomer in gray). In both panels, the C_α carbon of residue 132 is shown as a sphere (ice blue), as is Ca^{2+} (yellow). The residues W124, D275, and $NADP^+$ are shown as licorice with the carbon in cyan, the oxygen in red, the phosphorus is gold, nitrogen in blue, and hydrogen in white. The helices that are discussed in the text are labeled as indicated previously. **C.** The structure of IDH1 bound to $NADP^+$ versus the structure of IDH1 R132H bound to an analogue of BAY 1436032 (PDB 5LGE) is shown. **D.** The secondary structure units of IDH1 R132H bound to the inhibitor described in (C) is displayed in its monomeric form. **E.** The structure of IDH1 bound to $NADP^+$ versus the structure of IDH1 R132H bound to the inhibitor IDH146 (PDB 5SUN) is shown. **F.** The structure of the monomeric secondary structure units of IDH1 R132H bound to NADPH is displayed. This figure was originally published in https://portlandpress.com/biochemj/article-lookup/doi/10.1042/BCJ20180424 Avellaneda Matteo, D.; Wells, G. A.; Luna, L. A.; Grunseth, A. J.; Zagnitko, O.; Scott, D. A.; Hoang, A.; Luthra, A.; Swairjo, M. A.; Schiffer, J. M.; Sohl, C. D., Inhibitor potency varies widely among tumor-relevant human isocitrate dehydrogenase 1 mutants. *Biochem J* **2018,** *475* (20), 3221-3238.

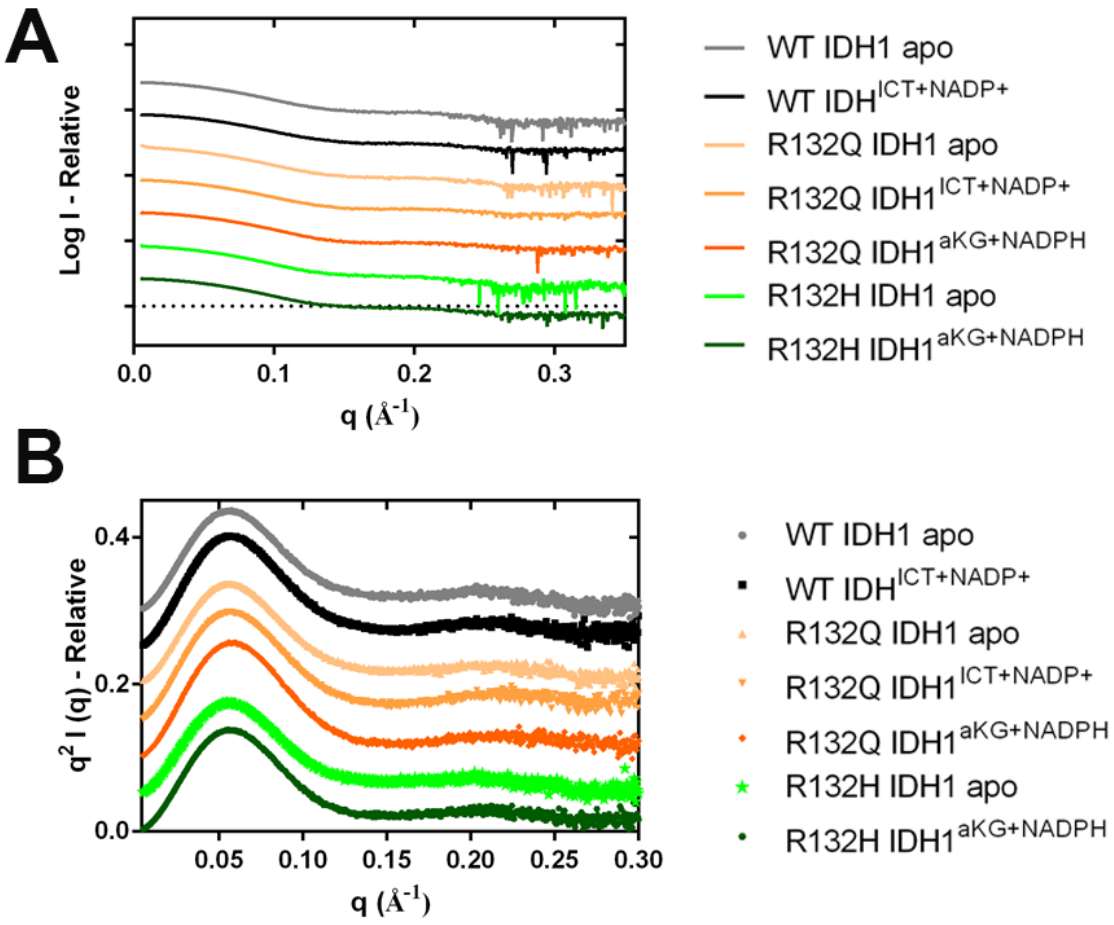

Supplemental Figure S2. Small angle X-ray scattering (SAXS) data for apo and ligand-bound forms of WT and mutant IDH1. **A.** Experimental scattering curves for WT IDH1^{apo} (grey), WT IDH1$^{ICT\ and\ NADP+}$ (black), R132Q IDH1^{apo} (light orange), R132Q IDH1$^{ICT\ and\ NADP+}$ (orange), R132Q IDH1$^{\alpha KG\ and\ NADPH}$ (dark orange), R132H IDH1^{apo} (light green), and R132H IDH1$^{\alpha KG\ and\ NADPH}$ (dark green). **B.** Kratky plots derived from SAXS data. The color scheme of graphs is identical to those used in panel (A). This figure was originally published in https://portlandpress.com/biochemj/article-lookup/doi/10.1042/BCJ20180424 Avellaneda Matteo, D.; Wells, G. A.; Luna, L. A.; Grunseth, A. J.; Zagnitko, O.; Scott, D. A.; Hoang, A.; Luthra, A.; Swairjo, M. A.; Schiffer, J. M.; Sohl, C. D., Inhibitor potency varies widely among tumor-relevant human isocitrate dehydrogenase 1 mutants. *Biochem J* **2018,** *475* (20), 3221-3238.

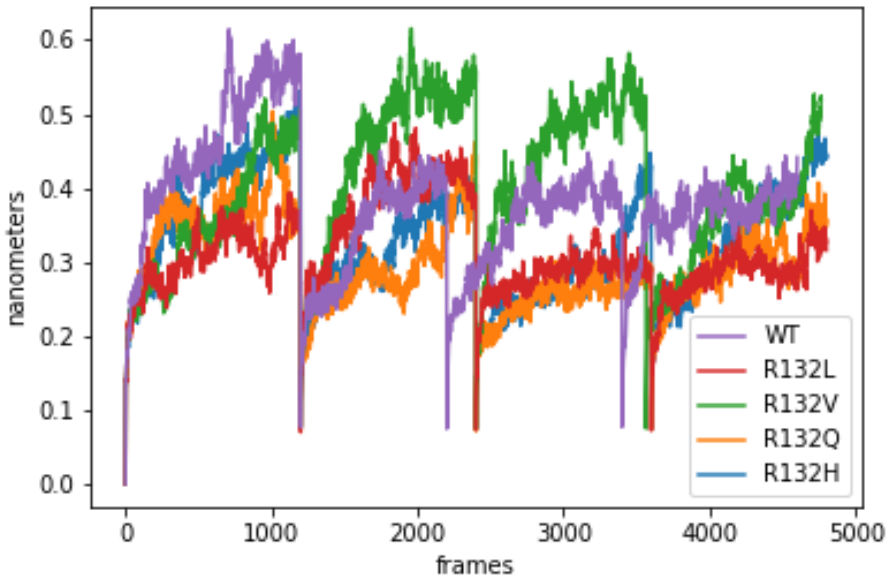

Supplemental Figure S3. RMSD analysis of IDH1 simulations**.** The RMSD over time for all five systems studied (WT IDH1 in purple, R132L IDH1 in red, R132V IDH1 in green, R132Q IDH1 in orange, and R132H IDH1 in blue) are shown across frames for all four replicates. WT, R132L, R132Q and R132H IDH1 follow similar trajectories, reaching equilibrium by the end of the frame. This Figure was originally published in https://portlandpress.com/biochemj/article-lookup/doi/10.1042/BCJ20180424 Avellaneda Matteo, D.; Wells, G. A.; Luna, L. A.; Grunseth, A. J.; Zagnitko, O.; Scott, D. A.; Hoang, A.; Luthra, A.; Swairjo, M. A.; Schiffer, J. M.; Sohl, C. D., Inhibitor potency varies widely among tumor-relevant human isocitrate dehydrogenase 1 mutants. *Biochem J* **2018,** *475* (20), 3221-3238.

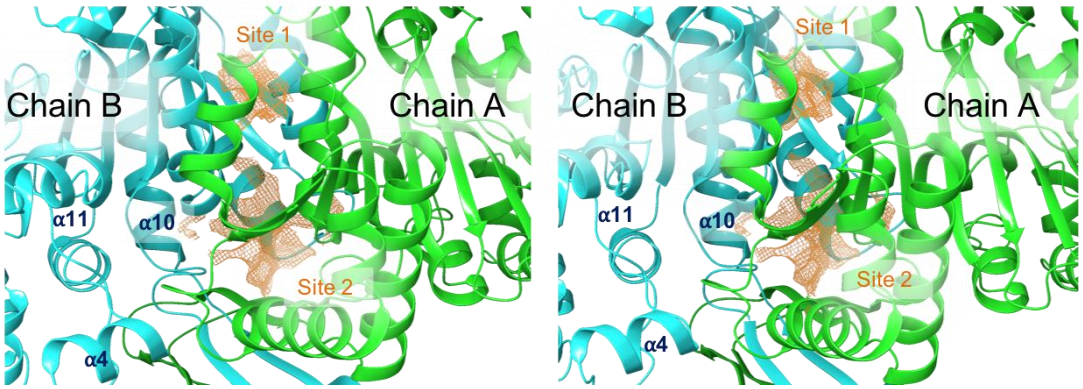

Supplemental Figure S4. Buried cavity shape of crystal structures. Two small, solvent-inaccessible pockets located between the α9 and α10 helices are highlighted as Site 1 and Site 2 in the previously solved crystal structures of PDB 4KZO. Images are taken from two slightly different angles. This figure was originally published in https://portlandpress.com/biochemj/article-lookup/doi/10.1042/BCJ20180424 Avellaneda Matteo, D.; Wells, G. A.; Luna, L. A.; Grunseth, A. J.; Zagnitko, O.; Scott, D. A.; Hoang, A.; Luthra, A.; Swairjo, M. A.; Schiffer, J. M.; Sohl, C. D., Inhibitor potency varies widely among tumor-relevant human isocitrate dehydrogenase 1 mutants. *Biochem J* **2018,** *475* (20), 3221-3238.

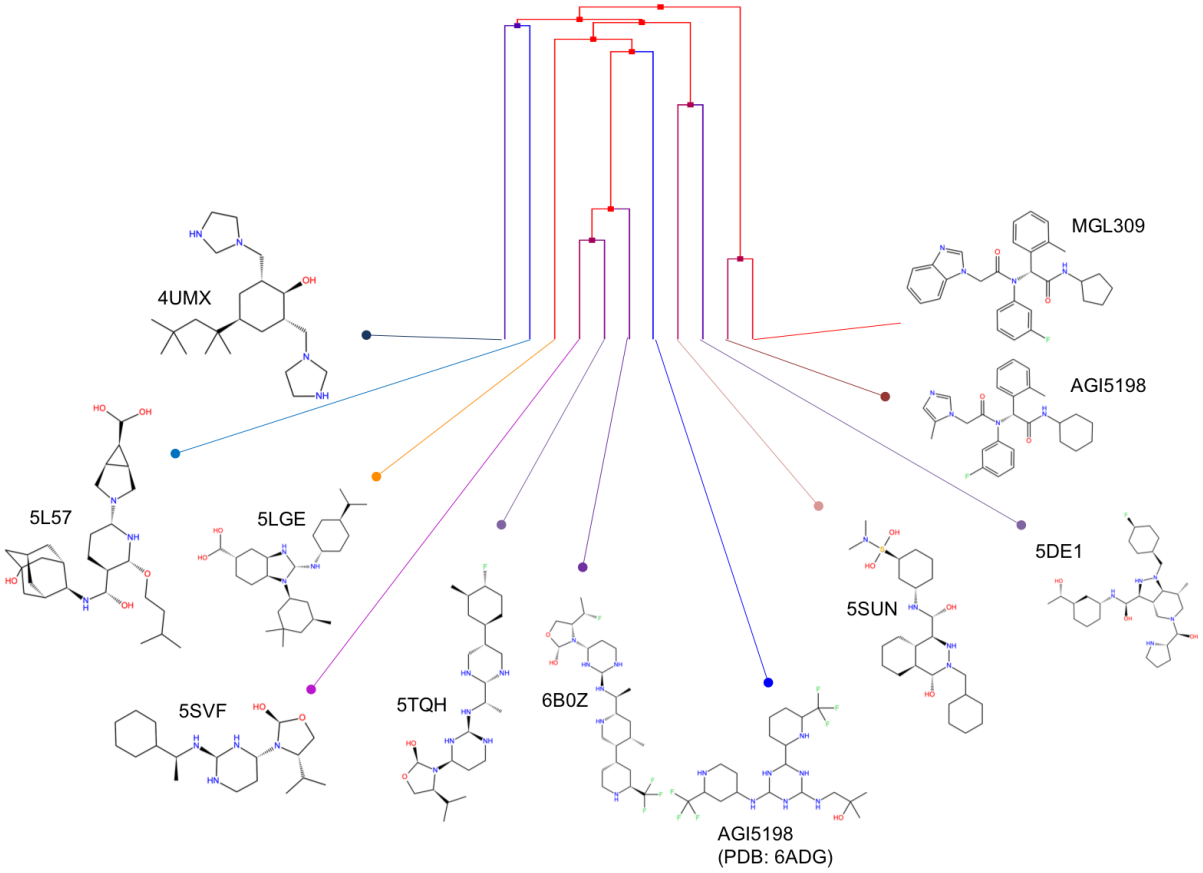

Supplementary Figure S5. Clustering of IDH1/2 Inhibitors based on linear fingerprints of each structure**.** Hierarchical clustering results performed within Canvas on the linear fingerprints of inhibitors known to bind to IDH1 from X-ray crystallography or of inhibitors used in this study. The inhibitors described in this work were grouped into their own hierarchical cluster separate from the crystallized inhibitors. This figure was originally published in https://portlandpress.com/biochemj/article-lookup/doi/10.1042/BCJ20180424 Avellaneda Matteo, D.; Wells, G. A.; Luna, L. A.; Grunseth, A. J.; Zagnitko, O.; Scott, D. A.; Hoang, A.; Luthra, A.; Swairjo, M. A.; Schiffer, J. M.; Sohl, C. D., Inhibitor potency varies widely among tumor-relevant human isocitrate dehydrogenase 1 mutants. *Biochem J* **2018,** *475* (20), 3221-3238.

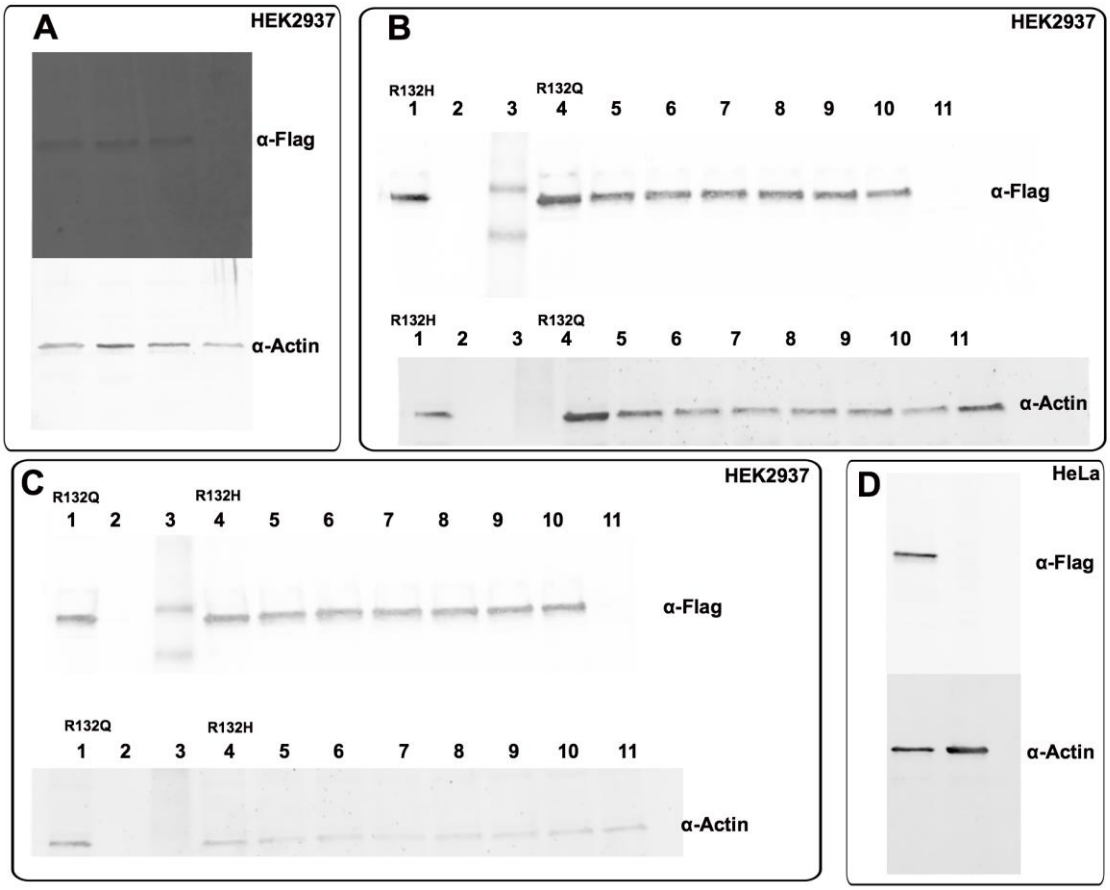

Supplemental Figure S6. Levels of transient overexpression of R132H and R132Q IDH1 in HEK293T cells vary within 2.6-fold. **A.**Transient transfection of WT IDH1 (lane 1), R132Q IDH1 (lane 2), R132H IDH1 (lane 3) all containing a Flag-tag, and a non-transfected HEK239T control. Whole cell lysates of HEK293T cells transiently transfected with R132Q or R132H IDH1 were loaded as follows: **B.** 1. R132H; 2. Empty; 3. Ladder; 4. R132Q; 5. R132Q + 20 nM AGI-5198; 6. R132Q + 40 nM AGI-5198; 7. R132Q + 90 nM AGI-5198; 8. R132Q + 180 nM AGI-5198; 9. R132Q + 500 nM AGI-9198; 10. R132Q + 3,000 nM AGI-5198; 11. Non-transfected control. **C.** 1. R132Q; 2. Empty; 3. Ladder; 4. R132H; 5. R132H + 20 nM AGI-5198; 6. R132H + 40 nM AGI-5198; 7. R132H + 90 nM AGI-5198; 8. R132H + 180 nM AGI-5198; 9. R132H + 500 nM AGI-9198; 10. R132H + 3,000 nM AGI-5198; 11. Non-transfected control. Upon normalizing to actin, panel **B.** indicates R132H expression is 3.0-fold higher than R132Q IDH1, and panel **C.** indicates that R132H IDH1 is 2.3-fold higher than R132Q IDH1. Thus, we took the average of these two values (3.0 and 2.3) to calculate that R132H IDH1 has 2.6-fold higher expression relative to R132Q IDH1 expression. **D.** Transient transfection of HeLa cells with R132Q IDH1 is also shown. Lane one shows the R132Q IDH1 transfection (Flag-tagged), and lane 2 shows a non-transfected HeLa control. This figure was originally published in https://portlandpress.com/biochemj/article-lookup/doi/10.1042/BCJ20180424 Avellaneda Matteo, D.; Wells, G. A.; Luna, L. A.; Grunseth, A. J.; Zagnitko, O.; Scott, D. A.; Hoang, A.; Luthra, A.; Swairjo, M. A.; Schiffer, J. M.; Sohl, C. D., Inhibitor potency varies widely among tumor-relevant human isocitrate dehydrogenase 1 mutants. *Biochem J* **2018,** *475* (20), 3221-3238.

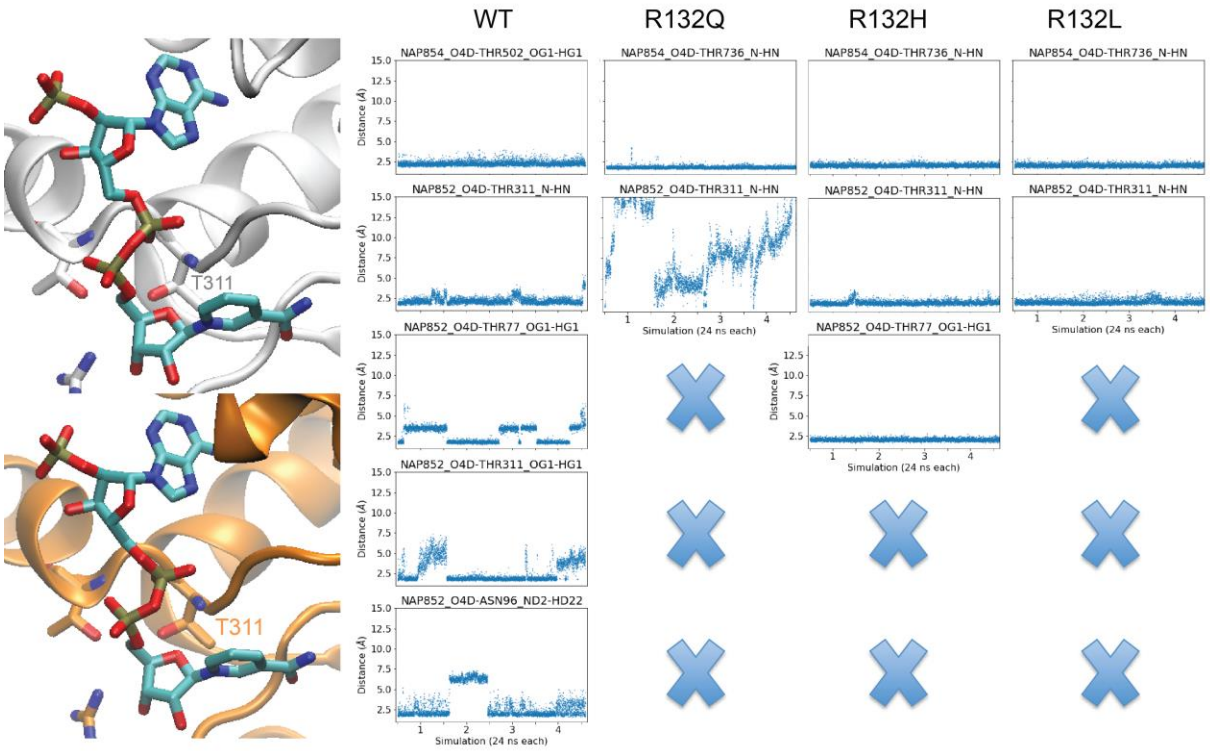

Supplemental Figure S7. Hydrogen bonding interactions between mutants and WT IDH1 and the $NADP^+$ ribose oxygen vary over MD simulations. The hydrogen bond distance between the ester oxygen of the nicotinamide riboside and neighboring threonine residues as compared to crystal structures of $NADP^+$-bound (white, top) and NADPH-bound (orange, below). This region of the molecule shows minimal differences in hydrogen bonding patterns when IDH1 is bound to $NADP^+$ versus NADPH. STable hydrogen bond interactions are shown as a constant clustering around 2.5 Å, while stochastic fluctuations show periods where hydrogen bonding is favorable or unfavorable. Hydrogen bonding that is impossible due to inappropriate bond lengths or angles are denoted as an "x" for the hydrogen bond donor/acceptor pair queried. WT IDH1 makes the most hydrogen bond interactions with the ester oxygen of the nicotinamide riboside portion of $NADP^+$, while the mutants show varying degree of hydrogen bond formation in this region. This region is likely less useful for comparing features of $NADP^+$ versus NADPH binding. This figure was originally published in https://portlandpress.com/biochemj/article-lookup/doi/10.1042/BCJ20180424 Avellaneda Matteo, D.; Wells, G. A.; Luna, L. A.; Grunseth, A. J.; Zagnitko, O.; Scott, D. A.; Hoang, A.; Luthra, A.; Swairjo, M. A.; Schiffer, J. M.; Sohl, C. D., Inhibitor potency varies widely among tumor-relevant human isocitrate dehydrogenase 1 mutants. *Biochem J* **2018,** *475* (20), 3221-3238.

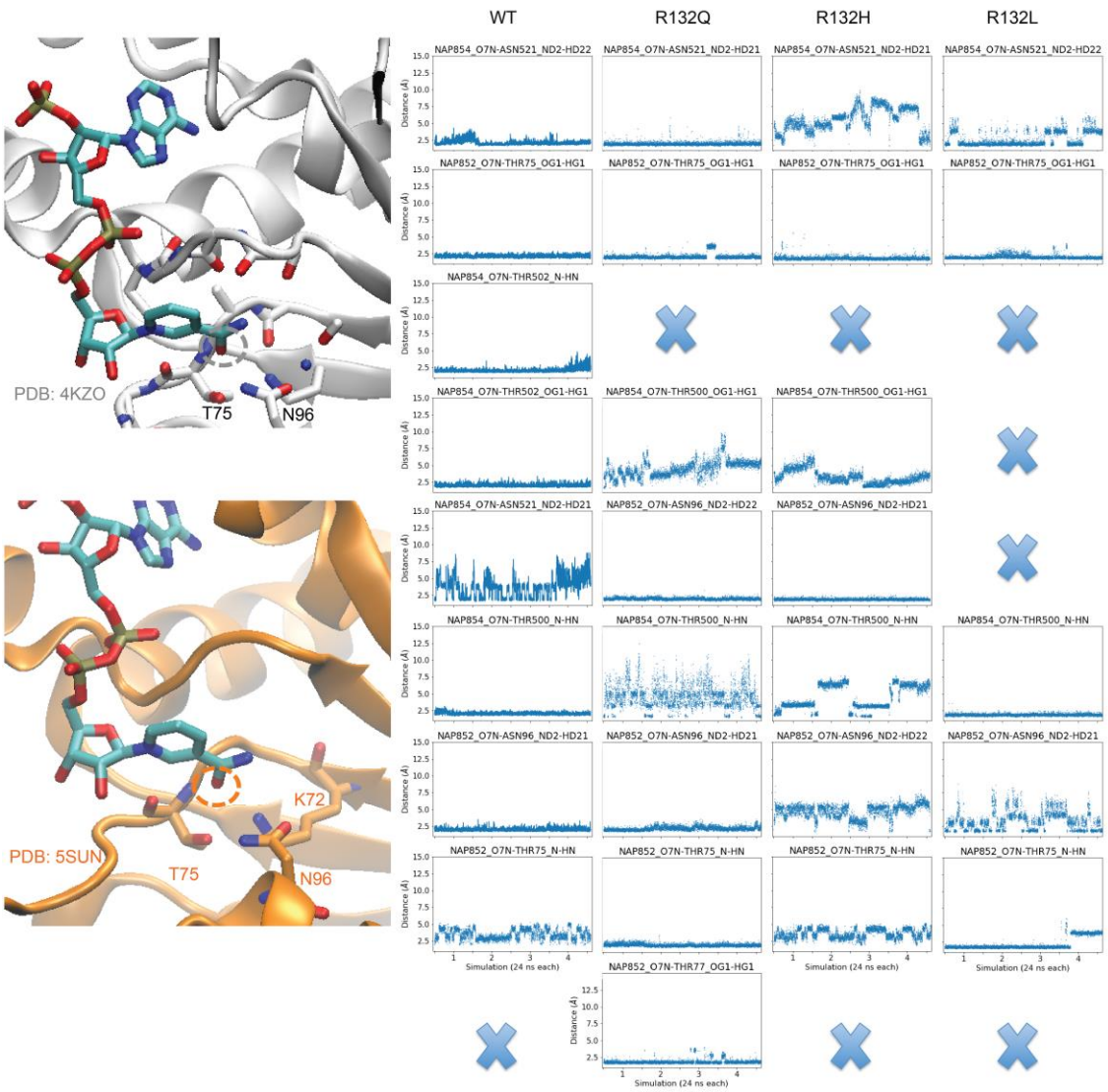

Supplemental Figure S8. Hydrogen bonding interactions between mutants and WT IDH1 and the NADP$^+$ amide oxygen vary over MD simulations. The hydrogen bond distance between the amide oxygen of the nicotinamide and neighboring threonine and arginine residues as compared to crystal structures of NADP$^+$-bound (white, top) and NADPH-bound (orange, below). This region of the molecule shows differences in hydrogen bonding patterns when IDH1 is bound to NADP$^+$ versus NADPH, indicating that this region is a good differentiator between NADP$^+$ versus NADPH binding. STable hydrogen bond interactions are shown as a constant clustering around 2.5 Å, while stochastic fluctuations show periods where hydrogen bonding is favorable or unfavorable. Hydrogen bonding that is impossible due to inappropriate bond lengths or angles are denoted as an "x" for the hydrogen bond donor/acceptor pair queried. Here, R132L IDH1 has the fewest hydrogen bonds in the amide oxygen of the nicotinamide, while WT IDH1 has the most sTable interactions. R132Q IDH1 has the largest number of sTable hydrogen bonding interactions of all the mutants. This figure was originally published in https://portlandpress.com/biochemj/article-lookup/doi/10.1042/BCJ20180424 Avellaneda Matteo, D.; Wells, G. A.; Luna, L. A.; Grunseth, A. J.; Zagnitko, O.; Scott, D. A.; Hoang, A.; Luthra, A.; Swairjo, M. A.; Schiffer, J. M.; Sohl, C. D., Inhibitor potency varies widely among tumor-relevant human isocitrate dehydrogenase 1 mutants. *Biochem J* **2018,** *475* (20), 3221-3238.

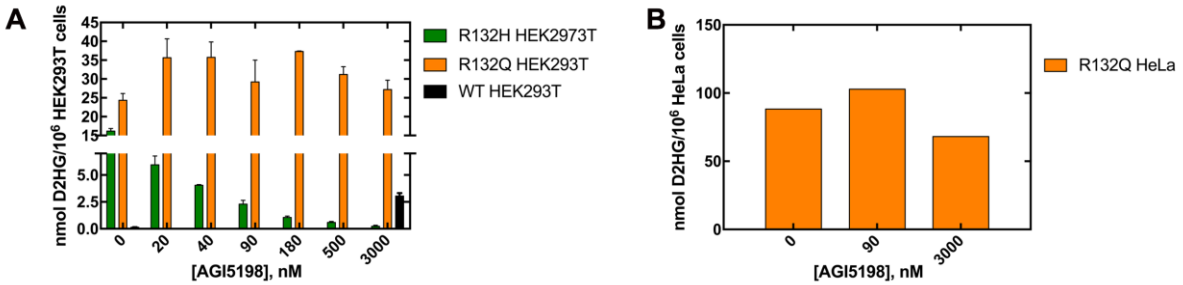

Supplemental Figure S9. AGI-5198 does not effectively inhibit R132Q IDH1. **A.** Quantitation (in duplicate) of D2HG in lysates of HEK2937 cells transiently transfected with R132H, R132Q, or WT and treated with AGI-5198 is shown. These data were used to calculate IC_{50} values shown in Figure 5. **B.** Quantitation (in singlicate) of D2HG in lysates of HeLa cells transiently transfected with R132Q IDH1 and treated with AGI-5198 is shown; only a subset of inhibitor concentrations were used. This figure was originally published in https://portlandpress.com/biochemj/article-lookup/doi/10.1042/BCJ20180424 Avellaneda Matteo, D.; Wells, G. A.; Luna, L. A.; Grunseth, A. J.; Zagnitko, O.; Scott, D. A.; Hoang, A.; Luthra, A.; Swairjo, M. A.; Schiffer, J. M.; Sohl, C. D., Inhibitor potency varies widely among tumor-relevant human isocitrate dehydrogenase 1 mutants. *Biochem J* **2018,** *475* (20), 3221-3238.

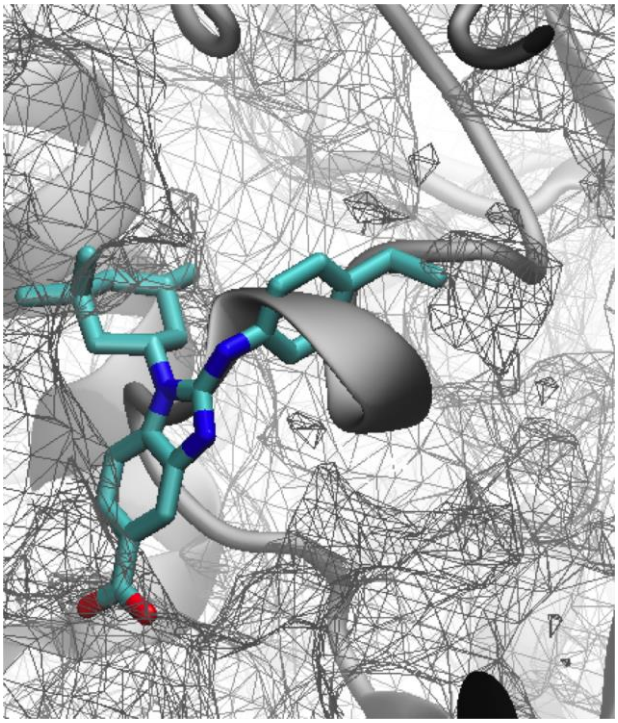

Supplemental Figure S10. Average buried cavity in the apo WT IDH1 simulation. An analogue of the inhibitor BAY1436032 from PDB 5LGE[53] is overlaid with the apo WT IDH1 simulations, which start from PDB 1T09[24]. This figure was originally published in https://portlandpress.com/biochemj/article-lookup/doi/10.1042/BCJ20180424 Avellaneda Matteo, D.; Wells, G. A.; Luna, L. A.; Grunseth, A. J.; Zagnitko, O.; Scott, D. A.; Hoang, A.; Luthra, A.; Swairjo, M. A.; Schiffer, J. M.; Sohl, C. D., Inhibitor potency varies widely among tumor-relevant human isocitrate dehydrogenase 1 mutants. *Biochem J* **2018,** *475* (20), 3221-3238.

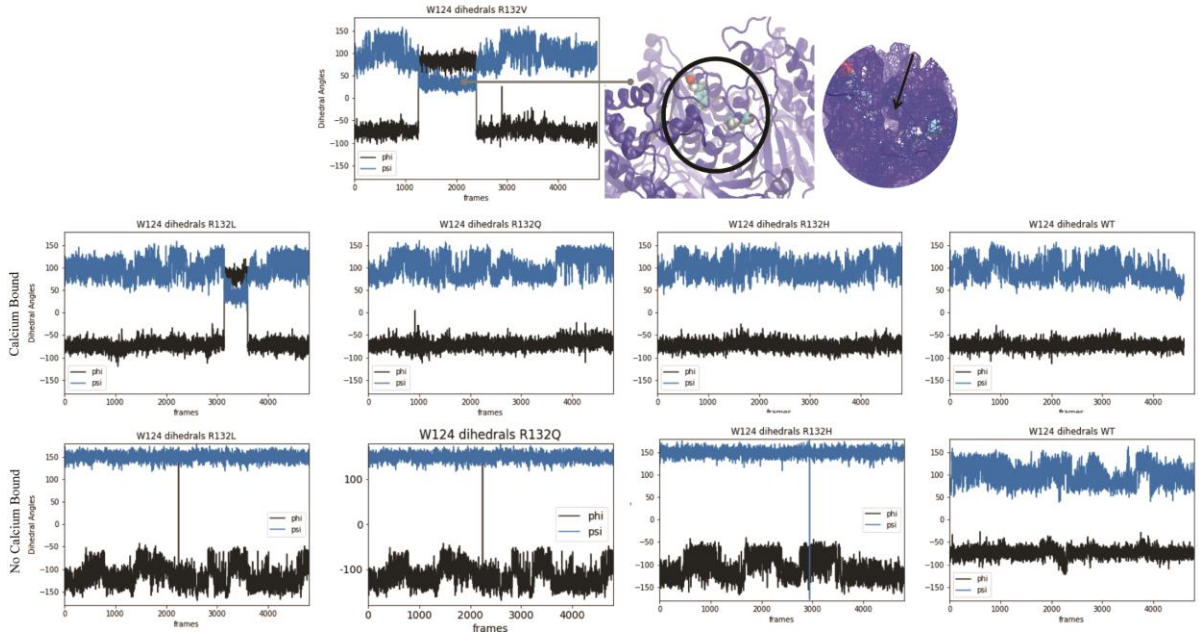

Supplementary Figure S11. Changes in the dihedral angle of residue W124 and the effects on an exposed buried cavity. The dihedral angle changes for residue W124, which sits on top of the buried cavity at the dimer interface, are shown. In the R132L and R132V IDH1 simulations, one of four trajectories results in flipping of W124 and exposure of the buried cavity to a small pocket opening as depicted. The psi angle changes are shown in blue while the phi angle changes are shown in black. This figure was originally published in https://portlandpress.com/biochemj/article-lookup/doi/10.1042/BCJ20180424 Avellaneda Matteo, D.; Wells, G. A.; Luna, L. A.; Grunseth, A. J.; Zagnitko, O.; Scott, D. A.; Hoang, A.; Luthra, A.; Swairjo, M. A.; Schiffer, J. M.; Sohl, C. D., Inhibitor potency varies widely among tumor-relevant human isocitrate dehydrogenase 1 mutants. *Biochem J* **2018,** *475* (20), 3221-3238.

3.8. Acknowledgement

Chapter 3 is reproduced and re-written in full with permission from Avellaneda Matteo, D.; Wells, G. A.; Luna, L. A.; Grunseth, A. J.; Zagnitko, O.; Scott, D. A.; Hoang, A.; Luthra, A.; Swairjo, M. A.; Schiffer, J. M.; Sohl, C. D., Inhibitor potency varies widely among tumor-relevant human isocitrate dehydrogenase 1 mutants. *Biochem J* **2018,** *475* (20), 3221-3238.

Dr. Jamie Schiffer performed the MD simulation computational experiments. Grace Wells performed cell culture and cellular inhibition assays. Dr. David Scott and Olga Zagnitko performed D2HG quantifications. Dr. Manal Swairjo and Dr. Amit Luthra performed SAXS experiments.

4. Using Pre-Steady-State Kinetics, Biochemical, and Biophysical Approaches to Determine a Comprehensive Catalytic Cycle for D2HG Catalysis by Tumor-Relevant IDH1 Mutants Revealed Kinetic Features Driving Neomorphic Activity

4.1. Abstract

Mutations in the IDH1 gene drive several cancers including gliomas, AML, and chondrosarcomas. IDH1 is a dimeric metabolic enzyme responsible for the reversible $NADP^+$-dependent oxidative decarboxylation of isocitrate to αKG in the cytosol and peroxisomes. Most tumor-relevant IDH1 mutants lack this oxidative decarboxylation activity but instead gain a neomorphic reaction: the reduction of αKG to D2HG. D2HG acts as an oncometabolite since it competitively inhibits αKG-dependent enzymes, including DNA and histone demethylases, to promote cell dedifferentiation and other pro-tumor pathways. We have previously shown that R132Q IDH1 is the only mutant found to date that conserves oxidative decarboxylation activity while catalyzing very highly efficient D2HG production. Moreover, this mutant has very low affinity for selective mutant IDH1 inhibitors. In this chapter, we used pre-steady-state kinetics as well as other biochemical and biophysical methods such as hydrogen-deuterium exchange (HDX-MS) and isothermal titration calorimetry (ITC), to characterize the catalytic cycle of the neomorphic reaction. R132Q IDH1 has high affinity for NADPH raising the question if the $NADP^+$-dependent αKG production is physiological relevant. Moreover, the rate of αKG binding to R132Q IDH1 was two orders of magnitude faster than R132H IDH1, suggesting difference in binding mechanism. HDX-MS data showed a large difference of deuterium uptake by WT IDH1 upon isocitrate binding, though a small difference for R132H IDH1 binding to αKG was observed. Hydride transfer was determined to be rate-limiting, consistent with findings with IDH found in *E. coli* IDH1. This work provides an extensive catalytic cycle for D2HG production by mutant

IDH1, revealing key kinetic features that may explain important mechanistic differences among WT, R132H, and R132Q IDH1.

4.2. Introduction

Changes in tumor metabolism was first described by Otto Warburg in the early 1900s[1, 2], though nearly a century passed before any metabolic enzymes were identified as drivers of tumorigenesis and tumor growth. An example of a metabolic enzyme that alters tumor metabolism is isocitrate dehydrogenase I (IDH1). The family of isocitrate dehydrogenases have three isoforms (IDH1, IDH2, and IDH3). IDH1 is responsible for the reversible-$NADP^+$ and Mg^{2+}-dependent oxidative decarboxylation of isocitrate to αKG in the cytosol and peroxisomes of the cell[3-5] (Figure 1A). IDH2 catalyzes the same reaction as IDH1, but it is located in the mitochondria[6]. IDH3, also located in the mitochondria, requires NAD^+ for the irreversible production of αKG from isocitrate. While mutations in IDH2, like IDH1 are oncogenic, IDH3 has not been implicated in cancer, likely due to its critical role in the TCA cycle. The incidence of mutations in IDH1 in tumors was not discovered until 2008[7].

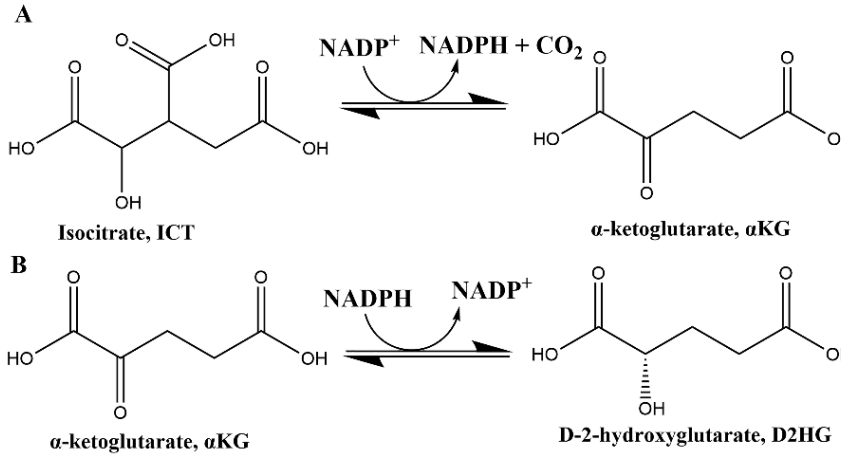

Figure 1. A. Reversible oxidative decarboxylation of isocitrate to αKG by WT IDH1. **B**. Reduction of αKG to D2HG by mutant IDH1

Parsons and colleagues discovered that mutations in the IDH1 gene were common within patients harboring GBMs[7]. Later, it was described that mutations in the IDH1 gene mostly affected residue R132 in patients with gliomas[8]. The frequency of mutations at position R132 was as high as 80% in lower grade gliomas and > 88% in secondary glioblastomas[8, 9]. The most common mutation seen in gliomas is R132H, although other mutations such as R132C, R132S, R132G, R132L, and R132V IDH1 are also observed[8]. IDH1 mutations are also associated with cancers including AML and chondrosarcomas, with R132C IDH1 being the most common in AML[10]. In chondrosarcomas, a small study showed half of the patients harboring IDH1 mutations, including 5% R132Q, R132L, and R132H IDH1 each, with R132C and R132G IDH1 representing the rest at 60% and 25%, respectively[11].

When IDH1 is mutated at R132, the ability to catalyze the oxidative decarboxylation of isocitrate is lost, but a neomorphic reaction is gained[12]. This neomorphic reaction is the NADPH-and-Mg^{2+}-dependent reduction of αKG to D-2-hydroxyglutarate (D2HG)[12] (Figure 1B). The oncometabolite D2HG acts as a competitive inhibitor to many αKG-dependent enzymes, such as JmjC lysine demethylases and methylcytosine dioxygenases, leading to gene hypermethylation that causes cellular de-differentiation[13, 14]. As a result of this neomorphic reaction, tumors harboring IDH1 mutation have buildup of tumor D2HG[15]. Pusch and colleagues quantified D2HG levels in tumors harboring R132H, R132C, R132G, and WT IDH1[15] and found the concentration of D2HG varied depending on the mutation present. In 2017, our laboratory performed an extensive steady-state kinetic analysis on many tumor-relevant IDH1 mutants, and we showed that the catalytic efficiencies for R132H, R132C, and R132G IDH1 correlated with the trends of D2HG levels in tumors reported by Pusch et al[4]. To identify the features that supported catalytically efficient D2HG catalysis, series of experimental IDH1 mutants were created to explore the effect

in size and hydrophobicity at residue R132[4]. We found that smaller and more hydrophobic residues tend to drive the neomorphic reaction[4]. Another major discovery was the dual enzymatic activity (αKG and D2HG production) catalyzed by R132Q IDH1[4].

In 2018, we expanded our kinetic work on additional tumor-relevant IDH1 R132 mutants[16], but showed that R132Q IDH1 remained the only mutant with this dual activity. Since the structure of R132Q IDH1 had not been solved, we used molecular dynamics (MD) to generate a model of R132Q IDH1 using a previously published R132H and R132C IDH1 structures[16-18]. We then performed MD simulations to compare the structural features of R132Q, R132H, and WT IDH1. These models suggest that R132Q IDH1 rapidly fluctuates between two conformations that are either more WT-like or more mutant-like[16], providing a possible explanation to R132Q IDH1's dual activity. However, an experimental crystal structure of R132Q IDH1 is critical in order to validate the previous MD findings. Extensive research has been done on IDH1, and it has become a therapeutic target due to high selectivity achieved by small molecules inhibitors to mutant IDH1 enzymes.

Inhibitor selectivity is always desired when designing small molecules for targeted therapeutics to minimize toxicity in patients. Many small molecule inhibitors have been designed capable of selectively inhibiting mutant IDH1 while not having affinity for WT IDH1. ML309 is an example of a small molecule inhibitor that shows IC_{50} values for R132H IDH1 to be 375-fold lower than WT IDH1[16, 19, 20]. AGI-5198 is another small molecule inhibitor for mutant IDH1 that has similar selectivity for the mutant form of IDH1[4, 20]. These inhibitors bind at the dimer interface right where the regulatory domain is located[20, 21]. In 2018, the FDA approved a mutant IDH1 inhibitor, AG-120 an optimization of AGI-5198, for non-solid tumors, which allosterically targets R132H and R132C IDH1[22]. Selective inhibition of mutant IDH1 indicates that there are key

structural changes between mutant and WT IDH1 that allow for inhibitors to be selective[21]. Most inhibitors had only been tested with R132C and R132H IDH1, but we performed an extensive inhibition studied on a wide range of mutant IDH1[16]. Our inhibition study showed that ML309 and AGI-5198 have affinity for most IDH1 mutants, except for R132Q IDH1, which had an inhibition profile similar to WT IDH1[16]. Since MD simulations suggested that R132Q IDH1 conserves WT-like conformations, possibly allowing for its dual activity, inhibitors lose affinity for mutants that have kinetic and structural features similar to WT IDH1[16]. Stablishing a catalytic cycle for D2HG production of R132Q versus R132H IDH1 may highlight kinetic differences that could explain R132Q IDH1's dual activity and its lack of affinity for small molecules inhibitors.

Rendina and colleagues first described the mechanism of substrate binding for the neomorphic reaction as ordered sequential catalyzed by R132H IDH1[17], with NADPH bindng first followed by αKG[17]. On the other hand, WT IDH1 has a random sequential mechanism for substrate binding for the normal reaction (Figure 1A)[17]. In 2010, Yang and colleagues described a conformational change in both WT and R132H IDH1 upon binding isocitrate[23]. This conformational change, which was also described in WT IDH1 in 2004[3], includes folding of the α10 helix upon binding of isocitrate (Figure 9)[3, 23]. This conformation has been observed in crystal structures of R132H IDH1 in complexed with αKG[17]. The conformational change of R132H IDH1 varies depending on whether isocitrate or αKG binds. The α10 helix in R132H IDH1 folds when αKG is the substrate but remains as a random coil when isocitrate binds[17, 23].

In 1995, a study on E.coli IDH showed that the rate limiting step of the catalytic cycle was hydride transfer k_{chem}[24, 25]. Moreover, Y139 is conserved among different organisms and it plays an important role in facilitating the acid/base chemistry performed by WT IDH1[26]. Since the C-3 carboxylate of isocitrate is missing in αKG, Y139 moves closer to αKG further promotes the

reduction of the C-2 carbonyl of αKG to produce D2HG[17]. Based on this, we hypothesized that the catalytic cycle for the conversion of αKG to D2HG consists of binding of NADPH followed by binding of αKG, as described by Rendina et al.[17]; a conformational change followed by rate-limiting hydride transfer, followed by product release (Figure 2A).

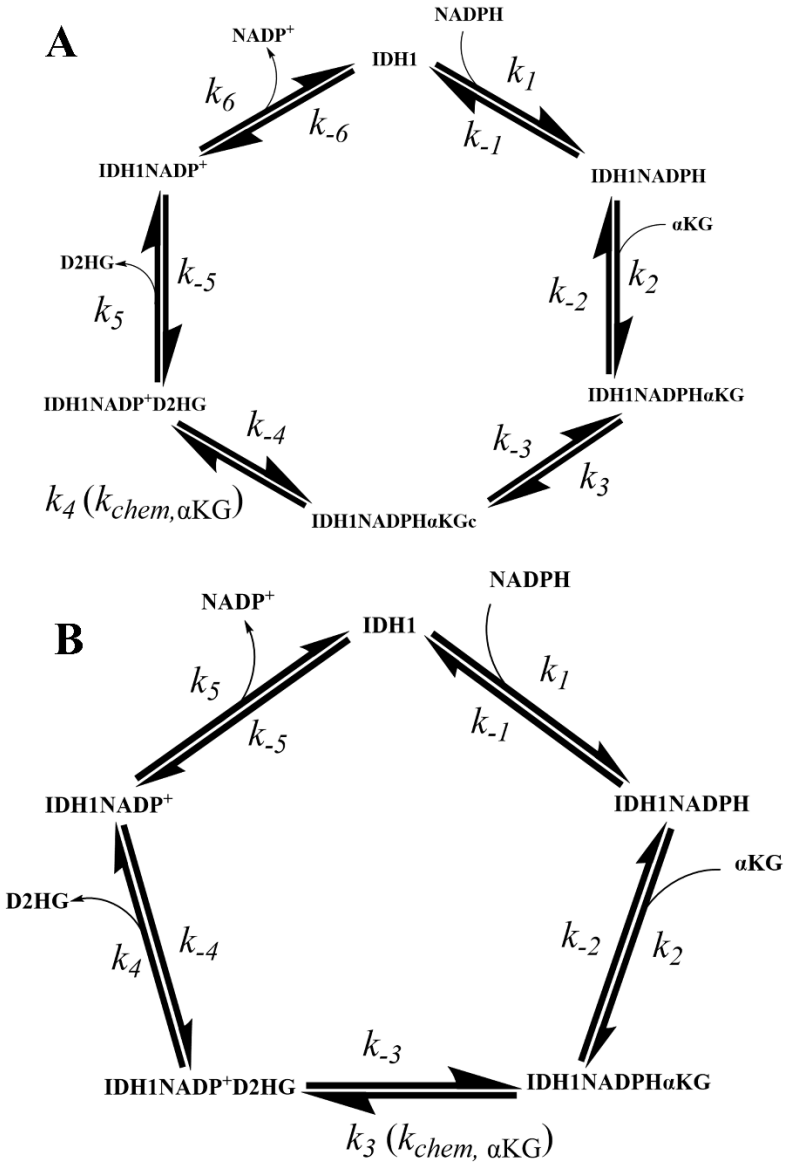

Figure 2. A. Complete catalytic cycle of mutant IDH1 producing D2HG, including conformational change. **B**. Catalytic cycle of mutant IDH1 producing D2HG without conformational change.

Understanding the complete catalytic cycle of the neomorphic reaction catalyzed by mutant IDH1 would allow us to identify key features of other metabolic dehydrogenases performing NADPH-dependent α-keto acid reduction. Moreover, this work will set the foundation for rational drug design by targeting specific steps in the catalytic cycle. We will use methods in enzymology as well as biochemistry and biophysics to elucidate features of the catalytic cycle of D2HG production. This is the first study where combining these methodologies provides important mechanistic information on the steps taken for D2HG synthesis by mutant IDH1.

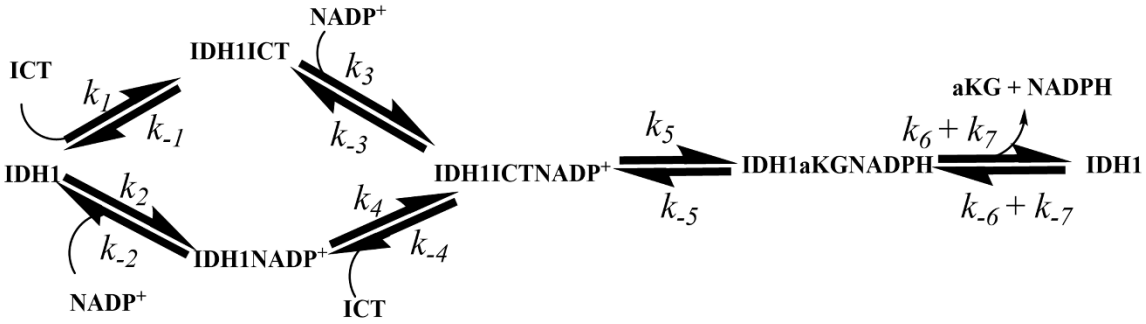

Figure 3. Catalytic cycle of the normal reaction. The binding mechanism for WT IDH1 catalyzing the oxidative decarboxylation of isocitrate to αKG is random sequential

4.3. Materials and Methods

4.3.1 Materials

Dithiothreitol (DTT), isopropyl 1-thio-β-D-galactopyranoside (IPTG), Titron X-100, α-ketoglutaric acid sodium salt (αKG), DL-isocitric acid trisodium salt hydrate, TCEP hydrochloride, sodium iodide, and magnesium chloride ($MgCl_2$) were obtained from Fisher Scientific (Hampton, NH). β-mercaptoethanol (β ME) was obtained from MP Biomedicals located in Santa Ana, CA. Both β-nicotinamide adenine dinuclotide phosphate reduced trisodium salt

(NADPH) and β-Nicotinamide adenine dinucleotide phosphate disodium salt ($NADP^+$) were obtained from EMD Millipore (Darmstadt, Germany). Nickel-nitrilotriacetic acid (Ni-NTA) resin was obtain from Qiagen (Valencia, CA). Stain free gels (4-12%) were obtained from Bio-Rad Laboratories (Hercules, CA). Protease inhibitor Tablets were obtained from Roche Applied Science (Penzberg, Germany).

4.3.2 Protein Expression and Purification

The expression and purification of R132H, R132Q, and WT IDH1 was performed as previously described in Chapter 2 and 3 of this dissertation. Briefly, the plasmids were transformed in BL21 gold (DE3) cells and incubated in TB media at 37°C until reaching an OD_{600} of 1.0-1.2. Once this OD_{600} was reached, the cultures were induced with 1mM IPT for 18-22 h at 18 °C. Each mutant IDH1 was purified with Ni-NTA affinity column chromatography yielding ~95% purity. For the NADPH binding kinetics and titrations, the enzyme was NADPH-depleted as previously published[17]. In short, for mutant IDH1 enzymes, 50mL of a solution containing 50 mM Tris-HCl pH 7.5 at ambient temperature, 500mM sodium chloride, 10mM magnesium chloride and 20mM αKG was passed through the column to react any bound NADPH to $NADP^+$. The less tightly bound $NADP^+$ was washed off with wash buffer (50 mM Tris-HCl pH 7.5 at ambient temperature, 500 mM sodium chloride, and 5 mM β-ME) previously described in Chapter 2[4]. For WT IDH1, the same solution was used instead100 mM of sodium bicarbonate was added since WT IDH1 performs the NADPH-dependent reductive carboxylation of αKG to ICT. The $NADP^+$ was washed off using wash buffer and eluted as previously described[4]. The enzymes were dialyzed overnight in 50 mM Tris-HCl pH 7.5 at 4 °C, 100mM sodium chloride, 20% glycerol, and 1 mM DTT[4].

For pre-steady state kinetic assays, protein was loaded onto a pre-equilibrated (50 mM Tris-HCl at 4°C and 100 mM sodium chloride) Superdex 16/600 size exclusion column following Ni-

NTA affinity chromatography to remove any protein aggregate. Protein was eluted with 50 mM Tris-HCl pH 7.5 at 4°C and 100mM sodium chloride. The fractions were collected and concentrated. For X-ray crystallography experiments, R132Q IDH1 was loaded to the Superdex 16/600 size exclusion column as described above to have a homogenous solution of protein. Here, R132Q IDH1 was eluted with 20 mM Tris-HCl pH 7.5 at 4 °C and 200 mM sodium chloride. Fractions were collected and concentrated to 14-20 mg/mL. For HDX-MS experiments, WT and R132H IDH1 were loaded to a Superdex 16/600 size exclusion column and eluted with 50 mM Tris-HCl pH 7.5 at 4 °C and 100 mM sodium chloride. Protein was then dialyzed (50 mM Tris-HCl pH 7.5 at 4 °C, 100mM sodium chloride, 20% glycerol, and 1 mM DTT) overnight[4]. Finally, protein used in ITC experiments was loaded into a Superdex16/600 size exclusion column after Ni-NTA affinity chromatography. Protein was eluted with 50 mM Tris-HCl pH 7.5 at 4 °C and 100 mM sodium chloride. Protein was then dialyzed into storage buffer containing 50 mM Tris-HCl pH 7.5 at 4°C, 100 mM sodium chloride, and 2 mM βME as reducing agent since it was compatible for ITC experiments. Purity of each protein prep was assessed with SDS-PAGE as described in Chapter 2.

4.3.3. NADPH Binding Kinetics

NADPH binding kinetics was performed to obtain rate constants corresponding to the first step of the catalytic cycle for the neomorphic reaction (k_1 and k_{-1}, see Figure 2). To obtain these rate constants, an RSM-stopped flow spectrophotometer (OLIS, Atlanta, Georgia) was used. The experiments were done as previously described by Rendina and colleagues[17]. However, due to low sensitivity of our stopped-flow spectrophotometer, the concentrations of NADPH and IDH1 were increased 10-fold. Unfortunately, this high concentration of NADPH yielded rates too fast to be detected by our instrument ($\leq 100\ s^{-1}$). Therefore, glycerol was used to slow down the binding of

NADPH to IDH1. Rates will thus be reported as > X s^{-1}. For WT IDH1, to slow the rate of binding of NADPH, the temperature was dropped to 10 ºC, while keeping the concentration of glycerol at 40%. Binding kinetics for R132H and R132Q IDH1 were performed at ambient temperature and at 10 ºC to have direct comparison to WT IDH1. The NADPH binding reactions at performed at ambient temperature were fit using simulation with Kintek Global Fitting Software, while the reactions at 10 ºC were fit to a single exponential using Graphpad Prism. The k_{obs} obtained from single exponential describes the equation $k_{obs} = k_1$[NADPH] + k_{-1}. Therefore, each k_{obs} value was plotted as a function of NADPH concentration. This yielded a linear graph indicating one-step bidning, with the slope equal to k_1 and the Y-intercept equal to k_{-1} (Figures 3 and 4). The NADPH binding kinetics for each mutant was performed as described in the Table below (Table 1).

Table 1. Experimental conditions of NADPH binding kinetics

Mutant and temperature	Excitation and emission wavelengths	Buffers concentration after 1:1 mixing (final concentration)	Number of points per second	Concentrations after 1:1 mixing (final concentration)	Number of shots averaged per concentration	Used in global fitting
R132Q IDH1 at ambient temperature	Ex: 340nm Scan emission: 410 to 460nm	100 mM Tris-HCl pH 8.0 RT, 40% glycerol, and 10 mM $MgCl_2$	1000	R132Q IDH1: 4μM NADPH: 4, 6, 8, 10 μM	7	Yes
R132Q IDH1 at 10ºC	Ex: 340nm Scan emission: 410 to 460nm	100 mM Tris-HCl pH 8.4 at 10ºC, 40% glycerol, and 10 mM $MgCl_2$	1000	R132Q IDH1: 4μM NADPH: 4, 6, 8, 10, 15 μM	10	No
R132H IDH1 ambient temperature	Ex: 340nm Scan emission: 410 to 460nm	100 mM Tris-HCl pH 8.0 RT, 20% glycerol, and 10 mM $MgCl_2$	1000	R132H IDH1: 4μM NADPH: 4, 6, 8, 10, 13, 15, 17 μM	10	Yes
R132H IDH1 at 10ºC	Ex: 340nm Scan emission: 410 to 460nm	100 mM Tris-HCl pH 8.4 at 10ºC, 40% glycerol, and 10 mM $MgCl_2$	1000	R132H IDH1: 4μM NADPH: 4, 6, 8, 10, 15 μM	10	No
WT IDH1 at 10ºC	Ex: 340nm Scan emission: 410 to 460nm	100 mM Tris-HCl pH 8.4 at 10ºC, 40% glycerol, and 10 mM $MgCl_2$	1000	WT IDH1: 4μM NADPH: 4, 6, 10, 15 μM	10	No

4.3.4. Isothermal Calorimetry to Determine Binding affinities for NADPH, Isocitrate, and αKG.

Due to large error in k_{off} when fitting our experimental NADPH binding data to a line, we performed ITC assays to measure the binding affinity (K_D) of NADPH for R132Q, R132H, and WT IDH1. This will allow us to solve for k_{off} ($K_D = k_{off}/k_{on}$). ITC was performed at the Sanford Burnham Prebys Protein Analysis Core, using Low Volume Affinity ITC calorimeter (TA Instruments) by Dr. Andrey Bobkov. For WT IDH1, 20 injections of 2 μL of 153 μM NADPH were titrated to 25 μM WT IDH1 at 23 ºC, for 150 s, and 200 rpm. For R132H and R132Q IDH1, 20 injections of 2.7 μL of 153 μM NADPH were titrated to 40 and 34 μM, of protein respectively, at 23 ºC, for 150 s, and 200 rpm. The ITC experiments were performed using assay buffer containing 50 mM Tris pH 7.5 at 4 °C, 100 mM NaCl, and 2 mM β-ME. Baseline control were collected by injecting ligand into the cell containing buffer only. ITC data were analyzed using Nanoanalyze software provided by TA Instrument to obtain the K_D, stoichiometry, $\Delta H_{binding}$, and -TΔS for each mutant upon binding of NADPH.

ITC titrations were performed with each IDH1 mutant to compare the binding affinities (K_D) for αKG and isocitrate. To determine the binding affinity of αKG for R132Q IDH1, 30 injections of 2 μL of 5 mM αKG were titrated to 0.12 mM of protein incubated with 0.4 mM NADPH at 25 ºC for 250 s and 200 RPM. For R132H IDH1, 20 injections of 4 μL of 10 mM αKG were titrated to 0.19 mM of protein incubated with 0.4 mM NADPH at 25 ºC for 150 s and 200 rpm. Both set of titrations were performed under assay buffer containing 50 mM Tris pH 7.5 at 4 °C , 100 mM NaCl, 10 mM $CaCl_2$, and 2 mM β-ME. $CaCl_2$ was used to avoid generating heat upon turnover of αKG to D2HG as Ca^{2+} competes with Mg^{2+} binding. Baseline control data were collected by injecting ligand into the cell containing buffer only. ITC data were analyzed using

Nanoanalyze software provided by TA Instrument in order to obtain the K_D, stoichiometry, $\Delta H_{binding}$, and -TΔS for each mutant upon binding of αKG.

The binding affinity of isocitrate was also determined via ITC. To determine the binding affinity of isocitrate for R132Q IDH1, 20 injections of 4 μL of 2.5 mM ICT were titrated to 0.12 mM of protein at 25 ºC for 200 s and 200 RPM. For R132H IDH1, 30 injections of 2 μL of 5 mM isocitrate were titrated to 0.13 mM of protein at 25 ºC for 150 s and 200 rpm. Finally, for WT IDH1, 20 injections of 4 μL of 0.6 mM ICT were titrated to 0.1 mM of protein at 23 ºC for 150 s and 200 rpm. All titrations were performed under assay buffer containing 50mM Tris pH 7.5 at 4 °C, 100 mM NaCl, 10 mM $CaCl_2$, and 2 mM β-ME. Baseline control data were analyzed using Nanoanalyze software provided by TA Instruments in order to obtain the K_D, stoichiometry, $\Delta H_{binding}$, and -TΔS for each mutant upon binding of isocitrate.

4.3.5. Single Turnover Pre-Steady-State Kinetic Assays

Single turnover pre-steady-state kinetic assays were used to obtain rate constants associated with steps in the catalytic cycle after NADPH binding (k_2, k_3, and k_4 in Figure 2A, and k_2 and k_3 in Figure 2B), excluding product release (k_5 and k_6 in Figure 2A, and k_4 and k_5 in Figure 2B). Single turnover pre-steady-state kinetic assays were performed for the neomorphic reaction at 37 ºC, using an RSM stopped-flow spectrophotometer. For the neomorphic reaction, depletion of NADPH as a function of time was monitored by exciting the sample at 340nm and scanning the emission spectrum from 410 to 460 nm. The change in fluorescence as a function of time was fit to a single exponential equation ($Y = A_0e^{-kt}$) using Graphpad Prism to obtain k_{obs}. For R132H IDH1, higher concentration of αKG was used since 1 mM αKG final had an initial lag time. This lag time was possibly due to the binding of αKG to R132H IDH1 before turnover of NADPH to $NADP^+$ happened. A single exponential equation ($Y = A_0e^{-kt}$) did not fit this change in fluorescence

well. To reduce the initial lag, a final αKG concentration of 20 mM was used to push the binding equilibrium forward and to reduce the initial lag time. The neomorphic single turnover reactions were performed using R132Q and R132H IDH1 as shown in Table 2.

Single turnover pre-steady-state kinetics were also performed for the normal reaction (Figure 1A) at 37 ºC to obtain rate constants associated with steps after $NADP^+$ binding through product release (Figure 3) using an RSM stopped-flow spectrophotometer. Both WT and R132Q IDH1 were studied (Table 3). NADPH formation as a function of time was similarly monitored by exciting at 340 nm and scanning the emission spectrum from 410 to 460 nm. The change in fluorescence as a function of time was fit to a single exponential equation ($Y = A_0e^{-kt}$) using Graphpad Prism and k_{obs} values were obtained.

Table 2. Neomorphic reaction single turnover conditions

Mutant	Excitation and emission wavelengths	Final buffer and salt concentrations	Number of points per second	Final concentration of ligands and enzyme	Number of shots averaged	Time (s)
R132Q IDH1	Ex: 340nm Scan emission: 410 to 460nm	50 mM Tris-HCl pH 7.5 37ºC, 150 mM NaCl, 0.1 mM DTT, and 10 mM $MgCl_2$	1000	R132Q IDH1: 40 µM NADPH: 10 µM αKG: 0.5 mM	6	1
R132H IDH1	Ex: 340nm Scan emission: 410 to 460nm	50 mM Tris-HCl pH 7.5 37ºC, 150 mM NaCl, 0.1 mM DTT, and 10 mM $MgCl_2$	1000	R132H IDH1: 30 µM NADPH: 10 µM αKG: 1 mM, 20 mM	1 (each)	4

Table 3. Normal reaction single turnover experimental conditions

Mutant	Excitation and emission wavelengths	Buffers concentration after 1:1 mixing (final concentration)	Number of points per second	Concentrations after 1:1 mixing (final concentration)	Number of shots averaged	Time (s)
R132Q IDH1	Ex: 340 nm Scan emission: 410 to 460 nm	50 mM Tris-HCl pH 7.5 37 ºC, 150 mM NaCl, 0.1 mM DTT, and 10 mM $MgCl_2$	1000	R132Q IDH1: 30 µM $NADP^+$: 10 µM ICT: 1mM	4	1
WT IDH1	Ex: 340 nm Scan emission: 410 to 460 nm	50 mM Tris-HCl pH 7.5 37ºC, 150 mM NaCl, 0.1 mM DTT, and 10 mM $MgCl_2$	1000	WT IDH1: 30µM $NADP^+$: 10 µM ICT: 0.5 mM	2	0.2

4.3.6. Burst kinetics analysis

Table 4. Neomorphic burst pre-steady-state kinetic assay experimental conditions

Mutant	Excitation and emission wavelengths	Buffers concentration after 1:1 mixing	Number of points per second	Concentrations after 1:1 mixing	Number of shots averaged	Time (s)
R132Q IDH1	Ex: 340 nm Scan emission: 410 to 460 nm	50 mM Tris-HCl pH 7.5 37ºC, 150 mM NaCl, 0.1 mM DTT, and 10 mM $MgCl_2$	64	R132Q IDH1: 10 µM NADPH: 50 µM αKG: 1 mM	1	13
R132H IDH1	Ex: 340 nm Scan emission: 410 to 460 nm	50 mM Tris-HCl pH 7.5 37ºC, 150 mM NaCl, 0.1 mM DTT, and 10 mM $MgCl_2$	64	R132H IDH1: 10µM NADPH: 50 µM αKG: 20 mM	1	18

Burst kinetic analysis was performed in order to determine if product release is rate-limiting (k_5 and k_6 inFigure 2A, and k_4 and k_5 in Figure 2B) using an RSM-1000 stopped-flow spectrophotometer. The burst kinetic assays were performed for the neomorphic reaction at 37 ºC. NADPH depletion as a function of time was monitored by exciting at 340 nm and scanning the emission spectrum from 410 to 460 nm. Burst kinetic assays were performed with R132Q and R132H IDH1 for the neomorphic reaction detailed as detailed in Table 4.

Similar to the neomorphic reaction described above, burst kinetic assays at 37ºC were performed using R132Q and WT IDH1 to assess whether product release is rate limiting in the normal reaction (Figure 1A), using an RSM-1000 stopped flow spectrophotometer to monitor NADPH concentration over time as a readout of NADPH formation in the normal reaction. Table 5 summarizes the experimental conditions for the burst pre-steady-state assays for the normal

reaction.

Table 5. Normal reaction burst pre-steady-state kinetic assay experimental conditions

Mutant	Excitation and emission wavelengths	Buffers concentration after 1:1 mixing (final concentrations)	Number of points per second	Concentrations after 1:1 mixing (final concentrations)	Number of shots averaged	Time (s)
R132Q IDH1	Ex: 340 nm Scan emission: 410 to 460 nm	50 mM Tris-HCl pH 7.5 37ºC, 150 mM NaCl, 0.1 mM DTT, and 10 mM $MgCl_2$	64	R132Q IDH1: 1 μM $NADP^+$: 10 μM ICT: 1 mM	1	8
WT IDH1	Ex: 340 nm Scan emission: 410 to 460 nm	50 mM Tris-HCl pH 7.5 37ºC, 150 mM NaCl, 0.1 mM DTT, and 10 mM $MgCl_2$	1000	WT IDH1: 10 μM $NADP^+$: 50 μM ICT: 1 mM	1	1

4.3.7. HDX-MS Experiments

Hydrogen/deuterium exchange mass spectrometry (HDXMS) was performed to probe differences in solvent accessibility upon binding of substrates for both the normal and neomorphic reaction. In addition to highlighting substrate binding pockets, such analysis provide evidence of conformational change (s). WT IDH1 was analyzed in complex with $NADP^+$, isocitrate, and in apo form. R132H IDH1 was analyzed in complexed with NADPH, with αKG and NADPH, and with αKG, NADPH and $CaCl_2$. HDX-MS experiments were performed at the University of California, San Diego (UCSD) by Dr. Steve Silletti. HDXMS was performed using Waters Synapt G2Si equipped with nanoACQUITY Ultra Performed Liquid Chromatography (UPLC) system with HDX technology and LEAP autosampler. Individual proteins were purified by size-exclusion

chromatography in 50 mM tris pH 7.5 at 4 °C, 100 mM NaCl, and 1 mM DTT immediately prior to analysis. The final concentrations of proteins in each sample were 5 μM. For each experiment time point, 4 μL complex was equilibrated to 25 ºC for 5 min and then mixed with 56 μL of D_2O (50mM tris pH 7.5 at 4 °C, 100 mM NaCl, and 1 mM DTT) for 0, 0.5, 1, 2, and 5 min. The exchange was quenched with an equal volume of quench solution (3M guanidine hydrochloride, pH 2.66).

The quenched sample (50 μL) was injected onto a sample loop, followed by digestion on an in-line pepsin column (immobilized pepsin, Pierce, Inc) at 15 ºC. The resulting peptides were captured on a BEH C18 Vanguard pre-column, and separated by analytical chromatography (Acquity UPLC BEH C18, 1.7 μM, 1.0 x 50 mm, Waters Corporation) using 7-85% acetonitrile gradient in 0.1% formic acid over 7.5 min, detection was performed with Waters SYNAPT G2Si quadrupole time-of-flight mass spectrometer. The mass spectrometer was set to collect data in the Mobility, ESI+ mode; with mass acquisition range of 200-2000 (m/z); scan time 0.4 s. Continuous lock mass correction was accomplished with infusion of leu-enkaphalin (m/z = 556.277) every 30 s (mass accuracy of 1 ppm for calibration standard). For peptide identification, the mass spectrometer was set to collect data in MS^E, ESI + mode instead.

The peptides were identified from triplicate MS^E (MS engine) analyses of 10 μM solution protein in (50 mM tris pH 7.5 at 4 °C, 100 mM NaCl, and 1 mM DTT), and data were analyzed using PLGS 3.0 (Waters Corporation). Peptide masses were identified using a minimum number of 250 ion counts for low energy peptides and 50 ion counts for their fragment ions. The peptides identified in PLGS were then analyzed in DynamX 3.0 (Waters Corporation) and deuterium uptake was corrected for back-exchange as previously described[27] using DECA Software (https://github.com/komiveslab/DECA). The relative deuterium uptake for each peptide was

calculated by comparing centroids of mass envelopes of deuterated samples vs. the undeuterated controls following previously published methods[28]. The experiments were performed in triplicate, and independent replicates of the triplicate experiment were performed to verify results.

4.3.8. R132Q Crystallography and Data Collection

X-ray crystallography was performed with R132Q IDH1 to gain an understanding on key structural features that may allow the mutant to perform both reactions. After size exclusion chromatography, R132Q IDH1 was concentrated to >14mg/mL. Incubations with ligands were performed with final enzyme concentrations ranging from 5 to 10 mg/mL. R132Q IDH1 was incubated with 75 mM αKG, 10 mM NADPH, and 10 mM $CaCl_2$ for an hour on ice. R132Q IDH1 was also incubated with 75 mM isocitrate, 10 mM $NADP^+$, and 10 mM $CaCl_2$ for an hour in ice in. Both conditions were performed in buffer containing 20 mM Tris pH 7.5 at 4ºC and 200 mM NaCl. These incubations were placed on microscope slides in drops of 2 to 6 µL using 1:1, 2:2, and 3:3 drop ratios of protein:crystallization buffer (100 mM bis-tris propane pH 6.5 at ambient temperature, 200 mM sodium iodide, 10 mM TCEP, and PEG 3350 (20-22%) or PEG 20000 (18-20%)) and allowed to equilibrate via hanging drop vapor diffusion overnight at ambient temperature. After 24 h, the trays were moved to 4 ^oC and the crystals were allowed to grow for one week. The crystals were then frozen under 100 mM bis-tris propane pH 6.5 at ambient temperature, 200 mM sodium iodide, 10 mM TCEP, PEG 3350 (20-22%) or PEG 20000 (18-20%), 75 mM ICT/αKG, 10 mM $NADP^+$/NADPH, and 10 mM $CaCl_2$. The crystals were flash-frozen under liquid nitrogen.

X-ray diffraction and data collection were performed remotely at Advanced Photon Source (APS) in Chicago, IL and the data was processed using HKL2000[29]. The energy of the beam was 12663.0eV and a current of 102.2 mAmps. Diffraction data were obtained from crystals containing

R132Q IDH1 with neomorphic and normal ligands. Data was obtained for the crystals for 0.5 s over 180º in 0.2º increments yielding to a total of 900 images. Due to poor quality data, molecular replacement was not performed.

4.3.9. Kintek Explorer Global Fitting

Global fitting computer simulations was performed to determine intrinsic rate constants in the catalytic cycle (Figure 2) by globally fitting data from 4 experiments simultaneously (NADPH binding kinetics and titrations, single turnover experiments, and burst assays). The NADPH binding kinetics at 21 ºC for R132Q and R132H IDH1 (Figure 3 and 4) as well as the single turnover assays to produce D2HG data (Figure 6) were uploaded to the Kintek Global Fitting software. The experimentally determined K_D of R132H IDH1 with αKG was used to lock together the rate of binding and dissociation (k_3 and k_{-3} in Figure 2A, and k_2 and k_{-2} in Figure 2B) since $k_{-3}/k_3 = K_{D,\,\alpha KG}$ inFigure 2A, and $k_{-2}/k_2 = K_{D,\,\alpha KG}$ in Figure 2B. In total, three models were created: a R132H IDH1 catalytic cycle including conformational change step; a more simplistic model of R132H IDH1 without conformational change (Figure 2B); and a R132Q IDH1 model similar to R132H IDH1 (Figure 2B). Observables were generated to model the change in fluorescence for both NADPH binding and the single turnover assay. The data were fit simultaneously for each model and a chi^2 threshold (determined by number of points per trace, Figure 3, 4, and 6) was determined to analyze goodness of fit. Computer simulation using 2D fitspace at the chi^2 threshold was performed to assess the accuracy of the individual rate constants determined in comparison with other rate constants in the catalytic cycle. The global fitting computer simulation was performed as shown in Table 6.

Table 6. Global fitting computer simulation parameters

Mutant	Reaction, Model	Experiment	Observable equations	Observable values		Chi^2-threshold used
R132Q IDH1	αKG→D2HG Figure 2B	NADPH binding	a*(NADPH + b*(IDH1NADPH))	a	7.98x10^{-7}	0.9945
				b	276600	
		Hydride transfer, single turnover conditions	d*(IDH1NADPH + f*(IDH1NADPHaKG)) + g*(IDH1NADP + IDH1NADPD2HG + NADP)	d	0.210	
				f	0.451	
				g	0.0336	
R132H IDH1	αKG→D2HG Figure 2A	NADPH binding	a*(NADPH + b*(IDH1NADPH))	a	0.407	0.9960
				b	4.50	
		Hydride transfer, single turnover conditions	d*(IDH1NADPH + f*(IDH1NADPHaKG)) + g*(IDH1NADP + IDH1NADPD2HG + NADP)	d	0.113	
				f	0.508	
				g	0.0148	
	αKG→D2HG Figure 2A	NADPH binding	a*(NADPH + b*(IDH1NADPH))	a	0.406	0.998
				b	4.51	
		Hydride transfer, single turnover conditions	d*(IDH1NADPH + f*(IDH1NADPHaKG + IDH1NADPHaKGc)) + g*(IDH1NADP + IDH1NADPD2HG + NADP)	d	0.116	
				f	0.494	
				g	0.0146	

4.4. Results

Measuring the intrinsic rate constant of each step of the catalytic cycle of mutant IDH1 when performing the neomorphic reaction has not yet been established. Previously, Rendina and colleagues described the substrate binding to mutant IDH1 as an ordered sequential reaction for

the neomorphic reaction, where NADPH binds before αKG[17]. When WT IDH1 catalyzes the normal reaction (Figure 1A), the binding mechanism is random sequential, where either isocitrate or $NADP^+$ can bind first[17]. It has been reported both that WT and R132H IDH1 undergo a conformational change upon binding isocitrate[3, 23]. This conformation change consists of the α10 regulatory domain transitioning from a loop to a helix in order to orient residue D275 towards the substrate[3, 23]. We hypothesized that the mutant IDH1 catalytic cycle for the neomorphic reaction would include sequential binding of NADPH followed by αKG, a conformational change to orient the substrates for hydride transfer between NADPH and αKG to form D2HG (rate of chemistry) as the rate-limiting step of the catalytic cycle (Figure 1A). The reaction would conclude with product release (k_5 and k_6 in Figure 2A, and k_4 and k_5 in Figure 2B), which we predict to be rapid. Understanding the catalytic cycle will highlight key features for the production of D2HG as well as providing insights in inhibition mechanism of mutant IDH1.

We used methods in steady-state and pre-steady-state kinetics as well as biophysical experiments to elucidate rate constants for the proposed catalytic cycle. Rates of NADPH binding will be determined using an RSM-stopped flow spectrophotometer (Figure 4) and isothermal titration calorimetry. In our experiments, a conformational change could not be measured, perhaps due to being spectroscopically silent. Instead, Dr. Steve Silleti performed HDX-MS experiments to assess regions of movement upon binding of ICT and αKG, though no rate information could be obtained. We also performed two types of pre-steady-state kinetic experiments: a single turnover to determine rates associated with product formation and burst assay in order to determine if product release is rate-limiting.

4.4.1. NADPH Binding Kinetics

Rendina and colleagues in 2013 described the mechanism of substrate binding (NADPH and αKG) of mutant IDH1 enzymes for the neomorphic reaction[17]. Here we expanded this study to include a comprehensive kinetic evaluation of NADPH binding kinetics of R132H, R132Q, and WT IDH1. We used an RSM-stopped flow spectrophotometer to monitor the rate of NADPH binding (k_1 inFigure 2) since the fluorescence intensity of NADPH increases upon binding to enzyme, as previously described[17]. With an RSM stopped-flow spectrophotometer, two syringes are pushed with compress air to rapidly mix each solution as they travel to the reaction cell (Figure 4). At the reaction cell, a continuous bright light coming from a 150 W Xenon lamp excited the NADPH and the light emitted is detected at a 90° angle to increase signal associated to the emission (Figure 4). The detector collects data at a rate of 1000 points/s and it is sent to the computer for data analysis (Figure 4). The stopped syringe collects the waste coming from the reaction cell (Figure 4). Unfortunately, our RSM stopped-flow spectrophotometer had a limit of detection of ≥ 4 μM (NADPH); therefore, we were not capable of reproducing the exact experimental parameters used by Rendina and colleagues[17]. Due to this issue, we increased the concentrations of enzyme and substrate by 10-fold. Since the binding of IDH1 to NADPH is a one-step process, the k_{obs} values mathematically equivalent to $k_1[S] + k_{-1}$ (Figures 3F and 4H), and thus there is a linear relationship of k_{obs} as a function of NADPH. As our experimental data fit well to this simplest model of substrate binding, we have proposed that binding of NADPH to IDH1 is a single step process.

Table 7. NADPH binding kinetic results

Mutant	NADPH binding at ambient temperature		NADPH binding at 10°C	
WT IDH1	N/A		k_1	>1.7 ± 0.9 $\mu M^{-1}s^{-1}$
			k_{-1}	3 ± 4 s^{-1}
R132Q IDH1	k_1	>3.9 ± 0.6 $\mu M^{-1}s^{-1}$	k_1	>0.9 ± 0.2 $\mu M^{-1}s^{-1}$
	k_{-1}	-0.5 ± 4.8 s^{-1}	k_{-1}	3 ± 1 s^{-1}
R132H IDH1	k_1	>1.6 ± 0.1 $\mu M^{-1}s^{-1}$	k_1	>0.002 ± 0.016 $\mu M^{-1}s^{-1}$
	k_{-1}	2 ± 1 s^{-1}	k_{-1}	2.7 ± 0.2 s^{-1}

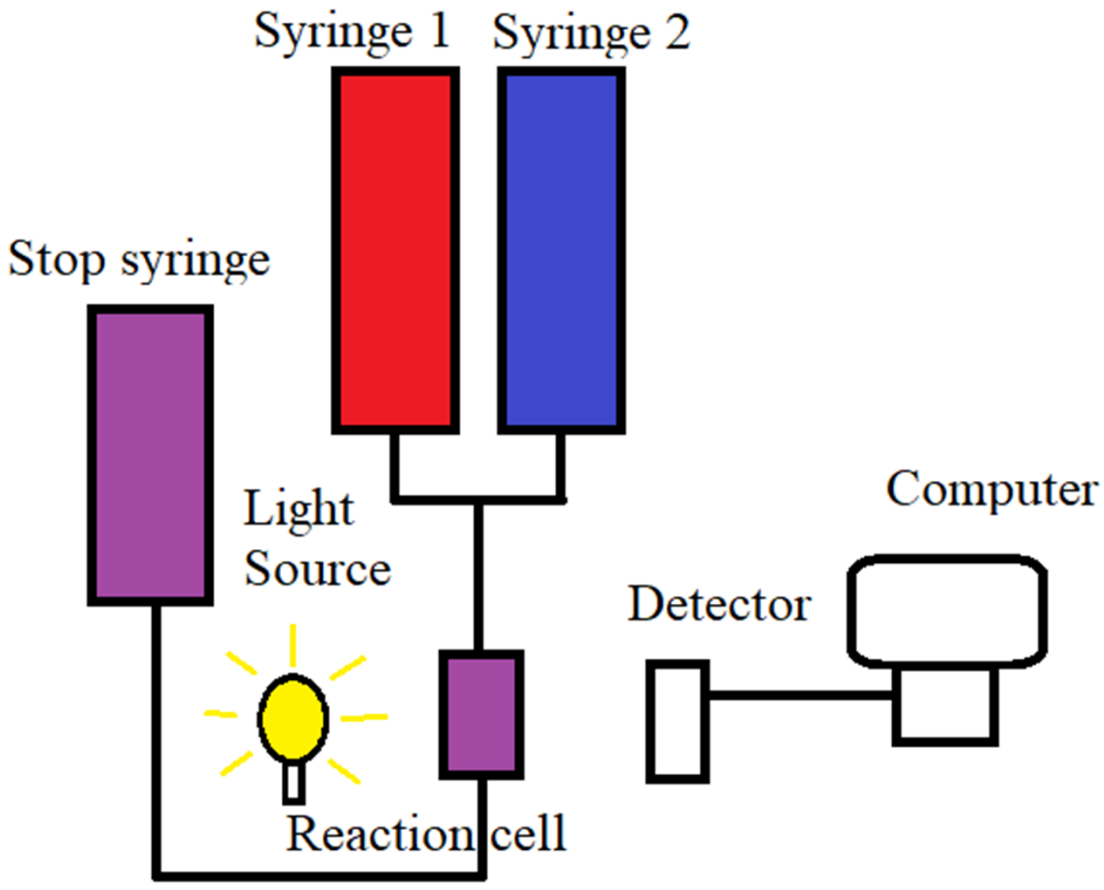

Figure 4. Stopped-flow spectrophotometer diagram. Different solutions are in each syringe and are shot together under compressed air. The two solutions mixed diluting by half components in the solution that is present in just one syringe. The solutions mixed rapidly and reach the reaction cell under 3 ms. A 150 W Xenon lamp produces light that excites the NADPH and the emission is scanned providing 1000 points/s. The stopped syringe collects the waste and it also determines the assay volume. The detector collects the data and it is processed by the computer.

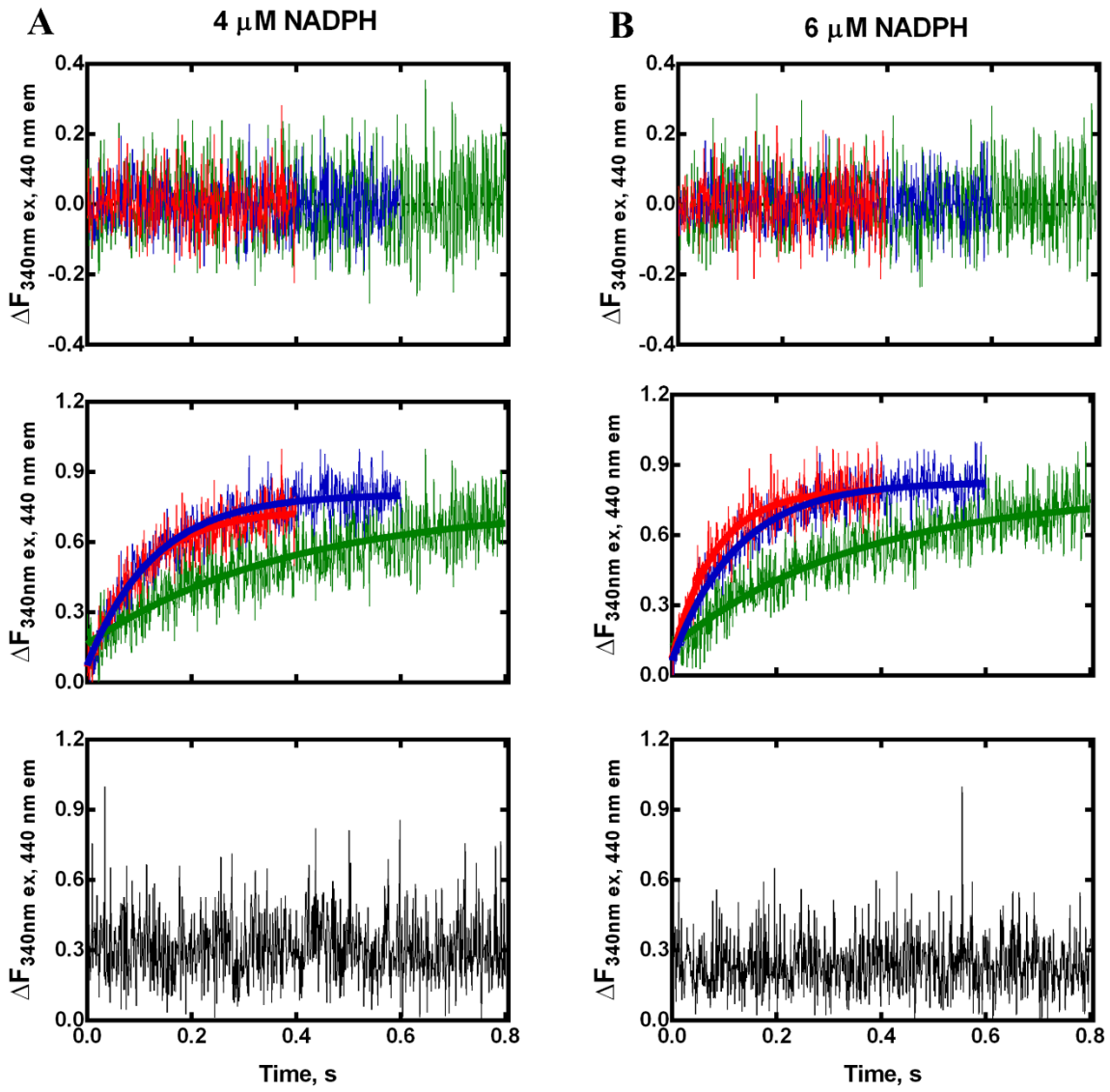

Figure 5. A-E. NADPH binding kinetics at 10 °C for WTIDH1 (red), R132Q IDH1 (blue), and R132H IDH1 (green). The change in fluorescence as a function of time was monitored with a stopped-flow spectrophotometer and the temperature was kept at 10 °C. The change in fluorescence was fit to a single exponential equation ($Y = A_0e^{-kt}$) and the goodness of fit was assessed with residuals. The single exponential equation yielded the k_{obs} for each mutant at each concentration (**A-E**). **F.** The k_{obs} values were plotted as a function of NADPH concentration yielding a linear progression. The linear relationship of k_{obs} and NADPH reveals a one step binding. The slope of the line is equal to k_{on} (k_1 in Figure 2) and the k_{off} (k_{-1} in Figure 2) is represented as the Y-intercept of each linear progression. WT IDH1 (red), R132Q IDH1 (blue), and R132H IDH1 (green). **A.** 4 μM NADPH, **B.** 6 μM NADPH, **C.** 8 μM NADPH, **D.** 10 μM NADPH, **E.** 15 μM NADPH. (Figure continues in next page)

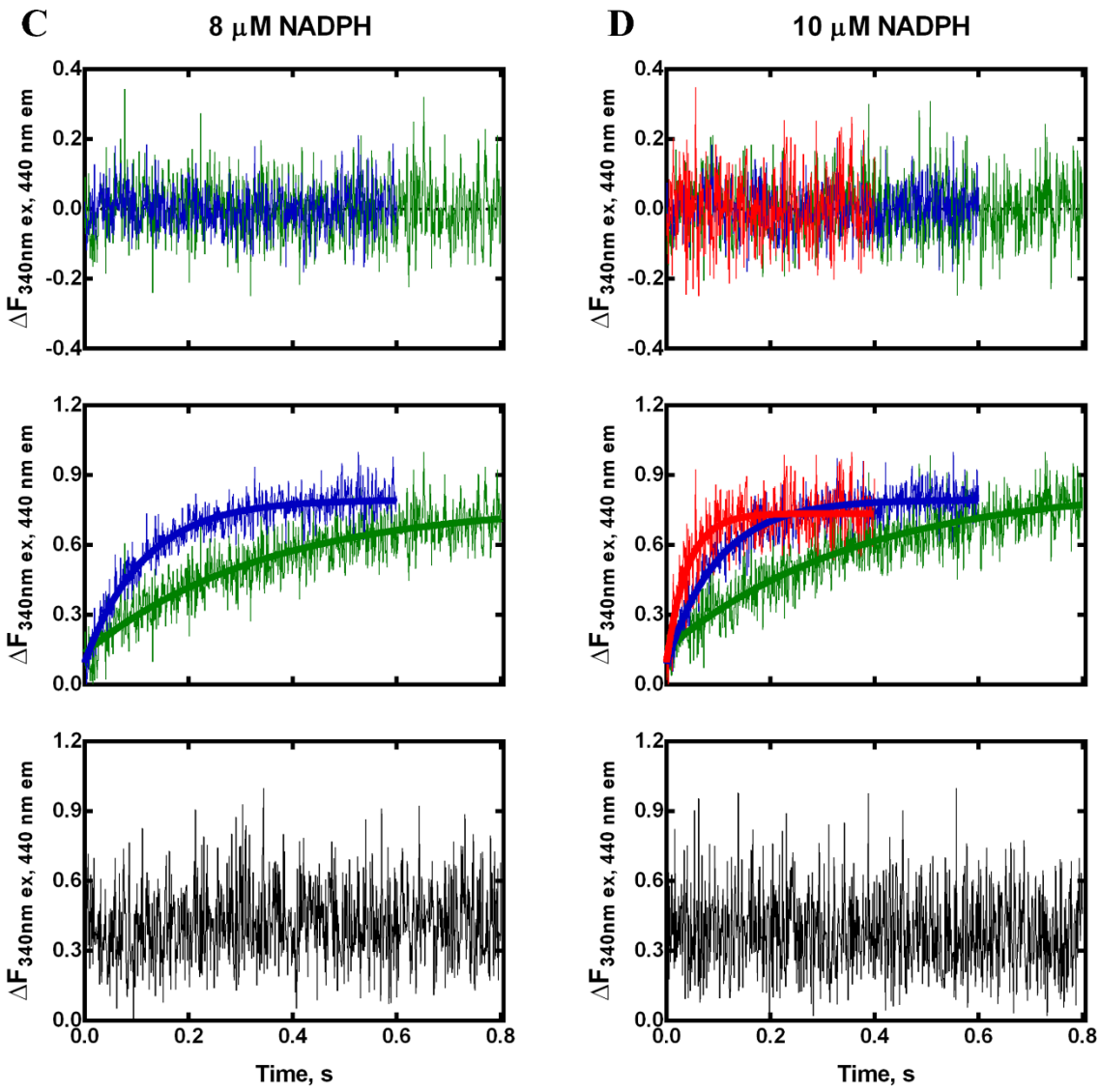

Figure 5. A-E. NADPH binding kinetics at 10 °C for WTIDH1 (red), R132Q IDH1 (blue), and R132H IDH1 (green). The change in fluorescence as a function of time was monitored with a stopped-flow spectrophotometer and the temperature was kept at 10 °C. The change in fluorescence was fit to a single exponential equation ($Y = A_0e^{-kt}$) and the goodness of fit was assessed with residuals. The single exponential equation yielded the k_{obs} for each mutant at each concentration (**A-E**). **F.** The k_{obs} values were plotted as a function of NADPH concentration yielding a linear progression. The linear relationship of k_{obs} and NADPH reveals a one step binding. The slope of the line is equal to k_{on} (k_1 in Figure 2) and the k_{off} (k_{-1} in Figure 2) is represented as the Y-intercept of each linear progression. WT IDH1 (red), R132Q IDH1 (blue), and R132H IDH1 (green). **A.** 4 μM NADPH, **B.** 6 μM NADPH, **C.** 8 μM NADPH, **D.** 10 μM NADPH, **E.** 15 μM NADPH. (Figure continues in next page)

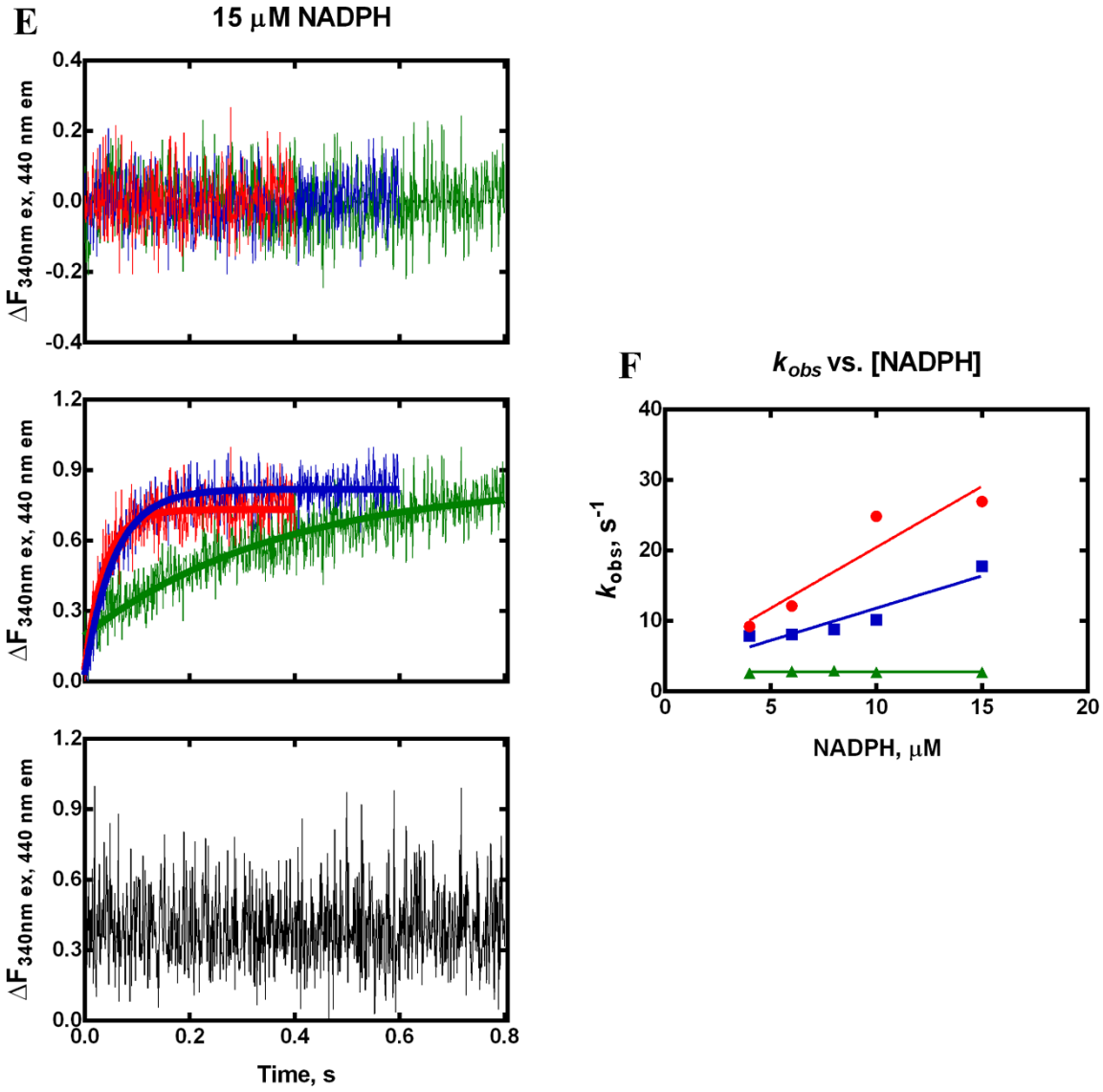

Figure 5. A-E. NADPH binding kinetics at 10 °C for WTIDH1 (red), R132Q IDH1 (blue), and R132H IDH1 (green). The change in fluorescence as a function of time was monitored with a stopped-flow spectrophotometer and the temperature was kept at 10 °C. The change in fluorescence was fit to a single exponential equation ($Y = A_0e^{-kt}$) and the goodness of fit was assessed with residuals. The single exponential equation yielded the k_{obs} for each mutant at each concentration (**A-E**). **F.** The k_{obs} values were plotted as a function of NADPH concentration yielding a linear progression. The linear relationship of k_{obs} and NADPH reveals a one step binding. The slope of the line is equal to k_{on} (k_1 in Figure 2) and the k_{off} (k_{-1} in Figure 2) is represented as the Y-intercept of each linear progression. WT IDH1 (red), R132Q IDH1 (blue), and R132H IDH1 (green). **A.** 4 μM NADPH, **B.** 6 μM NADPH, **C.** 8 μM NADPH, **D.** 10 μM NADPH, **E.** 15 μM NADPH.

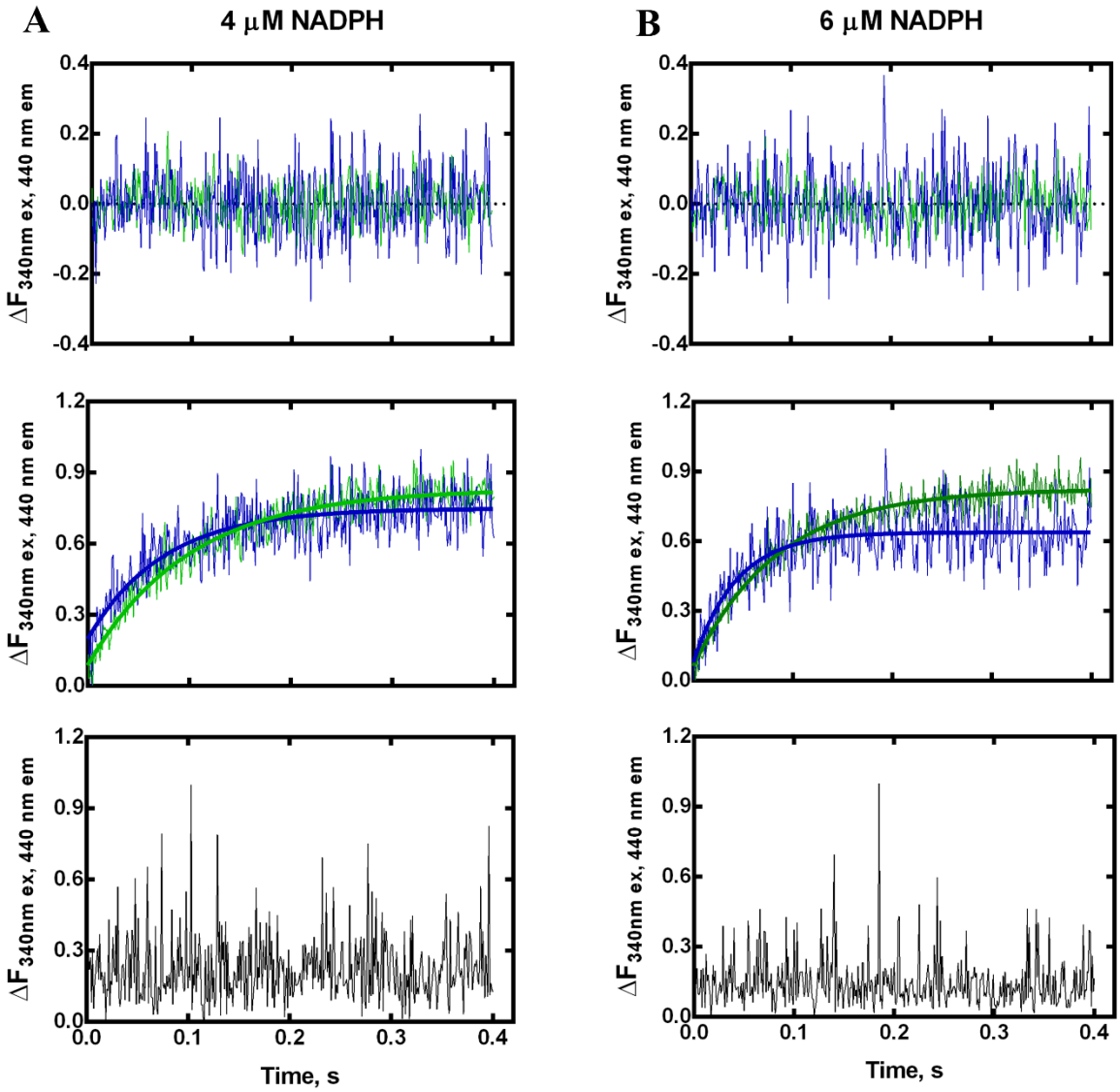

Figure 6. A-G. NADPH binding kinetics at ambient temperature R132Q IDH1 (blue), and R132H IDH1 (green). The change in fluorescence as a function of time was monitored with a stopped-flow spectrophotometer and the temperature was kept at 10 °C. The change in fluorescence was fit to a single exponential equation ($Y = A_0e^{-kt}$) and the goodness of fit was assessed with residuals. The single exponential equation yielded the k_{obs} for each mutant at each concentration (**A-G)**. **H.** The k_{obs} values were plotted as a function of NADPH concentration yielding a linear progression. The linear relationship of k_{obs} and NADPH reveals a one-step binding. The slope of the line is equal to k_{on} (k_1 in Figure 2) and the k_{off} (k_{-1} in Figure 2) is represented as the Y-intercept of each linear progression. WT IDH1 (red), R132Q IDH1 (blue), and R132H IDH1 (green). **A.** 4 µM NADPH, **B.** 6 µM NADPH, **C.** 8 µM NADPH, **D.** 10 µM NADPH, **E.** 13 µM NADPH, **F.** 15 µM NADPH, **G.** 17 µM NADPH. (Figure continues in next page)

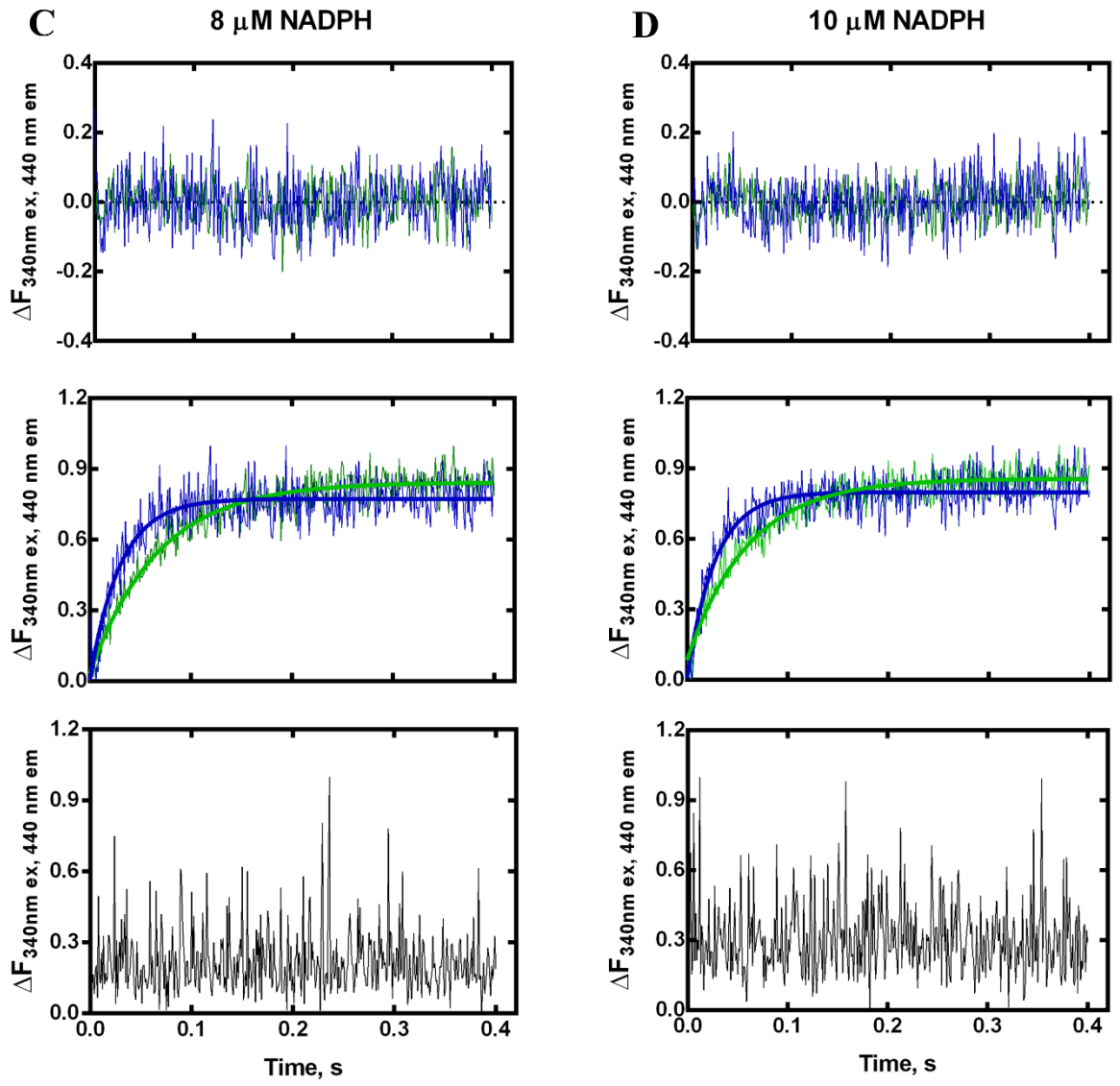

Figure 6. A-G. NADPH binding kinetics at ambient temperature R132Q IDH1 (blue), and R132H IDH1 (green). The change in fluorescence as a function of time was monitored with a stopped-flow spectrophotometer and the temperature was kept at 10 °C. The change in fluorescence was fit to a single exponential equation ($Y = A_0e^{-kt}$) and the goodness of fit was assessed with residuals. The single exponential equation yielded the k_{obs} for each mutant at each concentration (**A-G)**. **H.** The k_{obs} values were plotted as a function of NADPH concentration yielding a linear progression. The linear relationship of k_{obs} and NADPH reveals a one-step binding. The slope of the line is equal to k_{on} (k_1 in Figure 2) and the k_{off} (k_{-1} in Figure 2) is represented as the Y-intercept of each linear progression. WT IDH1 (red), R132Q IDH1 (blue), and R132H IDH1 (green). **A.** 4 μM NADPH, **B.** 6 μM NADPH, **C.** 8 μM NADPH, **D.** 10 μM NADPH, **E.** 13 μM NADPH, **F.** 15 μM NADPH, **G.** 17 μM NADPH. (Figure continues in next page)

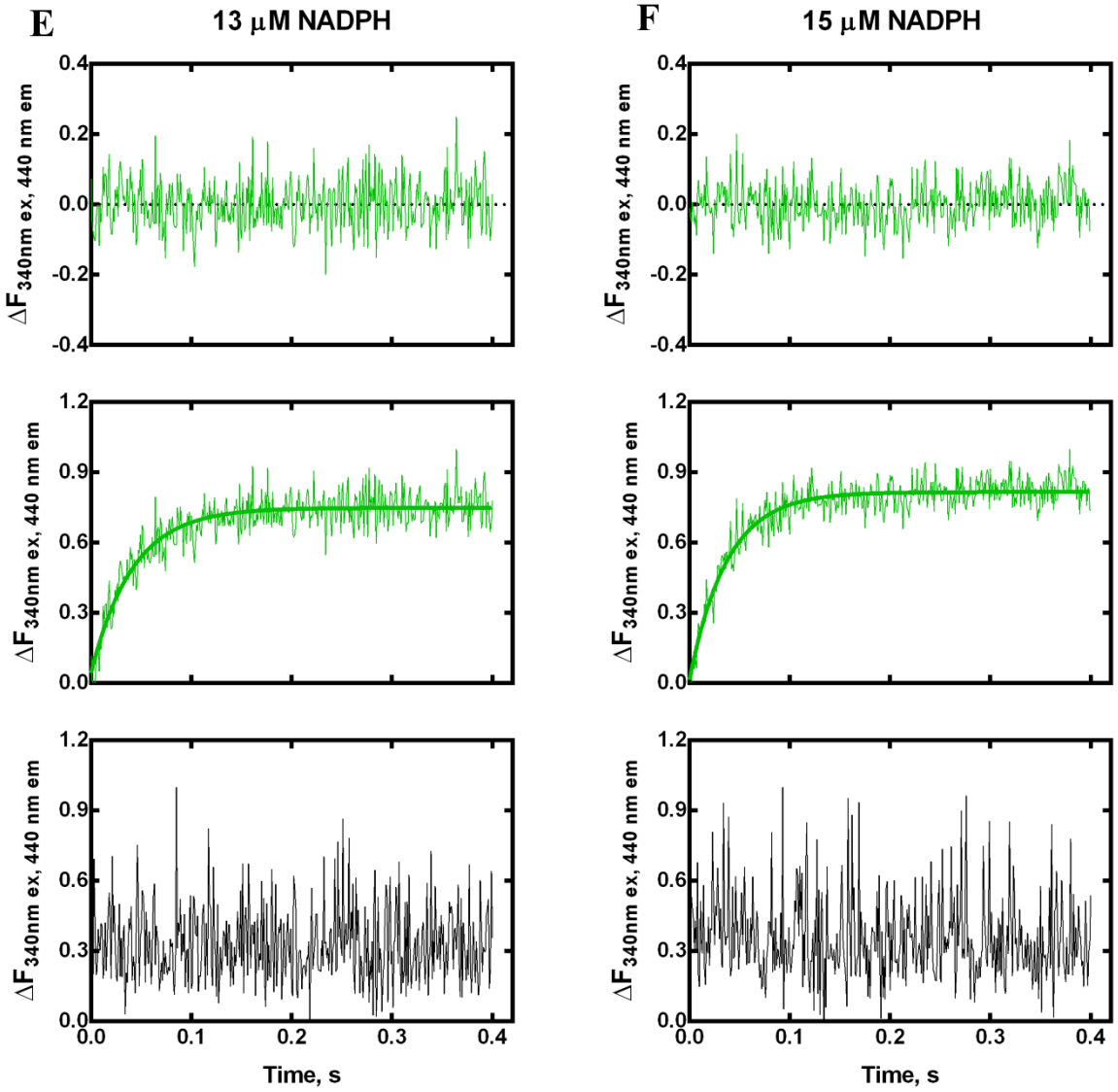

Figure 6. A-G. NADPH binding kinetics at ambient temperature R132Q IDH1 (blue), and R132H IDH1 (green). The change in fluorescence as a function of time was monitored with a stopped-flow spectrophotometer and the temperature was kept at 10 °C. The change in fluorescence was fit to a single exponential equation ($Y = A_0e^{-kt}$) and the goodness of fit was assessed with residuals. The single exponential equation yielded the k_{obs} for each mutant at each concentration (**A-G)**. **H.** The k_{obs} values were plotted as a function of NADPH concentration yielding a linear progression. The linear relationship of k_{obs} and NADPH reveals a one-step binding. The slope of the line is equal to k_{on} (k_1 in Figure 2) and the k_{off} (k_{-1} in Figure 2) is represented as the Y-intercept of each linear progression. WT IDH1 (red), R132Q IDH1 (blue), and R132H IDH1 (green). **A.** 4 μM NADPH, **B.** 6 μM NADPH, **C.** 8 μM NADPH, **D.** 10 μM NADPH, **E.** 13 μM NADPH, **F.** 15 μM NADPH, **G.** 17 μM NADPH. (Figure continues in next page)

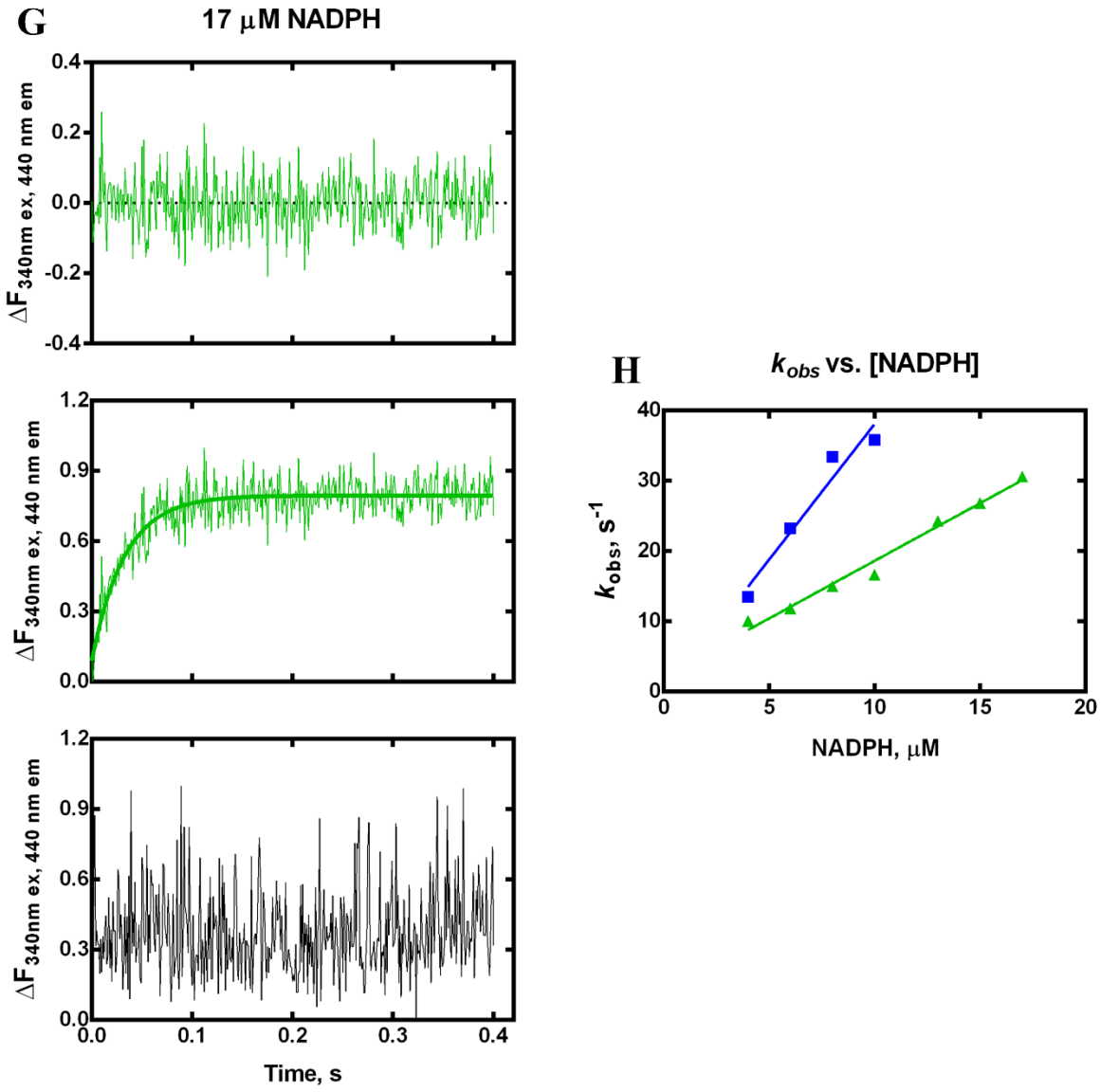

Figure 6. A-G. NADPH binding kinetics at ambient temperature R132Q IDH1 (blue), and R132H IDH1 (green). The change in fluorescence as a function of time was monitored with a stopped-flow spectrophotometer and the temperature was kept at 10 °C. The change in fluorescence was fit to a single exponential equation ($Y = A_0e^{-kt}$) and the goodness of fit was assessed with residuals. The single exponential equation yielded the k_{obs} for each mutant at each concentration (**A-G)**. **H.** The k_{obs} values were plotted as a function of NADPH concentration yielding a linear progression. The linear relationship of k_{obs} and NADPH reveals a one-step binding. The slope of the line is equal to k_{on} (k_1 inFigure 2) and the k_{off} (k_{-1} inFigure 2) is represented as the Y-intercept of each linear progression. WT IDH1 (red), R132Q IDH1 (blue), and R132H IDH1 (green). **A.** 4 μM NADPH, **B.** 6 μM NADPH, **C.** 8 μM NADPH, **D.** 10 μM NADPH, **E.** 13 μM NADPH, **F.** 15 μM NADPH, **G.** 17 μM NADPH

The concentrations of NADPH we used (> 4 μM) to allow detection of NADPH binding to IDH1 led to rates that were faster than the dead-time of the instrument (3 ms). Thus, the stopped-flow spectrophotometer was not able to detect the binding of NADPH to IDH1, under these conditions. To slow NADPH binding to allow us to report a rate of > X s^{-1}, we added 20% and 40% glycerol to NADPH binding assays with R132H and R132Q IDH1, respectively. These traces were used for global fitting to obtain rates associated with NADPH binding (Figure 6, Table 1) using simulations, without assuming a simple model for substrate binding. The change in fluorescence was also faster than the deadtime of the stopped-flow spectrophotometer for WT IDH1 at the same glycerol concentration used with R132Q IDH1 (Table1), so the temperature was decreased to 10°C to further slowdown the binding of NADPH for easier detection. To allow direct comparison, NADPH binding kinetics of R132H and R132Q IDH1 were also analyzed using the same conditions as WT (Figure 5, Table 1). WT IDH1 had the fastest on rate of NADPH binding, k_1, followed by R132Q, and finally R132H IDH1 (1.73, 0.92, and 0.0018 $\mu M^{-1}s^{-1}$, respectively) (Figure 5F). Due to the high concentrations of NADPH, the error of the value of the Y-intercept (k_{-1}) was too large to be determined via binding kinetics (Table 7). Therefore, we performed isothermal calorimetry assays to obtain a K_D value, allowing us to solve for the k_{-1} rates for each mutant.

4.4.2. Isothermal Calorimetry Shows High Affinity of NADPH for WT and Mutant

Previous work has shown that NADPH binds tightly to IDH1, with K_D values ranging from the mid nM to low μM range[17]. Due to low sensitivity with the stopped-flow spectrophotometer, Dr. Andrey Bobkov designed isothermal titration calorimetry (ITC) assays to measure the binding affinity of each mutant and WT IDH1 for NADPH to aid in calculating k_{-1} values. During an ITC experiment, a ligand is titrated an analyte (IDH1) and the heat released is measured (Figure 7 top

panel). As the analyte is saturated with ligand, the heat released decreases until the enzyme is completely saturated, thus no heat is release, yielding a sigmoidal curve (Figure 7 bottom panel). NADPH was titrated to against R132H and R132Q IDH1, resulting in K_D values were 60 nM for both mutants (Table 8). However, the lack of points in the linear portion of the sigmoidal curve may indicate infinitely tight binding for both mutants (Figure 7A and B). Due to this very high affinity, it is difficult to calculate with accuracy the k_{-1} values for both R132H and R132Q IDH1. NADPH was also titrated to WT IDH1, yielding a K_D value of 300 nM, which was significantly higher than the mutants (Table 8). Due to temperature difference in both the NADPH binding kinetics of WT IDH1 and the ITC experiments on the same enzyme, it is not possible to accurately calculate a k_{-1} for WT IDH1 and NADPH.

The stoichiometry and thermodynamics of binding can also be determined by ITC experiments. ITC experiments showed 1:1 stoichiometry of NADPH to WT, R132H, and R132Q IDH1 in this study (Table 8). The $\Delta H_{binding}$ of NADPH with R132Q IDH1 was the highest, followed by WT, and R132H IDH1 (Table 8). The temperature related entropy ($-T\Delta S$) of R132Q IDH1 was also the highest, followed by WT, and R132H IDH1 (Table 8), indicating that binding of NADPH to IDH1 is not entropically favored. The calculated ΔG values for R132H and R132Q IDH1, and WT IDH1 indicated that the binding of NADPH is driven by $\Delta H_{binding.}$ (Table 8).

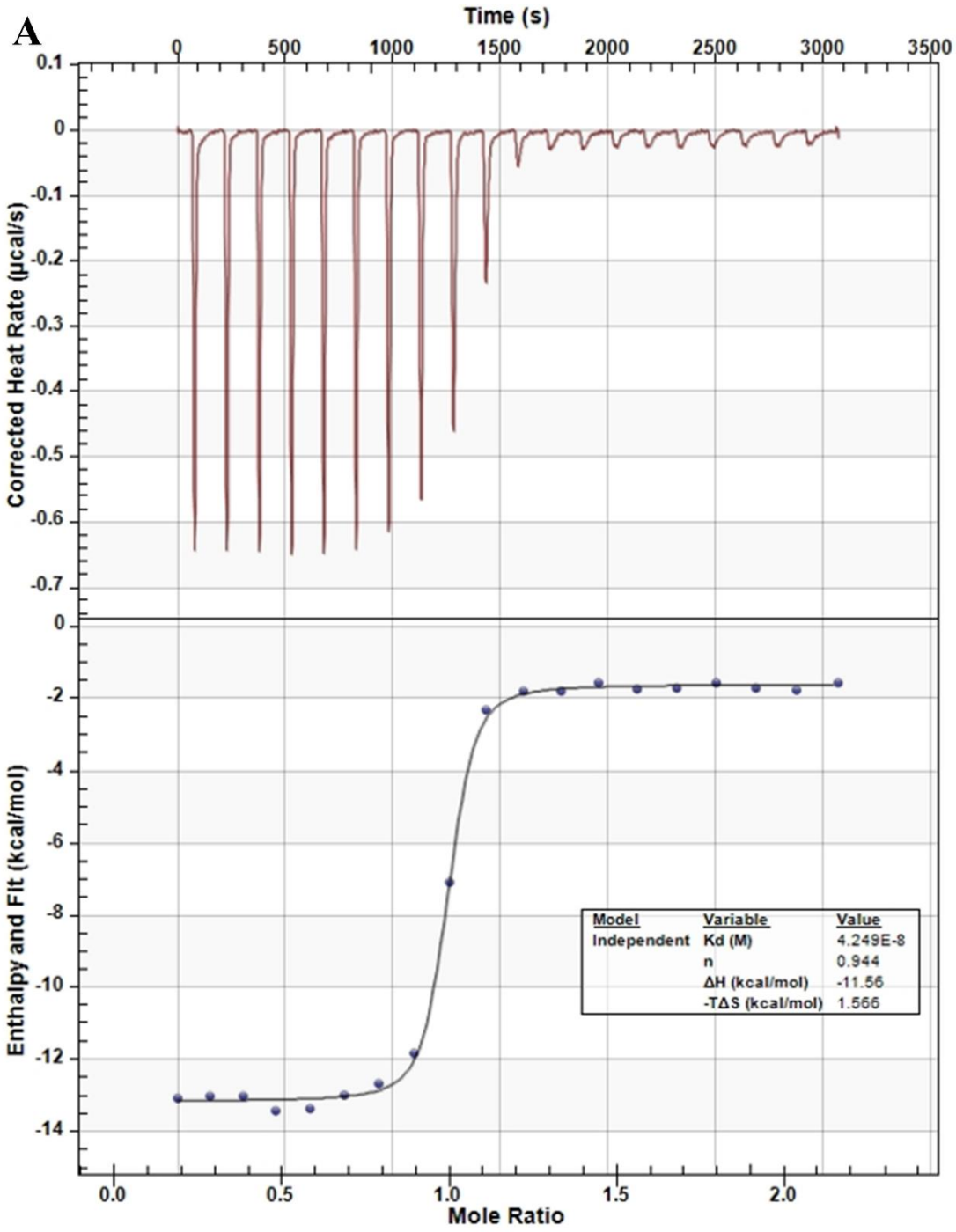

Figure 7. A-C. NADPH binding affinity (K_D) determination using ITC experiments for **A.** R132H IDH1, **B.** R132Q IDH1, and **C.** WT IDH1. In all cases, the top panel is the raw data as the heat generated as more NADPH is titrated, and the bottom panel shows the area under the curve results fit to a sigmoidal equation. As more NADPH is added, the enzyme is saturated, and the heat generated is less. At the inflection point of the linear portion in the sigmoidal curve represents the stoichiometry of binding. R132H and R132Q IDH1 show a lack of point in the linear part of the sigmoidal curve, representing infinitely tight binding of NADPH. (Figure continues in next page)

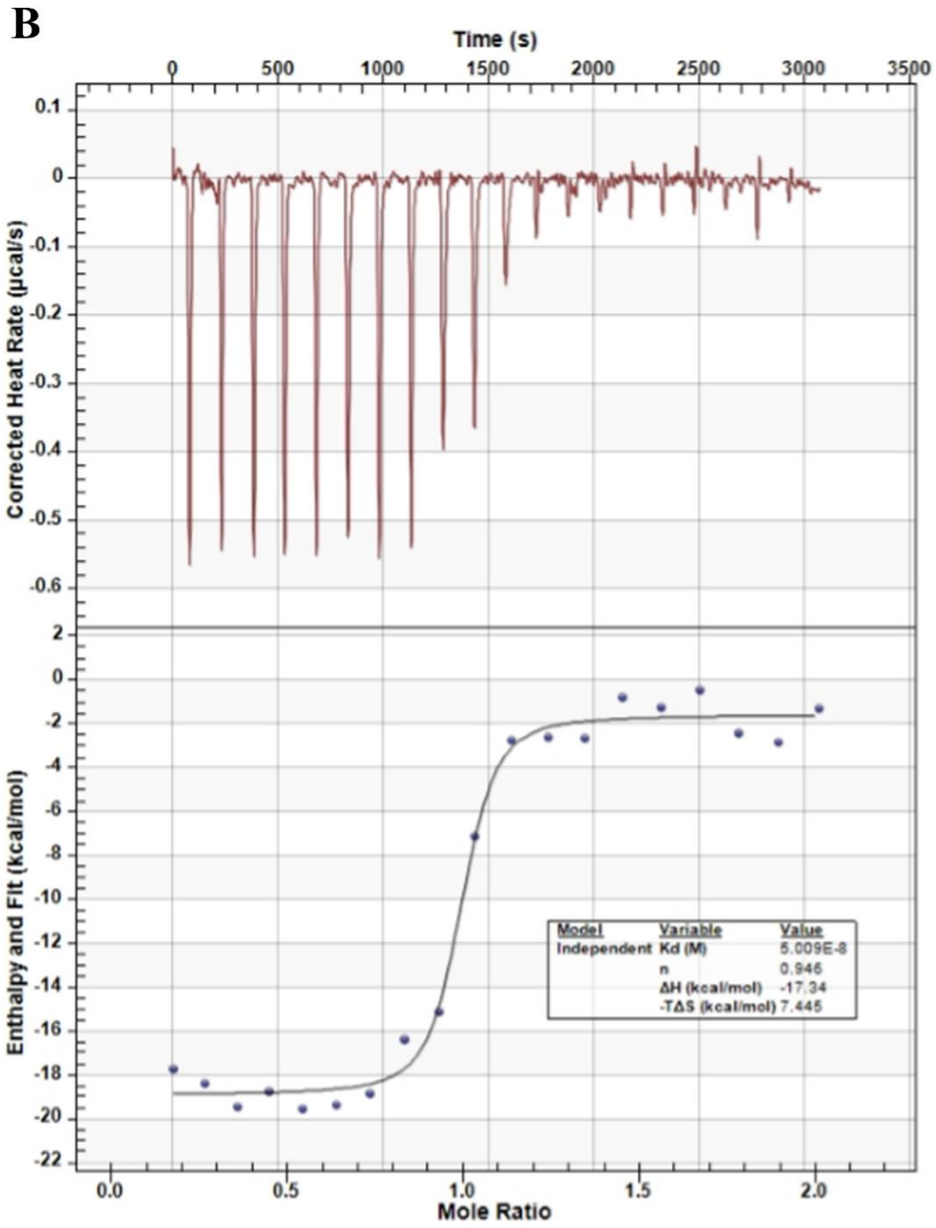

Figure 7. A-C. NADPH binding affinity (K_D) determination using ITC experiments for **A.** R132H IDH1, **B.** R132Q IDH1, and **C.** WT IDH1. In all cases, the top panel is the raw data as the heat generated as more NADPH is titrated, and the bottom panel shows the area under the curve results fit to a sigmoidal equation. As more NADPH is added, the enzyme is saturated, and the heat generated is less. At the inflection point of the linear portion in the sigmoidal curve represents the stoichiometry of binding. R132H and R132Q IDH1 show a lack of point in the linear part of the sigmoidal curve, representing infinitely tight binding of NADPH. (Figure continues in next page)

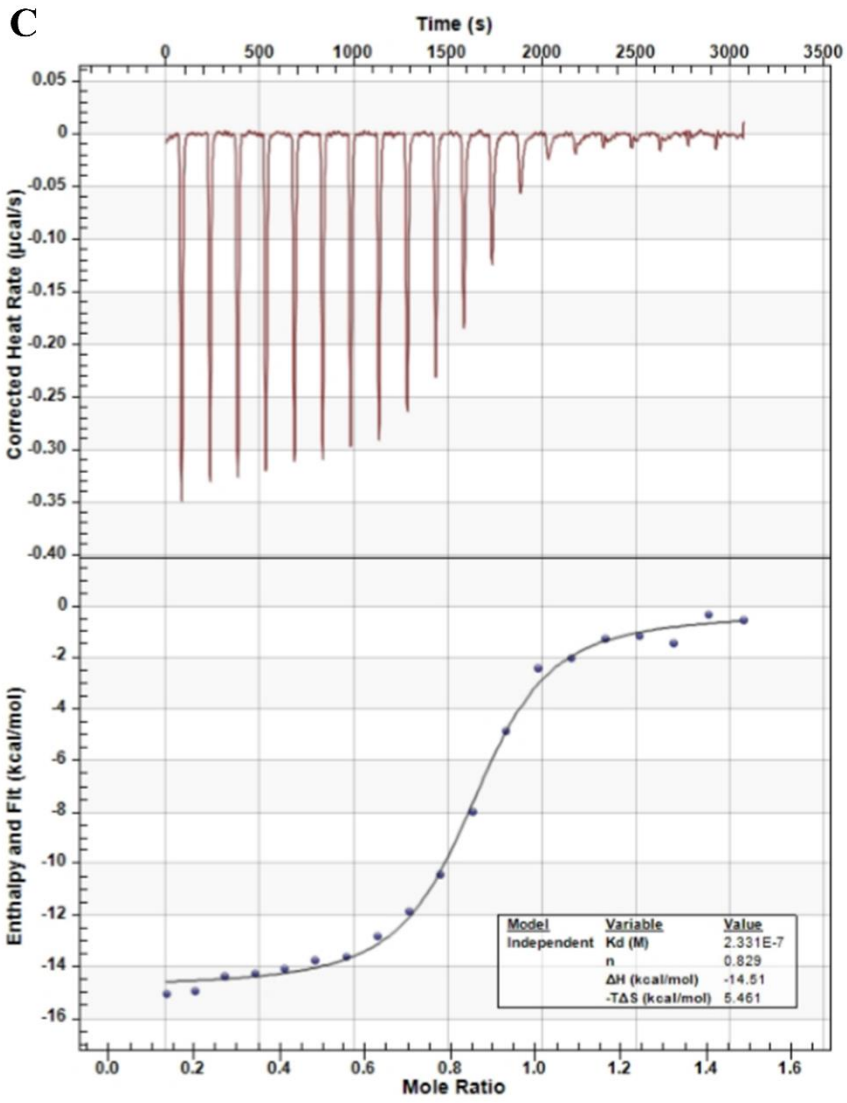

Figure 7. A-C. NADPH binding affinity (K_D) determination using ITC experiments for **A.** R132H IDH1, **B.** R132Q IDH1, and **C.** WT IDH1. In all cases, the top panel is the raw data as the heat generated as more NADPH is titrated, and the bottom panel shows the area under the curve results fit to a sigmoidal equation. As more NADPH is added, the enzyme is saturated, and the heat generated is less. At the inflection point of the linear portion in the sigmoidal curve represents the stoichiometry of binding. R132H and R132Q IDH1 show a lack of point in the linear part of the sigmoidal curve, representing infinitely tight binding of NADPH

Table 8. Stoichiometry and thermodynamic results from ITC experiments

Mutant	Substrate	Stoichiometry (N)	$\Delta H_{binding}$ (kcal/mol)	-TΔS (kcal/mol)	ΔG (kcal/mol) (calculated)	K_D (Experimental) (μM)	K_D (Simulated) (μM)
WT IDH1	NADPH	0.88 ± 0.05	-13.8 ± 0.7	5.0 ± 0.5	-8.8	0.3 ± 0.1	ND
	ICT	1.4 ± 0.1	-4.3 ± 0.1	-2.80 ± 0.05	-7.2	5.8 ± 0.9	ND
R132Q IDH1	NADPH	0.98 ± 0.04	-17.5 ± 0.2	7.7 ± 0.3	-9.8	0.06 ± 0.01	< 0.060
	ICT	1 (fixed)	-1.57 ± 0.04	-2.5 ± 0.1	-4.07	1000 ± 300	ND
	αKG	3.9 ± 0.6	-1.00 ± 0.06	-6.0 ± 0.2	-7.0	8 ± 2	41.0 (19.0 – 80.2) simulated
R132H IDH1	NADPH	0.99 ± 0.04	-11.3 ± 0.2	1.5 ± 0.1	-9.8	0.06 ± 0.01	0.407 (0.142 – 0.642)
	ICT	ND	ND	ND	ND	ND	ND
	αKG	1 (fixed)	0.33	-4.69	-4.36	621	621

ND- Not Determined

4.4.3. HDX analysis for conformational change

We used a stopped-flow spectrophotometer to assess enzyme dynamics upon binding of substrate by using intrinsic protein fluorescence. Tryptophan and tyrosine are spectroscopically active at 280 nm and emitting light at 340 nm. The experiments were rapidly mixing IDH1 with αKG or isocitrate, using Ca^{2+} to prevent turnover, and monitor intrinsic protein fluorescence as a function of time. Previously, it was described that the conformational change upon binding of isocitrate to IDH1 happened at the regulatory domain as it folds from a loop to an α-helix[3, 23]. Unfortunately, this region of the enzyme is spectroscopically silent. We tried attaching

fluorophores and perform the conformational change experiments but a change in fluorescence as a function of time was detected either. A possible way of detecting changes in fluorescence from IDH1 upon binding of substrates is by creating FRET pairings. However, this would be difficult since each fluorophore would have to be at the right distance to allow FRET to happen. Therefore, to have evidence of protein dynamics, we decided to use HDX-MS. Unfortunately, this methodology would not allow us to directly measure any intrinsic rate of conformational change.

HDX-MS is a powerful biochemical and analytical tool to find regions in the protein that are solvent accessible. Proteins are solvent exchanged with buffers that contain D_2O instead of normal water. The hydrogen-deuterium exchange happens between the hydrogen in the peptide bond and the deuterium from the solvent (Figure 8). Then, proteins are digested using pepsin and loaded to a UPLC to separate the fragments and then to a mass spectrometer (MS) to find the molecular weight of each digested peptide (Figure 8). It is powerful to determine protein-protein interactions since when two different proteins bind, the binding region it is not solvent accessible, so the protein will not be able to exchange hydrogens with deuterium from. In our experiments, we used HDX-MS to find regions in the enzyme that changes in deuterium uptake upon binding of substrates.

Since kinetic evidence for a conformational change was not observed upon binding of αKG to R132H IDH1, HDX-MS was performed to probe protein dynamics related to binding of substrate. Additionally, HDX experiments were also done on WT IDH1 to use as a comparison to R132H IDH1. Previous work described a folding of the α10 regulatory domain (N271-G285, Figure 9) upon binding isocitrate in the transition from an open inactive to a closed active conformation[3, 23]. The residues in α10 regulatory domain appear to be solvent exposed, so when this domain is in the unfolded loop conformation, we predict this domain would be more dynamic

and solvent exposed and thus have a higher uptake of deuterium. On the other hand, upon folding of this domain into a helix, we predict the residues would be less dynamic and less solvent exposed, thus, yielding a lower uptake of deuterium. We focused on α10 helix peptides in both WT and R132H IDH1. The best three resolved peptides from each system were used for analysis.

Table 9. HDX-MS results for three peptides in the α10 regulatory domain in WT and R132H IDH1

Mutant	Peptide	System	Max Possible Uptake (Da)	Average Uptake After 5 min Exposure (Da)	% Uptake
WT IDH1	Residue 266-291[a]	APO	25	14	56.0
		$NADP^+$	25	13.2	52.8
		Isocitrate	25	2.7	10.9
	Residue 268-291[b]	APO	23	13.6	59.1
		$NADP^+$	23	13.2	57.4
		Isocitrate	23	2.5	10.9
	Residue 279-288[c]	APO	9	6.15	68.3
		$NADP^+$	9	6.10	67.8
		Isocitrate	9	2.3	25.6
R132H IDH1	Residue 268-278[d]	APO	10	5.4	54.0
		NADPH	10	5.1	51.0
		NADPH + αKG	10	5.2	52.0
		NADPH + αKG + Ca^{2+}	10	5.0	50.0
	Residue 268-291[e]	APO	23	13.2	57.4
		NADPH	23	12.0	52.2
		NADPH + αKG	23	11.1	48.3
		NADPH + αKG + Ca^{2+}	23	11.4	49.6
	Residue 279-288[f]	APO	9	5.9	65.6
		NADPH	9	5.8	64.4
		NADPH + αKG	9	5.5	61.1
		NADPH + αKG + Ca^{2+}	9	5.3	58.9

a. IWACKNYDGDVQSDSVAQGYGSLGMM
b. ACKNYDGDVQSDSVAQGYGSLGMM
c. DSVAQGYGSL
d. ACKNYDGDVQS
e. ACKNYDGDVQSDSVAQGYGSLGMM
f. DSVAQGYGSL

WT IDH1 was analyzed using HDX-MS in the apo form, in complex with $NADP^+$, and in complex with isocitrate. Three peptides were analyzed in the region of the α10 regulatory domain (Table 9). The maximum allowed deuterium uptake is equal to the number of residues in the peptide that is analyzed (Figure 10, Table 9). All three peptides from WT IDH1 showed half uptake whenever isocitrate was not bound (Figure 10 A-C, Table 9). However, once isocitrate was bound, HDX-MS analysis revealed a significant decrease of deuterium uptake (Figure 10 A-C, Table 9) in all three peptides. This means a less dynamic α10 regulatory domain as predicted. These results support previous findings of the transition of the loop conformation to the folded helical conformation (Figure 9)[3, 23]. HDX-MS analysis was also used to determine dynamics at the α10 regulatory domain.

For R132H IDH1, HDX-MS analysis was performed in the apo form, in complex with NADPH, in complex with NADPH and αKG, and in complex with NADPH with αKG and Ca^{2+}. Due to the binding mechanism of mutant IDH1 when performing the neomorphic reaction, NADPH had to be in complex with IDH1 in order to have αKG bound. Moreover, Ca^{2+} was added to prevent turnover of αKG to D2HG. Similar to WT IDH1, three peptides in the α10 regulatory domain were analyzed (Table 9). The average deuterium uptake in all peptides was similar to WT IDH1 (Table 9). These results suggest that R132H IDH1 shows the loop conformation seen on WT IDH1. Interestingly, upon binding of αKG, none of the peptides showed a significant change in deuterium uptake as seen when WT IDH1 in complex with isocitrate (Figure 10 D-F, Table 9). These results suggest that the α10 regulatory domain remains unfolded upon binding of αKG.

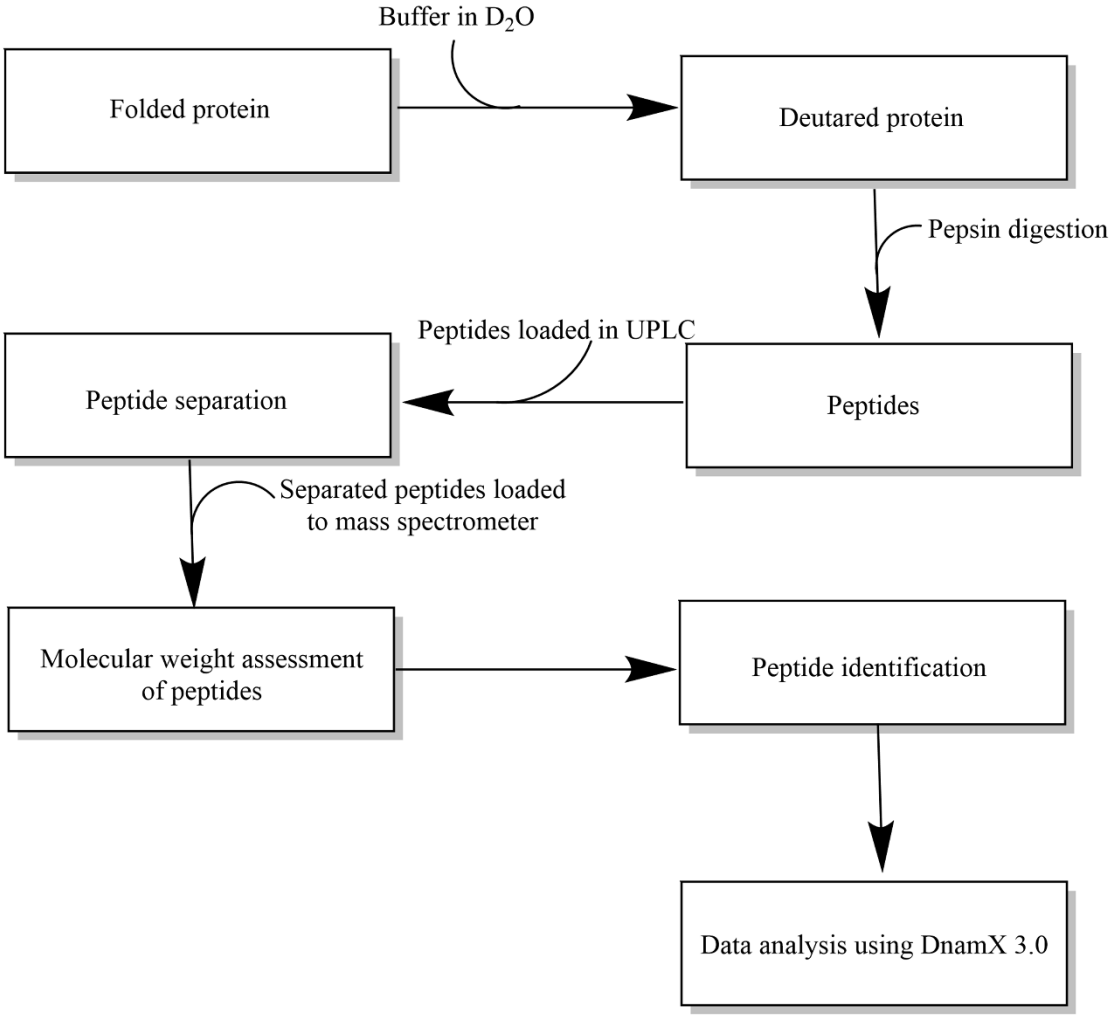

Figure 8. HDX-MS workflow. Pure IDH1 is solvent exchanged with buffer containing D_2O and allow to equilibrate for a certain amount of time. The amide hydrogens in the peptide bonds are rapidly exchange with the deuterium from the solvent as long as that peptide bond is solvent accessible. The enzyme is digested with pepsin and loaded to an UPLC for peptide separation. Subsequently, each separated peptide is loaded to a mass-spectrometer to assess the molecular weight for each peptide so they can be identified. DnamX 3.0 is the software used to analyze the data and assess the uptake of deuterium of each peptide in IDH1.

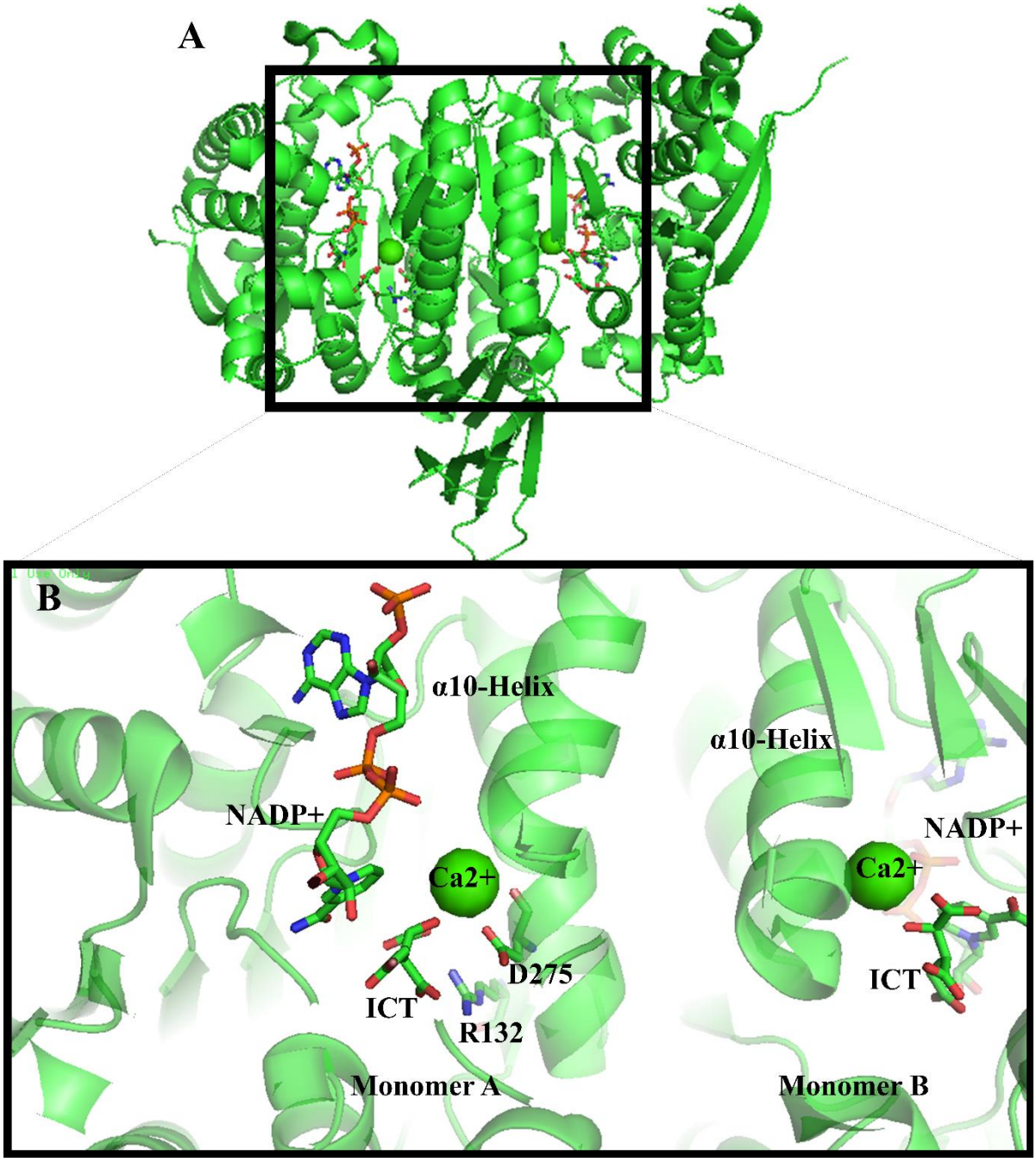

Figure 9. A. Crystal structure of WT IDH1 (1T0L[3]) showing a dimeric enzyme in complexed with $NADP^+$, isocitrate and Ca^{2+}. **B.** A closed up view of the dimer interface showing the α10 regulatory domain in its folded structure. The α10 regulatory domain is at the dimer interface of the enzyme. D275 is highlighted as the residue that coordinates with R132 in the apo form of WT IDH1. This interaction allows for the pre-binding state that then follows to the closed conformation upon binding of isocitrate, folding the α10 regulatory domain into a helix.

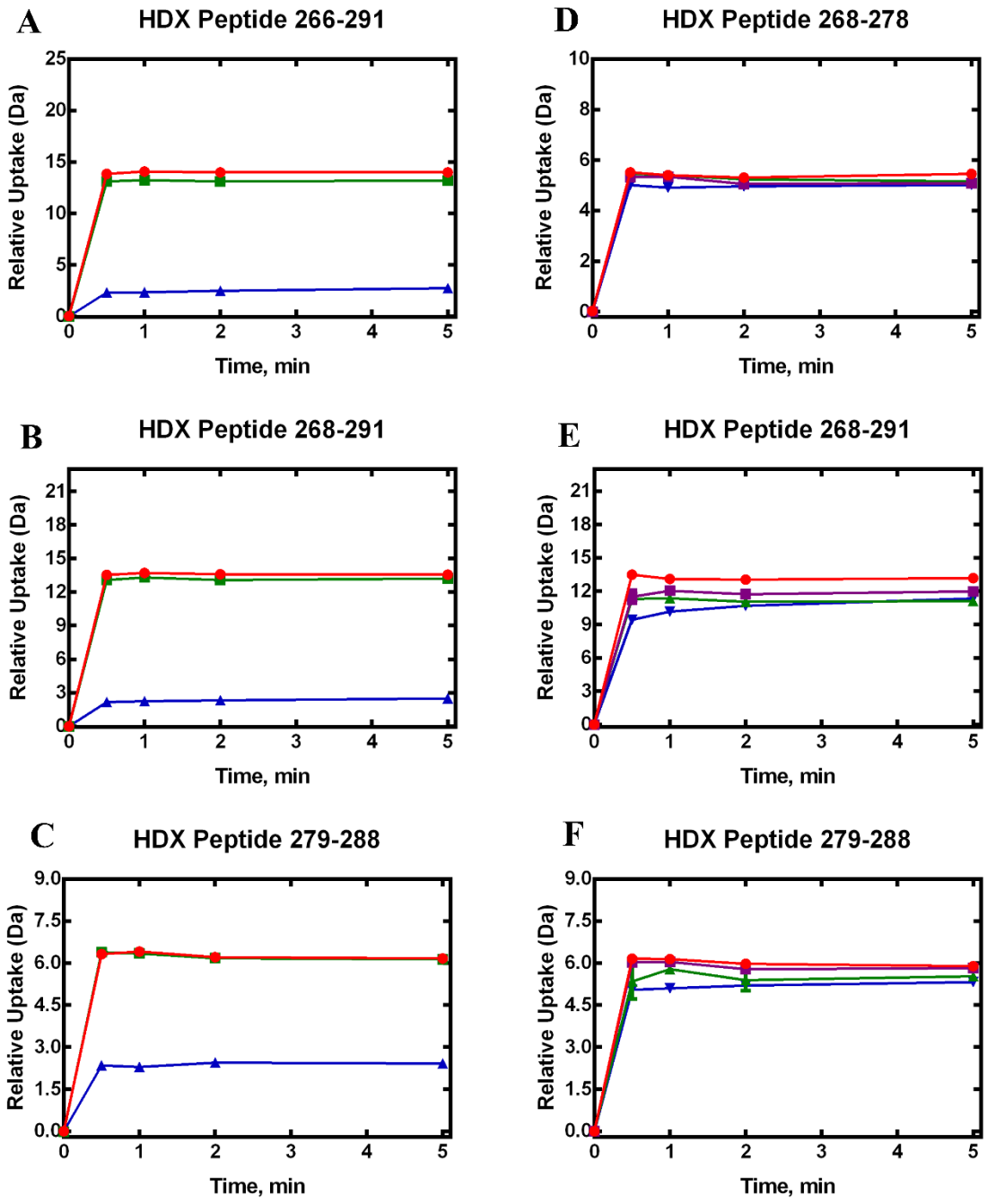

Figure 10. A-C. HDX-MS data analysis for three peptides in the α10 regulatory domain of WT IDH1 in apo (red), bound to $NADP^+$ (green), and bound to isocitrate (blue). The Y-axis represents the maximum uptake of deuterium given by the size of the number of amino acids in the peptide (**A-F)**. A large difference between apo (red) and isocitrate bound (blue) WT IDH1 suggests a loss of flexibility in the α10 regulatory domain attributed to folding of it (Figure 9). **D-F.** HDX-MS data analysis for three peptides in the α10 regulatory domain of R132H IDH1 in apo (red), bound to NADPH (purple), bound to NADPH and αKG (green), and bound to NADPH, αKG, and Ca^{2+} (blue). HDX-MS data analysis of the three peptides in the region revealed a small change in deuterium uptake between apo (red) and both substrates bound (green and blue). Although there is a slight decrease in uptake upon substrate binding, these results suggest that the α10 regulatory domain remains flexible.

4.4.4. ITC to Determine K_D Values for αKG and Isocitrate Binding to IDH1

Obtaining binding affinity for αKG and ICT for each mutant would provide important mechanistic information for the normal and neomorphic reactions. Since binding of αKG and ICT were spectroscopically silent, using stopped-flow fluorescence to measure NADPH binding, was not possible. Therefore, ITC was used to determine the binding equilibrium of αKG and ICT for R132H, R132Q, and WT IDH1. Since NADPH binds before αKG in the neomorphic reaction, R132Q and R132H IDH1 were pre-incubated with NADPH before ITC analysis. αKG was titrated to R132Q IDH1 bound to NADPH and the K_D value for αKG binding to R132Q IDH1 was 8 μM (Table 8). Since both heat being released and absorbed was observed (Figure 11A), this suggested that the heat detected was associated to multiple factors and not only to αKG binding to R132Q IDH1, thus the K_D and stoichiometry of R132Q IDH with αKG are not accurate (Figure 9A, Table 11). αKG was also titrated to R132H IDH1 bound to NADPH yielding a K_D of αKG binding of 621 μM and a stoichiometry of 1 (Figure 11D, Table 8). The $\Delta H_{binding}$ of αKG to R132H IDH1 was endothermic and the -TΔS was favorable enough to yield a negative ΔG (Table 8). Unlike NADPH binding for R132H IDH1, the favorable ΔG is driven by entropy rather than enthalpy.

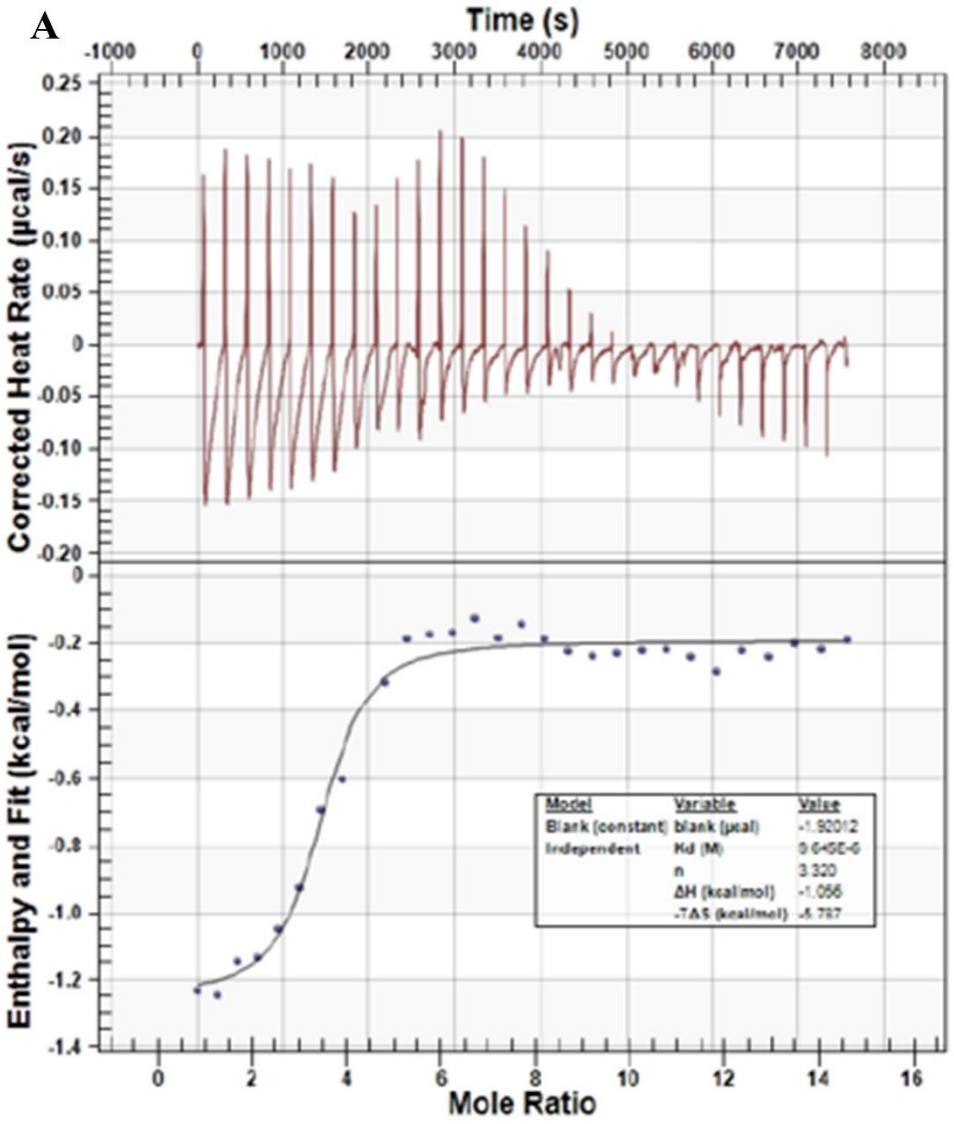

Figure 11. A-E. Isocitrate and αKG binding affinity (K_D) determined for R132Q IDH1 (**A-B**), R132H IDH1 (**C-D**), and WT IDH1 (**E**). Similar to the NADPH binding titrations (Figure 7), the heat generated, or absorbed, by the titration of either isocitrate or αKG is monitored. The top panel represents the raw heat data and the bottom panel shows the area under the curve. At the inflection point of the linear portion in the sigmoidal curve represents the stoichiometry of binding. **A.** αKG titrated to R132Q IDH1. **B.** Isocitrate titrated to R132Q IDH1. **C.** Isocitrate titrated to R132H IDH1. **D.** αKG titrated to R132H IDH1. **E.** Isocitrate titrated to WT IDH1. (Figure continues in next page)

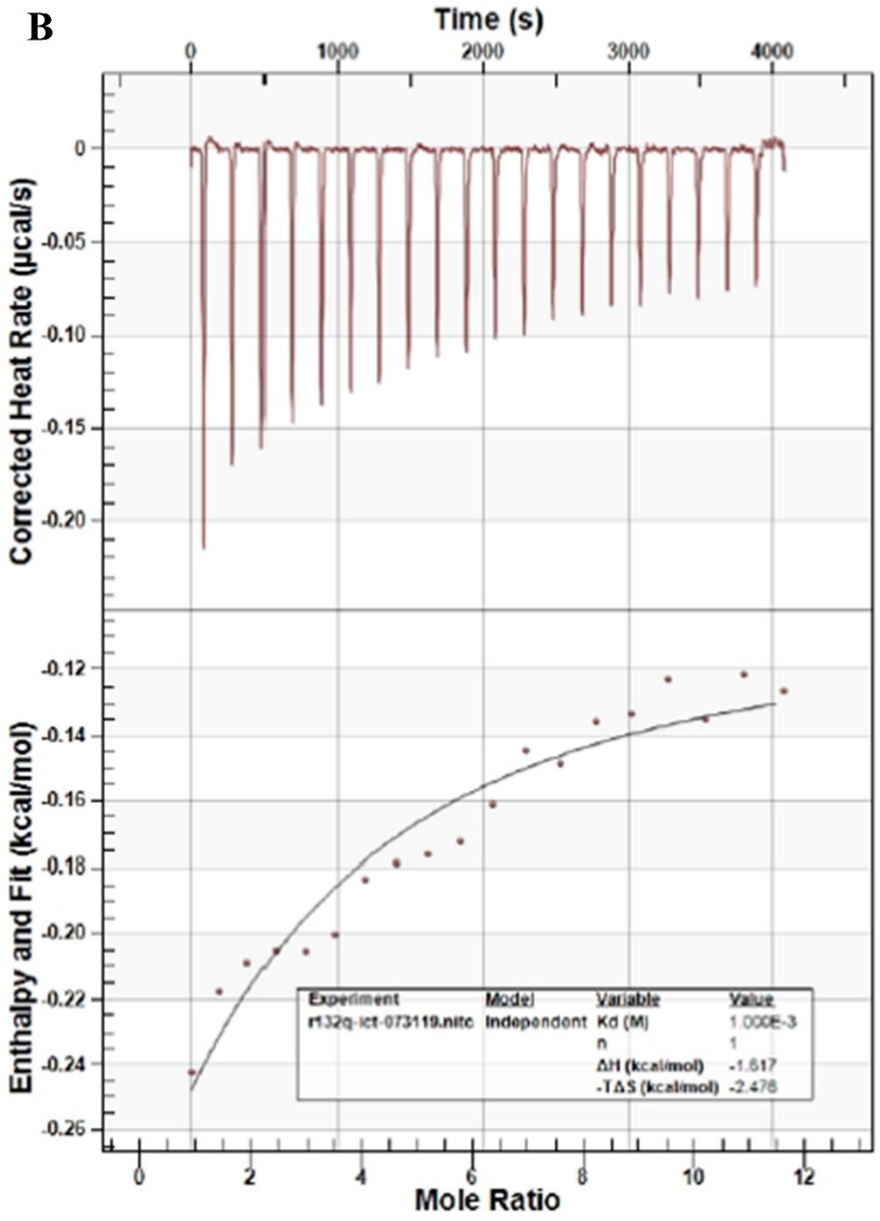

Figure 11. A-E. Isocitrate and αKG binding affinity (K_D) determined for R132Q IDH1 (**A-B**), R132H IDH1 (**C-D**), and WT IDH1 (**E**). Similar to the NADPH binding titrations (Figure 7), the heat generated, or absorbed, by the titration of either isocitrate or αKG is monitored. The top panel represents the raw heat data and the bottom panel shows the area under the curve. At the inflection point of the linear portion in the sigmoidal curve represents the stoichiometry of binding. **A.** αKG titrated to R132Q IDH1. **B.** Isocitrate titrated to R132Q IDH1. **C.** Isocitrate titrated to R132H IDH1. **D.** αKG titrated to R132H IDH1. **E.** Isocitrate titrated to WT IDH1. (Figure continues in next page)

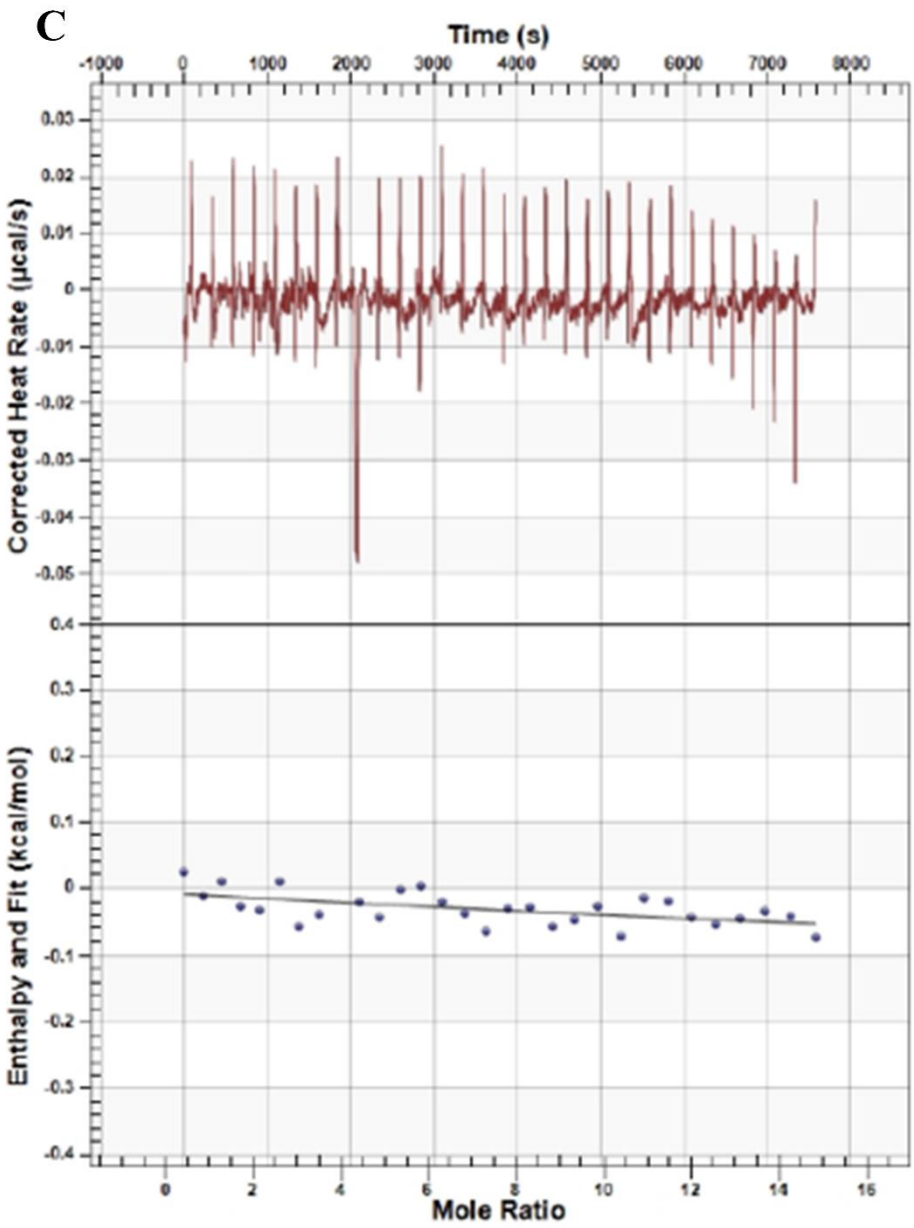

Figure 11. A-E. Isocitrate and αKG binding affinity (K_D) determined for R132Q IDH1 (**A-B**), R132H IDH1 (**C-D**), and WT IDH1 (**E**). Similar to the NADPH binding titrations (Figure 7), the heat generated, or absorbed, by the titration of either isocitrate or αKG is monitored. The top panel represents the raw heat data and the bottom panel shows the area under the curve. At the inflection point of the linear portion in the sigmoidal curve represents the stoichiometry of binding. **A.** αKG titrated to R132Q IDH1. **B.** Isocitrate titrated to R132Q IDH1. **C.** Isocitrate titrated to R132H IDH1. **D.** αKG titrated to R132H IDH1. **E.** Isocitrate titrated to WT IDH1. (Figure continues in next page)

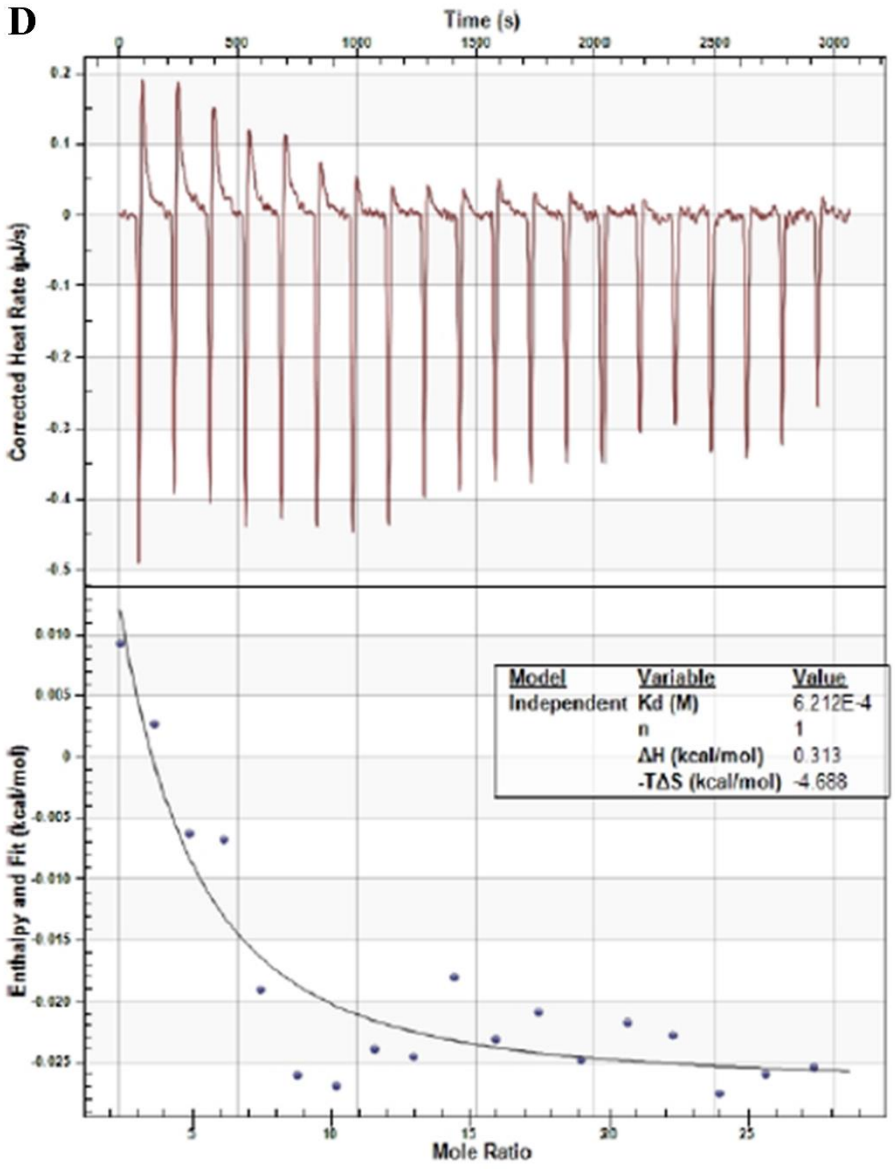

Figure 11. A-E. Isocitrate and αKG binding affinity (K_D) determined for R132Q IDH1 (**A-B**), R132H IDH1 (**C-D**), and WT IDH1 (**E**). Similar to the NADPH binding titrations (Figure 7), the heat generated, or absorbed, by the titration of either isocitrate or αKG is monitored. The top panel represents the raw heat data and the bottom panel shows the area under the curve. At the inflection point of the linear portion in the sigmoidal curve represents the stoichiometry of binding. **A.** αKG titrated to R132Q IDH1. **B.** Isocitrate titrated to R132Q IDH1. **C.** Isocitrate titrated to R132H IDH1. **D.** αKG titrated to R132H IDH1. **E.** Isocitrate titrated to WT IDH1. (Figure continues in next page)

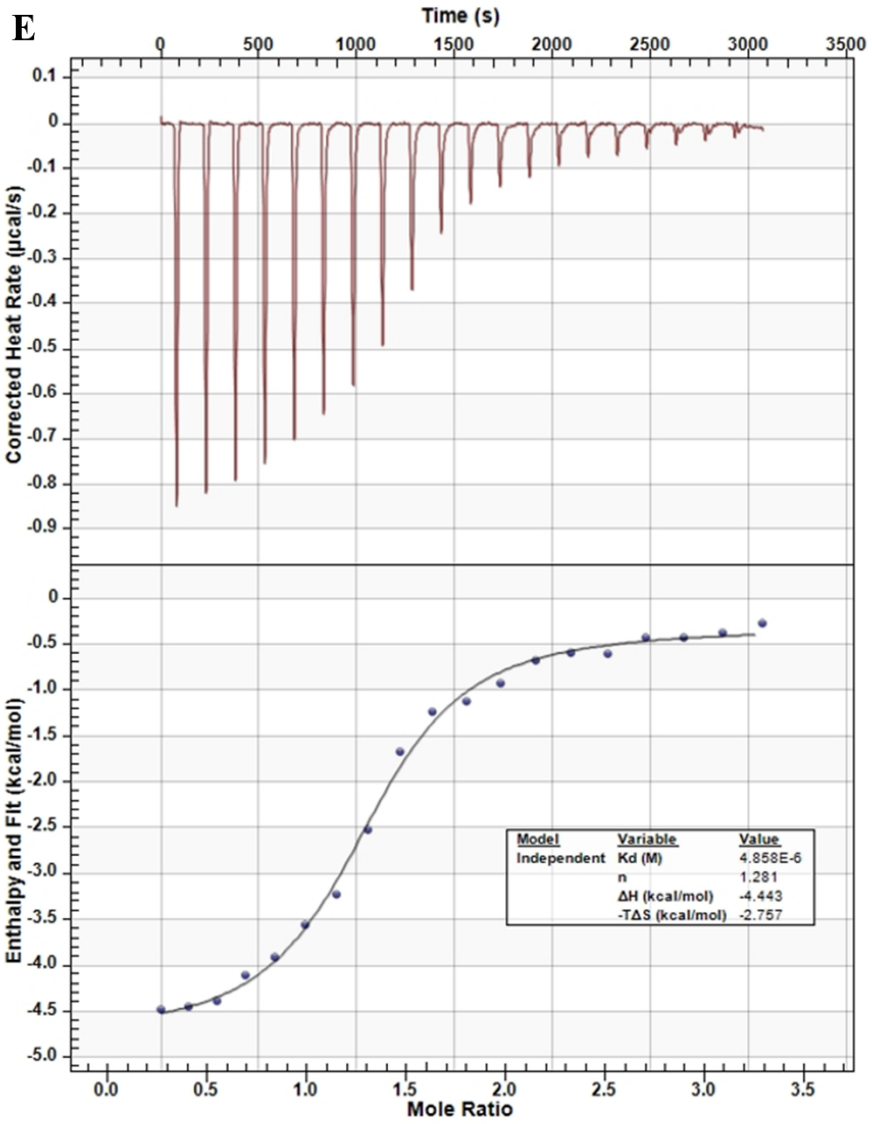

Figure 11. A-E. Isocitrate and αKG binding affinity (K_D) determined for R132Q IDH1 (**A-B**), R132H IDH1 (**C-D**), and WT IDH1 (**E**). Similar to the NADPH binding titrations (Figure 7), the heat generated, or absorbed, by the titration of either isocitrate or αKG is monitored. The top panel represents the raw heat data and the bottom panel shows the area under the curve. At the inflection point of the linear portion in the sigmoidal curve represents the stoichiometry of binding. **A.** αKG titrated to R132Q IDH1. **B.** Isocitrate titrated to R132Q IDH1. **C.** Isocitrate titrated to R132H IDH1. **D.** αKG titrated to R132H IDH1. **E.** Isocitrate titrated to WT IDH1

The binding affinity of R132Q, R132H, and WT IDH1 with isocitrate was also assessed. Isocitrate was titrated to each enzyme and the K_D value of R132Q IDH1 binding to isocitrate was 170-fold higher than WT IDH1 (Table 8). The stoichiometry of WT IDH1 binding to isocitrate was of 1:1.4 (IDH1 monomer:isocitrate) (Table 8). This could be due to the isocitrate solution containing the inactive *L*-enantiomer for IDH1. Therefore, more isocitrate solution is needed to be titrated to the analyte to reach the equivalence point, yielding a higher stoichiometry factor. The $\Delta H_{binding}$ and the -TΔS were both negative thus yielding a favorable ΔG (Table 8). Unlike R132H binding to αKG, both enthalpy and entropy drive a favorable ΔG. R132Q IDH1 showed very weak binding to isocitrate. To calculate the stoichiometry of 1 of R132Q IDH1 to isocitrate binding, the fit was extrapolated to complete the sigmoidal curve. Relative to WT IDH1 binding to isocitrate, the $\Delta H_{binding}$ of R132Q was 2.7-fold lower, but the -TΔS was comparable to WT IDH1 (Table 8). The calculated ΔG of R132Q binding to isocitrate was 1.8-fold lower relative to WT IDH1 (Table 8). Similar to WT IDH1, a favorable ΔG of binding of isocitrate to R132Q is driven by both enthalpy and entropy. Isocitrate was also titrated to R132H IDH1, though no binding was observed indicating a K_D of $\leq$ 5mM (Table 11). Yang and colleagues also used ITC to obtain the K_D of R132H IDH1 to isocitrate, though they did not observe any binding as well[23]. They concluded that R132H IDH1 does not bind to isocitrate since it does not have a pre-binding conformation, required for binding of isocitrate[23].

4.4.5. Single turnover assays to assess rate of hydride transfer.

During a single turnover experiment, enzyme is in excess of at least one substrate to avoid multiple turnovers. Here, product formation is monitored in a single turnover experiment. The observed rate, the k_{obs}, represents the binding of αKG, conformational change(s), and hydride transfer (Figure 2). To describe reaction mechanisms with individual rate constants, pre-steady-

state kinetic experiments need to be designed in such a way where reactions are prevented from moving forward, or the reaction species monitored reports on as few steps as possible. Often, experiments may not be designed in such a way where individual steps are isolated or measured, and in this case, observed rates (k_{obs}) will report on multiple steps. To remove the rate of binding of NADPH to IDH1, we pre-incubated R132H and R132Q IDH1 with NADPH, and then rapidly mixed this incubation with αKG to measure k_{obs} of a single turnover of the neomorphic reaction (Figure 1B). To measure the k_{obs} of a single turnover of the normal reaction, R132Q and WT IDH1 were first pre-incubated with $NADP^+$ to allow binding of this substrate to come to equilibrium. The same strategy was used to allow binding of NADPH to R132H and R132Q IDH1 to come to equilibrium when monitoring the neomorphic reaction. In the normal forward reaction (Figure 1A), enzyme (WT or R132Q IDH1) in binding equilibrium with $NADP^+$ was rapidly mixed using a stopped-flow spectrophotometer with isocitrate and Mg^{2+}, and the fluorescence signal corresponding to NADPH was monitored (Figure 12). Likewise, enzyme (R132Q and R132H IDH1) pre-bound to NADPH was rapidly mixed with αKG and Mg^{2+}, and the change in signal corresponding to NADPH depletion (Figure 12). We hypothesized that hydride transfer was the rate limiting step based on previous work on E.coli IDH1[24, 25]. Thus, we expect that fitting our observed single exponential increase of NADPH formation yield a k_{obs} value similar to our previously reported value of the maximal rate of steady-state formation of αKG, or k_{cat} of 4.7 and 1.5 s^{-1} for R132Q and R132H IDH1 respectively[4, 16] (Table 10). For the neomorphic reaction, the k_{obs} values from the single exponential fit of the NADPH depletion should be similar to the maximal rate of steady-state formation of D2HG, or k_{cat} values of 9.2 and 40 s^{-1} for R132Q and WT IDH1[4, 16], respectively (Table 10).

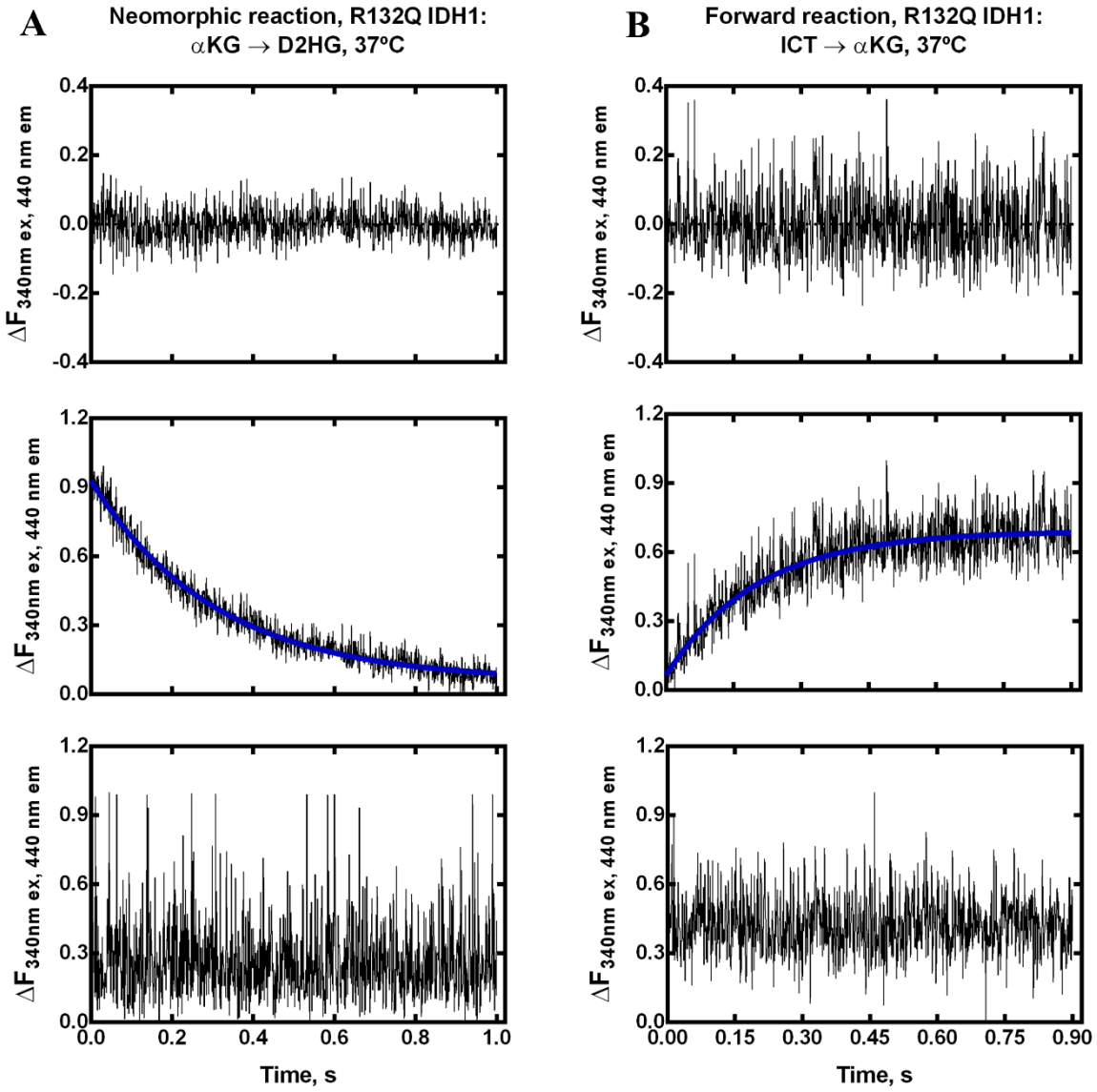

Figure 12. Single turnover experiments using a stopped-flow spectrophotometer. **A.** Single turnover experiment of R132Q IDH1 catalyzing the reduction of αKG to D2HG. **B.** Single turnover experiment of R132Q IDH1 catalyzing the oxidative decarboxylation of isocitrate to αKG. **C.** Single turnover experiment of R132H IDH1 catalyzing the reduction of αKG to D2HG. **D.** Single turnover of WT IDH1 catalyzing the oxidative decarboxylation of isocitrate to αKG. In all cases, NADPH (either depletion as in **A** and **C**, or formation as in **B** and **D**) is monitored as a function of time. A single exponential equation ($Y = A_0e^{-kt}$) was fit to each experiment and residuals were obtained to assess goodness of fit. The k_{obs} values for each experiment matched our previously published k_{cat} values, suggesting hydride transfer as the rate limiting step of the catalytic cycle.(Figure continues in next page)

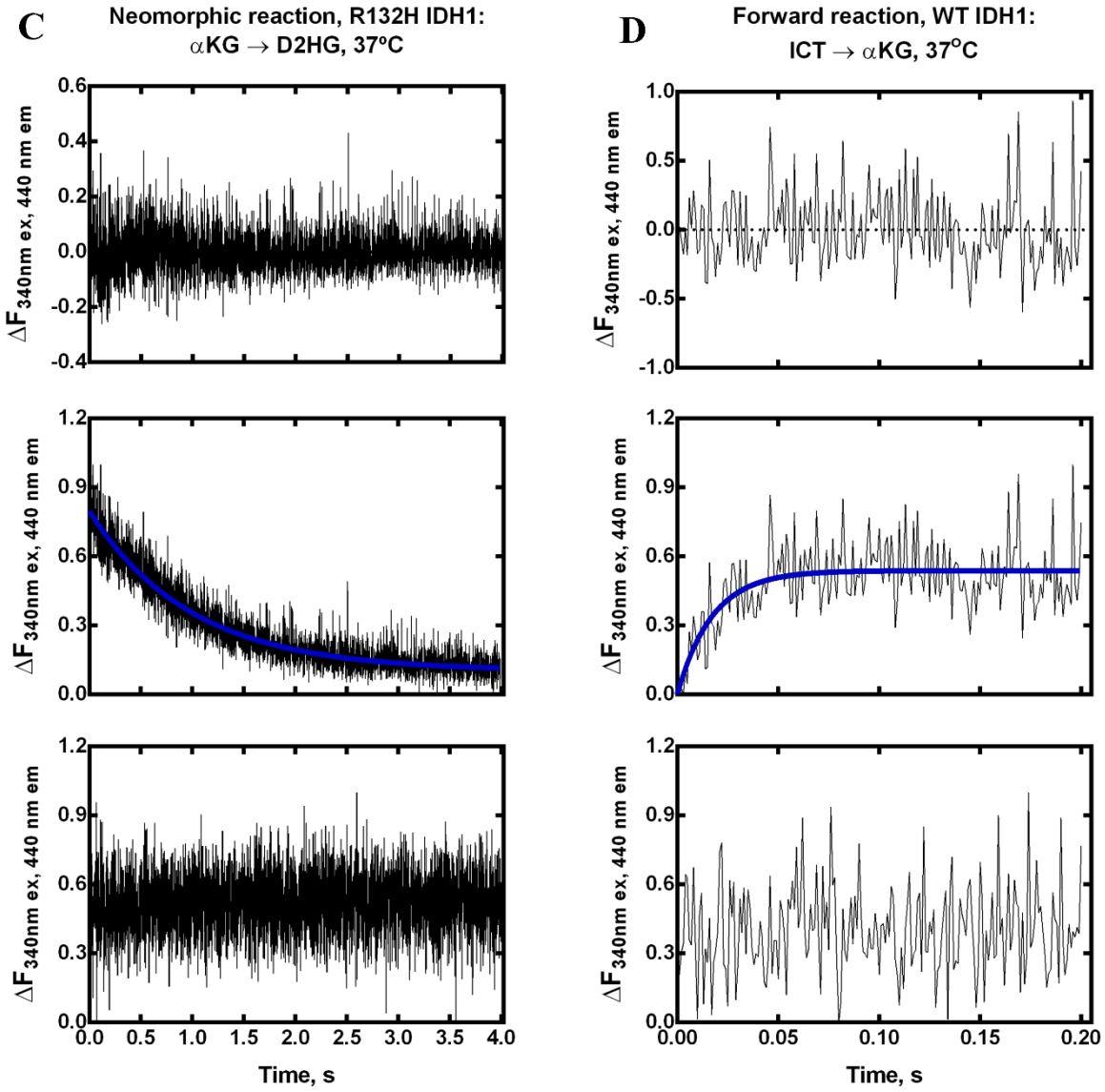

Figure 12. Single turnover experiments using a stopped-flow spectrophotometer. **A.** Single turnover experiment of R132Q IDH1 catalyzing the reduction of αKG to D2HG. **B.** Single turnover experiment of R132Q IDH1 catalyzing the oxidative decarboxylation of isocitrate to αKG. **C.** Single turnover experiment of R132H IDH1 catalyzing the reduction of αKG to D2HG. **D.** Single turnover of WT IDH1 catalyzing the oxidative decarboxylation of isocitrate to αKG. In all cases, NADPH (either depletion as in **A** and **C**, or formation as in **B** and **D**) is monitored as a function of time. A single exponential equation ($Y = A_0e^{-kt}$) was fit to each experiment and residuals were obtained to assess goodness of fit. The k_{obs} values for each experiment matched our previously published k_{cat} values, suggesting hydride transfer as the rate limiting step of the catalytic cycle.

R132Q IDH1 showed a $k_{chem,\ \alpha KG}$ (rate of hydride transfer for the neomorphic reaction) that was 1.4-fold lower than the k_{cat} value that we reported previously[4, 16] (Table 10). R132H IDH1 also showed a 1.5-fold lowered $k_{chem,\ \alpha KG}$ compared to the reported k_{cat}[16] (Table 10). However, high concentrations of αKG were needed to reduce the initial lag phase, that is likely linked to slow binding of the substrate to the enzyme. The single turnover rate ($k_{chem,\ ICT}$) of the conversion of isocitrate to αKG by WT IDH1 was 58 s^{-1} (Table 10), which was 1.5-fold higher than the k_{cat}[16]. The measure $k_{chem,\ ICT}$ of R132Q IDH1 for the normal reaction was 2-fold lower than the k_{cat} associated with the normal reaction of R132Q IDH1[4] (Table 10). These rates are in close agreement with our previously published k_{cat} values[4, 16], supporting our hypothesis that the rate-limiting step of the catalytic cycle is hydride transfer for WT and all mutant variants studied.

Table 10. Single turnover experiment fitting results.

Mutant	$k_{chem,\ ICT}$ (s^{-1})	$k_{chem,\ \alpha KG}$ (s^{-1})
WT IDH1	58 ± 10	ND
R132Q IDH1	4.9 ± 0.2	3.27 ± 0.06
R132H IDH1	ND	1.01 ± 0.01

ND- Not Determined

4.4.6. Burst kinetics analysis of IDH1

In order to ensure a step after chemistry (for example, product release) is not rate limiting, we performed a burst kinetics pre-steady-state assay. When performing burst kinetic assays, excess substrate (about 5-fold higher) relative to enzyme is used to determine a single turnover phase (pre-steady state) followed by a multiple turnover phase (steady state) as observed on a plot of product formation versus time (Figure 13). This occurs only if the rate limiting step of the catalytic cycle occurs after chemistry. If the enzyme "bursts," the data are fitted to a biphasic equation that has single exponential followed by a linear phase ($Y = Ae^{-kt} + mx + c$, Figure 7). The single

exponential corresponds to the pre-steady state portion of the experiment and the linear phase describes the steady-state rate (Figure 13).

In order to assess if a step after chemistry is rate limiting, we again used a stopped-flow spectrophotometer to monitor the formation (normal forward reaction) or depletion of NADPH (neomorphic reaction). The reactions were monitored for longer time points in order to observe multiple turn overs. R132Q and R132H IDH1 were incubated with 5-fold higher concentration of NADPH relative to enzyme concentration. For the neomorphic reaction, R132Q and R132H IDH1 were pre-incubated with NADPH to reach binding equilibrium, and this incubation was rapidly mixed with and the NADPH depletion was monitored. The depletion of NADPH did not show evidence of burst kinetics (a single exponential followed by a linear phase) for both mutants (Figure 14), instead, a steady-state reaction was observed. These results indicate that product release is the rate-limiting for the neomorphic reaction.

For the normal forward reaction, R132Q and WT IDH1 were incubated with 5-fold higher concentration of $NADP^+$ relative to enzyme concentration. R132Q and WT IDH1 were pre-incubated with $NADP^+$ to reach binding equilibrium, and they were rapidly mixed with isocitrate and Mg^{2+} using a stopped-flow spectrophotometer, and the signal changed associated with NADPH formation was monitored. Similar to the neomorphic reaction, the formation of NADPH did not show evidence of burst kinetics (Figure 14), and instead a steady-state-state reaction was observed. This again suggests that for the normal forward reaction, product release is not rate-limiting.

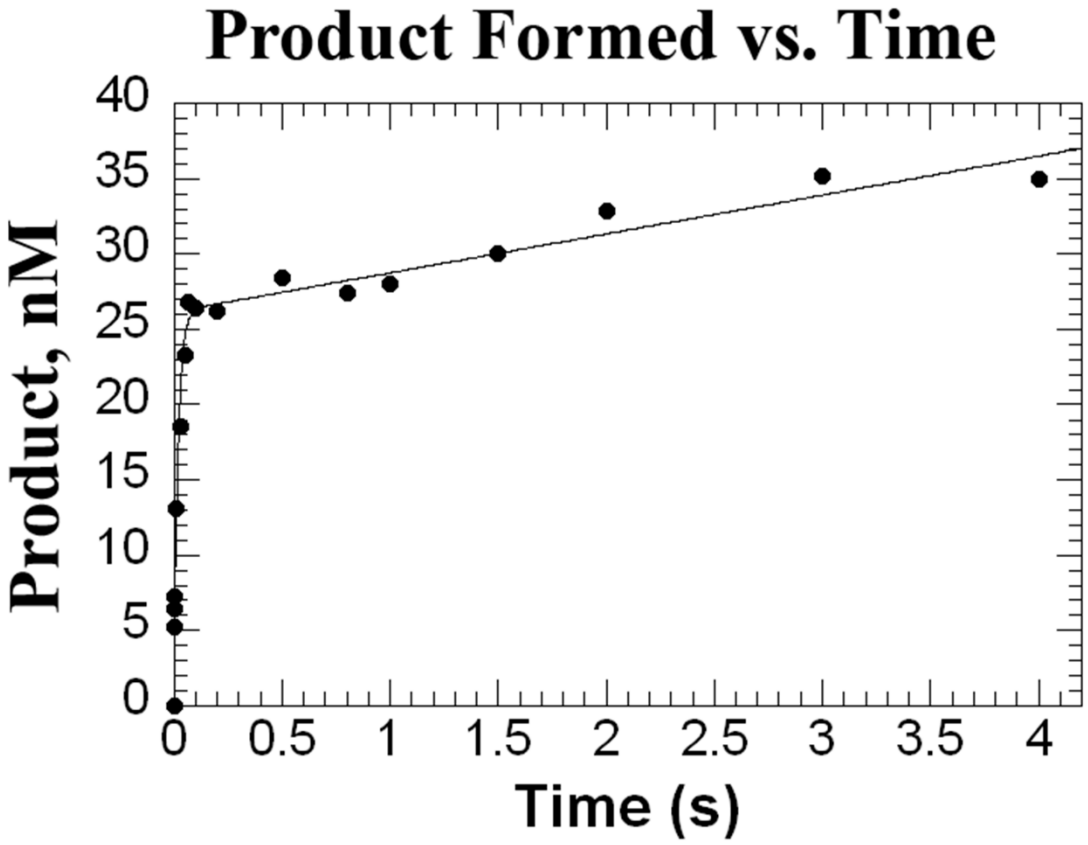

Figure 13. An example of a burst kinetic assay results. Under burst conditions, a slight excess of substrate is added to enzyme to allow for multiple turnovers. The short time points for each experiment allow us to identify the pre-steady state portion (as a single exponential) and the steady-state portion (as a linear phase). The biphasic nature of this graph is associated as the rate-limiting step happens after chemistry.

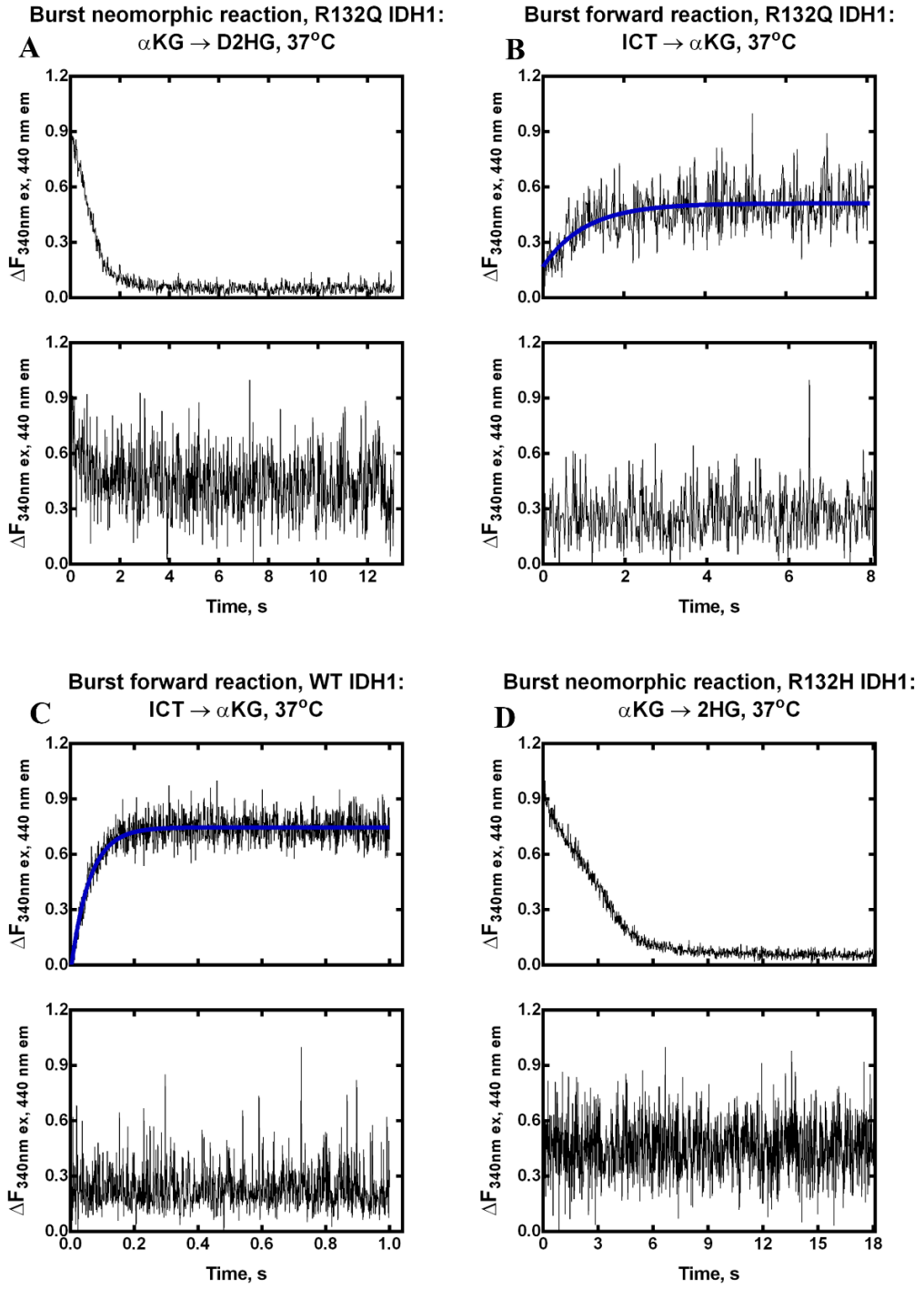

Figure 14. Burst kinetic assays for each mutant studied using a stopped-flow spectrophotometer. **A** and **D.** NADPH depletion was monitored as a function of time. **B** and **C.** NADPH formation was monitored as a function of time. In all cases, a burst behavior was not observed as any of the mutant forms studied show a biphasic profile. These results confirm that hydride transfer is the rate-limiting step for both the normal and the neomorphic reaction. **A.** R132Q IDH1 catalyzing the neomorphic reaction. **B.** R132Q IDH1 catalyzing the normal reaction. **C.** WT IDH1 catalyzing the normal reaction. **D.** R132H IDH1 catalyzing the neomorphic reaction.

4.4.7. Global Fitting Software to Determine Intrinsic Rate Constants in the Catalytic Cycle of the Neomorphic Reaction

The proposed catalytic cycle of mutant IDH1 catalyzing the neomorphic reaction consists of ordered binding mechanism of NADPH followed by αKG[17], a conformational change[3, 23], chemistry (hydride transfer), and product release (Figure 2A). Experiments were designed to elucidate rate constants for as many steps as possible and to have kinetic evidence that each step is occurring in the catalytic cycle. Usually, enzymologists use mathematical functions (analytical fitting), such as a single exponential equation, to describe a pattern observed in an experiment. The downside of analytical fitting is that simplifying assumptions are made, and it is not possible to fit simultaneously multiple kinetic experiments that monitor different steps in the cycle. Kintek Explorer Global Fitting Software uses computer simulations[30, 31] to fit globally experimental data from different steps in the catalytic cycle to predict individual rate constants. Moreover, with computer simulations, it is not necessary to perform simplifying assumptions and mathematical functions are not required. Kintek Global Fitting Software performs 2D Fitspace analysis (Figure 15). It consists in comparing the boundaries for each rate constant with each other, providing a more accurate and precise solutions for each rate constant value. With the help of our pre-steady state kinetic and ITC experiments, we were able to create two possible models for the catalytic cycle of mutant IDH1 catalyzing D2HG production.

The first model is more complex, including a conformational change (Figure 2A), while the second-simpler model, omits this conformational change since we could not measure this step experimentally (Figure 2B). The models were used to fit data describing R132H IDH1 catalysis and for R132Q IDH1. In the case of R132Q IDH1, only the simpler model was reported because

an accurate K_D could not be obtained (Table 8), precluding us from constraining the rates of binding and dissociation of αKG.

Table 11. Global fitting results

Mutant	Kinetic Parameters		Lower Boundary	Upper Boundary
R132Q IDH1	k_1	5.77 $\mu M^{-1}s^{-1}$	5.34	6.35
	k_{-1}	<0.345 s^{-1}	ND	ND
	k_2	0.775 $\mu M^{-1}s^{-1}$	0.620	1.07
	k_{-2}	31.8 s^{-1}	20.4	49.7
	k_3 ($k_{chem,\ \alpha KG}$)	3.57 s^{-1}	3.21	3.93
	k_{-3}	0 s^{-1}	ND	ND
	k_4	100 s^{-1}	ND	ND
	k_{-4}	0 $\mu M^{-1}s^{-1}$	ND	ND
	k_5	100 s^{-1}	ND	ND
	k_{-5}	0 $\mu M^{-1}s^{-1}$	ND	ND
R132H IDH1	k_1	2.08 $\mu M^{-1}s^{-1}$	2.01	2.19
	k_{-1}	0.846 s^{-1}	0.312	1.29
	k_2	0.00472 $\mu M^{-1}s^{-1}$	0.00241	0.00737
	k_{-2}	2.93 s^{-1}	ND	ND
	k_3 ($k_{chem,\ \alpha KG}$)	1.05 s^{-1}	0.974	1.13
	k_{-3}	0 s^{-1}	ND	ND
	k_4	100 s^{-1}	ND	ND
	k_{-4}	0 $\mu M^{-1}s^{-1}$	ND	ND
	k_5	100 s^{-1}	ND	ND
	k_{-5}	0 $\mu M^{-1}s^{-1}$	ND	ND

ND-Not Determined

R132H and R132Q IDH1 were modeled as shown inFigure 2B. The NADPH binding kinetics experiments performed at ambient temperature for R132Q and R132H IDH1 were used for global fitting. The k_1 (k_{on} for NADPH binding) for R132Q IDH1 was 2.8-fold greater than

R132H IDH1 (Table 11). Well constrain k_1 values for these rates as indicated by Fitspace editor suggests high confidence for this rate constant for both mutants (Table 11). In particular, the high quality data of NADPH binding kinetic experiments for R132H IDH1 allowed for a highly constrain k_{-1} (k_{off} for NADPH) value that was narrowly bounded (Table 12). However, R132Q IDH1 had lower quality NADPH binding kinetic data, thus, only an upper limit was reported (Table 11). However, the k_{-1} rate for NADPH binding to R132Q IDH1 was at least 2.5-fold lower than R132H IDH1. These simulation results suggest higher affinity of NADPH for R132Q than R132H IDH1 (Table 11). Moreover, the NADPH binding kinetic experiments for R132Q IDH1 had higher concentration of glycerol (Table 11), and thus, the NADPH binding likely favors R132Q over R132H IDH1 to a higher degree than shown here.

The rates of binding of R132Q and R132H IDH1 to αKG were modeled (Figure 2B). The rate of binding of αKG (k_2) to R132Q IDH1 was 160-fold faster than R132H IDH1 (Table 11). The k_2 values were well constrained for both mutants (Table 11). Since the K_D of αKG binding to R132H IDH1 was measured (Table 11), the k_{-2} value (rate of dissociation of αKG) was constrained with k_2 in such way that the ratio of these rates was equal to 621 μM ($K_D = k_{-2}/k_2$, Table 8). Since an accurate K_D for R132Q IDH1 was not determined (Table 11), the rate of dissociation of αKG (k_{-2}) was allowed to vary (i.e. not constrained in a ratio with k_2). Therefore, only lower and upper boundaries were determined for the rate of dissociation of αKG (Table 11). The rate of dissociation of αKG was 11-fold faster for R132Q than R132H IDH1 (Table 11). However, the simulated K_D of R132Q IDH1 with αKG is > 7.7-fold lower (Table 11), suggesting a very fast on rate of αKG binding to R132Q IDH1.

Single turnover experiments for the neomorphic reaction were also used in global fitting software in order to determine the rate of chemistry ($k_{chem,\ \alpha KG}$). The rate of chemistry for R132H

and R132Q IDH1 was consistent with our previously reported k_{cat}[4, 16] (Table 11), suggesting that αk_3 is the rate-limiting step of the catalytic cycle. Tight boundaries for the rate of chemistry were determined, allowing us to have high confidence on our values (Table 11, Figure 15). The rate of chemistry for R132Q IDH1 was 3.4-fold faster than R132H IDH1 (Table 11). Since the neomorphic reaction is not predicted to be reversible, since there is buildup of D2HG in tumors harboring IDH1 mutations, thus suggesting an irreversible process[15], the k_{-3} was set to 0 s^{-1}. Since product release is not rate-limiting, k_4 and k_5 were set to 100 s^{-1}, while k_{-4} and k_{-5} were set to 0 $\mu M^{-1}s^{-1}$ (Table 12). Locking these rate constants as such indicated that the rate of product release was not rate limiting.

Table 12. Global fit results for R132H IDH1 mechanism including conformational change

Mutant	Kinetic Parameters		Lower Boundary	Upper Boundary
R132H IDH1	k_1	2.06 $\mu M^{-1}s^{-1}$	1.99	2.14
	k_{-1}	0.843 s^{-1}	ND	ND
	k_2	0.0047$\mu M^{-1}s^{-1}$	0.00376	0.00652
	k_{-2}	2.92 s^{-1}	ND	ND
	k_3	53.2 s^{-1}	14	183
	k_{-3}	7.49x10^{-7} s^{-1}	7.49x10^{-10}	7.49x10^{-6}
	αk_4 (k_{chem})	0.979 s^{-1}	0.942	1.08
	k_{-4}	0 s^{-1}	ND	ND
	k_5	100 s^{-1}	ND	ND
	k_{-5}	0 $\mu M^{-1}s^{-1}$	ND	ND
	k_6	100s^{-1}	ND	ND
	k_{-6}	0 $\mu M^{-1}s^{-1}$	ND	ND

ND-Not Determined

Since R132H IDH1 had better quality NADPH binding kinetic data as well as reliable ITC data, global fitting was performed in order to probe what rates associated to conformational change (Figure 2A), though this model is admittedly more speculative. The rate of binding of NADPH and αKG were the same as the previous model (Table 12). Since the k_{-1} (rate of NADPH dissociation) from the previous model of R132H IDH1 yielded tight boundaries, the rate of binding and dissociation of NADPH were constrained together so that the ratio was equal to 0.407 μM (Table 13). This minimized the number of solutions for rates associated of conformational change (k_3 and k_{-3} from Figure 2A). Likewise, rates associated to αKG binding (k_2 and k_{-2} from Figure 2A) were constrained so that the ratio of these rates was equal to the K_D of R132H IDH1 with αKG as in the previous model (Table 12). The simulated rate of conformational change (k_3 from Figure 2A) was equal to 53 s^{-1}. However, due to lack of experimental data to determine or at least constrain conformational change rates, the boundaries were large (Table 12). Moreover, the k_{-3} (Figure 2A) was very slow, suggesting that if a conformational change takes place, this physical process is almost unidirectional (Table 12), which seems unlikely, especially given our MD data[16]. The other rate constants in this model matched the ones from the previous model of R132H IDH1 (Table 12).

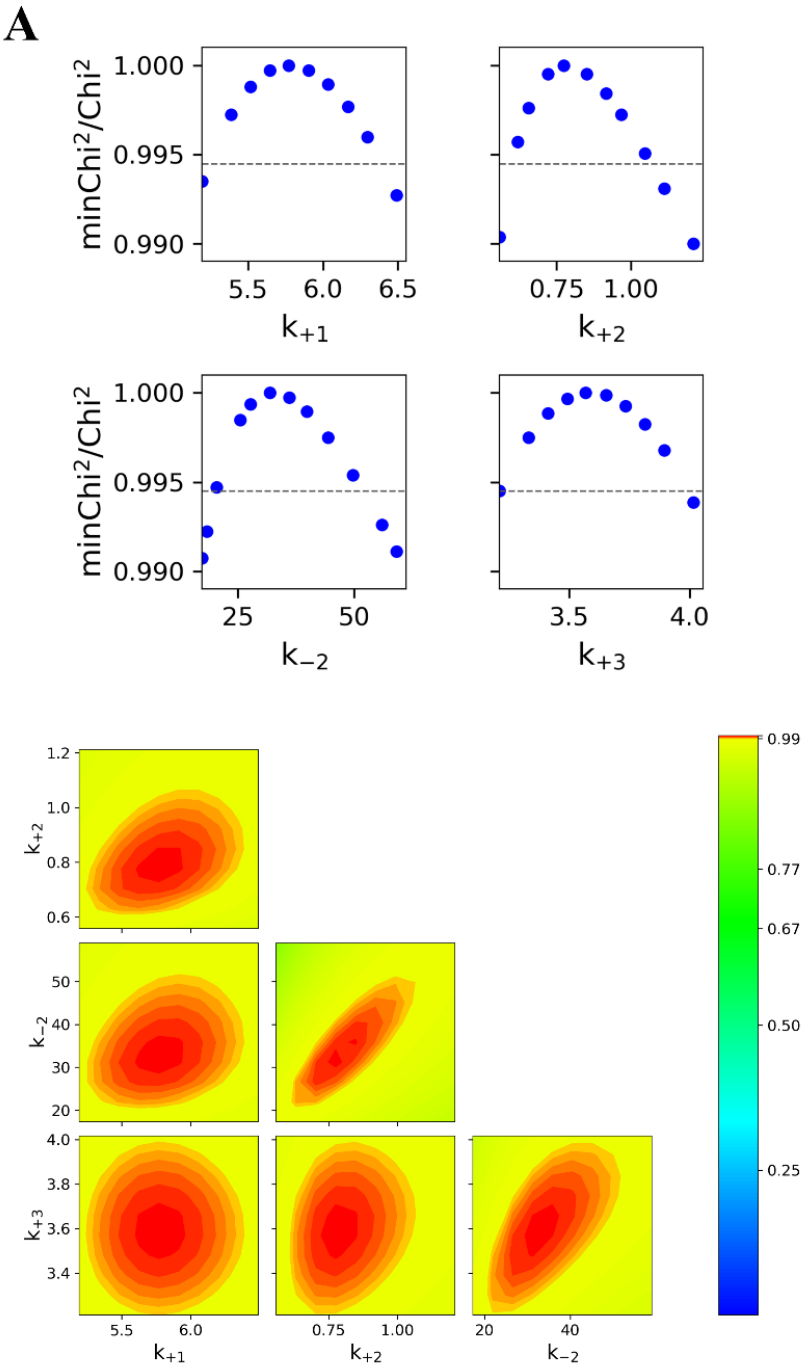

Figure 15. 2D Fitspace results from Kintek Global Fitting Software. In all cases, each intrinsic rate constant is assessed for lower and upper limits to determine how constrain each rate is (top panel) and then compared within each other to calculate how each rate constant compare with each other. The brighter red indicates that the value for that specific rate constant is constrain within those parameters as compared with a different rate constant. **A.** R132Q IDH1 Fitspace results following the model inFigure 2B. **B.** R132H IDH1 Fitspace results following the model inFigure 2B. **C.** R132H IDH1 Fitspace results following the model inFigure 2A. (Figure continues in next page)

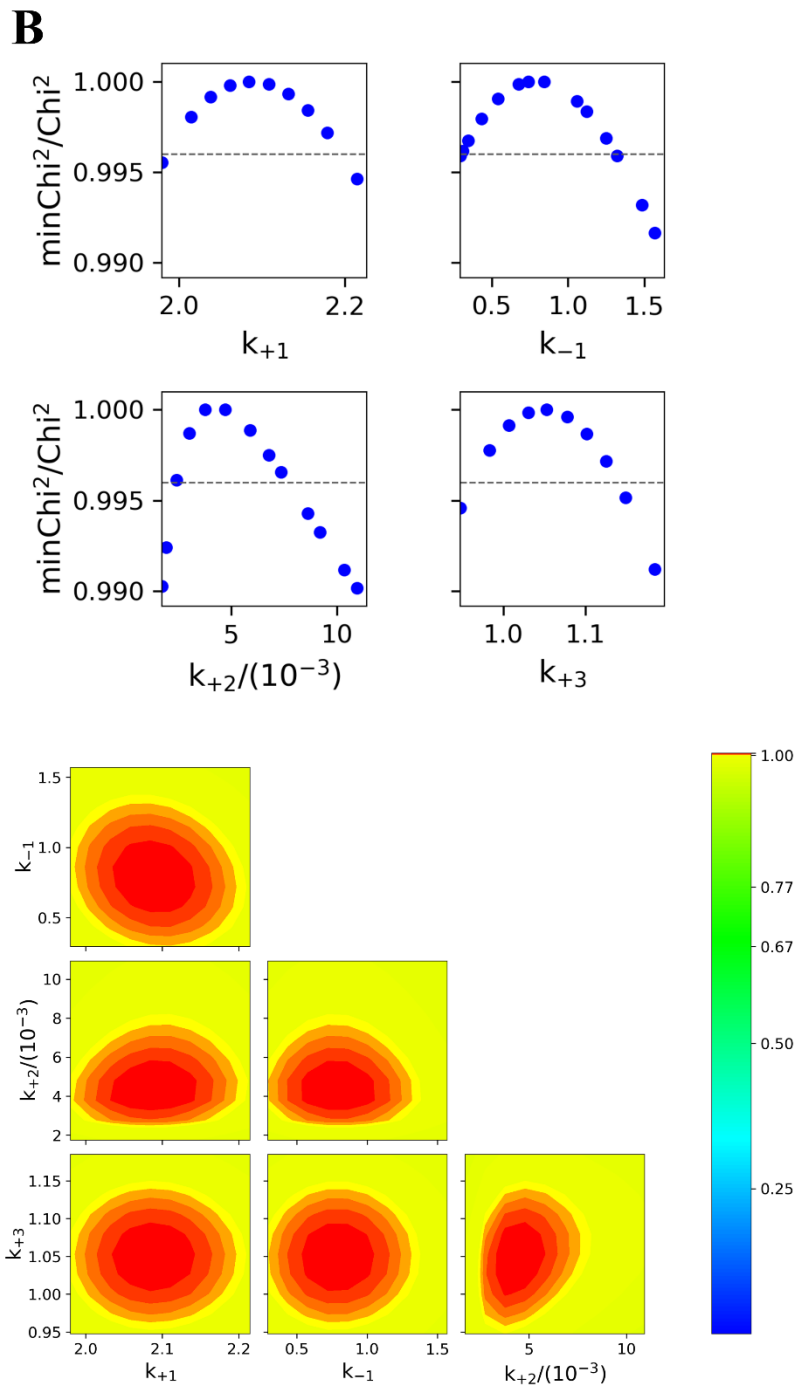

Figure 15. 2D Fitspace results from Kintek Global Fitting Software. In all cases, each intrinsic rate constant is assessed for lower and upper limits to determine how constrain each rate is (top panel) and then compared within each other to calculate how each rate constant compare with each other. The brighter red indicates that the value for that specific rate constant is constrain within those parameters as compared with a different rate constant. **A.** R132Q IDH1 Fitspace results following the model inFigure 2B. **B.** R132H IDH1 Fitspace results following the model inFigure 2B. **C.** R132H IDH1 Fitspace results following the model inFigure 2A. (Figure continues in next page)

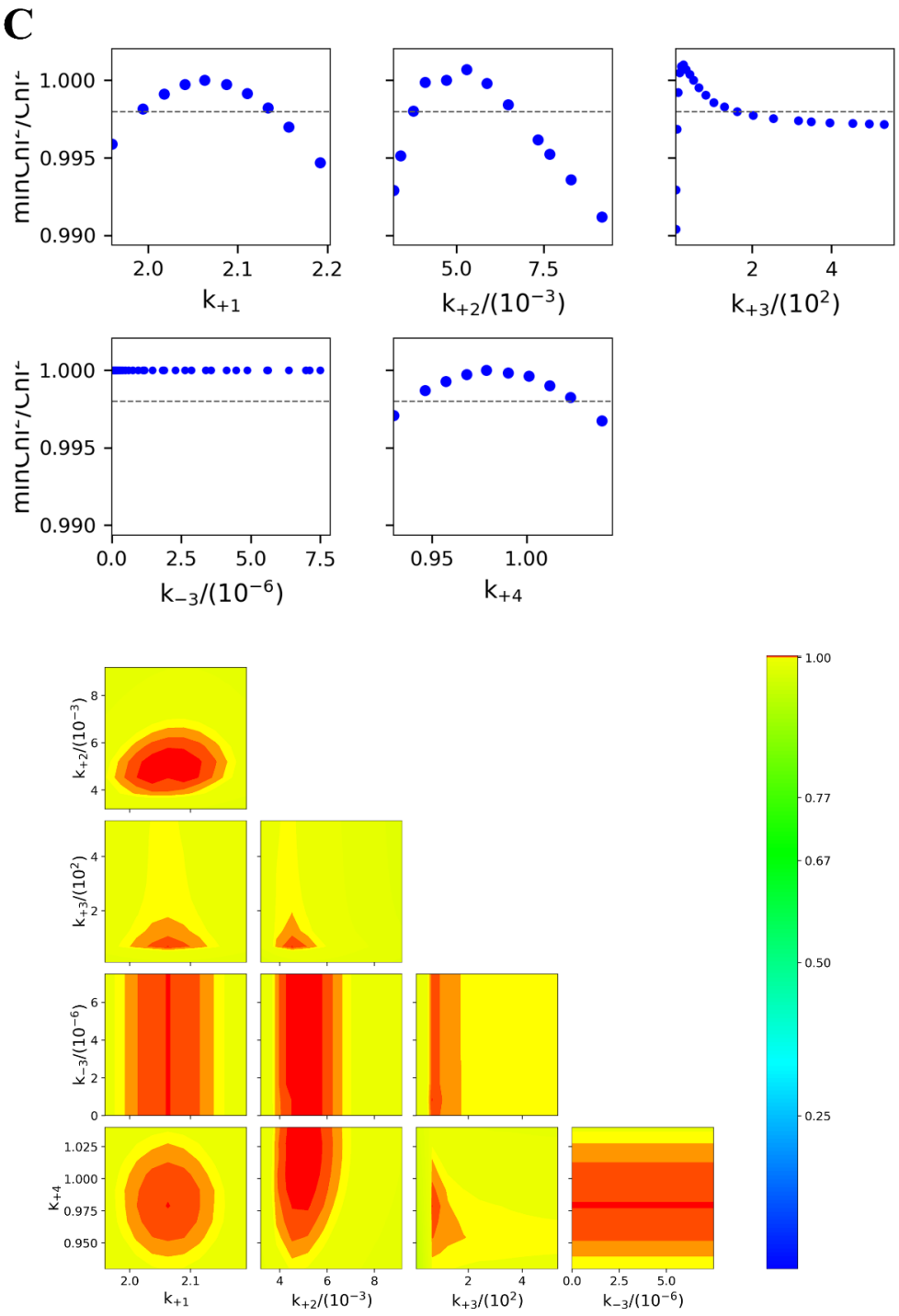

Figure 15. 2D Fitspace results from Kintek Global Fitting Software. In all cases, each intrinsic rate constant is assessed for lower and upper limits to determine how constrain each rate is (top panel) and then compared within each other to calculate how each rate constant compare with each other. The brighter red indicates that the value for that specific rate constant is constrain within those parameters as compared with a different rate constant. **A.** R132Q IDH1 Fitspace results following the model inFigure 2B. **B.** R132H IDH1 Fitspace results following the model inFigure 2B. **C.** R132H IDH1 Fitspace results following the model inFigure 2A.

4.4.8. Progress on Obtaining Structural Information for R132Q IDH1 Using X-ray Crystallography

The structure of R132Q IDH1 has not yet been determined. As this mutant uniquely performs the neomorphic reaction while conserving some normal activity, a comparison of its structural features with WT and R132H IDH1 would be highly valuable[4, 16]. Moreover, this mutant is not susceptible to inhibition by mutant IDH1 small molecule inhibitors, similar to WT IDH1[16]. Therefore, we predict that if a mutant IDH1 enzyme conserves WT activity, then it would not be susceptible to small molecule inhibitor binding. MD simulations suggested that R132Q IDH1 interconverts between mutant-like and WT-like conformations[16]. Yang and colleagues described the pre-binding conformation of WT IDH1 is maintained at least in part by an interaction of R132 with D275, which is lost in R132H IDH1[23]. We predict that R132Q IDH1 may conserve this interaction; thus, allowing for WT activity and poor inhibitor affinity. To test this hypothesis, we sought to solve the structure of R132Q IDH1 in apo and holo (NADPH and αKG bound, and $NADP^+$ and isocitrate bound) forms.

Hanging drop vapor diffusion was performed as the method to obtain crystals. Nucleation happened overnight and crystal grew for about one week. The crystals were thin plates and diffracted weakly (Figure 16). R132Q IDH1 in complex with the neomorphic and WT ligands grew under the same conditions, while conditions for successfully growing apo R132Q IDH1 crystals were not determined. Data collection occurred at the Advanced Photon Source in Chicago. The highest resolution obtain was 3.38 Å (Table13, Figure 16). However, a low I/sigma value for the outer shell suggested that the reflections were below the signal-to-noise threshold (Table 13). The Rmerge was high overall at 25 % at overall diffraction (Table 14), while an R_{merge} of < 5% is preferred. Therefore, this data set was not suiTable for processing. The space group determined

was P 1 21 with unit cell dimensions of 85.16, 193.21 and 90.00 Å with α, β, and γ angles of 90.00, 103.64, and 90.00º, respectively. The diffraction showed low mosaicity at 0.15684º.

Table 13. Data collection results for R132Q IDH1 bound to isocitrate, $NADP^+$, and Ca^{2+} diffracting to 3.38 Å

	Overall	Inner Shell	Outer shell
High resolution limit	3.38	12.20	3.38
Low resolution limit	96.61	96.61	3.52
Completeness	98.0	96.8	95.5
Multiplicity	3.5	3.5	3.6
I/sigma	4.2	14.4	0.8
CC (1/2)	0.985	0.989	0.316
Rmerge	0.250	0.080	1.821
Rmerge (anomalous)	0.213	0.074	1.555

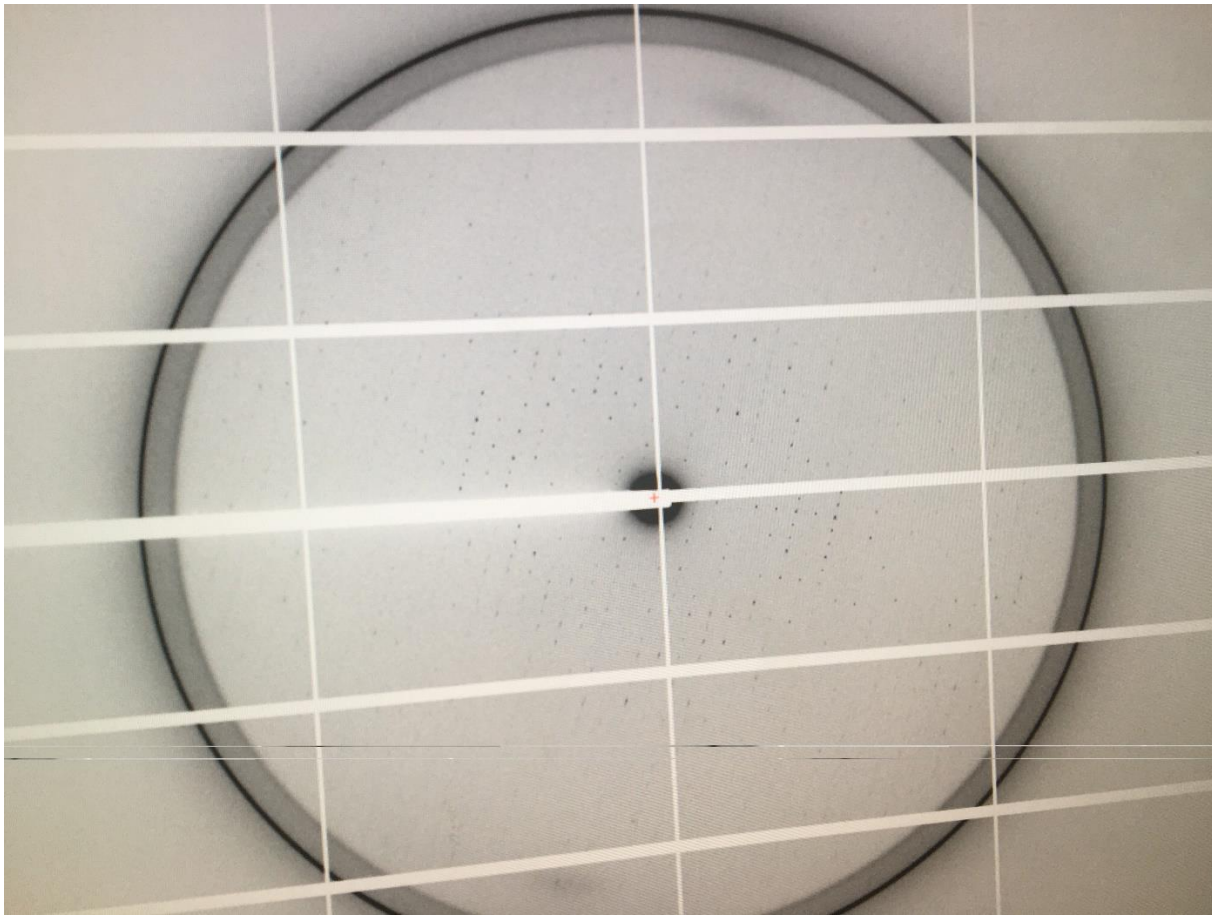

Figure 16. X-ray diffraction of R132Q IDH1 bound to isocitrate, $NADP^+$, and Ca^{2+}. Weak diffraction was observed as the reflections at higher resolution were below the signal-to-noise ratio.

4.5. Discussion

In this work, we reported rate parameters for the catalytic cycle of mutant IDH1 for the conversion of αKG to D2HG that are primarily experimentally derived. Previous work determined the binding mechanism of NADPH and αKG with mutant IDH1 as ordered sequential, where NADPH binds before αKG[17]. Structural studies of WT and R132H IDH1 described conformational changes that the enzyme undergoes in order to perform catalysis following binding of isocitrate[3, 23]. The catalytic rate (k_{cat}) for several IDH1 mutations have been determined[4, 16], though rate parameters for the catalytic cycle for D2HG production has not been proposed. Moreover, comparing the intrinsic rate constant associated for this catalytic cycle between R132H and R132Q

IDH1 will further highlight catalytic features that make R132Q IDH1 a better D2HG producer than R132H IDH1. Understanding the catalytic cycle of mutant IDH1 when catalyzing the neomorphic reaction provides insights on inhibitor selectivity and highlights kinetic features that may be extrapolated to the reduction of α-keto acids by other metabolic dehydrogenases, such as lactate and malate dehydrogenase[32]. This work may also aid in developing inhibitors selective for R132Q IDH1.

The mechanism of substrate binding for the neomorphic reaction is ordered sequential, where NADPH binds first[17]. We confirmed that binding of NADPH to mutant IDH1 is likely a one-step process[17]. This is due to our finding that when a single exponential equation is fit to an experiment measuring changes in fluorescence upon NADPH binding to mutant IDH1, there is a linear progression relationship between NADPH concentration and the k_{obs} (Figure 5F and 6H). WT IDH1 showed the fastest rate of NADPH binding (k_1), followed by R132Q and R132H IDH1 (Figure 5, 6, Table 7). Interestingly, ITC experiments revealed that NADPH had higher affinity for R132Q and R132H IDH1 compared to WT IDH1 (Figure 7). These results suggest that the rate of dissociation of NADPH (k_{-1}) for WT IDH1 is the fastest out of the three forms of the enzyme, meaning that the lower affinity of WT IDH1 for NADPH compared to the mutants results from much higher off rates (k_{-1}). R132Q and R132H IDH1 showed tighter binding of NADPH (Figure 7) relative to WT IDH1, and the lack of points in the linear phase of the sigmoidal curve suggested an infinitely tight binding of substrate; thus, the K_D values obtained by the fit are error-prone. These results suggest that the binding mechanism for the neomorphic reaction may be ordered sequential due to the tight binding of NADPH to the enzyme – a truly apo form of the enzyme is rarely available to bind αKG. On the other hand, WT IDH1 has a random sequential binding

mechanism of NADPH and αKG for the reverse reaction (isocitrate formation)[17], which can be driven by weaker affinity of NADPH for WT IDH1.

The NADPH binding kinetics were also performed at ambient temperature for R132Q and R132H IDH1 since the quality of the data was better at this temperature, and these data were both analytically (fitting a single exponential equation) and globally fit. Analytical fitting of the NADPH binding kinetics for R132Q IDH1 showed a k_1 value (Figure 2) almost half of what the global fitting predicted (Table 11 and 7). On the other hand, R132H IDH1 had similar k_1 values when using analytical fitting and Global Fitting computer simulations. It is important to highlight that the true rates of NADPH binding are equal or greater than what it is reported here due to artificially slowing down the binding reaction with glycerol. The rate of NADPH dissociation (k_{-1}) was not determined analytically due to larger error in fitting. Global fitting computer simulation allowed us to obtain more accurate results for k_{-1}. The data quality for R132H IDH1 was sufficient that the global fitting software reported tight boundaries when assessing error. On the other hand, R132Q IDH1 had lower data quality, and only an upper limit for k_{-1} was determined. In general, R132Q IDH1 has a slower k_{-1} rate compared to R132H IDH1. Using the rate constants determined by global fitting, R132Q IDH1 bound NADPH more tightly than R132H IDH1. Although previous work has shown that R132Q IDH1 has conserved WT activity[4], the caveat of steady state kinetic experiments is the vast excess of $NADP^+$ relative to enzyme. In these experiments, concentrations of $NADP^+$ in the range of 200 μM were used, while intracellular concentration of NADPH is higher than $NADP^+$[33]. Though this higher concentration of $NADP^+$ may be able to outcompete the very tightly bound NADPH in the artificial conditions of steady-state kinetics experiments, in the cell, $NADP^+$ levels may not be high enough to outcompete the NADPH. As a result, R132Q IDH1

would not be able to perform the normal reaction in physiological relevant conditions, meaning that its dual activity in the cell may not be relevant.

Binding affinities for WT, R132Q, and R132H IDH1 were determined for isocitrate and αKG. WT IDH1 showed a low μM K_D for isocitrate compared to R132Q IDH1. As described in 2010[23], ITC experiments showed no measurable binding of isocitrate to R132H IDH1. Yang and colleagues described a pre-binding conformation in WT IDH1 whereby R132 and D275 interact to stabilize the regulatory domain in the dimer interface[23]. Mutation to R132H IDH1 presumably ablates this interation, and thus disrupting isocitrate binding[23]. Therefore, the transition of the α10 regulatory domain from a helix to a random coil at least in part promotes mutant IDH1 for inhibitor binding at the dimer interface[18, 21]. Although R132Q IDH1 showed a weak binding for isocitrate, it may be possible that this mutant conserves the pre-binding conformation to at least some degree, thus stabilizing the regulatory domain of R132Q IDH1. Moreover, this pre-binding conformation may block inhibitor binding; thus, explaining lack of susceptibility of this mutant to mutant IDH1 inhibitors[16]. Crystal structures will be required to determinate this.

The K_D of R132Q IDH1 with αKG was not accurately determined with ITC. The expected stoichiometry between αKG and the IDH1 homodimer is 1, as shown with R132H IDH1 (Table 8). However, our ITC experiments showed a stoichiometry of 4; thus, any binding affinity determined by the fit would not be accurate. Interestingly, the raw data showed spikes in heat going in both directions (either absorbed or released) (Figure 11A). These results may suggest that other phenomena may have taken place in the ITC cell during the experiments. Nevertheless, global fitting computer simulations allowed us to model possible rate constants associated with αKG binding for R132Q as well as R132H IDH1.

The rate of binding of αKG (k_2 Figure 2) for R132Q IDH1 was > 100-fold faster than seen with R132H IDH1. Interestingly, global fitting computer simulations showed that the rate of αKG dissociation (k_{-2} inFigure 2) is > 10-fold faster for R132Q than R132H IDH1. The simulated K_D of αKG with R132Q IDH1 is > 10-fold tighter than R132H IDH1. These results suggest that binding of αKG to mutant IDH1 is driven mostly by the rate of binding (k_{on}) rather than the rate of dissociation (k_{off}). These results are opposite to NADPH binding where the rate of dissociation (k_{-1}) drives substrate affinity. It is possible that if a pre-binding conformation in the α10 regulatory domain exists for R132Q IDH1, this may facilitate binding of αKG for this mutational variant by increasing the rate of substrate binding. In contrast, R132H IDH1 does not appear to have this pre-binding conformation[23], perhaps slowing the rate. Although this binding mechanism was characterized for isocitrate and not αKG, Yang and colleagues described that WT IDH1 has this pre-binding conformation (an unfolded loop) before binding of any substrate due to the interaction between resdiues D275 and R132[23]. Moreover, they mentioned that the α10 regulatory domain folds in both WT and R132H IDH1 when substrate is bound, as seen in crystal structures of R132H IDH1 when bound to αKG[17, 23]. In the case of R132Q IDH1, the size and shape of Q132 may likely conserve mild interactions with D275, as seen on WT IDH1, thus having this pre-binding conformation, allowing for isocitrate binding and a tighter binding for αKG relative to R132H IDH1. This pre-binding state of WT IDH1, and possibly R132Q IDH1, may provide highlights in their lack of inhibitor affinity, since a well-defined unfolded loop in the α10 regulatory domain may prevent inhibitors from binding[16, 19, 20].

HDX-MS experiments were performed to understand the dynamics associated with substrate binding. The peptides we focused on were those spanning in the α10 regulatory domain in both WT and R132H IDH1. The relative uptake for apo WT IDH1 was between 50 and 60% of

the total possible for the specific peptide (Figure 10). This may be due to less dynamic secondary structures happening before and after the regulatory domain. Once isocitrate bound, the uptake of deuterium dropped drastically. These results are in agreement with previous structural work on WT IDH1[3, 23], where the regulatory domain folds into the α10 helix. A helix is a less dynamic secondary structure than a loop, thus, explaining the difference in deuterium uptake between apo and isocitrate bound with WT IDH1.

Interestingly, HDX-MS experiments on R132H IDH1 showed a smaller difference in uptake upon binding of αKG (Figure 10D-F) compared to WT IDH1. The difference between apo and with αKG, NADPH, and Ca^{2+} for R132H IDH1 was between 4-6% lower. Although the degree of flexibility of the α10 regulatory domain in R132H IDH1 is similar to WT IDH1, both in apo form, the change in deuterium uptake by R132H IDH1 in holo form is similar to its apo form, in contrast to WT IDH1 that a significant decreased of deuterium uptake is observed (Figure 10). These results indicate that α10 regulatory domain of WT IDH1 in holo form is more rigid than R132H IDH1 when bound to αKG. Since R132H IDH1 in holo form has a more flexible α10 regulatory domain than WT IDH1, also in holo form, small molecule inhibitors find it easier to get to the allosteric binding pocket in R132H IDH1[21], than in WT IDH1 due to a more rigid domain. Although HDX-MS did not show compelling evidence of a conformational change in R132H IDH1 upon binding of αKG, FRET pairing experiments between a fluorophore and an unnatural tryptophan based amino acid in the α10 regulatory domain may provide the output required for detection of any movement (as a change in fluorescence as a function of time), thus providing evidence of this structural change before hydride transfer as proposed on Figure 2A.

Previously, we have performed an extensive steady state kinetic characterization of non-tumor and tumor-relevant IDH1 mutations[4, 16]. The catalytic rates obtained in steady-state kinetics

describe the rate limiting step of the catalytic cycle. When performing single turnover experiments, WT IDH1 showed a slightly higher k_{obs} compared to our previously reported k_{cat} for the production of αKG (Table 10)[4, 16]. These results are not surprising since we assumed that 100% of the enzyme present was able to catalyze substrate turnover in our steady-state kinetic experiments. Therefore, when performing single turnover experiments, we use an analytical function to fit the data that is not dependent on active enzyme concentration (Figure 12), thus, showing a faster rate than out previously reported. On the other hand, R132Q IDH1 showed a k_{obs} for αKG production about half of what we had reported. Since the k_{cat} is the slowest rate in the catalytic cycle, it is impossible that a slower rate could be observed. The slowest rate could be attributed to a low stability of R132Q IDH1 in the stopped-flow, as we observed protein precipitation after each assay. Similar results were obtained from the neomorphic single turnover pre-steady-state assays done on R132H IDH1. Moreover, computer simulations also showed that the rate of chemistry for the neomorphic reaction ($k_{chem,\ \alpha KG}$) further providing supportive evidence of chemistry as the rate-limiting step of the cycle. Since our single turnover experiments rates agreed well with our k_{cat} for the normal and neomorphic reaction (Figure 1A and B, respectively), chemistry is indeed the rate-limiting step in the catalytic cycle for αKG and D2HG production.

Unfortunately, X-ray crystallography was not completed for apo and holo forms of R132Q IDH1. Although crystals were grown, the diffraction obtained from them was poor (Figure 1). With X-ray crystallography, it would be possible to understand whether R132Q IDH1 shows a pre-binding conformation as described by Yang and colleagues on WT IDH1[23]. This would provide important insights in explaining the difference in binding affinity for both αKG and isocitrate compared to R132H and WT IDH1. Moreover, a crystal structure of R132Q IDH1 would clarify why this mutant can catalyze both the normal and neomorphic reactions, and perhaps

provide a mechanism of why it has low affinity for mutant IDH1 inhibitors[23]. Although several conclusions were drawn from our kinetic work, X-ray crystallography would support these findings at the molecular level.

R132Q IDH1 is a unique and interesting mutant that is not fully understood yet. This mutant's high affinity for NADPH suggests that its dual activity may not be relevant in physiological conditions. Quantification of αKG levels in cells expressing R132Q IDH1 relative to cells expressing WT IDH1 will determine whether R132Q IDH1 catalyzes the oxidative decarboxylation of isocitrate in cells. Finding kinetic evidence of conformational change will not only provide intrinsic rate constants associated to this step in the catalytic cycle, it will also elucidate different kinetic features between mutant and WT IDH1 during catalysis. FRET experiments on the α10 regulatory domain will provide the necessary output to probe for a conformational change. This step of the catalytic cycle is particularly important since it could highlight the inhibitor affinity differences between R132H IDH1 and R132Q and WT IDH1. Thus, providing a step in the catalytic cycle that may be targeted with small molecule inhibitor so R132Q IDH1 is inhibited. Although this work has revealed important mechanistic features of mutant IDH1, solving the structure of R132Q IDH1 as well as probing for conformational change will set a solid foundation for understanding the molecular mechanism of mutant IDH1 in tumors and ways to gain better selectivity among all IDH1 mutants.

4.6. References

1. Warburg, O., Über den Stoffwechsel der Carcinomzelle. *Klin Wochenschr* **1925,** *4*, 534-536.

2. Warburg, O., Origin of cancer cells. *Oncologia* **1956,** *9* (2), 75-83.

3. Xu, X.; Zhao, J.; Xu, Z.; Peng, B.; Huang, Q.; Arnold, E.; Ding, J., Structures of human cytosolic NADP-dependent isocitrate dehydrogenase reveal a novel self-regulatory mechanism of activity. *J Biol Chem* **2004,** *279* (32), 33946-57.

4. Avellaneda Matteo, D.; Grunseth, A. J.; Gonzalez, E. R.; Anselmo, S. L.; Kennedy, M. A.; Moman, P.; Scott, D. A.; Hoang, A.; Sohl, C. D., Molecular mechanisms of isocitrate dehydrogenase 1 (IDH1) mutations identified in tumors: The role of size and hydrophobicity at residue 132 on catalytic efficiency. *J Biol Chem* **2017,** *292* (19), 7971-7983.

5. Leonardi, R.; Subramanian, C.; Jackowski, S.; Rock, C. O., Cancer-associated isocitrate dehydrogenase mutations inactivate NADPH-dependent reductive carboxylation. *J Biol Chem* **2012,** *287* (18), 14615-20.

6. Mardis, E. R.; Ding, L.; Dooling, D. J.; Larson, D. E.; McLellan, M. D.; Chen, K.; Koboldt, D. C.; Fulton, R. S.; Delehaunty, K. D.; McGrath, S. D.; Fulton, L. A.; Locke, D. P.; Magrini, V. J.; Abbott, R. M.; Vickery, T. L.; Reed, J. S.; Robinson, J. S.; Wylie, T.; Smith, S. M.; Carmichael, L.; Eldred, J. M.; Harris, C. C.; Walker, J.; Peck, J. B.; Du, F.; Dukes, A. F.; Sanderson, G. E.; Brummett, A. M.; Clark, E.; McMichael, J. F.; Meyer, R. J.; Schindler, J. K.; Pohl, C. S.; Wallis, J. W.; Shi, X.; Lin, L.; Schmidt, H.; Tang, Y.; Haipek, C.; Wiechert, M. E.; Ivy, J. V.; Kalicki, J.; Elliott, G.; Ries, R. E.; Payton, J. E.; Westervelt, P.; Tomasson, M. H.; Watson, M. A.; Baty, J.; Heath, S.; Shannon, W. D.; Nagarajan, R.; Link, D. C.; Walter, M. J.; Graubert, T. A.; DiPersio, J. F.; Wilson, R. K.; Ley, T. J., Recurring mutations found by sequencing an acute myeloid leukemia genome. *N Engl J Med* **2009,** *361* (11), 1058-66.

7. Parsons, D. W.; Jones, S.; Zhang, X.; Lin, J. C.; Leary, R. J.; Angenendt, P.; Mankoo, P.; Carter, H.; Siu, I. M.; Gallia, G. L.; Olivi, A.; McLendon, R.; Rasheed, B. A.; Keir, S.; Nikolskaya, T.; Nikolsky, Y.; Busam, D. A.; Tekleab, H.; Diaz, L. A., Jr.; Hartigan, J.; Smith, D. R.; Strausberg, R. L.; Marie, S. K.; Shinjo, S. M.; Yan, H.; Riggins, G. J.; Bigner, D. D.; Karchin, R.; Papadopoulos, N.; Parmigiani, G.; Vogelstein, B.; Velculescu, V. E.; Kinzler, K. W., An integrated genomic analysis of human glioblastoma multiforme. *Science* **2008,** *321* (5897), 1807-12.

8. Balss, J.; Meyer, J.; Mueller, W.; Korshunov, A.; Hartmann, C.; von Deimling, A., Analysis of the IDH1 codon 132 mutation in brain tumors. *Acta Neuropathol* **2008,** *116* (6), 597-602.

9. Bleeker, F. E.; Lamba, S.; Leenstra, S.; Troost, D.; Hulsebos, T.; Vandertop, W. P.; Frattini, M.; Molinari, F.; Knowles, M.; Cerrato, A.; Rodolfo, M.; Scarpa, A.; Felicioni, L.; Buttitta, F.; Malatesta, S.; Marchetti, A.; Bardelli, A., IDH1 mutations at residue p.R132 (IDH1(R132)) occur frequently in high-grade gliomas but not in other solid tumors. *Hum Mutat* **2009,** *30* (1), 7-11.

10. Cerami, E.; Gao, J.; Dogrusoz, U.; Gross, B. E.; Sumer, S. O.; Aksoy, B. A.; Jacobsen, A.; Byrne, C. J.; Heuer, M. L.; Larsson, E.; Antipin, Y.; Reva, B.; Goldberg, A. P.; Sander, C.; Schultz, N., The cBio cancer genomics portal: an open platform for exploring multidimensional cancer genomics data. *Cancer Discov* **2012,** *2* (5), 401-4.

11. Hirata, M.; Sasaki, M.; Cairns, R. A.; Inoue, S.; Puviindran, V.; Li, W. Y.; Snow, B. E.; Jones, L. D.; Wei, Q.; Sato, S.; Tang, Y. J.; Nadesan, P.; Rockel, J.; Whetstone, H.; Poon, R.; Weng, A.; Gross, S.; Straley, K.; Gliser, C.; Xu, Y.; Wunder, J.; Mak, T. W.; Alman, B. A., Mutant IDH is sufficient to initiate enchondromatosis in mice. *Proc Natl Acad Sci U.S.A* **2015,** *112* (9), 2829-34.

12. Dang, L.; White, D. W.; Gross, S.; Bennett, B. D.; Bittinger, M. A.; Driggers, E. M.; Fantin, V. R.; Jang, H. G.; Jin, S.; Keenan, M. C.; Marks, K. M.; Prins, R. M.; Ward, P. S.; Yen, K. E.; Liau, L. M.; Rabinowitz, J. D.; Cantley, L. C.; Thompson, C. B.; Vander Heiden, M. G.; Su, S. M., Cancer-associated IDH1 mutations produce 2-hydroxyglutarate. *Nature* **2009,** *462* (7274), 739-44.

13. Figueroa, M. E.; Abdel-Wahab, O.; Lu, C.; Ward, P. S.; Patel, J.; Shih, A.; Li, Y.; Bhagwat, N.; Vasanthakumar, A.; Fernandez, H. F.; Tallman, M. S.; Sun, Z.; Wolniak, K.; Peeters, J. K.; Liu, W.; Choe, S. E.; Fantin, V. R.; Paietta, E.; Lowenberg, B.; Licht, J. D.; Godley, L. A.; Delwel, R.; Valk, P. J.; Thompson, C. B.; Levine, R. L.; Melnick, A., Leukemic IDH1 and IDH2 mutations result in a hypermethylation phenotype, disrupt TET2 function, and impair hematopoietic differentiation. *Cancer Cell* **2010,** *18* (6), 553-67.

14. Chowdhury, R.; Yeoh, K. K.; Tian, Y. M.; Hillringhaus, L.; Bagg, E. A.; Rose, N. R.; Leung, I. K.; Li, X. S.; Woon, E. C.; Yang, M.; McDonough, M. A.; King, O. N.; Clifton, I. J.; Klose, R. J.; Claridge, T. D.; Ratcliffe, P. J.; Schofield, C. J.; Kawamura, A., The oncometabolite 2-hydroxyglutarate inhibits histone lysine demethylases. *EMBO Rep* **2011,** *12* (5), 463-9.

15. Pusch, S.; Schweizer, L.; Beck, A. C.; Lehmler, J. M.; Weissert, S.; Balss, J.; Miller, A. K.; von Deimling, A., D-2-Hydroxyglutarate producing neo-enzymatic activity inversely correlates with frequency of the type of isocitrate dehydrogenase 1 mutations found in glioma. *Acta Neuropathol Commun* **2014,** *2*, 19.

16. Avellaneda Matteo, D.; Wells, G. A.; Luna, L. A.; Grunseth, A. J.; Zagnitko, O.; Scott, D. A.; Hoang, A.; Luthra, A.; Swairjo, M. A.; Schiffer, J. M.; Sohl, C. D., Inhibitor potency varies widely among tumor-relevant human isocitrate dehydrogenase 1 mutants. *Biochem J* **2018,** *475* (20), 3221-3238.

17. Rendina, A. R.; Pietrak, B.; Smallwood, A.; Zhao, H.; Qi, H.; Quinn, C.; Adams, N. D.; Concha, N.; Duraiswami, C.; Thrall, S. H.; Sweitzer, S.; Schwartz, B., Mutant IDH1 enhances the production of 2-hydroxyglutarate due to its kinetic mechanism. *Biochemistry* **2013,** *52* (26), 4563-77.

18. Merk, A.; Bartesaghi, A.; Banerjee, S.; Falconieri, V.; Rao, P.; Davis, M. I.; Pragani, R.; Boxer, M. B.; Earl, L. A.; Milne, J. L.; Subramaniam, S., Breaking Cryo-EM resolution barriers to facilitate drug discovery. *Cell* **2016,** *165* (7), 1698-707.

19. Davis, M. I.; Gross, S.; Shen, M.; Straley, K. S.; Pragani, R.; Lea, W. A.; Popovici-Muller, J.; Delabarre, B.; Artin, E.; Thorne, N.; Auld, D. S.; Li, Z.; Dang, L.; Boxer, M. B.; Simeonov, A.,

Biochemical, cellular and biophysical characterization of a potent inhibitor of mutant isocitrate dehydrogenase IDH1. *J Biol Chem* **2014,** *289*, 13717-13725.

20. Deng, G.; Shen, J.; Yin, M.; McManus, J.; Mathieu, M.; Gee, P.; He, T.; Shi, C.; Bedel, O.; McLean, L. R.; Le-Strat, F.; Zhang, Y.; Marquette, J. P.; Gao, Q.; Zhang, B.; Rak, A.; Hoffmann, D.; Rooney, E.; Vassort, A.; Englaro, W.; Li, Y.; Patel, V.; Adrian, F.; Gross, S.; Wiederschain, D.; Cheng, H.; Licht, S., Selective inhibition of mutant isocitrate dehydrogenase 1 (IDH1) via disruption of a metal binding network by an allosteric small molecule. *J Biol Chem* **2015,** *290* (2), 762-74.

21. Xie, X.; Baird, D.; Bowen, K.; Capka, V.; Chen, J.; Chenail, G.; Cho, Y.; Dooley, J.; Farsidjani, A.; Fortin, P.; Kohls, D.; Kulathila, R.; Lin, F.; McKay, D.; Rodrigues, L.; Sage, D.; Toure, B. B.; van der Plas, S.; Wright, K.; Xu, M.; Yin, H.; Levell, J.; Pagliarini, R. A., Allosteric mutant IDH1 inhibitors reveal mechanisms for IDH1 mutant and isoform selectivity. *Structure* **2017,** *25* (3), 506-513.

22. Norsworthy, K. J.; Luo, L.; Hsu, V.; Gudi, R.; Dorff, S. E.; Przepiorka, D.; Deisseroth, A.; Shen, Y. L.; Sheth, C. M.; Charlab, R.; Williams, G. M.; Goldberg, K. B.; Farrell, A. T.; Pazdur, R., FDA Approval Summary: Ivosidenib for Relapsed or Refractory Acute Myeloid Leukemia with an Isocitrate Dehydrogenase-1 Mutation. *Clin Cancer Res* **2019,** *25* (11), 3205-3209.

23. Yang, B.; Zhong, C.; Peng, Y.; Lai, Z.; Ding, J., Molecular mechanisms of "off-on switch" of activities of human IDH1 by tumor-associated mutation R132H. *Cell Res* **2010,** *20* (11), 1188-200.

24. Bolduc, J. M.; Dyer, D. H.; Scott, W. G.; Singer, P.; Sweet, R. M.; Koshland, D. E., Jr.; Stoddard, B. L., Mutagenesis and Laue structures of enzyme intermediates: isocitrate dehydrogenase. *Science* **1995,** *268* (5215), 1312-8.

25. Lee, M. E.; Dyer, D. H.; Klein, O. D.; Bolduc, J. M.; Stoddard, B. L.; Koshland, D. E., Jr., Mutational analysis of the catalytic residues lysine 230 and tyrosine 160 in the NADP(+)-dependent isocitrate dehydrogenase from Escherichia coli. *Biochemistry* **1995,** *34* (1), 378-84.

26. Aktas, D. F.; Cook, P. F., A lysine-tyrosine pair carries out acid-base chemistry in the metal ion-dependent pyridine dinucleotide-linked beta-hydroxyacid oxidative decarboxylases. *Biochemistry* **2009,** *48* (16), 3565-77.

27. Ramsey, K. M.; Dembinski, H. E.; Chen, W.; Ricci, C. G.; Komives, E. A., DNA and IkappaBalpha Both Induce Long-Range Conformational Changes in NFkappaB. *J Mol Biol* **2017,** *429* (7), 999-1008.

28. Wales, T. E.; Fadgen, K. E.; Gerhardt, G. C.; Engen, J. R., High-speed and high-resolution UPLC separation at zero degrees Celsius. *Anal Chem* **2008,** *80* (17), 6815-20.

29. Otwinowski, Z.; Minor, W., Processing of X-ray diffraction data collected in oscillation mode. *Methods Enzymol* **1997,** *276*, 307-26.

30. Johnson, K. A., Fitting enzyme kinetic data with KinTek Global Kinetic Explorer. *Methods Enzymol* **2009,** *467*, 601-26.

31. Johnson, K. A.; Simpson, Z. B.; Blom, T., FitSpace explorer: an algorithm to evaluate multidimensional parameter space in fitting kinetic data. *Anal Biochem* **2009,** *387* (1), 30-41.

32. Intlekofer, A. M.; Wang, B.; Liu, H.; Shah, H.; Carmona-Fontaine, C.; Rustenburg, A. S.; Salah, S.; Gunner, M. R.; Chodera, J. D.; Cross, J. R.; Thompson, C. B., L-2-Hydroxyglutarate production arises from noncanonical enzyme function at acidic pH. *Nat Chem Biol* **2017,** *13* (5), 494-500.

33. Blacker, T. S.; Duchen, M. R., Investigating mitochondrial redox state using NADH and NADPH autofluorescence. *Free radical biology & medicine* **2016,** *100*, 53-65.